

Isogeometric Analysis for Smart Plate Structures

Isogeometrische Analyse voor Slimmeplaatconstructies

Phuc Phung Van

Promotoren: prof. dr. ir. M. Abdel Wahab, prof. dr. H. Nguyen Xuan

Proefschrift ingediend tot het behalen van de graad van

Doctor in de Ingenieurswetenschappen: Werktuigkunde-Elektrotechniek

Vakgroep Elektrische Energie, Systemen en Automatisering

Voorzitter: prof. dr. ir. Jan Melkebeek

Faculteit Ingenieurswetenschappen en Architectuur

Academiejaar 2015 - 2016



ISBN 978-90-8578-876-8

NUR 978

Wettelijk depot: D/2016/10.500/8

Promoters

Prof. dr. ir. Magd Abdel Wahab, Ghent University, Belgium

Assoc. Prof. dr. Nguyen Xuan Hung, HUTECH University, Vietnam

Examination Committee

Prof. dr. ir. Rik Van de Walle (Chair)

Ghent University, Belgium

Prof. dr. ir. Magd Abdel Wahab

Ghent University, Belgium

Assoc. Prof. dr. Nguyen Xuan Hung

HUTECH University, Vietnam

Prof. dr. ir. Guido De Roeck

University of Leuven, Belgium

Prof. dr. ir. Mia Loccufier

Ghent University, Belgium

Prof. dr. ir. Joris Degrieck

Ghent University, Belgium

Prof. dr. Stéphane Pierre Alain Bordas

University of Luxembourg, Luxembourg

Research Institute

Laboratory Soete

Department of Electrical Energy, Systems and Automation

Faculty of Engineering and Architecture

Ghent University

Technologiepark 903

B-9052 Zwijnaarde

Belgium

Email: Phuc.PhungVan@UGent.be, phucphungvan@gmail.com

<http://www.soetelaboratory.ugent.be>

To my whole family ...

Acknowledgements

The research reported in this dissertation has been carried out in the Finite Element Modeling Research group, Department of Electrical Energy, Systems and Automation, Faculty of Engineering and Architecture, Ghent University, Belgium. This process has been a wonder adventure and very exciting time. Nevertheless, it has not been without its share of pain and I could not have achieved this work without the support, help and encouragement of many people around me.

Firstly, I would like to express my deepest gratitude to my thesis advisors, Prof. Magd Abdel Wahab, Department of Electrical Energy, Systems and Automation, Ghent University, and Assoc. Prof. Nguyen Xuan Hung from Center for Interdisciplinary Research in Technology, Ho Chi Minh City University of Technology (HUTECH), Vietnam, for having accepted me as their PhD student and for the guidance, trust, encouragement and freedom, which they have offered during my research. Working with both of them was always a pleasure. Moreover, I am grateful to Prof. Nguyen Dang Hung at University of Liège and Assoc. Prof. Nguyen Hoai Son at University of Technical Education Ho Chi Minh City for having helped and supported me to overcome many difficulties in my life. I would like to thank Assoc. Prof. Nguyen Thoi Trung for his helpful guidance at first step of doing research and as my master's supervisor.

I would like also to acknowledge VLIR-UOS awards scholarships, CWO, Faculty of Engineering and Architecture, Ghent University and Erasmus Mundus Action 2, Lotus Unlimited Project for their financial assistance throughout my research without their support this thesis would not have been completed.

This work involves a huge amount of computer implementation of numerical methods, which could not have been easier without the constant help of Dr. Thai Hoang Chien and MSc. Tran Vinh Loc. I am in debt to them for various advices on programming issues, and for the cooperation and the understanding during my study.

I take this chance to thank Prof. Stephane Bordas at University of Luxembourg, Prof. Kim Meow Liew at City University of Hong Kong and Prof. António Joaquim Mendes Ferreira at University of Porto, for their assistance, insightful suggestions, and collaborations in research.

It has been fortunate for me to have some very nice colleagues at Laboratory Soete to whom I would like to say “thank you for your help and friendly support”. The constructive suggestions, professional opinions and interactive discussion among our group definitely helped me to improve the quality of my research work.

Living abroad far away from my family would be much harder without the company of many Vietnamese people to whom I particularly give thanks to family of Le Tam Phuoc and Huynh Nguyen Bao Loan, family of Nguyen Phuc Thuong and Pham Thi Lan Phuong, family of Pham Huu Ha Giang and Phan Phuong, Truong Quoc Thai, Huynh Thai Nguyen, family of Tran Tan Huy and Ngo Thi Thuy An, Huynh Thanh Toi, Vo Van Tuan, family of Luong Duc Anh and Doan Thanh Thuy, Nguyen Van Hung, family of Do Hoai Duc and Trinh Thi Huong Giang, etc., for the time we have spent together. A gratitude is devoted to Dr. Cao Duc Toan for his support during my stay in Germany.

Last but not least, I would like to express my biggest gratitude to my parents and my sister for everything. This thesis is dedicated to my beloved parents.

Phung Van Phuc

Ghent, Belgium

January 2016

Summary

Smart materials are material classes, which have several properties, such as coupling electrical and mechanical properties, changing properties from one surface to the other across the thickness, high strength and stiffness, moisture resistance, etc. Some of the most popular and common types of smart materials are as follows:

- Piezoelectric materials are materials in which a voltage is produced when load/stress is applied and vice versa.
- Carbon nanotube-reinforced composites are a class of new materials, which are being developed to take advantage of electrical conductivity and the high tensile strength of carbon nanotube materials. Regarding mechanical properties, carbon nanotubes are the stiffest and strongest materials yet discovered in terms of elastic modulus and tensile strength. This strength leads to the covalent sp^2 bonds formed between the individual carbon atoms.
- Shape memory alloys (SMA) are materials that through stress changes (pseudo-elasticity) or temperature changes, large deformation can be produced and recovered. This is due to the martensitic phase change and induced elasticity at higher temperatures. And this phenomenon is called the shape memory effect.

The smart materials offer a considerable interest in many practical applications, such as micro-electromechanical systems (MEMS), automotive sensors, actuators, transducers, active damping devices and smart material systems, especially in the medical and aerospace industries. With these complex problems, i.e., coupling problems,

Nano-structures, etc., it is very difficult or impossible to find exact solutions or analytical solutions by solving the partial differential equations (PDEs). Hence, approximated solutions or numerical solutions are considered to be the most suitable in order to analyze and simulate these problems.

For numerical methods, isogeometric analysis (IGA) has been recently proposed as a useful numerical method of computational analysis with the aim of integrating Finite Element Analysis (FEA) and Computer Aided Design (CAD) into one model. Data generated from CAD can be used directly for FEA. It means that the IGA uses Non-Uniform Rational B-Splines (NURBS), which are commonly used in CAD in order to describe both the geometry and the unknown variables for analyzed problems. Hence, the exact geometry is expressed in both design and mechanical analysis. Therefore, the process of re-meshing in IGA can be omitted. And an advantage of NUBRS is its ability to easily control the continuity, as C^{p-1} continuity is obtained by using p -th order NURBS.

In this thesis, IGA is developed for analyzing and simulating smart plate structures. Four main contributions have been obtained from the results of the research as follows:

- Firstly, a simple and effective formulation using IGA based on higher-order shear deformation theory (HSDT) is presented to investigate dynamic control of piezoelectric composite plates. There are two field variables, which need to be approximated, including mechanical displacement field and electrical potential field. In composite plates, the mechanical displacement field is approximated according to the HSDT model with five degrees of freedom per each control point using isogeometric elements based on Non-Uniform Rational B-Spline (NURBS) basis functions. These achieve naturally any desired degree of continuity through the choice of the interpolation order, so that the method easily fulfils the C^1 -continuity requirement of the HSDT model. To simulate numerical results, NURBS with quadratic, cubic and quartic functions are considered. Besides, the electric potential is assumed to vary linearly through the thickness for each piezoelectric sublayer. Finally, governing equations of piezoelectric composite plates for static, free vibration analyses and dynamic control are expressed. In control section, a displacement and velocity feedback control algorithm is used for the active control of the static deflection and of the dynamic

response of the plates through a closed-loop control with bonded or embedded distributed piezoelectric sensors (the bottom layer) and piezoelectric actuators (the top layer). The displacement feedback control is based on the actuator, and the velocity feedback control gives the velocity component. The accuracy and reliability of the proposed method is verified by comparing its numerical predictions with those of other available numerical approaches.

- Secondly, IGA based on a generalized shear deformation theory for geometrically nonlinear transient analysis of smart piezoelectric functionally graded material (FGM) plates is developed. In this part, the electrical field is assumed to be independent on each layer and the mechanical displacements are approximated by the generalized higher order shear deformation theory. The nonlinear transient formulation for plates is formed with the total Lagrange approach based on the von Kármán strains. For nonlinear transient solution, Newmark's method and Newton-Raphson method are used to find displacements, velocities and accelerations at each time step. Besides, thermo-piezoelectric effects are also considered. Temperature distributions of the bottom surface and top surface of piezoelectric FGM model are assumed to be constant. The temperature variation along the thickness is obtained by solving the one-dimensional steady state heat equation. The material properties vary through the thickness of FGM and are assumed to follow the rule of mixture. To consider the interactions among the constituents, the Mori-Tanaka scheme is used. For numerical results, many examples are investigated and compared to other available numerical methods to show the accuracy and effectiveness of the present method. The effects of volume fraction exponents on frequencies and displacements of the piezoelectric FGM plates are examined. And the effects of thermo-electro-mechanical loads on the behavior of the plates are also studied.
- Thirdly, IGA based HSDT is proposed to investigate the static and dynamic vibration behavior of functionally graded carbon nanotube-reinforced composite plates. The material properties of functionally graded carbon nanotube-reinforced composites (FG-CNTRCs) are assumed to be graded through the thickness direction according to several linear distributions of the volume fraction of carbon nanotubes. Four distributions are considered UD (uniform), FG-V, FG-O and FG-X. For the FG-V type, the top surface of the CNTRC plate is CNT-rich.

In FG-X, the top and the bottom surface of CNTRC plate are CNT-rich. And in case of FG-O, the CNT-rich zone is in the middle of the CNTRC plate. The displacements of the CNTRC plates are approximated according to the third-order shear deformation theory. Numerical results proved the high accuracy and reliability of the proposed method in comparison with other available numerical approaches.

- Fourthly, an efficient computational approach based on a generalized unconstrained approach in conjunction with IGA are proposed for dynamic control of smart piezoelectric composite plates. A new function for the unconstrained third order shear deformation theory (UHSdT) is introduced. In this theory, there are seven degrees of freedom per control point. Constant gains of the displacement feedback control and velocity feedback control are used in active control analysis in order to predict geometrically nonlinear transient response of the piezoelectric composite plates. An optimization procedure using genetic algorithm (GA) is considered to search optimal design for actuator input voltages. Various numerical examples are investigated to demonstrate the effectiveness of the proposed method.

Samenvatting

Slimme materialen zijn materiaalsoorten met verschillende voordelen. Zo kunnen in deze materialen elektrische en mechanische eigenschappen aan elkaar gekoppeld worden en kunnen bepaalde kenmerken (zoals dikte, sterkte, hardheid, weerstand tegen vocht) van verschillende oppervlakken variëren. De meest voorkomende vormen van slimme materialen zijn de volgende:

- Piezo-elektrische materialen zijn materialen waarin elektrische spanning wordt geproduceerd door druk, en andersom, druk op de structuren tot stand komt wanneer er elektrische spanning op wordt aangelegd.
- Koolstofnanobuiscomposieten zijn een klasse van nieuwe materialen die worden ontwikkeld om te profiteren van de elektrische geleidbaarheid en de hoge treksterkte van koolstofnanobuismaterialen. Wat betreft mechanische eigenschappen, zijn koolstofnanobuisjes op het vlak van elasticiteitsmodule en treksterkte de stijfste en sterkste materialen tot dusver ontdekt. Deze sterkte leidt tot covalente sp^2 -binding tussen de afzonderlijke koolstofatomen.
- Geheugenmetaal is een materiaal dat door spanningsveranderingen (pseudo-elasticiteit) of temperatuurveranderingen grote deformatie kan produceren, maar ook naar diens originele geometrie kan terugkeren. Dit is het gevolg van een martensitische faseverandering en geïnduceerde elasticiteit bij hogere temperaturen. Dit fenomeen heet het vormgeheugeneffect.

Slimme materialen kennen vele praktische toepassingen, zoals micro-elektromechanische systemen, sensoren voor automobielen, actuatoren, transducers, actieve dempingapparaten, vooral gebruikt in de medische en luchtvaartindustrie. Deze

toepassingen zijn bijzonder complex en onderzoekers worden geconfronteerd met verschillende problemen, zoals koppelingsproblemen en problemen met nanostructuren. Het is zeer moeilijk of onmogelijk om exacte of analytische oplossingen te vinden voor deze problemen door het oplossen van partiële differentiaalvergelijkingen. Vandaar dat benaderende of numerieke oplossingen het meest geschikt zijn om deze problemen te analyseren en te simuleren.

Een bruikbare numerieke methode die recent werd voorgesteld is de isogeometrische analyse (IGA). Deze methode heeft als doel eindige-elementenanalyse en computerondersteund ontwerp in een model te integreren. Computerondersteunde ontwerpgegevens kunnen direct worden gebruikt voor eindige-elementenanalyse. Dit betekent dat IGA niet-uniforme rationale B-splines (NURBS) gebruikt, die vaak aangewend worden bij computerondersteunde ontwerpen om zowel de geometrie als de onbekende variabelen te beschrijven. De precieze geometrie wordt dus zowel in het ontwerp als in de mechanische analyse uitgedrukt. Vandaar dat in IGA de techniek van re-meshing kan worden weggelaten. Bovendien is een voordeel van NURBS de gemakkelijke continuïteitscontrole, gezien C^{p-1} continuïteit verkregen wordt door het gebruiken van NURBS tot de p^{de} orde.

In dit proefschrift wordt IGA gebruikt voor het ontwikkelen, analyseren en simuleren van slimmeplaatconstructies. Het onderzoek heeft de volgende vier bijdragen opgeleverd:

- Ten eerste wordt, met toepassing van IGA en op basis van de hogere-orde theorie voor afschuifvervorming, een eenvoudige en effectieve formulering voorgesteld om de dynamische controle te onderzoeken van piëzo-composietplaten. Er zijn twee variabele velden die moeten worden benaderd inclusief het mechanische verplaatsingsveld en het elektrische potentiaalveld. In de composietplaat wordt het mechanische verplaatsingsveld benaderd volgens het model van de hogere-orde theorie voor afschuifvervorming, met vijf vrijheidsgraden per controlepunt, en worden isogeometrische elementen gebruikt gebaseerd op NURBS basisfuncties. Zoals bekend, bereiken deze basisfuncties elke gewenste mate van continuïteit door de keuze van de orde van interpolatie, zodat de werkwijze gemakkelijk voldoet aan de C^1 -continuïteitsverplichting. Om numerieke resultaten te simuleren, worden NURBS met tweede, derde en vierde orde functies in aanmerking genomen. Daarnaast wordt verondersteld dat de

elektrische potentiaal lineair varieert doorheen de dikte van elke piëzo-elektrische onderlaag. Tot slot worden differentiaalvergelijkingen van piëzo-elektrische composietplaten voor statische, vrijetrillinganalyses en dynamische controle uitgedrukt. In de sectiecontrole wordt een controlealgoritme voor verplaatsings- en snelheidsterugkoppeling gebruikt voor de actieve controle van de statische afbuiging en de dynamische respons van de platen door middel van een gesloten regelkring met gebonden of ingesloten gelijkmatig verdeelde piëzo-elektrische sensoren (de onderste laag) en piëzo-elektrische actuatoren (de bovenste laag). De verplaatsingsterugkoppeling is gebaseerd op de actuator en de snelheidsterugkoppeling geeft de snelheidscomponent weer.

De nauwkeurigheid en betrouwbaarheid van de voorgestelde methode werden geverifieerd door vergelijking met de numerieke voorspellingen die via andere beschikbare numerieke benaderingen berekend werden.

- Ten tweede werd, op basis van de algemene theorie voor afschuifvervorming, IGA ontwikkeld voor de geometrische, niet-lineaire, tijdsafhankelijke analyse van slimme, piëzo-elektrische, functionele gradiënt materialen (FGM's). In dit deel wordt verondersteld dat het elektrische veld op elke laag onafhankelijk is en de mechanische verplaatsingen worden benaderd vanuit de algemene theorie voor afschuifvervorming van een hogere orde. De niet-lineaire, tijdsafhankelijke formulering voor platen wordt gevormd vanuit de totale Lagrange benadering op basis van de von Karman rekken. Voor de niet-lineaire tijdsafhankelijke oplossing worden de Newton-Raphson methode en de Newmark methode gebruikt om de verplaatsingen, snelheden en versnellingen van elke tijdstap te vinden. Daarnaast wordt het thermo-piezo-electrisch effect in aanmerking genomen. De temperatuurverdeling van het onder- en bovenvlak van het model dat samengesteld is uit piëzo-functionele gradient materialen wordt verondersteld constant te zijn. Het temperatuurverloop langs de plaatdikte wordt berekend door het oplossen van de eendimensionale constantewarmtestroomvergelijking. De eigenschappen van het materiaal variëren doorheen de plaatdikte van de FGM's en worden berekend door de mengregels. Om de interacties tussen de bestanddelen te bestuderen wordt de Mori-Tanaka methode toegepast. Voor numerieke resultaten werden verschillende voorbeelden onderzocht en vergeleken met andere beschikbare numerieke methodes om de nauwkeurigheid en efficiëntie van de voorgestelde werkwijze aan te tonen.

Het effect van volumefractie-exponenten van frequenties en verplaatsingen op de platen samengesteld uit slimme, piëzo-elektrische, functionele gradiënt materialen werd onderzocht. Bovendien werd het effect van thermoelektromechanische krachten op het gedrag van de platen bestudeerd.

- Ten derde wordt een systeem van isogeometrische analyse gebaseerd op de hogere-orde theorie voor afschuifvervorming voorgesteld om de statische en dynamische trillingen van composietplaten samengesteld uit functionele gradiënt koolstof nano-materiaal te onderzoeken. De materiaaleigenschappen van deze composietplaten worden verondersteld gegradeerd te zijn doorheen de dikterichting volgens verschillende lineaire volumefractiedistributies van de koolstofnanobuisjes. Vier verschillende mogelijke distributies worden in aanmerking genomen, met name UD (uniform), FG-V, FG-O en FG-X. Bij het type FG-V is de bovenkant van de plaat met koolstofnanobuisjes versterkt. In het type FG-X zijn de boven- en onderkanten van de plaat met koolstofnanobuisjes versterkt. En in het geval van FG-O is de middenzone van de plaat met koolstofnanobuisjes versterkt. De verplaatsingen van de platen worden benaderd vanuit de derde-orde theorie voor afschuifvervorming. Numerieke resultaten toonden een hoge nauwkeurigheid en betrouwbaarheid van de voorgestelde werkwijze in vergelijking met andere beschikbare numerieke benaderingen.
- Ten vierde wordt, op basis van een algemene benadering in combinatie met IGA, een efficiënte computerondersteunde aanpak voorgesteld voor de dynamische controle van slimme piëzo-elektrische composietplaten. Er wordt een nieuwe functie voor de algemene derde-orde theorie voor afschuifvervorming geïntroduceerd. In deze theorie zijn er zeven vrijheidsgraden per controlepunt. Constante versterkingen van de verplaatsings- en snelheidsterugkoppeling worden gebruikt in de actieve controleanalyse om de geometrische, niet-lineaire, tijdsafhankelijke respons van de piëzo-elektrische composietplaten te voorspellen. Een optimalisatieprocedure met behulp van een genetisch algoritme (GA) wordt in aanmerking genomen om een optimaal ontwerp te zoeken voor deingangsspanningen van actuatoren. De nauwkeurigheid en betrouwbaarheid van de voorgestelde werkwijze werden geverifieerd door vergelijking van de numerieke voorspellingen met berekeningen op basis van andere beschikbare numerieke benaderingen.

Contents

Acknowledgements	i
Summary	iii
Samenvatting	vii
Contents	xi
List of figures	xv
List of tables	xxi
Nomenclature	xxiii

Chapter 1 Introduction

1.1 Introduction	2
1.2 An historical development of IGA	3
1.3 Smart materials	4
1.4 Motivation of the thesis	6
1.5 Organization of the thesis	6
1.6 Concluding remarks	8

Chapter 2 Literature review

2.1 Overview	10
2.2 Literature review	10
2.2.1 Piezoelectric composite plates	10
2.2.2 Piezoelectric functionally graded materials plates	13
2.2.3 Functionally graded carbon nanotube-reinforced composite plates....	14
2.3 Goal of the thesis	17
2.4 Concluding remarks	17

Chapter 3 Smart materials and plate theories

3.1 Overview	20
3.2 Effective material properties	20
3.2.1 Piezoelectric plates	20
3.2.1.1 Composite materials	20
3.2.1.2 Functionally graded materials	24
3.2.2 Functionally graded carbon nanotube-reinforced composites	28
3.3 Plate theories	31
3.3.1 Classification of plate theories	31
3.3.2 An overview of composite plate theories	31
3.3.2.1 The classical laminated plate theory	31
3.3.2.2 The first-order shear deformation theory	33
3.3.2.3 The third-order shear deformation theory	34
3.3.2.4 The generalized higher-order shear deformation theory	35
3.4 Concluding remarks	37

Chapter 4 Isogeometric analysis

4.1 Overview	40
4.2 B-Spline	40
4.2.1 Basic functions	40
4.2.2 B-spline geometries	43
4.2.2.1 B-spline curve	43
4.2.2.2 B-spline surface	44
4.2.3 Refinement	44
4.2.3.1 Knot insertion (h -refinement)	47
4.2.3.2 Order elevation (p -refinement)	47
4.2.3.3 k -refinement	48
4.3 Non-Uniform Rational B-Splines	48
4.3.1 NURBS basic functions	48
4.3.2 NURBS curves	49
4.3.3 NURBS surfaces	50
4.4 Isogeometric discretization	51
4.5 The spatial derivatives	52
4.6 Numerical integration	54
4.6 Comparison between IGA and FEM	55
4.7 Concluding remarks	55

Chapter 5 Piezoelectric composite plates

5.1 Overview	58
5.2 Governing equations for smart piezoelectric plates	59
5.2.1 Weak form for piezoelectric composite plates	59
5.2.1.1 Approximation of the mechanical displacement field	59
5.2.1.2 Approximation of the electrical potential field	61
5.2.2 Governing equations	62
5.3 Active control	63
5.4 Numerical results	64
5.4.1 Free vibration analysis	64
5.4.2 Static analysis	69
5.4.2.1 A smart piezoelectric bimorph beam	69
5.4.2.2 A smart piezoelectric composite plate	70
5.4.3 Dynamic control of the plate	73
5.5 Concluding remarks	74

Chapter 6 Smart piezoelectric functionally graded materials plate

6.1 Overview	78
6.2 The piezoelectric FGM model	78
6.3 The generalized higher order shear deformation theory	80
6.4 Approximation of mechanical field	82
6.5 The governing equations for piezoelectric FGM plates	83
6.6 Nonlinear transient solution	84
6.6.1 Time integration	84
6.6.2 Iterative method	84
6.7 Numerical results	85
6.7.1 Free vibration and static analyses of piezoelectric FGM plates	85
6.7.1.1 Free vibration analysis	85
6.7.1.2 Static analysis	92
6.7.2 Nonlinear transient analysis of piezoelectric FGM plates	93
6.7.2.1 An orthotropic plate	93
6.7.2.2 Geometrically nonlinear static analysis	93
6.7.2.3 Geometrically nonlinear transient analysis	97
6.8 Concluding remarks	102

Chapter 7 Functionally graded carbon nanotube-reinforced composite plates	
7.1 Overview	106
7.2 Governing equations for functionally graded CNTRC plates	106
7.2.1 Displacement field	106
7.2.2 Weak form equations	107
7.2.3 NURBS-based novel CNTRC plate formulation	108
7.3 Numerical results	110
7.3.1 Static and free vibration analyses of CNTRC plates	110
7.3.2 Free vibration of CNTRC plates	117
7.3.2.1 A square plate	117
7.3.2.2 A circular plate	122
7.3.3 Time-dependent dynamic analysis of CNTRC plates	125
7.4 Concluding remarks	128
 Chapter 8 The generalized unconstrained plate theory	
8.1 Overview	130
8.2 The unconstrained third-order shear deformation theory	130
8.3 NURBS-based novel smart plate formulation	133
8.4 Numerical validations	134
8.4.1 Static and free vibration analyses	134
8.4.1.1 Static analysis	134
8.4.1.2 Free vibration	139
8.4.2 Nonlinear analysis of smart plates	142
8.4.3 Dynamic control and optimization	143
8.4.3.1 Nonlinear transient vibration	144
8.4.3.2 Optimization	147
8.5 Concluding remarks	149
 Chapter 9 Conclusions and recommendations	
9.1 Conclusions	152
9.2 Recommendations for future work	154
 List of publications	157
References	163

List of figures

Figure 1.1	Two models of piezoelectric material plates: (a) piezoelectric composite plates and (b) piezoelectric functionally graded material plates.	5
Figure 3.1	Configuration of a laminated composite.	22
Figure 3.2	Material and global coordinates of the laminated composite.	25
Figure 3.3	Two approaches for the volume fraction of the FGMs model: (a) a piecewise variation and (b) a continuous variation.	25
Figure 3.4	Volume fraction V_c versus thickness.	26
Figure 3.5	Effect of rule of mixture (dash dot lines) and Mori-Tanaka scheme (solid lines) on the effective modulus.	27
Figure 3.6	Volume fraction V_c versus the thickness of CNTRC.	30
Figure 3.7	Undeformed and deformed plates in CPLT.	32
Figure 3.8	Undeformed and deformed plates in FSDT.	33
Figure 3.9	Deformation of transverse normal using CLPT, FSDT and TSDT.	34
Figure 3.10	Function $f(z)$ through the thickness of the plates.	35
Figure 3.11	Derivation of the function $f(z)$ through the thickness of the plates.	36
Figure 4.1	1D B-spline basic functions with $p = 1, 2, 3, 4$.	40
Figure 4.2	1D and 2D cubic B-spline basic functions.	41
Figure 4.3	A quadratic B-spline curve.	43
Figure 4.4	A NURBS surface.	44
Figure 4.5	Knot insertion (h -refinement).	45

Figure 4.6	Order elevation (p -refinement).	46
Figure 4.7	A NURBS curve for the circle.	49
Figure 4.8	Effect of weight on NURBS curve.	50
Figure 4.9	NURBS surface and control mesh.	51
Figure 4.10	Parametric and physical space with quadratic B-splines.	53
Figure 5.1	Model of a piezoelectric composite plate.	58
Figure 5.2	A schematic diagram of a laminated plate with integrated piezoelectric sensors and actuators.	63
Figure 5.3	Model of a 5-ply piezoelectric composite plate.	65
Figure 5.4	Shape of the first six eigenmodes of a simply supported piezoelectric composite plate: (a) mode 1, (b) mode 2, (c) mode 3, (d) mode 4, (e) mode 5 and (f) mode 6.	67
Figure 5.5	Model of the smart piezoelectric bimorph beam.	69
Figure 5.6	Deformed shape and centerline deflection of the smart piezoelectric bimorph beam subjected to different input voltages.	70
Figure 5.7	Square piezoelectric composite plate model.	71
Figure 5.8	Centerline deflection of the plate under different input voltage and a uniform load.	72
Figure 5.9	Effect of the displacement feedback control on the deflection of a plate under a uniform load.	73
Figure 5.10	Effect of the velocity feedback control on the dynamic deflection response of the piezoelectric composite plate.	74
Figure 6.1	(a) Configuration of a piezoelectric FGM plate; (b) The sandwich plate with piezoelectric skins and FGM core.	79
Figure 6.2	Temperature distributions through the thickness of Al/ZrO ₂ -1 FGM plate corresponding to different values of volume fraction exponents n .	80
Figure 6.3	Square plate models and their discretization: (a) simply supported plate, (b) clamped plate and (c) meshing of 13×13 cubic elements.	86
Figure 6.4	The first eight natural frequencies of the simply supported (SSSS) and clamped (CCCC) piezoelectric FGM plate with	88

	different volume fraction exponents.	
Figure 6.5	Shape of the first eight eigenmodes of the piezoelectric FGM plates with $n=1$.	90
Figure 6.6	Centerline deflection of the CFFF plate under mechanical load and electro-mechanical load.	91
Figure 6.7	Centerline deflection of the CFFF plate under thermo-electro-mechanical load.	91
Figure 6.8	Displacement of the plate under step uniform load.	92
Figure 6.9	Effect of volume fraction exponent n on deflection of piezoelectric FGM (Al ₂ O ₃ /Ti ₆ Al ₄ V) plates under mechanical load.	93
Figure 6.10	Effect of volume fraction exponent n on deflection of piezoelectric FGM (Al/ZrO ₂ -2) plates subjected to mechanical load.	94
Figure 6.11	Effect of temperature on deflection of piezoelectric FGM (Al/ZrO ₂ -2) plates with $n = 5$ under thermo-mechanical load.	95
Figure 6.12	Effect of input voltage on deflection of piezoelectric FGM (Al/ZrO ₂ -2) plates with $n = 100$ under thermo-electro-mechanical load.	95
Figure 6.13	Effect of volume fraction exponent n on deflection of piezoelectric FGM (Al/ZrO ₂ -2).	96
Figure 6.14	Types of load: step, triangular, sinusoidal and explosive blast.	97
Figure 6.15	Effect of volume fraction <i>exponent</i> n on nonlinear transient responses of piezoelectric FGM plates subjected to step load.	98
Figure 6.16	Effect of volume fraction <i>exponent</i> n on nonlinear transient responses of piezoelectric FGM plates subjected to triangular load.	99
Figure 6.17	Effect of volume fraction <i>exponent</i> n on nonlinear transient responses of piezoelectric FGM plates subjected to sine load.	99
Figure 6.18	Effect of volume fraction <i>exponent</i> n on nonlinear transient responses of piezoelectric FGM plates subjected to	99

	explosive blast load.	
Figure 6.19	Linear and nonlinear transient responses of piezoelectric FGM plates subjected to step load with $n = 0.5$.	100
Figure 6.20	Linear and nonlinear transient responses of piezoelectric FGM plates subjected to triangular load with $n = 0.5$.	100
Figure 6.21	Linear and nonlinear transient responses of piezoelectric FGM plates subjected to sine load with $n = 0.5$.	100
Figure 6.22	Linear and nonlinear transient responses of piezoelectric FGM plates subjected to explosive blast load with $n = 0.5$.	101
Figure 6.23	Nonlinear transient responses of piezoelectric FGM plates under step load with $n = 10$.	101
Figure 6.24	Nonlinear transient responses of piezoelectric FGM plates under triangular load with $n = 10$.	101
Figure 6.25	Nonlinear transient responses of piezoelectric FGM plates under sinusoidal load with $n = 10$.	102
Figure 6.26	Nonlinear transient responses of piezoelectric FGM plates under explosive blast load with $n = 10$.	102
Figure 7.1	Non-dimensional central deflection of CNTRC plates with $h/a = 0.1$.	113
Figure 7.2	Non-dimensional axial stress of SSSS CNTRC plate with $h/a = 0.1$ and $V_{CNT}^* = 0.11$.	114
Figure 7.3	Non-dimensional axial stress of CCCC CNTRC plate with $h/a = 0.1$ and $V_{CNT}^* = 0.11$.	114
Figure 7.4	The six lowest non-dimensional natural frequencies of CNTRC plates with $h/a = 0.1$ and $V_{CNT}^* = 0.11$.	115
Figure 7.5	(a) Circular FG-CNTRC composite plate model; (b) meshing of 18×18 cubic elements.	122
Figure 7.6	Effects of ratios $2R/h$ to non-dimensional frequency of CNTRC circle plate with $V_{CNT}^* = 0.11$.	123
Figure 7.7	Shape of the first six eigenmodes of a simply supported CNTRC circle plate with $2R/h = 10$: (a) mode 1, (b) mode 2, (c) mode 3, (d) mode 4, (e) mode 5 and (f) mode 6.	124

Figure 7.8	Central deflection of the square laminated plate subjected to step loading.	126
Figure 7.9	Central deflection of the square laminated plate subjected to triangular loading.	126
Figure 7.10	Central deflection of the square laminated plate subjected to sinusoidal loading.	127
Figure 7.11	Central deflection of the square laminated plate subjected to explosive blast loading.	127
Figure 8.1	The configuration of piezoelectric composite plates.	131
Figure 8.2	Square piezoelectric composite plate model.	134
Figure 8.3	Effect of actuator input voltages on deflection of the piezoelectric composite plate $[pie/-45/45]_{as}$ subjected to a uniform loading.	136
Figure 8.4	Centerline deflection of the plate subjected to different input voltages and a uniform load.	137
Figure 8.5	Effect of the stacking sequence scheme and the fiber orientations on deflection of piezoelectric composite plate under uniform load and different input voltages.	138
Figure 8.6	The deflection of the piezoelectric composite plates with various boundary conditions.	138
Figure 8.7	Model of an n -ply piezoelectric composite plate.	139
Figure 8.8	Shape of the first six eigenmodes of a simply supported piezoelectric composite plate.	140
Figure 8.9	Effect of input voltages on nonlinear deflection of the piezoelectric composite plates $[-45/pie/45]_{as}$.	144
Figure 8.10	Effect of different fiber orientation angles on deflection of the plate subjected to input voltage 8V.	144
Figure 8.11	Effect of the gain Gd of the displacement feedback control on static deflection of the piezoelectric composite plate.	145
Figure 8.12	Effect of the control gain on the geometrically nonlinear response of the piezoelectric composite plate under step load.	146
Figure 8.13	Effect of the control gain on the geometrically nonlinear response of the piezoelectric composite plate under triangular load.	147

Figure 8.14	Effect of the control gain on the geometrically nonlinear response of the piezoelectric composite plate under explosive blast load.	147
Figure 8.15	Convergence of objective function using GA with 20 generations.	148

List of tables

Table 3.1	Material properties of piezoelectric and composite materials	21
Table 3.2	Some transverse shear functions	37
Table 4.1	Control points and weights for the circle with radius $R = 1$	50
Table 4.2	Differences between IGA and FEM [1]	55
Table 4.3	Similarities between IGA and FEM [1]	55
Figure 5.1	Dimensionless first natural frequency of the simply supported square piezoelectric composite plate $[pie/0/90/0/pie]$	65
	Convergence of the first five natural frequencies of the square piezoelectric composite plate $[pie/0/90/0/pie]$ for the open circuit condition case	66
Table 5.3	Convergence of the first five natural frequencies of the square piezoelectric composite plate $[pie/0/90/0/pie]$ for the close circuit condition case	66
Table 5.4	Deflections of the piezoelectric bimorph beam at various locations ($\times 10^{-6}m$)	68
Table 5.5	Tip deflections of the beam ($\times 10^{-4}m$)	70
Table 5.6	Central deflection of the smart piezoelectric composite plate under a uniform load and input voltages ($\times 10^{-4}m$)	71
Table 6.1	Material properties of some FGMs	81
Table 6.2	Natural frequencies of the first seven modes of the piezoelectric FGM (SSSS) plate	87
Table 6.3	Natural frequencies of the first seven modes of the piezoelectric FGM (CCCC) plate	89

Table 7.1	Non-dimensional central deflection of the simply supported CNTRC plate under a uniform load	111
Table 7.2	Non-dimensional central deflection of the clamped CNTRC plate under a uniform load	112
Table 7.3	The first six non-dimensional frequency parameters of the SSSS CNTRC plate with $V_{CNT}^* = 0.11$	116
Table 7.4	The first six non-dimensional frequency parameters of the SSSS CNTRC plate with $V_{CNT}^* = 0.14$	117
Table 7.5	The first six non-dimensional frequency parameters of the SSSS CNTRC plate with $V_{CNT}^* = 0.17$	118
Table 7.6	The first six non-dimensional frequency parameters of the CCCC CNTRC plate with $V_{CNT}^* = 0.11$	119
Table 7.7	The first six non-dimensional frequency parameters of the CCCC CNTRC plate with $V_{CNT}^* = 0.14$	120
Table 7.8	The first six non-dimensional frequency parameters of the CCCC CNTRC plate with $V_{CNT}^* = 0.17$	121
Table 8.1	Central control point/node deflection of the simply supported piezoelectric composite plate subjected to a uniform load and different input voltages ($\times 10^{-4}$ m).	135
Table 8.2	Dimensionless first natural frequency of the simply supported square piezoelectric composite plate $[pie/0/90/0/pie]$	139
Table 8.3	Convergence of the first five natural frequencies of the square piezoelectric composite plate $[pie/0/90/0/pie]$	140
Table 8.4	The first ten natural frequencies of the square piezoelectric composite plate $[pie/-45/45]_{as}$	143
Table 8.5	Energy of plate with different input voltage and optimal input voltage	148

Nomenclature

J	Jacobian matrix
B	Gradient matrix
D	Matrix of material
\ddot{u}	Acceleration
\dot{u}	Velocity
u	Displacement
K	Global stiffness matrix
M	Global mass matrix
f	Global force vector
C	Global damping matrix
P	Control points
R	Rational basic function
ϵ	Strain field
ϵ_{xx}	Normal stress in x direction
ϵ_{yy}	Normal stress in y direction
γ_{xy}	Shear stress in xy direction
γ_{yz}	Shear stress in yz direction
γ_{zx}	Shear stress in zx direction
σ	Stress field
g	Dielectric constant matrix
e	Piezoelectric constant matrix
q_s	The surface charges
Q_p	The point charges

\mathbf{E}	The gradient of the electric potential field
ϕ	The electric potential field
N	Shape functions
E	Young's modulus
h	Thickness
ω	Natural frequency
ρ	Mass density
ξ, η	Parametric coordinates
G_d	The constant displacement feedback control gain
G_v	The constant velocity feedback control gain
α, β	The Rayleigh damping coefficients
d	Piezoelectric coefficient
p	Electric permittivities
k	Thermal conductivity
t	Time
V_c	The volume fraction of the ceramic
V_m	The volume fraction of the metal
K_e	The effective bulk modulus
G_e	The shear modulus
η_1, η_2, η_3	CNT efficiency parameters
1D	One dimension
2D	Two dimension
3D	Three dimension
CAD	Computer Aided Design
CAE	Computer Aided Engineering
CLPT	Classical Laminate Plate Theory
CPT	Classical Plate Theory
DQM	Differential Quadrature Method
FEM	Finite Element Method
FEA	Finite Element Analysis
BEM	Boundary Element Method
SFEM	Smoothed Finite Element Method
ELS	Equivalent Single Layer

FGM	Functionally Graded Material
FSDT	First-Order Shear Deformation Theory
HSDT	Higher-Order Shear Deformation Theory
TSDT	Third-Order Shear Deformation Theory
FSM	Finite Strip Method
GSDT	Generalized Shear Deformation Theory
IGA	Isogeometric Analysis
NURBS	Non-Uniform Rational B-splines
RPIM	Radial Point Interpolation Method
UTSDT	Unconstrained Third-Order Shear Deformation Theory
DOF	Degree of Freedom
CNT	Carbon Nanotube
FG-CNTRC	Functionally Graded Carbon Nanotube-Reinforced Composite
CNTRC	Carbon Nanotube-Reinforced Composite
GA	Genetic Algorithm
IMSC	Independent Modal Space Control
LQR	Linear Quadratic Regulators
MEMS	Micro-Electro-Mechanical Systems
SMA	Shape Memory Alloys
MD	Molecular Dynamics

Chapter 1

Introduction

1.1 Introduction

Almost all physical phenomena in the real life, such as fluid mechanics, heat transfer, electric and magnetic fields, structure mechanics, wave propagation, etc., can be expressed using partial differential equations (PDEs). And sometimes it is very hard or impossible to solve analytically the PDEs, especially for problems with multi field coupling, such as fluid-structure interaction, thermo-electro-mechanics coupling, etc. This is because these phenomena depend on physical geometry, boundary conditions, material properties and loading conditions, which are very complicated. Hence, various numerical methods have been proposed and developed to find suitable approximated solutions of the PDEs. The basic idea in almost all numerical methods is to discrete continuous domain into infinite unknowns to obtain discrete problem domain. Then, numerical methods and computer aided design (CAD) simulate, calculate and analyze the complicated problems. Therefore, developing numerical methods with low computational cost, high accuracy, and easy implementation is the key issue in a numerical simulation.

With advantages of the numerical techniques, many numerical methods have been proposed, such as boundary element method (BEM), finite element method (FEM), finite difference method (FDM), mesh-free method, finite volume method (FVM), etc. Generally speaking, we can divide the numerical methods into two groups:

- Group 1: methods that require meshing; e.g. FEM, FDM, BEM and FVM.
- Group 2: methods that do not require meshing; e.g. mesh-free methods.

Among the methods with meshing, the FEM is considered to be the most popular. This method has been widely used in all engineering and science research domains. However, the FEM still has some major shortcomings, such as overestimated stiffness, inaccuracy in stress solutions of linear elements, meshing issues, etc. In order to overcome these shortcomings, there are three proposed ways, as follows [1]:

- Improve the variational method.
- Improve the finite element spaces.
- Improve both the variational method and the finite element spaces.

Recently, based on the finite elements spaces, Hughes et al. [2] proposed isogeometric analysis (IGA). The next section will present an historical development of IGA, and more detail will be given in chapter 4.

1.2 An historical development of IGA

The basic idea of IGA proposed by Hughes et al. [2] in 2005 is to integrate CAD and finite element analysis (FEA) into one model. Geometric models generated in CAD are directly used for FEA without mesh generators.

In the past, before the existence of computers, almost all engineering drawings were manually made and splines were used to design automobile chassis and aircraft wings [3]. When computers were invented, Pierre Bézier of Renault and Paul de Faget de Casteljau of Citroën developed computer aided geometric design (CAGD) to generate curves and surfaces in 1960. This was the new software that allowed designers to draw smooth curves on a computer screen. Contribution of Bézier paved the road for CAD software's such as Maya, 3D Max, AutoCad, etc. Moreover, Paul de Faget de Casteljau proposed the Casteljau algorithm, which is the most common way to evaluate Bézier curves. Today, most engineering drawings including applications to automobile, aerospace, architectural design, shipbuilding, etc., have been done in CAD [4].

In 1946, Schoenberg [5] introduced Bézier spline (B-spline) basic functions. In computer science field, B-splines have been represented as polynomial curves [6], which have been considered as tools to create smooth curves and surfaces in computer graphics. The B-spline basic functions provide a higher continuity of derivatives.

In 1962, faster and stable algorithms were proposed by Carl De Boor [7] in order to calculate spline interpolation functions. Nowadays, B-splines are popularly used in the graphic design and CAD industry for creating smooth curves and surfaces.

During 1970s, various fundamental contributions on B-splines were made and begun with Riesenfeld's PhD thesis [8] in 1972. Furthermore, PhD thesis about rational B-splines was completed by Versprille [9] in 1975, which have known as Non-uniform rational B-splines (NURBS). There were many efficient and numerically stable algorithms, which have been proposed and developed using B-splines, such as the Cox-de Boor recursion [10-12], the Oslo algorithms [13], polar forms and blossoms [14,15], etc. NURBS are the current industry standard for computational geometry design and a generalization of Bézier splines. They are tools in CAD including straight lines, curves, complex surfaces, circles, spheres, which can be represented exactly.

Nowadays, computer aided engineering (CAE) becomes the popular computer software. In CAE, FEM is used to solve partial differential equations. In FEM, variational or weak form formulations are used and formed by multiplying trial functions in the partial differential equations, which are called strong form. The basic functions are defined by Lagrange interpolating polynomials with finite elements such as triangles, quadrilaterals, etc. In particular, it can be seen that there exists a gap between CAD and FEA. The design and the analysis are independent of each other. The concept of isogeometric analysis was examined by Hughes et al. [2] with the aim of integrating FEA with CAD. Data generated from CAD can be used directly for FEA. Hence, the exact geometry is expressed in both design and mechanical analyses. An advantage of NUBRS is its ability to easily control continuity, as C^{p-1} continuity is obtained by using p -th order NURBS [1].

Recently, IGA has been developed in several fields such as fluid mechanics [16-20], fluid-structure interaction problems investigated by Bazilevs et al. [21-24], contact problems studied by Wriggers's group [25-28], gradient elasticity [29], explicit gradient damage models [30], fracture mechanics [31-37], etc. For structural mechanics problems, NURBS in IGA have been also used to analyze and simulate practical structures including Euler-Bernoulli beam [38-40], plate structures using FSDT and HSDT [41-46], layerwise theory [47,48], and shell structures [49-52]. So far, there are few published materials related to geometrically nonlinear vibrations using IGA for composite plates based on FSDT [53-54] and HSDT [55], solid-shell [56], continuum shell [57] and Euler-Bernoulli beam [58]. And recently, a combination between IGA and boundary element method (BEM), known as IGABEM, has drawn the attention of researchers. The IGABEM has been applied in some fields [59-62].

1.3 Smart materials

Smart materials are material classes, which have several properties such as coupling electrical and mechanical properties, changed properties from one surface to the other across the thickness, high strength and stiffness, moisture, etc., [63-65]. In the papers of Washington [63] and Reddy [114], some of the most popular and common types of smart materials are piezoelectric materials, shape memory alloys (SMA), electrostrictive

materials, carbon nanotubes (CNTs) materials, magnetostrictive, etc. [63]. In this thesis, we choose two types of smart materials to study as follows:

- Piezoelectric materials discovered by Pierre Curie and Jacques Curie are one of the most popular intelligent material classes. Important features of piezoelectric materials are transformations of mechanical energy into electrical energy when the plates are subjected to mechanical loading and vice versa. And this phenomenon is known as piezoelectric effect and the converse phenomenon. Many applications using piezoelectric materials can be listed as structural health monitoring, automotive sensors, actuators, vibration and noise suppression, shape control and precision positioning, etc.
- Carbon nanotubes (CNTs) proposed by Iijima [66], which was called the “material for the 21st century” [67], have attracted a considerable interest for researchers in many engineering fields [68,69]. This is because CNTs possess high strength and stiffness, and low density.

In the first type, piezoelectric materials, two models are considered for this research including piezoelectric composite plates as shown in Figure 1.1a and piezoelectric functionally graded material plates as illustrated in Figure 1.1b. Effective material properties of smart structures are described in more detail in chapter 3.

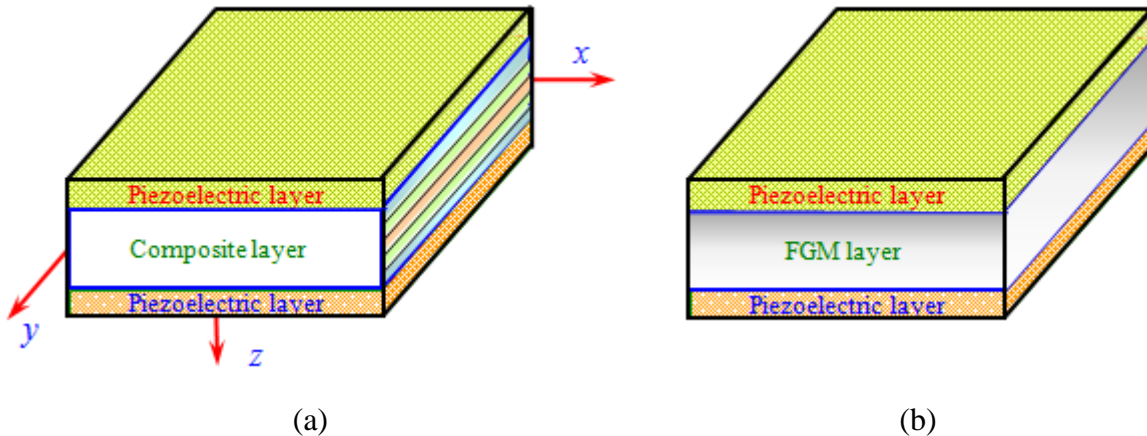


Figure 1.1. Two models of piezoelectric material plates: (a) piezoelectric composite plates and (b) piezoelectric functionally graded material plates.

1.4 Motivation of the thesis

Based on section 1.2, there are no much researches on isogeometric analysis for smart structures. Hence, the aim of this thesis focuses on the development of isogeometric finite element for smart plate structures. Firstly, a new isogeometric formulation for piezoelectric composite plates and carbon-nanotube reinforced plates is investigated. Next, geometrically nonlinear transient isogeometric analysis and dynamic control of smart piezoelectric functionally graded material plates are investigated. The objectives of the thesis are presented in detail in section 2.3 of chapter 2.

1.5 Organization of the thesis

The thesis consists of nine chapters and is organized as follows:

Chapter 1: Introduction and the historical development of IGA are presented. The motivation of the thesis is clearly described.

Chapter 2: Three models of smart plate structures are presented. Literature review of smart plate structures are also discussed in detail including literature review of piezoelectric composite plates, functionally graded carbon nanotube-reinforced composite plates and smart piezoelectric functionally graded plates. Finally, the objectives of the thesis are described.

Chapter 3: Descriptions of smart material properties and plate theories are presented. Firstly, smart material properties are described. Two types of smart materials are introduced, namely piezoelectric materials and functionally graded carbon nanotube-reinforced materials. Next, some equivalent single-layer theories are presented.

Chapter 4: An overview of B-spline, non-uniform rational B-splines (NURBS) and isogeometric analysis (IGA) is presented. This includes basic functions, B-spline geometries, refinement, NURBS basic functions, NURBS curves, NURBS surfaces. The spatial derivatives and comparisons of isogeometric analysis with finite element method are also presented.

Chapter 5: The governing equations for smart piezoelectric plates are presented and the weak form is established. The electric potential and the mechanical displacement field are explained in details. For the active control of plates, a displacement and velocity feedback control algorithm is described. Finally, numerical examples are presented to show accuracy and reliability of the present method.

Chapter 6: Isogeometric approach based on a generalized shear deformation theory for geometrically nonlinear transient vibrations of smart piezoelectric functionally graded material (FGM) plates is introduced. The generalized shear deformation theory is derived. The nonlinear transient formulation for plates is formed in the total Lagrange approach based on the von Kármán strains, which includes thermo-piezoelectric effects, and solved by Newmark time integration scheme. Many numerical results are investigated to illustrate the effectiveness of the present method.

Chapter 7: A simple and effective formulation using IGA based on higher-order shear deformation theory (HSDT) to investigate the static and dynamic vibration behaviors of functionally graded carbon nanotube-reinforced composite plates is presented. The governing equation is approximated according to the HSDT model using isogeometric elements based on Non-Uniform Rational B-Spline (NURBS) basis functions. This achieves naturally any desired degree of continuity through the choice of the interpolation order, so that the method easily fulfils the C^1 -continuity requirement of the HSDT model. Numerical results are verified by comparing them with those of other available numerical approaches to show the accuracy and reliability of the present method.

Chapter 8: An efficient computational approach based on a generalized unconstrained approach in conjunction with isogeometric analysis (IGA) are proposed for dynamic control of smart piezoelectric composite plates. A new unconstrained third-order shear deformation theory is introduced. Linear analysis, geometrically nonlinear analysis, dynamic control and optimization are studied in this chapter. For optimization problems, a procedure using genetic algorithm (GA) is considered to search an optimal design for actuator input voltages. Several numerical examples are provided to demonstrate the excellent performance of the present method.

Finally, chapter 9 presents concluding remarks and some recommendations for future work.

1.6 Concluding remarks

In this chapter, a short introduction about advantages of the numerical techniques, IGA and the smart materials is presented. Besides, the motivation of this thesis is also described and the organization of the thesis with nine chapters is reported.

Chapter 2

Literature review

2.1 Overview

In this chapter, literature reviews of three models of smart plates, i.e., piezoelectric composite plates, piezoelectric functionally graded material plates and functionally graded carbon nanotube-reinforced composite plates, are presented. Next, the objectives of the research are described in more detail.

2.2 Literature review

2.2.1 Piezoelectric composite plates

Piezoelectric materials belong to a smart material class that expresses electromechanical coupling. The development of smart structures integrated with sensors and actuators offers a considerable interest in many engineering applications: structural health monitoring, automotive sensors, actuators, vibration and noise suppression, shape control and precision positioning, etc. The main feature of smart materials is the transformation between mechanical energy and electric energy. When electric field is applied to piezoelectric structures, mechanical deformation is generated. This is known as the converse phenomenon of piezoelectric effect [63,67].

Due to the attractive properties of piezoelectric composite structures, various numerical methods have been devised. For free vibration and static analysis, Hong and Chopra [70] applied special properties of the piezoelectric layers into the laminate plates. Effect of the stiffness and mass of layers on mode shapes and natural frequencies was examined by Yang and Lee [71]. Results of comparison between FEA and experiments for smart cantilever plate were reported by Kim et al. [72]. A consistent modeling for piezo laminate shells was investigated by Pletner and Abramovich [73]. Willberg et al. [74] studied a three-dimensional piezoelectric solid structure using isogeometric finite elements. Wang et al. [75] used FEM to investigate dynamic stability of piezoelectric composite plates, where the governing equations of motion using Lyapunov's energy [76] with active damping was used. Ray and Mallik [77] used FEM to study smart structures containing piezoelectric fiber-reinforced composite actuator. Analyses of smart piezoelectric composite plates and beams using FE models were investigated in Refs [78-86].

For vibration control, some theories based on numerical methods have been devised and can be generally classified into two main categories, namely the analytical methods and the equivalent single-layer theories. In the framework of analytical methods, Bailey et al. [87] and Shen et al. [88] investigated smart beams integrated with layers using analytical solutions. Tzou and Tseng [89] used a thin hexahedron solid element to examine dynamic control of piezoelectric plates and shells.

The three most popular equivalent single-layer theories are the Classical Lamination Theory (CLT), the First-order Shear Deformation Theory (FSDT), and the Higher-order Shear Deformation Theory (HSDT). In the CLT, which is based on the assumptions of Kirchhoff's plate theory, the interlaminar shear deformation is neglected. Following this framework, Hwang and Park [90] studied piezoelectric plates using the discrete Kirchhoff quadrilateral (DKQ) element and the Newmark β -method to analyze the direct time responses of the plate subjected to negative velocity feedback control. The radial point interpolation method (RPIM) combined with the first order shear deformation theory (FSDT) and the CPT with rectangular plate bending element were investigated by Liu et al. [91-92]. Suleman and Venkayya [93] used the classical laminate theory (CLT) with four-node finite element to investigate static and vibration behaviors of a laminated composite with piezoelectric layer based on hourglass stabilization and reduced numerical integration. Victor et al. [94] developed the higher order finite element formulations based on an analytical solution to investigate the mechanics of composite structures integrated with actuators and sensors. Liew et al. [95] studied post-buckling of FGM plates integrated with piezoelectric under thermo-electro-mechanical loadings using a semi-analytical solution with Galerkin differential quadrature integration algorithm based on the higher-order shear deformation theory (HSDT). In those works, the formulation of vibration control simulation was based on the classical plate theory and the Radial Point Interpolation Method (RPIM).

In FSDT, a constant transverse shear deformation is assumed through the entire thickness of the plate and hence stress-free boundary conditions at the top and bottom layers of the panel are violated. Using this theory, Liew et al. [96] analyzed piezoelectric patches laminated beams and plates based on the element-free Galerkin method. Milazzo and Orlando [97] studied free vibration analysis of thick composite plates integrated with piezoelectric. The mesh-free model based on FSDT was presented by Liew et al. [96] to simulate shape control of piezoelectric composite plates with different boundary

conditions. Phung-Van et al. [98] developed the cell-based smoothed discrete shear gap method in order to simulate dynamic control analysis of piezoelectric composite plates. Some FE models for analyzing smart plates and plates/shells were studied in Refs [99-112].

In both CLT and FSDT theories, a shear correction factor is required to ensure the stability of the solution. In order to improve the accuracy of transverse shear stresses and to avoid the introduction of shear correction factors, the HSDT based on the FE method has been proposed to study piezoelectric plates [94,113,114]. A HSDT-layerwise generalized finite element formulation [115] and the layerwise based on analytical formulation [116] were investigated to study piezoelectric composite plates. Finite element (FE) formulations based on HSDT for the analysis of smart laminated plates was studied in [114]. In this theory, quadratic, cubic or higher-order variations of surface-parallel displacements are assumed through the entire thickness of the plate to model the behavior of the structure. It is worth mentioning that the HSDT requires at least C^1 -continuity of generalized displacements due to the presence of their second-order derivatives in the stiffness formulation. This is a source of difficulty in standard finite elements featuring C^0 inter-element continuity. Among HSDTs, the unconstrained third order shear deformation theory (UTSDT) [117] showed an alternative and effective approach for laminated plate structures. In addition, UTSDT allows us to relax traction-free boundary condition at the top and bottom surfaces of plates, which is commonly required in HSDTs. The appearance of the unconstrained theory opens frontiers for future applications of the UTSDT to the problems considering flow field, in which the boundary layer of stresses is significant. The differential equations for UTSDT are of similar complexity to those of TSDT. This approach produces more accurate solutions [118]. Responses of the laminated plates using UTSDT were also investigated in [118]. Free vibration and static analyses of composite plates using radial point interpolation method (RPIM) combined with UTSDT were reported in [119]. In UTSDT, the displacement field includes seven displacement components. More importantly, we herein propose a generalized unconstrained HSDT that also uses seven displacement components like UTSDT, but the higher order rotations depend on an arbitrary function $f(z)$ through the plate thickness.

For optimal control, Kumar et al. [120] and Rao et al. [121] used GA to study the optimization problems for finding optimal piezo location on a cantilever plate and a two-

bay truss. Chang-Qing et al. [122] investigated optimal control of piezoelectric structures using independent modal space control (IMSC). Optimal location of piezoelectric using GA for vibration control of structures was investigated by Bruant et al. [123]. In their work, two variables for each piezoelectric device in an optimization problem, i.e. the location of its center and its orientation, are considered. A closed-form solution based on linear quadratic regulators (LQR) for the optimal control of piezoelectric composite plates was reported in [124].

As it emerges from the above review, the available studies have focused on the dynamic analysis of smart piezoelectric plates using smoothed finite element method (SFEM), classical FEM or mesh-free methods. This thesis aims at further contributing to the dynamic analysis of piezoelectric composite plates using an isogeometric approach based on Non-Uniform B-Spline (NURBS) basis functions. In particular, we show that a HSDT formulation fulfilling C^1 -continuity requirements is easily achieved in the isogeometric framework. Moreover, there are no researches on geometrically nonlinear transient based on isogeometric analysis for the piezoelectric composite plates. Hence, we propose an efficient approach to fill in this research gap via a generalized UHSDT and IGA. For reference, it is termed as IGA-UHSDT.

2.2.2 Piezoelectric functionally graded materials plates

A new class of non-homogeneous composites known as functionally graded materials (FGMs) was first proposed by Koizumi [125]. Material properties are continuous and smooth change from one surface to the other along thickness direction. Specially, they are capable of withstanding severe high temperature gradients, while maintaining structural integrity [125]. Piezoelectric materials are also an intelligent material class, which has coupled electrical and mechanical properties. Hence, the integration of FGM and piezoelectric offers a considerable interest in many practical applications, such as micro-electromechanical systems (MEMS) and smart material systems, especially in the medical and aerospace industries [126], etc.

Because of their coupled thermal, electrical and mechanical properties, numerous methods on a wide range of topics related to FGMs and piezoelectric FGM have been proposed. Praveen and Reddy [127] studied nonlinear response of functionally graded ceramic-metal plates using FEM based on FSDT. Zhao and Liew [128] also used FSDT combining the element-free kp -Ritz method to investigate geometrically nonlinear

analysis of functionally graded plates (FGPs). Geometrically nonlinear analysis of FGM plates subjected to thermal-mechanical load was studied in [129]. In the nonlinear formulation, smoothed finite element method (S-FEM) based on the von Kármán strains and the C^0 -type high-order shear deformation plate theory (C0-HSDT) were presented. In addition, HSDTs [130-133] were also devised to solve nonlinear behavior of FGM composite structures.

For piezoelectric FGM plates, a finite element model based on variational principle and linear piezoelectricity theory was developed by Liew et al. [134] for investigating the active control of FGM integrated with piezoelectric sensors and actuators. Reddy and Cheng [135] proposed a 3D asymptotic solution for smart FGM plates using the transfer matrix formulation and the asymptotic expansion. The nonlinear frequencies of a FGM plate with piezoelectric layers in thermal environments were examined by the Huang and Shen [136] using HSDT. The nonlinear thermo-electro-mechanical bending response of piezoelectric FGM plates was investigated by Yang et al. [137]. Butz et al. [138] developed geometrically and materially non-linear effects and formulation based on Timoshenko beam theory using FEM for the three-dimensional piezoelectric beam. Nonlinear analysis of smart FGPs integrated with a layer of piezoelectric fiber reinforced composite using FSDT was presented by Panda and Ray [139]. The based-HSDT finite element formulations for geometrically nonlinear analysis of functionally graded piezoelectric plates were also reported in Refs. [140-142]. Besides, there have been a few investigations concerned with nonlinear transient analysis of smart FGM plates using the generalized shear deformation theory. Therefore, this thesis tries to fill in this research gap by using IGA based on the generalized shear deformation theory for geometrically nonlinear transient analysis of the piezoelectric FGM plates. The nonlinear formulation for plates based on the von Kármán strains is formulated using total Lagrange method and solved by Newmark time integration associated with the iteration methods. The electric potential of each piezoelectric layer is assumed linearly through the thickness of each piezoelectric layer. The material properties of FGM are assumed to vary through the thickness by the rule of mixture and the Mori–Tanaka scheme.

2.2.3 Functionally graded carbon nanotube-reinforced composite plates

Carbon nanotubes (CNTs) discovered by Iijima [66], which was called the “material for the 21st century” [143], have attracted a considerable interest by researchers in many

engineering fields [68,69]. This is because CNTs possess high strength, high stiffness and low density. CNTs are considered as potential candidates for the reinforcement of polymer composites providing that good interfacial bond between CNTs and polymer and proper dispersion of the individual CNTs in the polymeric matrix can be guaranteed [144].

Due to the attractive properties of CNTs, numerical methods and various experiments have been developed to analyze and simulate their behaviors. Based on molecular dynamics (MD) simulations and experimental method, Gou et al. [145] investigated the interfacial bonding of single-walled nanotube (SWNT) reinforced epoxy composites. Vodenitcharova and Zhang [146] investigated the bending and buckling behavior of a nanocomposite beam reinforced by a single-walled carbon nanotube. Based on a multiscale approach, Wuite and Adali [147] analyzed nanocomposite reinforced beams, which were made of stacked isotropic layers reinforced by CNTs in different aligned directions and isotropic beams composed of randomly oriented CNTs dispersed in a polymer matrix. Post-buckling analysis of FG-CNTRC cylindrical shells subjected to mechanical loading in thermal environments was also conducted by Shen [148]. Based on the classical laminated plate theory, buckling behavior of laminated composite plates with different boundary conditions was investigated by Arani et al. [149]. In this research, optimal orientations of CNTs were computed to achieve the corresponding mode shapes and the highest critical load. By using FEM and FSDT, Zhu et al. [150] studied static and free vibration analyses of carbon nanotube-reinforced composite plates. A nonlinear free vibration analysis of FG-CNTRC Timoshenko beams was investigated by Ke et al. [151]. Shen [152] studied the effect of thermal environment on nonlinear bending of functionally graded carbon nanotube-reinforced composite plates. Wang and Shen [153] investigated the nonlinear vibration and bending behavior of sandwich plates with nanotube-reinforced composite face sheets. Besides, by using mesh-free methods based on FSDT, Liew et al. [154] analyzed post-buckling of carbon nanotube-reinforced functionally graded cylindrical panels under axial compression. Lei et al. [155] studied free vibration analysis of FG-CNTRC plates. In addition, large deflection analysis of FG-CNTRC plates was also conducted by Lei et al. [156]. Based on the theory of elasticity, Alibeigloo [157-158] investigated the bending behavior of FG-CNTRC plates and cylindrical panels embedded in piezoelectric layers. Alibeigloo and Kiew [159] studied thermos-elastic properties of FG-CNTRC plates. The bending and buckling analyses of FG-CNTRC beams resting on elastic foundation were

analytically examined by Wattanasakulpong and Ungbhakorn [160]. They found that higher-order shear deformation theories show an important role for predicting shear stress. Based on the Eshelby Mori Tanaka approach, Sobhani et al. [161] investigated the natural frequencies characteristics of FG-CNTRC cylindrical panels using a 2D generalized differential quadrature method. Yas et al. [162] studied free vibration of FG-CNTRC cylindrical panels using 3D theory of elasticity. They found that when orientations of carbon nanotubes are 2π and $\pi/6$, the normalized frequency was the highest. Based on Timoshenko beam theory, Ke et al. [163] investigated free vibration of single-walled CNT beam using the Ritz method. In this research, it was found that free vibration frequencies of beam with symmetrical CNT distribution are higher than those with uniform or asymmetrical CNT distribution. Dynamic behaviors of functionally graded multi-walled carbon nanotube-polystyrene nanocomposite beams under multi-moving loads were studied by Heshmati and Yas [164]. Yas and Samadi [165] conducted free vibration of nanocomposite beam reinforced with single-walled CNTs resting on the elastic foundation using Hamilton's principle to derive the governing equations, which were solved using the generalized differential quadrature method.

For buckling and post-buckling analyses, Rafiee et al. [166] investigated nonlinear thermal buckling of FG-CNTRC beams integrated with piezoelectric layers. The buckling load increases for CNTRC piezoelectric beam because of the functionally graded reinforcement. A unified formulation for analysis of the 3D buckling of FG-CNTRC piezoelectric plates subjected to bi-axial compressive loads was studied by Wu and Chang [167]. Shen and Zhang [168] investigated thermal post-buckling analyses of nanocomposite shell reinforced by single-walled CNTs. A two-step perturbation technique was proposed by Shen and Zhu [169] to define the thermal buckling load and post buckling equilibrium paths of nanotube-reinforced composite plates resting on elastic foundations. Furthermore, post-buckling analyses of FG-CNTRC plates/shells were carried out under axial compression and thermal environments in Refs. [170-174]. Available studies have focused on the Nano-reinforced composite plates using FEM, theory of elasticity or mesh-free methods. Besides, it is seen that the literature related to the analysis of functionally graded carbon nanotube-reinforced composite plates using HSDT is somewhat limited. This thesis hence aims to fill in this gap by developing isogeometric finite element based on Non-Uniform B-Spline (NURBS) basis functions.

In particular, we show that a HSDT formulation fulfilling C^1 -continuity requirements is easily achieved in the framework of isogeometric analysis.

2.3 Goal of the thesis

Based on literature reviews of smart structures in this chapter and the historical development of IGA in chapter 1, the overall aim of this research is to develop IGA for the smart plate structures. Some main problems have to be achieved in order to realize this aim:

- Develop IGA for dynamic response of composite plates integrated with piezoelectric materials.
- Investigate dynamic response of functionally graded carbon nanotube-reinforced composite plates.
- Study nonlinear transient of smart piezoelectric functionally graded material plates.
- Develop a new shear deformation theory for control of nonlinear transient of smart piezoelectric composite plates.

2.4 Concluding remarks

Reviews of piezoelectric composite plates, piezoelectric functionally graded material plates and functionally graded carbon Nano-tube-reinforced composite plates are presented in this chapter. Based on the literature reviews, four main objectives for this thesis are proposed.

Chapter 3

Smart materials and plate theories

3.1 Overview

In this chapter, we present descriptions of smart material properties and plate theories. Firstly, smart material properties are expressed. Two types of smart materials, i.e., piezoelectric plates and functionally graded carbon nanotube-reinforced composite plates, are introduced. Next, some equivalent single-layer theories are presented.

3.2 Effective material properties

3.2.1 Piezoelectric plates

The piezoelectric material is described by both laws of electromagnetics and mechanics, and the piezoelectric effect is considered to be linear. Hence, there are two fields in the piezoelectric problem: mechanical and electrical fields. Table 3.1 shows the material properties of some piezoelectric and composite materials, including elastic modulus (E), Poisson's ratio (ν), mass density (ρ), piezoelectric coefficient (d), and electric permittivity (p). Table 3.1 will be also used in chapters 5, 6 and 8.

The material behavior of piezoelectric plates is expressed as [86,175]:

$$\begin{bmatrix} \boldsymbol{\sigma} \\ \mathbf{D} \end{bmatrix} = \begin{bmatrix} \mathbf{c} & -\mathbf{e}^T \\ \mathbf{e} & \mathbf{g} \end{bmatrix} \begin{bmatrix} \bar{\boldsymbol{\epsilon}} \\ \mathbf{E} \end{bmatrix} \quad (3.1)$$

where $\boldsymbol{\sigma}$ and $\bar{\boldsymbol{\epsilon}}$ are the stress and strain vectors of the mechanical field, respectively; \mathbf{D} is the dielectric displacement; \mathbf{E} is the electric field vector; \mathbf{g} and \mathbf{e} denote the dielectric and piezoelectric constant matrix, respectively, which are defined as [86]:

$$\mathbf{e} = \begin{bmatrix} 0 & 0 & 0 & 0 & d_{15} & 0 \\ 0 & 0 & 0 & d_{15} & 0 & 0 \\ d_{31} & d_{32} & d_{33} & 0 & 0 & 0 \end{bmatrix} ; \quad \mathbf{g} = \begin{bmatrix} p_{11} & 0 & 0 \\ 0 & p_{22} & 0 \\ 0 & 0 & p_{33} \end{bmatrix} \quad (3.2)$$

In this research, piezoelectric composite plates and piezoelectric functionally graded plates are investigated. Therefore, next section presents an overview of composite materials and functionally graded materials (FGMs).

3.2.1.1 Composite materials

Composite materials are formed by integrating two or more materials so that they have some superior properties, such as strength-to-weight ratio, corrosion resistance, fatigue

life, etc., [176]. Most composite materials are made from: fiber, reinforcement material, and matrix (a base material).

Table 3.1: Material properties of piezoelectric and composite materials [91,92,116]

Properties	PVDF	PZT-4	PZT-G1195N	T300/979	Gr/Ep
Elastic properties					
E_{11} (GPa)	2	81.3	63.0	150	132.38
E_{22} (GPa)	2	81.3	63.0	9.0	10.76
E_{33} (GPa)	2	64.5	63.0	9.0	10.76
G_{12} (GPa)	1	30.6	24.2	7.1	3.61
G_{13} (GPa)	1	25.6	24.2	7.1	5.65
G_{23} (GPa)	1	25.6	24.2	2.5	5.65
ν_{12}	0.29	0.33	0.30	0.3	0.24
ν_{23}	0.29	0.43	0.30	0.3	0.24
ν_{13}	0.29	0.43	0.30	0.3	0.49
Mass density					
ρ (kg/m ³)	1800	7600	7600	1600	1578
Piezoelectric coefficient					
$d_{31} = d_{32}$ (m/V)	0.046	-1.22e-10	2.54e-10	-	-
d_{15} (m/V)	-	-	-	-	-
d_{33} (m/V)	-	-2.85e-10	-	-	-
Electric permittivity					
p_{11} (F/m)	0.1062e-9	1475	15.3e-9	-	-
p_{22} (F/m)	0.1062e-9	1475	15.3e-9	-	-
p_{33} (F/m)	0.1062e-9	1300	15.0e-9	-	-

There are three different types of composite materials, i.e. [176]:

- Type 1: Fibrous composites, i.e. fibers of one material in a matrix material of another.
- Type 2: Particulate composites, i.e. macro size particles of one material in a matrix of another.
- Type 3: Laminated composites, i.e. each layer has a different material, include one of the first two types of composite materials.

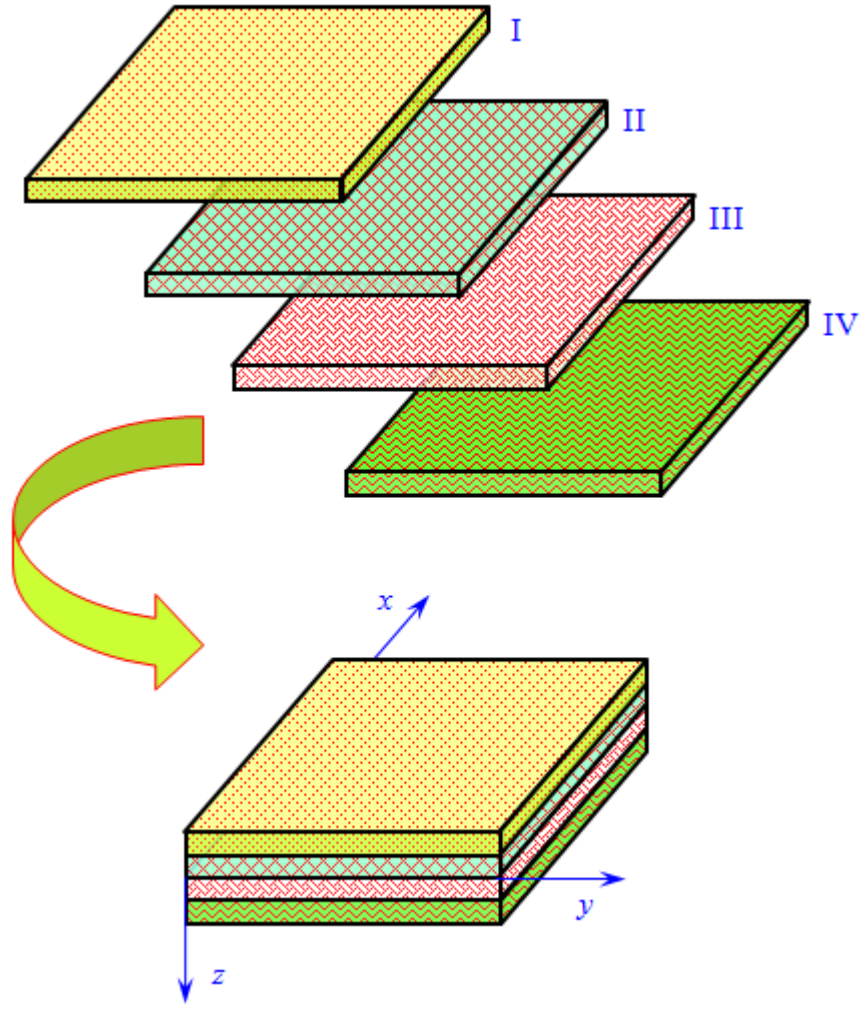


Figure 3.1. Configuration of a laminated composite.

In this research, we choose type 3, which is shown in Figure 3.1 in order to study the mechanical behavior. In Figure 3.1, symbols, I, II, III and IV represent layers with different materials or different fiber orientations. Besides, in the formulations of constitutive equations of a layer (a lamina), we assume the following [176]:

- A lamina is continuous material, i.e., there is no gaps or empty spaces.
- Behaviors of a lamina are linear.

The Hooke's law for an anisotropic material is expressed by:

$$\sigma_i = Q_{ij} \varepsilon_j \quad (3.3)$$

Where σ_i are the stress components, ε_j are the strain components and Q_{ij} are the “reduced” material coefficients for 2D with i, j refer to the components of Cartesian coordinate (x, y, z) .

Based on Young’s moduli, E_f, E_m ; Poisson’s ratios, ν_f, ν_m , and volume fractions, ν_f, ν_m , where f and m refer to fiber and matrix of laminated composites, respectively, the lamina constants are defined as follows (using rule of mixture):

$$\begin{aligned} E_1 &= E_f \nu_f + E_m \nu_m & \nu_{12} &= \nu_f \nu_f + \nu_m \nu_m \\ E_2 &= \frac{E_f E_m}{E_f \nu_m + E_m \nu_f} & G_{12} &= \frac{G_f G_m}{G_f \nu_m + G_m \nu_f} \end{aligned} \quad (3.4)$$

Where 1 and 2 represent directions of axes x, y , respectively, and G_{12} is the shear modulus defined by:

$$G_f = \frac{E_f}{2(1+\nu_f)} \quad ; \quad G_m = \frac{E_m}{2(1+\nu_m)} \quad (3.5)$$

In the laminate, the constitutive equation of the k^{th} anisotropic layer in material coordinates or local coordinates, as shown in Figure 3.2, can be defined from Hooke’s law as:

$$\begin{Bmatrix} \sigma_{xx} \\ \sigma_{yy} \\ \tau_{xy} \\ \tau_{xz} \\ \tau_{yz} \end{Bmatrix}^{(k)} = \begin{bmatrix} Q_{11} & Q_{12} & Q_{16} & 0 & 0 \\ Q_{21} & Q_{22} & Q_{26} & 0 & 0 \\ Q_{61} & Q_{62} & Q_{66} & 0 & 0 \\ 0 & 0 & 0 & Q_{55} & Q_{54} \\ 0 & 0 & 0 & Q_{45} & Q_{44} \end{bmatrix}^{(k)} \begin{Bmatrix} \varepsilon_{xx} \\ \varepsilon_{yy} \\ \gamma_{xy} \\ \gamma_{xz} \\ \gamma_{yz} \end{Bmatrix}^{(k)} \quad (3.6)$$

Where

$$\begin{aligned} Q_{11} &= \frac{E_1}{1-\nu_{12}\nu_{21}}, Q_{12} = \frac{\nu_{12}E_2}{1-\nu_{12}\nu_{21}}, Q_{22} = \frac{E_2}{1-\nu_{12}\nu_{21}} \\ Q_{66} &= G_{12}, Q_{55} = G_{13}, Q_{44} = G_{23} \end{aligned} \quad (3.7)$$

In which G_{12} , G_{23} and G_{13} are the shear moduli in the x - y , y - z and x - z planes, respectively.

The laminate is usually made of many layers with differently oriented orthotropic directions. The stress-strain relation (with arbitrary fiber orientation) for the k^{th}

orthotropic lamina in the global reference system, as illustrated in Figure 3.2, is defined as:

$$\begin{Bmatrix} \sigma_{xx} \\ \sigma_{yy} \\ \tau_{xy} \\ \tau_{xz} \\ \tau_{yz} \end{Bmatrix}^{(k)} = \begin{bmatrix} \bar{Q}_{11} & \bar{Q}_{12} & \bar{Q}_{16} & 0 & 0 \\ \bar{Q}_{21} & \bar{Q}_{22} & \bar{Q}_{26} & 0 & 0 \\ \bar{Q}_{61} & \bar{Q}_{62} & \bar{Q}_{66} & 0 & 0 \\ 0 & 0 & 0 & \bar{Q}_{55} & \bar{Q}_{54} \\ 0 & 0 & 0 & \bar{Q}_{45} & \bar{Q}_{44} \end{bmatrix}^{(k)} \begin{Bmatrix} \varepsilon_{xx} \\ \varepsilon_{yy} \\ \gamma_{xy} \\ \gamma_{xz} \\ \gamma_{yz} \end{Bmatrix}^{(k)} \quad (3.8)$$

Where \bar{Q}_{ij} are the transformed material constants and defined as [176]:

$$\begin{aligned} \bar{Q}_{11} &= Q_{11} \cos^4 \theta + 2(Q_{12} + 2Q_{66}) \sin^2 \theta \cos^2 \theta \\ \bar{Q}_{12} &= (Q_{11} + Q_{22} - 4Q_{66}) \sin^2 \theta \cos^2 \theta + Q_{12} (\sin^4 \theta + \cos^4 \theta) \\ \bar{Q}_{22} &= Q_{11} \sin^4 \theta + 2(Q_{12} + 2Q_{66}) \sin^2 \theta \cos^2 \theta + Q_{22} \cos^4 \theta \\ \bar{Q}_{16} &= (Q_{11} - Q_{22} - 2Q_{66}) \sin \theta \cos^3 \theta + (Q_{12} - Q_{22} + 2Q_{66}) \cos \theta \sin^3 \theta \\ \bar{Q}_{26} &= (Q_{11} - Q_{21} - 2Q_{66}) \sin^3 \theta \cos \theta + (Q_{12} - Q_{22} + 2Q_{66}) \cos^3 \theta \sin \theta \\ \bar{Q}_{66} &= (Q_{11} + Q_{22} - 2Q_{12} - 2Q_{66}) \sin^2 \theta \cos^2 \theta + Q_{66} (\sin^4 \theta + \cos^4 \theta) \\ \bar{Q}_{44} &= Q_{44} \cos^2 \theta + Q_{55} \sin^2 \theta \\ \bar{Q}_{45} &= (Q_{55} - Q_{44}) \sin \theta \cos \theta \\ \bar{Q}_{55} &= Q_{55} \cos^2 \theta + Q_{44} \sin^2 \theta \end{aligned} \quad (3.9)$$

3.2.1.2 Functionally graded materials

FGMs usually consist of two phases of materials with different properties, e.g., metal and ceramic. The effective properties of FGMs, such as strength, resistant to high temperatures, etc., depend on the volume fractions, which are function of position through their thickness, between two phases of materials.

In FGMs model, there are two approaches as follows [177]:

- In the first approach, FGM is divided into several layers through the thickness and each layer has the same volume fraction, as shown in Figure 3.3a. We may call this model as FGM model with a piecewise variation.

- In the second approach, the volume fractions are assumed continuously through the thickness of FGM, as shown in Figure 3.3b. This model may be called FGM model with a continuous variation.

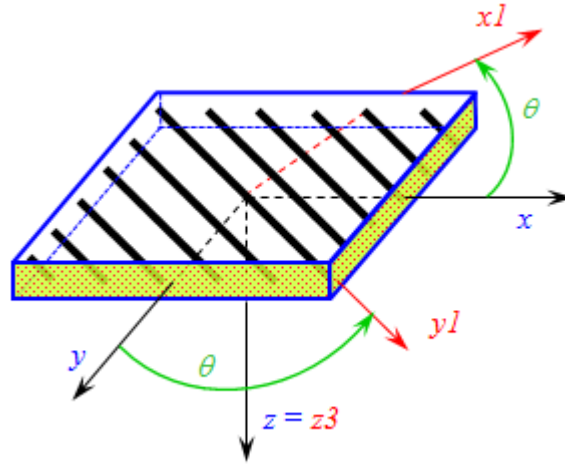


Figure 3.2. Material and global coordinates of the laminated composite.

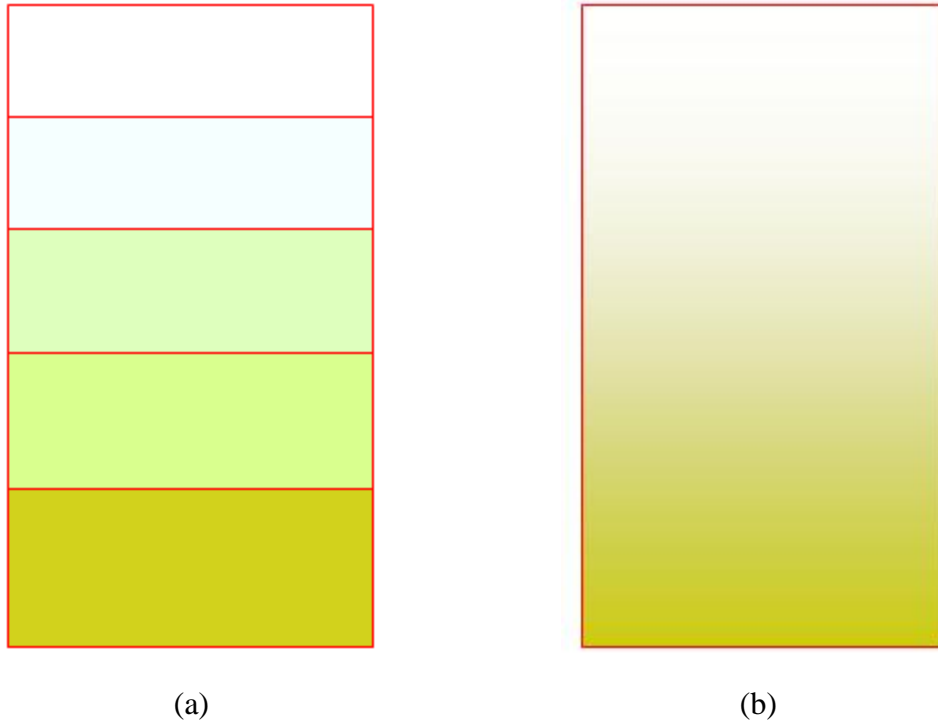


Figure 3.3. Two approaches for the volume fraction of the FGMs model: (a) a piecewise variation and (b) a continuous variation.

Referring to Reddy et al. [178-180], we choose the second approach in this research. The volume fraction of metal and ceramic phase across the thickness can be expressed as follows [177,181]:

$$V_c = \left(\frac{1}{2} + \frac{z}{h} \right)^n \quad (n \geq 0) \quad (3.10)$$

$$V_m = 1 - V_c \quad (3.11)$$

where subscripts c and m refer to the ceramic and metal constituents, respectively, n is a volume fraction exponent, V_c is the volume fraction of the ceramic, V_m is the volume fraction of the metal, h is the thickness of the plate and z and $-h/2 \leq z \leq h/2$, is the thickness coordinate. Effect of change of the volume fraction exponent on the volume fraction across the thickness is illustrated in Figure 3.4.

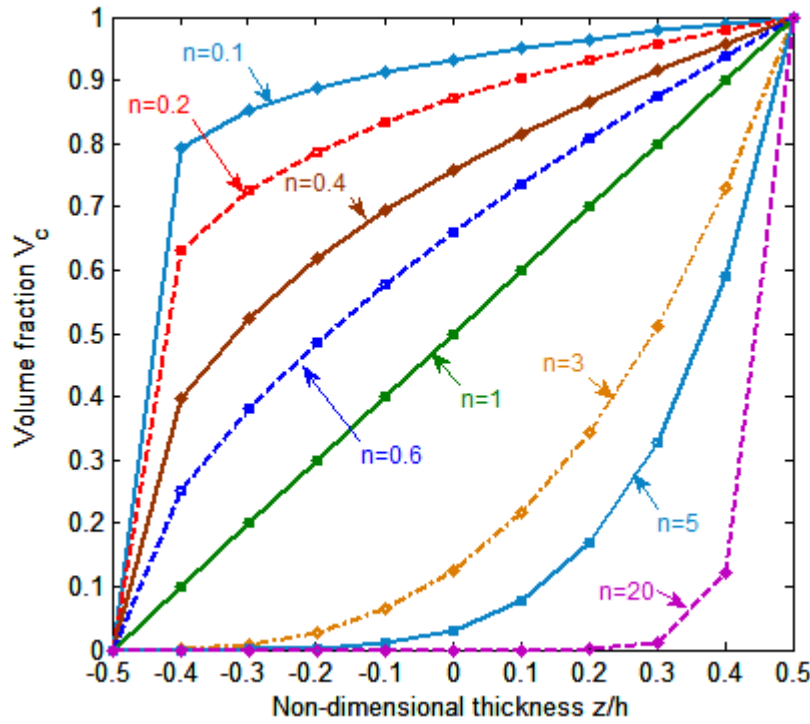


Figure 3.4. Volume fraction V_c versus thickness for different exponents n .

In this research, two power law distributions, rule of mixtures [176,182] and Mori-Tanaka scheme [183,184], are used. A comparative study between these two methods was also examined in Ref. [161].

In the rule of mixtures, the effective material property is assumed to be graded through the thickness as follows [176,182]:

$$P(z) = (P_c - P_m)V_c + P_m \text{ or } P(z) = P_c V_c + P_m V_m \quad (3.12)$$

where P represents the effective material properties, including Young's modulus E , density ρ , Poisson's ratio ν , thermal conductivity k and thermal expansion α . P_c and P_m denote the properties of the ceramic and metal, respectively.

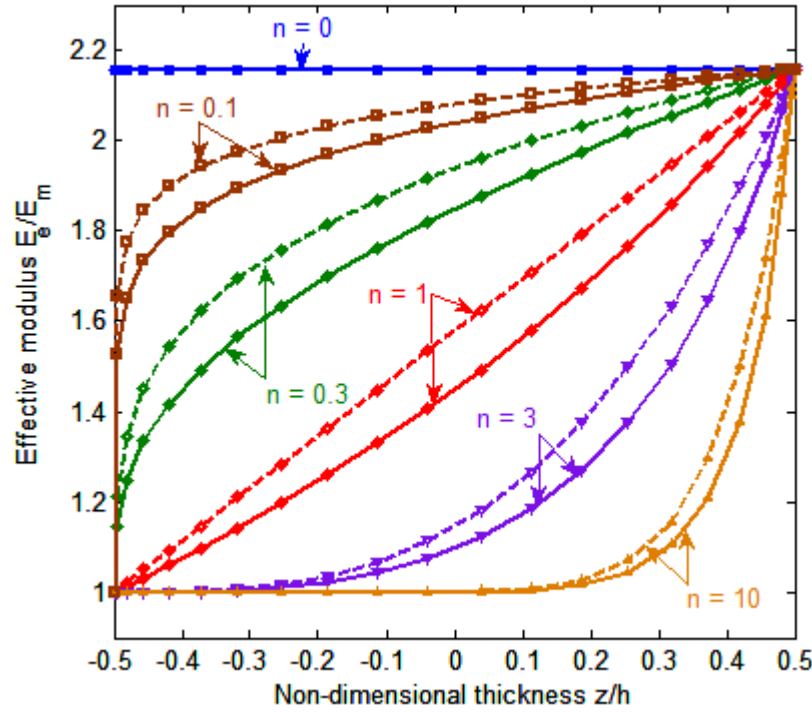


Figure 3.5. Effect of rule of mixture (dash dot lines) and Mori-Tanaka scheme (solid lines) on the effective modulus.

To consider interactions among the constitutions, the Mori-Tanaka scheme is used. The effective bulk modulus K_e , the shear modulus G_e , thermal expansion coefficient α_e and thermal conductivity can be expressed as [183,184,150]:

$$\frac{K_e - K_m}{K_c - K_m} = \frac{V_c}{1 + V_m \frac{K_c - K_m}{K_m + \frac{4}{3}G_m}} \quad (3.13)$$

$$\frac{G_e - G_m}{G_c - G_m} = \frac{V_c}{1 + V_m \frac{G_c - G_m}{G_m + f_1}} \quad (3.14)$$

$$\frac{\alpha_e - \alpha_m}{\alpha_c - \alpha_m} = \frac{\frac{1}{K_e} - \frac{1}{K_c}}{\frac{1}{K_c} - \frac{1}{K_m}} \quad (3.15)$$

$$\frac{\kappa_e - \kappa_m}{\kappa_c - \kappa_m} = \frac{V_c}{1 + V_m \frac{\kappa_c - \kappa_m}{3\kappa_m}} \quad (3.16)$$

Where $f_1 = \frac{G_m(9K_m + 8G_m)}{6(K_m + 2G_m)}$. Poisson's ratio and Young's modulus are defined as:

$$E_e = \frac{9K_e G_e}{3K_e + G_e} \quad (3.17)$$

$$\nu_e = \frac{3K_e - 2G_e}{2(3K_e + G_e)} \quad (3.18)$$

Figure 3.5 shows effect of the rule of mixture and the Mori–Tanaka scheme via the power index n on the effective Young's modulus of FGM made by Al/ZrO₂, i.e., a bottom layer is Al with Young's modulus $E_m = 70 \times 10^9$ Pa and an upper layer is ZrO₂ with Young's modulus $E_c = 151 \times 10^9$ Pa. It can be seen that Young's modulus calculated by the rule of mixture is larger than that calculated by the Mori-Tanaka scheme.

3.2.2 Functionally graded carbon nanotube-reinforced composites

Carbon nanotubes (CNTs) are considered as potential candidates for the reinforcement of polymer composites providing that good interfacial bond between CNTs and polymer and proper dispersion of the individual CNTs in the polymeric matrix can be guaranteed [144].

Let us consider four types of distributions of CNTs in FG-CNTRC plates with length a , width b and thickness h as shown in Figure 3.6. The uniform distribution is represented by UD-CNTRC, while the functionally graded distributions of CNTs in the thickness direction of the composite plates are represented by FG-V, FG-O and FG-X. For the FG-V type, the top surface of the CNTRC plate is CNT-rich. In FG-X, the top and the bottom surface of CNTRC plate are CNT-rich as shown in Figure 3.6. And in case of

FG-O, the CNT-rich zone is in the middle of the CNTRC plate. The material properties of the CNT-reinforced nanocomposites, which is a mixture of isotropic polymer (matrix) and CNTs (fiber), can be defined according to the Mori-Tanaka scheme [184,150] or the rule of mixtures [182]. Besides, the accuracy of the rule of mixtures was also discussed and an excellent agreement with Mori-Tanaka was reported in Ref. [185]. For convenience and simplicity, in this present study, the rule of mixtures is used to express the effective material properties of CNTRC plates as follows [152]:

$$E_{11} = \eta_1 V_{CNT} E_{11}^{CNT} + V_m E^m \quad (3.19)$$

$$\frac{\eta_2}{E_{22}} = \frac{V_{CNT}}{E_{22}^{CNT}} + \frac{V_m}{E^m} \quad (3.20)$$

$$\frac{\eta_3}{G_{12}} = \frac{V_{CNT}}{G_{12}^{CNT}} + \frac{V_m}{G^m} \quad (3.21)$$

Where E_{11}^{CNT} , E_{22}^{CNT} and G_{12}^{CNT} are longitudinal, transverse Young's moduli and shear modulus of CNT, respectively; and E^m and G^m indicate Young's modulus and shear modulus of the isotropic matrix, respectively. As the load transferred between the nanotube and polymeric phases is less than perfect (due to surface effects, strain gradients effects, intermolecular coupled stress effects, etc.), CNT efficiency parameters, η_1 , η_2 and η_3 were introduced in Ref. [152] to consider the size-dependent material properties. V_{CNT} and V_m are the CNT and matrix volume fractions and the relation between them is given by:

$$V_{CNT} + V_m = 1 \quad (3.22)$$

Similarly, Poisson's ratio ν_{12} and density ρ of CNTRC plates can be determined by:

$$\nu_{12} = V_{CNT}^* \nu_{12}^{CNT} + V_m \nu^m \quad (3.23)$$

$$\rho = V_{CNT} \rho^{CNT} + V_m \rho^m \quad (3.24)$$

Where ν_{12}^{CNT} , ρ^{CNT} and ν^m , ρ^m are Poisson's ratio and density of CNT and matrix, respectively.

The distributions of carbon nanotubes along the thickness direction of the CNTRC plate can be expressed as [150]:

$$V_{CNT} = \begin{cases} V_{CNT}^* & \text{(UD)} \\ (1 + \frac{2z}{h})V_{CNT}^* & \text{(FG-V)} \\ 2(1 - \frac{2|z|}{h})V_{CNT}^* & \text{(FG-O)} \\ 2(\frac{2|z|}{h})V_{CNT}^* & \text{(FG-X)} \end{cases} \quad (3.25)$$

Where

$$V_{CNT}^* = \frac{w_{CNT}}{w_{CNT} + (\rho_{CNT} / \rho_m) - (\rho_{CNT} / \rho_m)w_{CNT}} \quad (3.26)$$

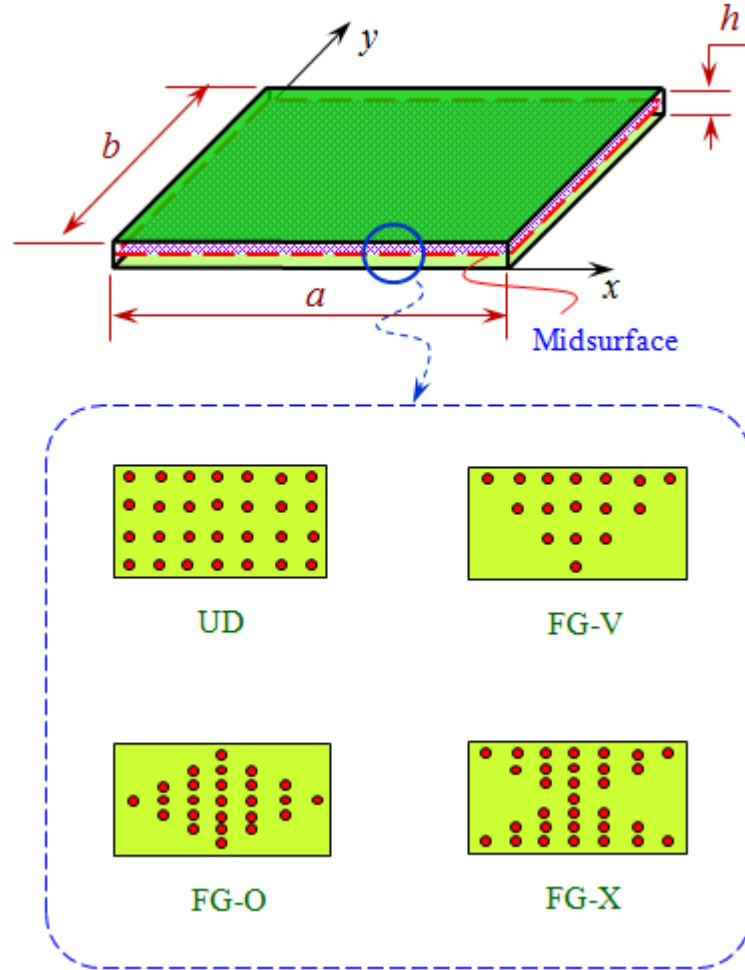


Figure 3.6. Volume fraction V_c versus the thickness of CNTRC.

In which w_{CNT} is the mass fraction of the carbon nanotubes in the CNTRC plate. Note that the UD-CNTRC and the three FG-CNTRC plates have the same CNT mass and volume fractions.

3.3 Plate theories

3.3.1 Classification of plate theories

Composite laminates are made of many layers of different materials or fiber orientations. In composite plates, thickness dimensions are smaller than planar dimensions. In analyses of the composite plates, several theories have been developed [186]:

- Equivalent single layer theories (2D); e.g. classical laminated plate theory (CLPT) and shear deformation laminated plate theories.
- Three dimensional elasticity theory (3D); e.g. traditional 3D elasticity formulations and layerwise theories.
- Multiple model methods (2D and 3D).

In this research, we choose the equivalent single layer (ESL) plate theories in order to calculate and simulate the composite plates. The ESL plate theories are derived from 3D elasticity theory by considering the kinematics of stresses or deformations state through the thickness of the plates. This allows us to reduce 3D models to 2D models.

3.3.2 An overview of composite plate theories

3.3.2.1 *The classical laminated plate theory*

The classical laminated theory (CLPT) is the simplest theory of the ELS laminated plates. In CLPT, based on Love-Kirchhoff, we assume that [186]:

- Straight lines are transverse normal to the mid-surface before deformation remain straight and transverse normal to the mid-surface after deformation, i.e., the transverse displacement is not dependent on the through thickness coordinates of plates.
- The transverse normal do not experience elongation, i.e. the transverse strain is zero.

- The transverse normal rotation is to remain perpendicular to the mid-surface after deformation, i.e. the transverse shear strains are zero.

We now consider a plate shown in Figure 3.7, displacement field of any arbitrary point (x, y, z) in CPLT are defined as follows:

$$\begin{aligned} u(x, y, z, t) &= u_0(x, y, t) + z \frac{\partial w_0}{\partial x} \\ v(x, y, z, t) &= v_0(x, y, t) + z \frac{\partial w_0}{\partial y} \\ w(x, y, z, t) &= w_0(x, y, t) \end{aligned} \quad (3.27)$$

Where u_0, v_0, w_0 are the mid-surface displacements along axis x, y, z , respectively. From the assumption of this theory, effects of the transverse shear and transverse normal are neglected and deformation is due to bending.

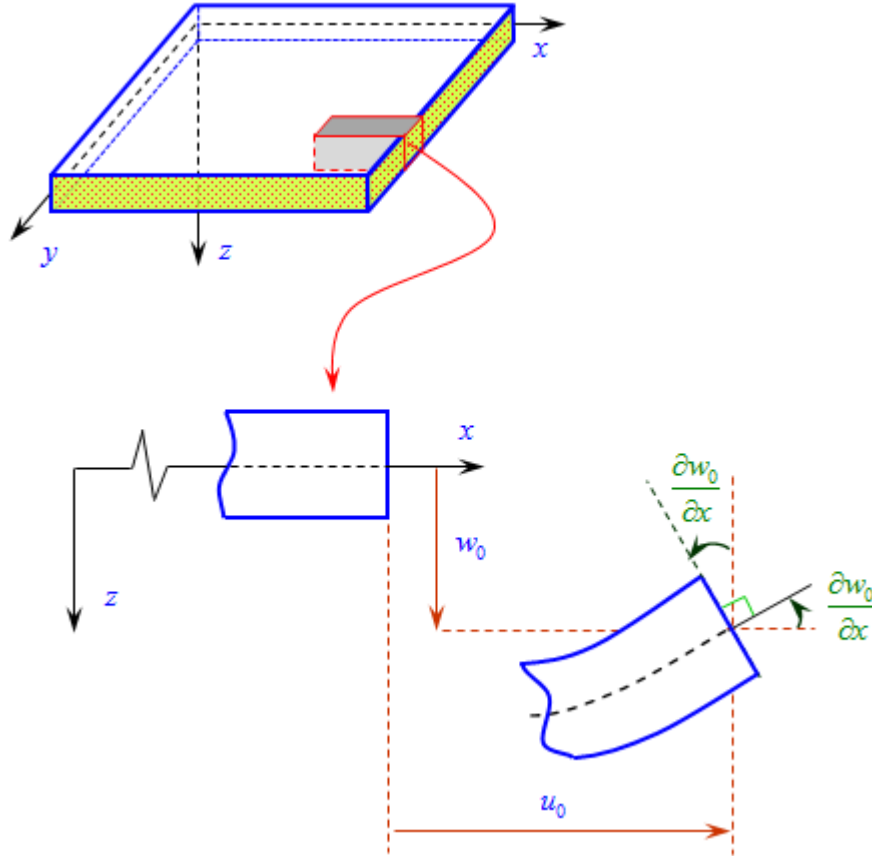


Figure 3.7. Undeformed and deformed plates in CPLT.

3.3.2.2 The first-order shear deformation theory

Compared to CLPT, in the first-order shear deformation theory (FSDT) [187,188], the transverse normal do not remain perpendicular to the mid-surface after deformation as shown in Figure 3.8. This means that the transverse shear strains are not zero in this theory.

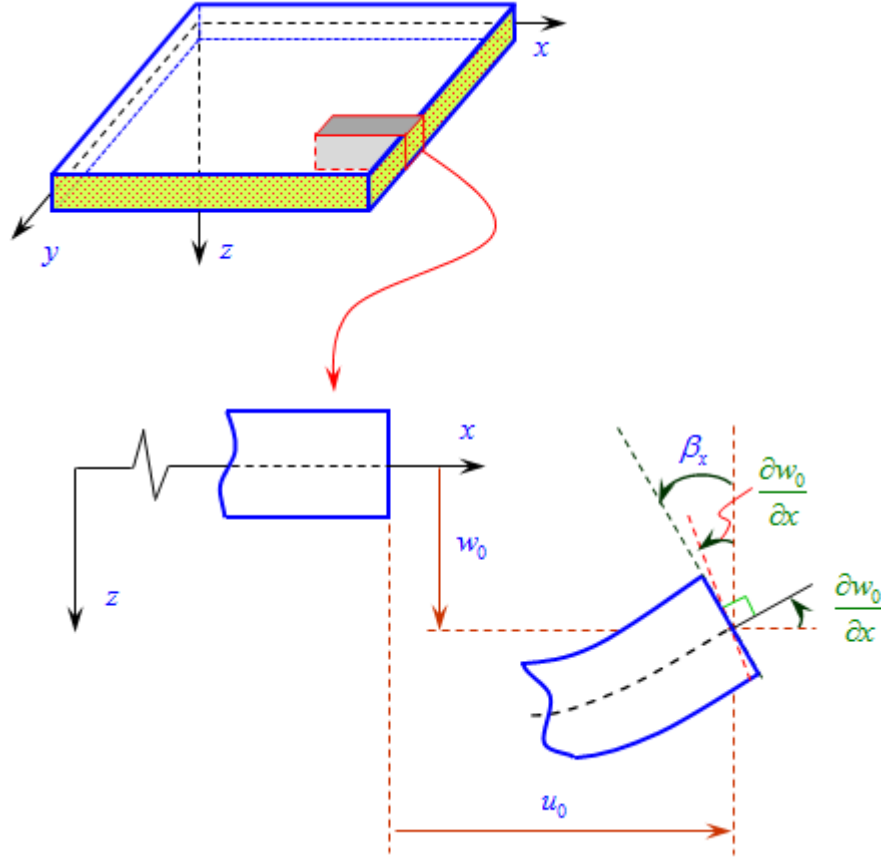


Figure 3.8. Undeformed and deformed plates in FSDT.

Displacement field of the FSDT is in the form:

$$\begin{aligned} u(x, y, z, t) &= u_0(x, y, t) + z\beta_x(x, y, t) \\ v(x, y, z, t) &= v_0(x, y, t) + z\beta_y(x, y, t) \\ w(x, y, z, t) &= w_0(x, y, t) \end{aligned} \quad (3.28)$$

Where u_0 , v_0 , w_0 are unknown displacements of a point on the mid-plan and β_x , β_y are unknown rotations around y-axis and x-axis, respectively, where the positive direction follows the right hand rule.

In the FSDT, shear correction factors are required and discussed in detail in Refs. [189,190]. However, they are difficult to determine for arbitrarily laminated composite plates.

3.3.2.3 The third-order shear deformation theory

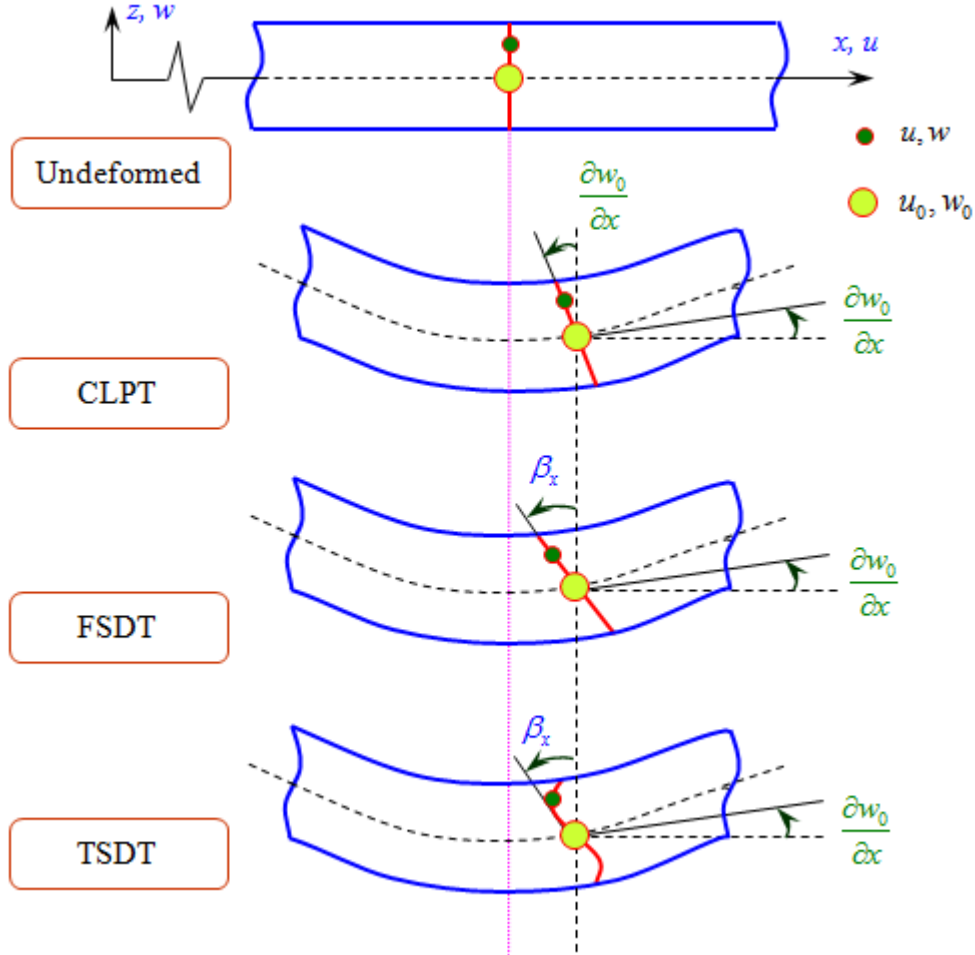


Figure 3.9. Deformation of transverse normal using CLPT, FSDT and TSDT.

The third-order shear deformation theory (TSDT) proposed by Reddy [191] is examined. In this theory, the displacements are cubic functions of thickness direction as given in [191]. The displacement field can be expressed as follows:

$$\begin{aligned}
u(x, y, z, t) &= u_0(x, y, t) + z\beta_x(x, y, t) + cz^3\left(\beta_x + \frac{\partial w_0}{\partial x}\right) \\
v(x, y, z, t) &= v_0(x, y, t) + z\beta_y(x, y, t) + cz^3\left(\beta_y + \frac{\partial w_0}{\partial x}\right) \\
w(x, y, z, t) &= w_0(x, y, t)
\end{aligned} \tag{3.29}$$

Where $c = 4/3h^2$.

Compared to FSDT, the shear correction factors in TSDT are not required. Moreover, the condition of zero transverse shear stresses on the boundary is satisfied.

3.3.2.4 The generalized higher-order shear deformation theory

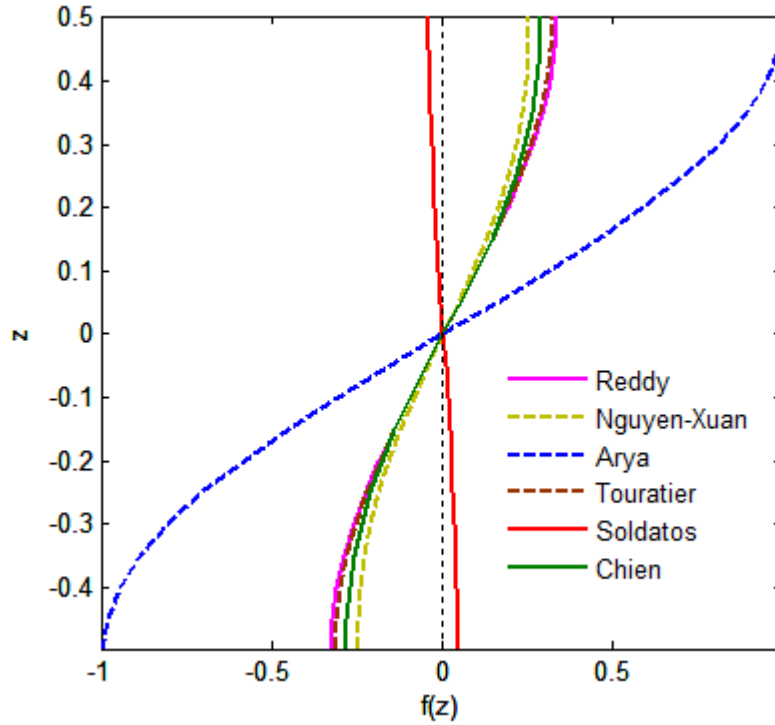


Figure 3.10. Function $f(z)$ through the thickness of the plates.

In the generalized higher order shear deformation theory, the displacement field is expressed as follows [192-194]:

$$\begin{aligned}
u(x, y, z, t) &= u_0(x, y, t) - z \frac{\partial w_0}{\partial x} + f(z) \beta_x(x, y, t) \\
v(x, y, z, t) &= v_0(x, y, t) - z \frac{\partial w_0}{\partial y} + f(z) \beta_y(x, y, t) \\
w(x, y, z, t) &= w_0(x, y, t)
\end{aligned} \tag{3.30}$$

Where the function $f(z)$ is a continuous function through the plate thickness chosen so that tangential stress at the top and bottom layer of the plates are zeros. Several functions $f(z)$ have been found and are shown in Table 3.2. It can be seen that by substituting function $f(z)$ of Reddy [191] into Eq. (3.30), it becomes Eq. (3.29). Hence, the form of Eq. (3.30) is called the generalized form for the higher order shear deformation theory.

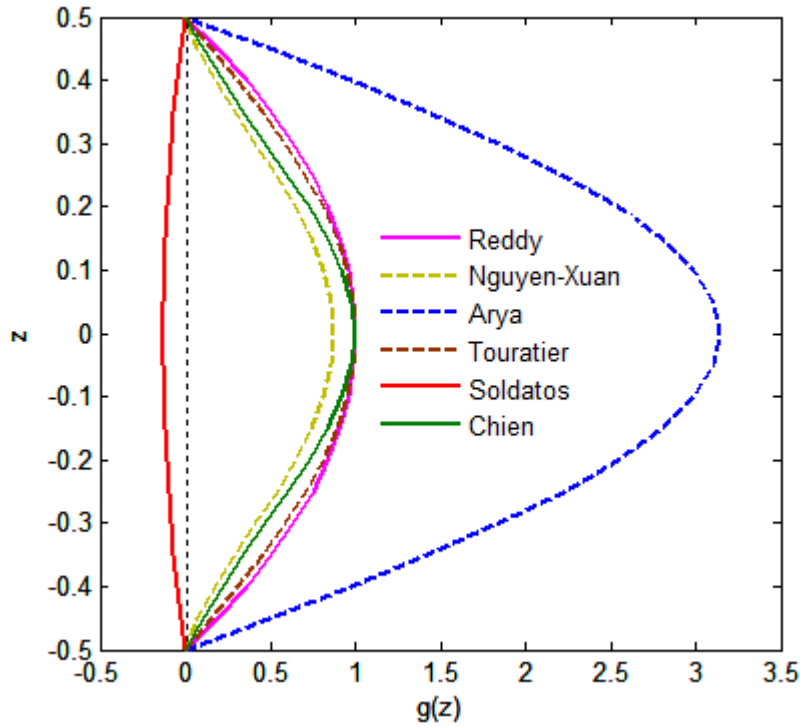


Figure 3.11. Derivation of the function $f(z)$ through the thickness of the plates.

Further, shapes of function $f(z)$ and its derivation through the thickness of the plates are illustrated in Figure 3.10 and Figure 3.11, respectively. We can see that the obtained results satisfy the free stress conditions at the top and bottom of the plates.

Table 3.2: Some transverse shear functions

Model	Function $f(z)$	Function $g(z) = f'(z)$
Reddy [191]	$f(z) = z - \frac{4}{3h^2} z^3$	$g(z) = 1 - \frac{4}{h^2} z^2$
Nguyen-Xuan et al. [195]	$f(z) = \frac{7}{8} z - \frac{2}{h^2} z^3 + \frac{2}{h^4} z^5$	$g(z) = \frac{7}{8} - \frac{6}{h^2} z^2 + \frac{10}{h^4} z^4$
Arya et al. [196]	$f(z) = \sin\left(\frac{\pi z}{h}\right)$	$g(z) = \frac{\pi}{h} \cos\left(\frac{\pi z}{h}\right)$
Touratier [194]	$f(z) = \frac{h}{\pi} \sin\left(\frac{\pi z}{h}\right)$	$g(z) = \cos\left(\frac{\pi z}{h}\right)$
Soldatos [193]	$f(z) = h \sinh\left(\frac{z}{h}\right) - z \cosh\left(\frac{1}{2}\right)$	$g(z) = \cosh\left(\frac{z}{h}\right) - \cosh\left(\frac{1}{2}\right)$
Chien et al. [197]	$f(z) = h \arctan\left(\frac{2z}{h}\right) - z$	$g(z) = \frac{2}{1 + \left(\frac{2z}{h}\right)^2} - 1$

3.4 Concluding remarks

In this chapter, we present material properties of the smart plates. Some general formulations of composite plates, functionally graded material plates and functionally graded carbon nanotube-reinforced composite plates are also derived. And they are the basic formulations in order to support the researches in this thesis, which will be presented in chapter 5, 6, 7, 8. Besides, four plate theories are presented, which are fundamentally required to develop a new function for the plate theory, which will be introduced in chapter 8.

Chapter 4

Isogeometric analysis

4.1 Overview

An overview of B-spline, non-uniform rational B-splines (NURBS) and isogeometric analysis (IGA) are discussed in this chapter. Most of the algorithms used to implement B-spline and NURBS are given in Ref [198] and isogeometric analysis in Ref. [1].

4.2 B-Spline

4.2.1 Basic functions

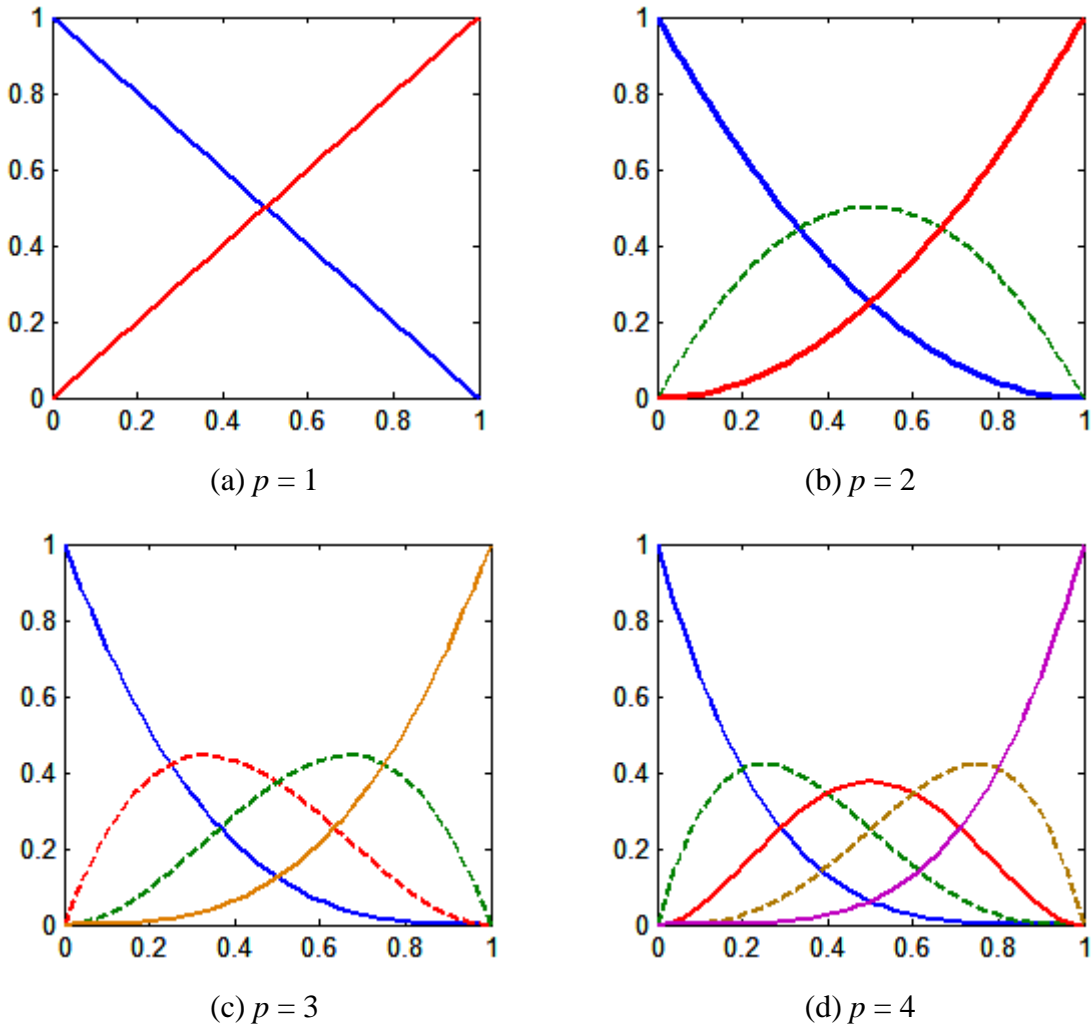


Figure 4.1. 1D B-spline basic functions with $p = 1, 2, 3, 4$.

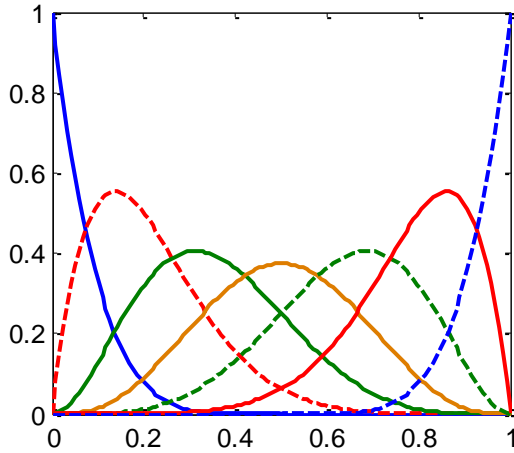
B-splines are constructed from knot vectors and thus a discussion of the knot vectors is a natural starting point for this study. A knot vector in one dimension, $\Xi = \{\xi_1, \xi_2, \dots, \xi_{n+p+1}\}$, is a non-decreasing sequence of parameter values $\xi_i \in \mathbb{R}$, $i=1, \dots, n+p$, where p is the polynomial order and n is the number of basic functions, which is used to build the B-spline curve. If the knots are equally spaced, the knot vector is uniform. A knot vector is called open if the first and the last knot values of the knot vector appear $p+1$ times. A B-spline basis function is C^∞ continuous inside a knot span and C^{p-1} continuous at a single knot. A knot value can appear more than once that is called a multiple knot.

Using Cox-de Boor algorithm [10-12], the B-spline basis functions with order $p = 0$, $N_{i,p}(\xi)$, are defined in Ref. [198] as:

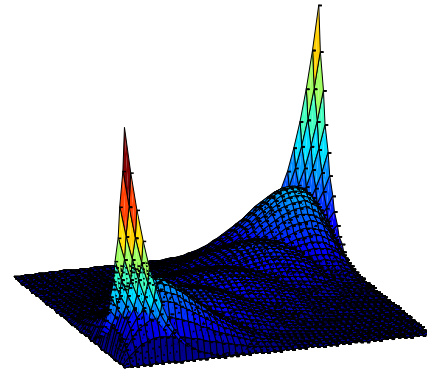
$$N_{i,0}(\xi) = \begin{cases} 1 & \text{if } \xi_i \leq \xi < \xi_{i+1} \\ 0 & \text{otherwise} \end{cases} \quad (4.1)$$

For $p = 1, 2, 3, \dots$, they can be written as:

$$N_{i,p}(\xi) = \frac{\xi - \xi_i}{\xi_{i+p} - \xi_i} N_{i,p-1}(\xi) + \frac{\xi_{i+p+1} - \xi}{\xi_{i+p+1} - \xi_{i+1}} N_{i+1,p-1}(\xi) \quad (4.2)$$



(a) 1D



(b) 2D

Figure 4.2. 1D and 2D cubic B-spline basic functions.

With $p = 0$ and 1 , the B-spline basis functions are similar to standard piecewise constant and linear finite element functions, respectively. According to Ref. [2], the B-spline

basic functions with $p \geq 2$ are considered in isogeometric analysis (IGA). Figure 4.1 shows the B-spline basis function with $p = 0, 1, 2, 3$.

Consider an open uniform knot vectors $\mathbf{H} = \{0, 0, 0, 0, 0, 0, \frac{1}{2}, 1, 1, 1, 1, 1, 1\}$, one dimensional (1D) and two dimensional (2D) cubic B-spline basic functions are shown in Figure 4.2.

Several important properties of B-spline can be expressed as follows [1]:

- The basic functions constitute a partition of unity, $\sum_{i=1}^n N_{i,p}(\xi) = 1, \forall \xi$
- The basic functions are nonnegative over the domain, $N_{i,p}(\xi) \geq 0, \forall \xi$
- The basic functions are linearly independent, $\sum_{i=1}^n \alpha_i N_{i,p}(\xi) = 0 \Leftrightarrow \alpha_k = 0, k = 0, 1, 2, \dots, n$
- The support of the B-spline function of order p is $p + 1$ knot spans, i.e., $N_{i,p}(\xi)$ is not zero over $[\xi_i, \xi_{i+p+1}]$.
- The basic functions with order p have $p - m_i$ continuous derivatives across knot ξ_i , where m_i is the multiplicity of knot ξ_i .
- Scaling or translating the knot vector does not alter the basic functions.
- The B-spline basic functions are generally only for approximation and not interpolation, i.e., they do not satisfy the Kronecker delta property $N_{i,p}(\xi_j) \neq \delta_{ij}$. Only in the case $m_i = p$, $N_{i,p}(\xi) = 1$

Consider a polynomial order p and knot vector $\Xi = \{\xi_1, \xi_2, \dots, \xi_{n+p+1}\}$, the first derivative of the basic functions can be defined as:

$$\frac{d}{d\xi} N_{i,p}(\xi) = \frac{p}{\xi_{i+p} - \xi_i} N_{i,p-1}(\xi) - \frac{p}{\xi_{i+p+1} - \xi_{i+1}} N_{i+1,p-1}(\xi) \quad (4.3)$$

And the higher derivatives are generally given as:

$$\frac{d^k}{d\xi^k} N_{i,p}(\xi) = \frac{p}{\xi_{i+p} - \xi_i} \left(\frac{d^{k-1}}{d\xi^{k-1}} N_{i,p-1}(\xi) \right) - \frac{p}{\xi_{i+p+1} - \xi_{i+1}} \left(\frac{d^{k-1}}{d\xi^{k-1}} N_{i+1,p-1}(\xi) \right) \quad (4.4)$$

4.2.2 B-spline geometries

4.2.2.1 B-spline curve

B-spline curves are formed by combining B-spline basic functions. Given n basic functions $N_{i,p}(\xi)$ and control points \mathbf{P}_i , the B-spline curve is defined by:

$$\mathbf{C}(\xi) = \sum_{i=1}^n N_{i,p}(\xi) \mathbf{P}_i \quad (4.5)$$

An example for a quadratic B-spline curve with a knot vector $\Xi = \{0, 0, 0, 1, 2, 3, 4, 5, 5, 5\}$ is illustrated in Figure 4.3. The B-spline curve is interpolated from the first and the last control points of the knot vector.

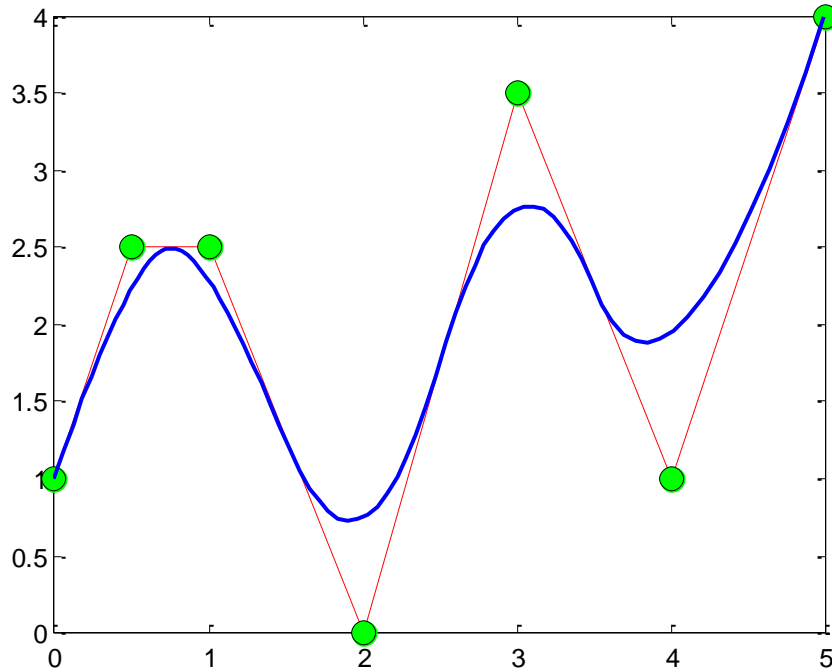


Figure 4.3. A quadratic B-spline curve.

Properties of B-spline curves are similar to those of their basic functions and discussed in detail in Ref. [198].

4.2.2.2 B-spline surface

We now consider a control net $\mathbf{P}_{i,j}$ and two knot vectors $\Xi = \{\xi_1, \xi_2, \dots, \xi_{n+p+1}\}$ and $\mathbf{H} = \{\eta_1, \eta_2, \dots, \eta_{m+q+1}\}$ with polynomial order p and q . A tensor product B-spline surface can be defined as:

$$\mathbf{S}(\xi, \eta) = \sum_{i=1}^n \sum_{j=1}^m N_{i,p}(\xi) M_{j,q}(\eta) \mathbf{P}_{i,j} \quad (4.6)$$

Where $N_{i,p}(\xi)$ and $M_{j,q}(\eta)$ are B-spline basic functions.

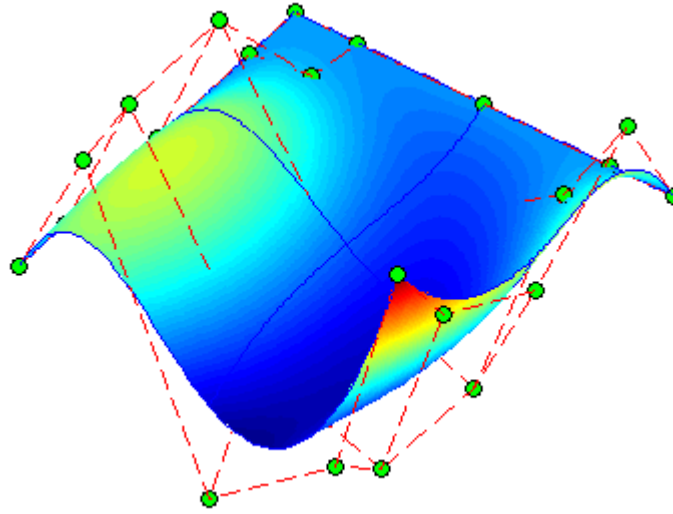


Figure 4.4. A NURBS surface.

Introducing a shape function $N_I^b(\xi, \eta) = N_{i,p}(\xi) M_{j,q}(\eta)$ associated with “node” I [51], Eq. (4.6) can be rewritten as follows:

$$\mathbf{S}(\xi, \eta) = \sum_{I=1}^{n \times m} N_I^b(\xi, \eta) \mathbf{P}_{i,j} \quad (4.7)$$

And a NURBS surface with $\Xi = \{0, 0, 0, 0, 0.5, 1, 1, 1, 1\}$ and $\mathbf{H} = \{0, 0, 0, 0.5, 1, 1, 1\}$ is shown in Figure 4.4.

4.2.3 Refinement

In B-spline, there are three ways to enrich or refine the mesh, namely h -refinement, p -refinement and k -refinement [1]. In computer aided geometric design (CAD) notation, these are referred to as knot insertion, degree elevation and continuity elevation,

respectively. And h - and p -refinements have a direct analogue to standard FEM, while k -refinement does not have similarity with FEM.

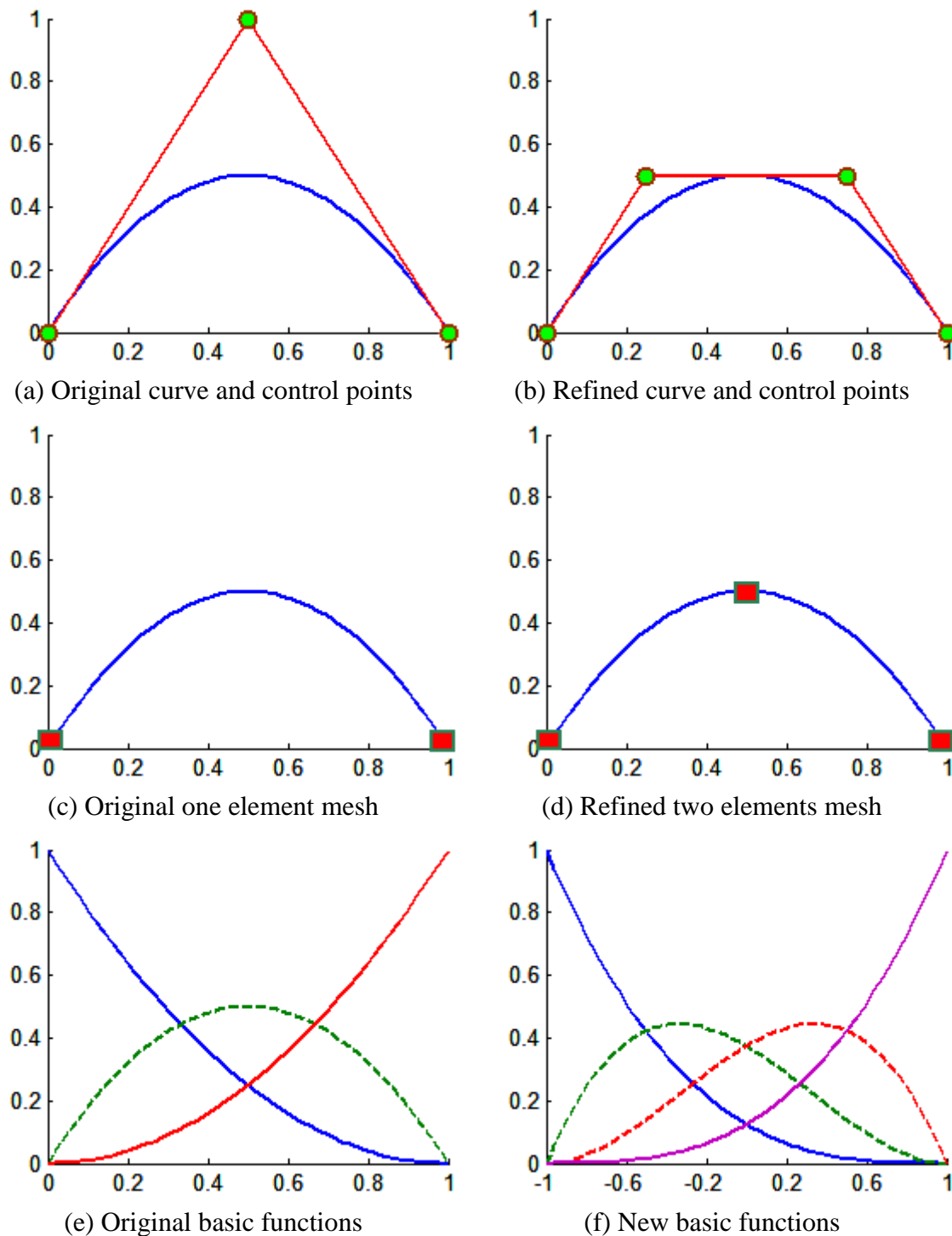
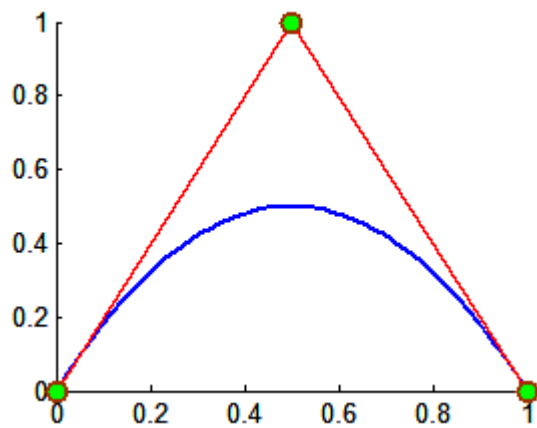
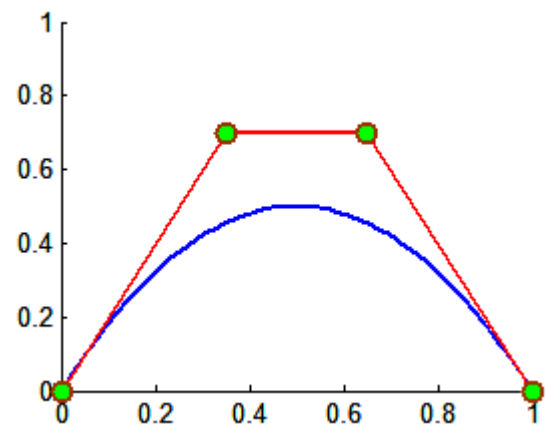


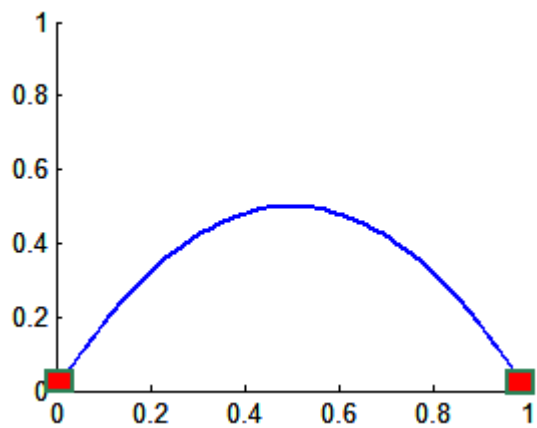
Figure 4.5. Knot insertion (h -refinement).



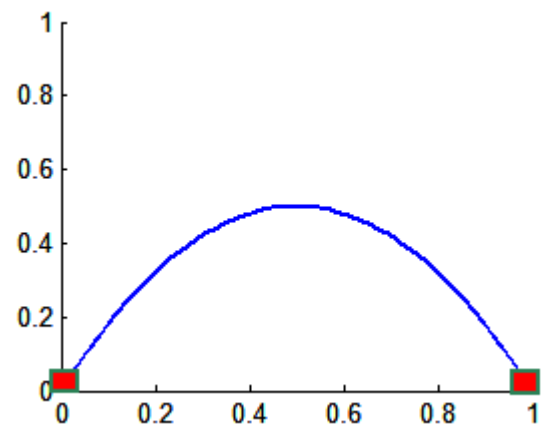
(a) Original curve and control points



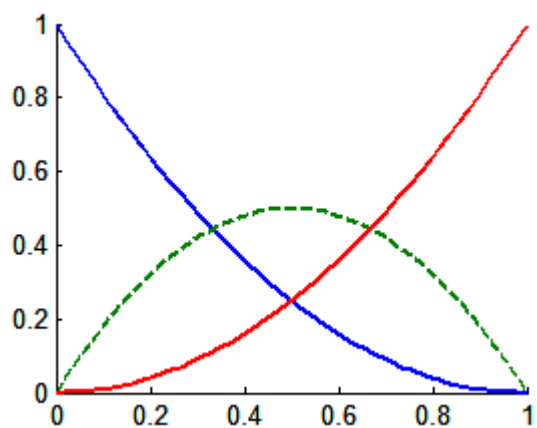
(b) Refined curve and control points



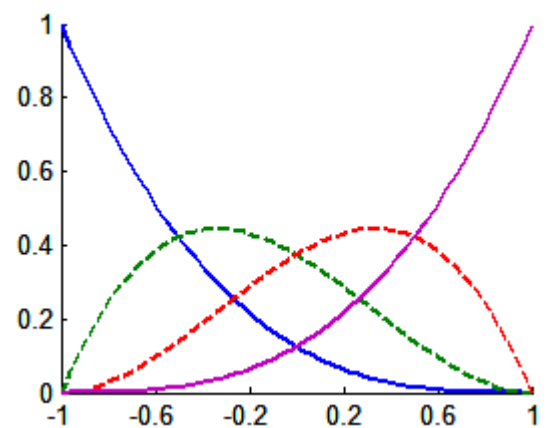
(c) Original one element mesh



(d) Refined two elements mesh



(e) Original basic functions



(f) New basic functions

Figure 4.6. Order elevation (p -refinement).

4.2.3.1 Knot insertion (*h-refinement*)

Consider a knot vector $\Xi = \{\xi_1, \xi_2, \dots, \xi_{n+p+1}\}$ and the corresponding control points \mathbf{P}_i , an extended knot vector is introduced as $\bar{\Xi} = \{\bar{\xi}_1 = \xi_1, \bar{\xi}_2, \dots, \bar{\xi}_{n+m+p+1} = \xi_{n+p+1}\}$ and formed from m knots. The $n + m$ new control points, $\bar{\mathbf{P}}_i$, can be defined using the following expression:

$$\bar{\mathbf{P}}_i = \alpha_i \mathbf{P}_i + (1 - \alpha_i) \mathbf{P}_{i-1} \quad (4.8)$$

Where

$$\alpha_i = \begin{cases} 1 & 1 \leq i \leq k - p \\ \frac{\bar{\xi} - \xi_i}{\bar{\xi}_{i+p} - \xi_i} & k - p + 1 \leq i \leq k \\ 0 & k + 1 \leq i \leq n + p + 2 \end{cases} \quad (4.9)$$

An example for knot insertion of a quadratic B-spline curve is depicted in Figure 4.5. The original knot vector is $\Xi = \{0, 0, 0, 1, 1, 1\}$. The control points, element mesh and basic functions of the original curve are shown in Figure 4.5a, c, e, respectively. With *h*-refinement, one knot point at $\xi = 0.5$ is inserted into the original knot vector and the new one becomes $\Xi = \{0, 0, 0, 0.5, 1, 1, 1\}$. Geometry of the curve is not changed but the knot vector, the mesh, the basic function is changed as illustrated in Figure 4.5b, d, f. They are richer, i.e. one more control point, one more element mesh and one more basic function than in the original case. And we can continue to refine by adding more basic functions of the same order, while leaving the curve unchanged.

4.2.3.2 Order elevation (*p-refinement*)

The process, *p*-refinement, involves raising the polynomial order of the basic functions used to represent the geometry. In *p*-refinement, the multiplicity of each knot value is increased by one, but no new knot values are inserted. Compared to *h*-refinement, either the geometry or the parameterization is not changed.

Similar to *h*-refinement, an example of *p*-refinement for a curve is also shown in Figure 4.6. As considered in Figure 4.5, the unrefined curve with the control points, mesh and quadratic basic functions are depicted on the left-hand side of Figure 4.6. The original knot vector becomes $\Xi = \{0, 0, 0, 1, 1, 1\}$. Through order elevation procedure by repeating

value of the knot control point one time, the new knot vector is $\Xi = \{0, 0, 0, 0, 1, 1, 1, 1\}$. And the refined curve is illustrated on the right-hand side of Figure 4.6.

4.2.3.3 *k-refinement*

k-refinement is the process, in which order elevation is used by knot insertion procedure. This process leads to a higher order and higher continuity basic functions than the process if knot insertion followed by order elevation. This noncommutative nature of refinement was first proposed in Ref. [2].

4.3 Non-Uniform Rational B-Splines

Non-uniform rational B-Splines (NURBS) are rational functionals of B-splines and inherit all their properties. Circles, cylinders, ellipses, etc., in conic section can be exactly constructed by NURBS, i.e., projective transformations of piecewise quadratic curves. And this is one of defining features of isogeometric analysis [1].

4.3.1 NURBS basic functions

NURBS basic functions can be expressed as [1]:

$$R_{i,p}(\xi) = \frac{N_{i,p}(\xi)w_i}{W(\xi)} = \frac{N_{i,p}(\xi)w_i}{\sum_{j=1}^n N_{j,p}(\xi)w_j} \quad (4.10)$$

Where $N_{i,p}(\xi)$ is the i^{th} B-spline basic function with order p and w_i is a positive weight.

Note that the weights have an important role in defining the NURBS basic functions, but they are separated from any explicit geometric interpretation in this process, and there is a freedom to choose control points independently from their associated weights. For a special case, the weights are all equal, the curve is polynomial and the NUBRS basic functions are the B-spline basic functions. In simple geometries cases, the weights are given by the analytical method [198]. And in complex geometries case, the weights are defined from CAD packages.

Derivatives of NURBS basic function can be defined as:

$$\frac{d}{d\xi} R_{i,p}(\xi) = w_i \frac{N'_{i,p}(\xi)W(\xi) - N_{i,p}(\xi)W'(\xi)}{W^2(\xi)} \quad (4.11)$$

Where $N'_{i,p}(\xi)$ and $W'(\xi)$ are calculated by:

$$N'_{i,p}(\xi) = \frac{dN_{i,p}(\xi)}{d\xi} \quad ; \quad W'(\xi) = \sum_{\hat{i}=1}^n N'_{\hat{i},p}(\xi) w_{\hat{i}} \quad (4.12)$$

Higher-order derivatives of NURBS can be expressed as follows [1]:

$$\frac{d^k}{d\xi^k} R_{i,p}(\xi) = \frac{A_i^{(k)}(\xi) - \sum_{j=1}^k \frac{k!}{j!(k-j)!} W^{(j)}(\xi) \frac{d^{(k-j)}}{d\xi^{(k-j)}} R_{i,p}(\xi)}{W(\xi)} \quad (4.13)$$

Where

$$A_i^{(k)}(\xi) = w_i \frac{d^k}{d\xi^k} N_{i,p}(\xi) \quad ; \quad W^{(k)}(\xi) = \frac{d^k}{d\xi^k} W(\xi) \quad (4.14)$$

4.3.2 NURBS curves

NURBS curves can be defined as:

$$\mathbf{C}(\xi) = \sum_{i=1}^n R_{i,p}(\xi) \mathbf{P}_i \quad (4.15)$$

Where \mathbf{P}_i is control points.

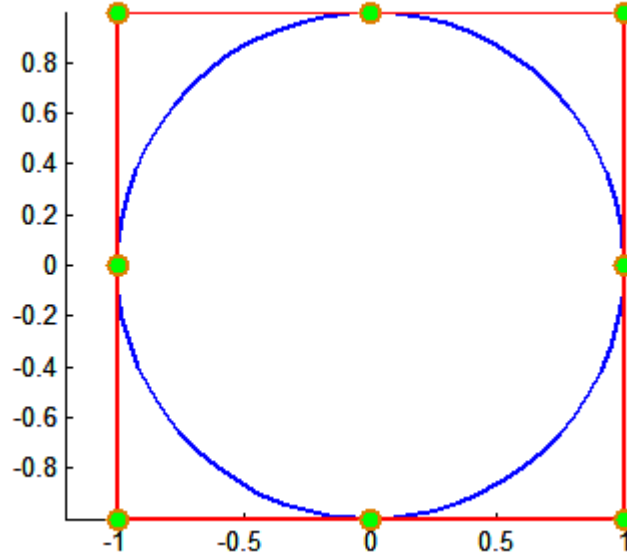


Figure 4.7. A NURBS curve for the circle.

Table 4.1: Control points and weights for the circle with radius $R = 1$

i	1	2	3	4	5	6	7	8	9
x_i	1	1	0	-1	-1	-1	0	1	1
y_i	0	1	1	1	0	-1	-1	-1	0
w_i	1	$\sqrt{2}/2$	1	$\sqrt{2}/2$	1	$\sqrt{2}/2$	1	$\sqrt{2}/2$	1

To make it clear, a circle as an example, is considered. In this problem, a NURBS quadratic basic function is enough to construct the circle exactly. The control points are illustrated in Table 4.1 and Figure 4.7.

Further, the effect of weights on the NURBS curve is investigated in Figure 4.8. It can be seen that when the weight decreases from 1 to 0.25 and 0.05, the curve is pulled towards the associated control point.

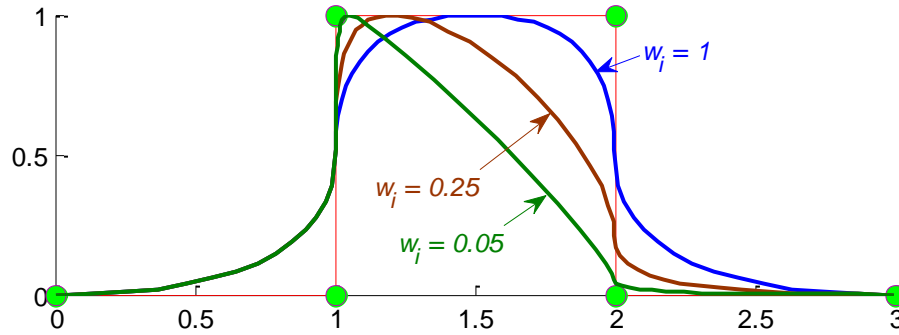


Figure 4.8. Effect of weight on NURBS curve.

4.3.3 NURBS surfaces

Consider two knot vectors $\Xi = \{\xi_1, \xi_2, \dots, \xi_{n+p+1}\}$, $\mathbf{H} = \{\eta_1, \eta_2, \dots, \eta_{m+q+1}\}$ and a control net \mathbf{P}_i , a tensor-product NURBS surface can be defined as:

$$\mathbf{S}(\xi, \eta) = \sum_{i=1}^n \sum_{j=1}^m R_{i,j}^{p,q}(\xi, \eta) \mathbf{P}_{i,j} \quad (4.16)$$

Where $R_{i,j}^{p,q}(\xi, \eta)$ are the bivariate basic functions expressed by:

$$R_{i,j}^{p,q}(\xi, \eta) = \frac{N_i(\xi) M_j(\eta) w_{i,j}}{\sum_{\bar{i}=1}^n \sum_{\bar{j}=1}^m N_{\bar{i}}(\xi) M_{\bar{j}}(\eta) w_{\bar{i},\bar{j}}} \quad (4.17)$$

And Figure 4.9 illustrates a NURBS surface and control mesh.

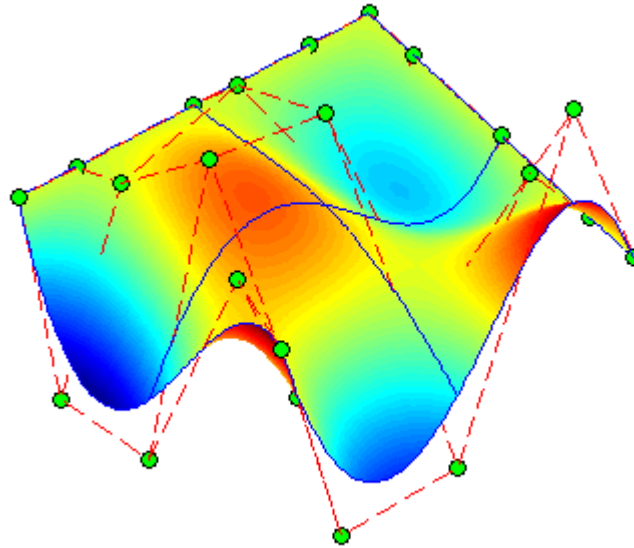


Figure 4.9. NURBS surface and control mesh.

4.4 Isogeometric discretization

Isogeometric concept, the most important concept in the element technology [1], refers to the use of the same basic functions for both the geometry and unknown field approximations. This concept is used in both finite element method (FEM) and isogeometric analysis (IGA), but there are some differences:

- In FEM, the basic functions are chosen to approximate the geometry, which are also used to approximate the unknown fields. Thus, both the geometry and the unknown fields are approximated. Finite element basic functions are typically interpolatory and called interpolation functions or shape functions. Refinement may be required for both the geometry and the unknown fields.
- In IGA, the basic functions are not interpolatory, are chosen to exactly capture the geometry and are used to approximate the unknown fields. Refinement may be only required for the unknown field, but not for geometry because the geometry is exact.

In FEM, there are mesh and elements. The elements have two representations, i.e. one in the parent domain and one in the physical space. Elements are defined by their nodes

and the degrees-of-freedom are defined at the nodes. In contrast, in IGA, the geometry is obtained from CAD model and there are two types of meshes, namely the control mesh and the physical mesh. The control points define the control mesh, which does not conform to the actual geometry. The physical mesh is an exact geometry. However, the degrees-of-freedom are located at control points. A schematic illustration of the ideas of the IGA computation is depicted in Figure 4.10.

In two-dimensional analysis, the parametric domain is a square. The mapping from the parametric domain to the physical domain is expressed as:

$$\mathbf{x} = \sum_I^n \mathbf{R}_I(\xi, \eta) \mathbf{P}_I \quad (4.18)$$

Where n is the number of control points, $\mathbf{R}_I(\xi, \eta)$ is the NUBRS basic function, I is the control point and (ξ, η) are the parametric coordinates. The displacement field in isogeometric formulation is approximated from the value of the displacement field at the control point I , \mathbf{u}_I , by using the same basic function as:

$$\mathbf{u} = \sum_I^n \mathbf{R}_I(\xi, \eta) \mathbf{u}_I \quad (4.19)$$

4.5 The spatial derivatives

To compute the spatial derivatives of Eq. (4.18), the Jacobian matrix of the geometry needs to define as follows:

$$\mathbf{J}_\xi = \begin{bmatrix} x_{,\xi} & x_{,\eta} \\ y_{,\xi} & y_{,\eta} \end{bmatrix} \quad (4.20)$$

The spatial derivatives of Eq. (4.18) can be expressed as:

$$\frac{\partial x_i}{\partial \xi_i} = \frac{\partial R_I}{\partial \xi_i} P_{iI} \quad (4.21)$$

Where P_{iI} is the i coordinate of control point I . The derivatives of the basic functions in the physical domain coordinates can be given by:

$$\begin{bmatrix} R_{I,x} & R_{I,y} \end{bmatrix} = \begin{bmatrix} R_{I,\xi} & R_{I,\eta} \end{bmatrix} \begin{bmatrix} \xi_{,x} & \xi_{,y} \\ \eta_{,x} & \eta_{,y} \end{bmatrix} = \begin{bmatrix} R_{I,\xi} & R_{I,\eta} \end{bmatrix} \mathbf{J}_\xi^{-1} \quad (4.22)$$

Where $R_{I,\xi}$ and $R_{I,\eta}$ are defined in Eq. (4.3).

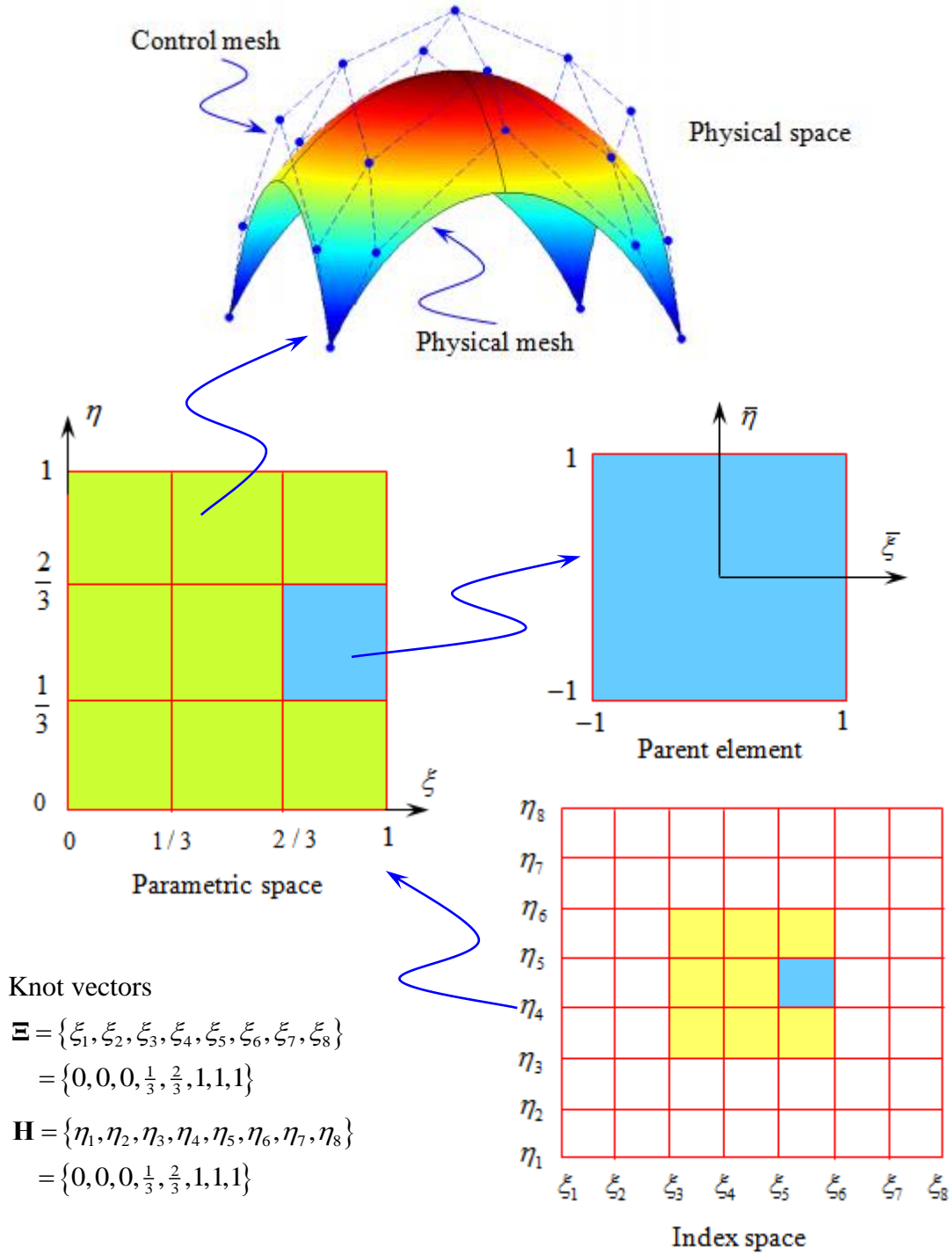


Figure 4.10. Parametric and physical space with quadratic B-splines.

The spatial second derivatives of the basic functions can be expressed as follows:

$$\begin{bmatrix} R_{I,xx} & R_{I,yy} & R_{I,xy} \end{bmatrix} = \begin{bmatrix} R_{I,\xi\xi} & R_{I,\eta\eta} & R_{I,\xi\eta} \end{bmatrix} - \begin{bmatrix} R_{I,x} \\ R_{I,y} \end{bmatrix} \begin{bmatrix} x_{,\xi\xi} & x_{,\eta\eta} & x_{,\xi\eta} \\ y_{,\xi\xi} & y_{,\eta\eta} & y_{,\xi\eta} \end{bmatrix} \mathbf{J}_2^{-1} \quad (4.23)$$

Where

$$\mathbf{J}_2 = \begin{bmatrix} x_{,\xi\xi} & y_{,\xi\xi} & 2x_{,\xi}y_{,\xi} \\ x_{,\eta\eta} & y_{,\eta\eta} & 2x_{,\eta}y_{,\eta} \\ x_{,\xi}x_{,\eta} & y_{,\xi}y_{,\eta} & x_{,\xi}y_{,\eta} + y_{,\xi}x_{,\eta} \end{bmatrix} \quad (4.24)$$

Equation (4.23) is used to calculate the stiffness matrix later in chapter 7. In addition, isogeometric basis functions were shown to deliver significant advantages for the analysis, independently from the integration with CAD. One of their most notable features is that they can achieve any desired degree of smoothness through the choice of the interpolation order, as opposed to traditional FEM, where C^0 inter-element continuity is automatically achieved, whilst lower continuity can be built in easily through knot insertion [199-201]. If p is the order of the discretization, C^{p-1} inter-element continuity is achieved when no repeated entries in the knot vectors are present. Hence, IGA easily fulfils the C^1 -continuity requirements for plate elements stemming from the HSDT, which is of interest in this study.

4.6 Numerical integration

Integration over the entire physical domain is split into element integrals. These integrals are pulled back to the parametric element via the geometry mapping as shown in Eq. (4.18). And then, integrals over the parametric element are pulled back to the parent domain, as shown in Figure 4.10.

Using standard Gauss-Legendre quadrature, a $(p+1) \times (q+1)$ Gaussian quadrature rule is adopted for this work with p, q are the orders of NURBS in the ξ and η directions, respectively. In IGA, Gaussian quadrature is not optimal.

The transformation from the parent domain into the parametric domain is given by:

$$\begin{aligned} \xi &= \frac{1}{2} \left[(\xi_{i+1} - \xi_i) \bar{\xi} + (\xi_{i+1} + \xi_i) \right] \\ \eta &= \frac{1}{2} \left[(\eta_{j+1} - \eta_j) \bar{\eta} + (\eta_{j+1} + \eta_j) \right] \end{aligned} \quad (4.25)$$

Therefore, the Jacobian of this transformation is defined as:

$$J_{\xi} = \frac{1}{4} \left[(\xi_{i+1} - \xi_i) + (\eta_{j+1} - \eta_j) \right] \quad (4.26)$$

4.6 Comparison between IGA and FEM

Table 4.2: Differences between IGA and FEM [1]

Isogeometric analysis	Finite element analysis
- Exact geometry	- Approximate geometry
- Control points	- Nodal points
- Control variables	- Nodal variables
- Basic functions do not interpolate control points and variables NURBS basic	- Basic functions interpolate nodal points and variables polynomial basic
- High, easily controlled continuity	- C^0 -continuity, always fixed
- hpk -refinement space	- hp -refinement space

Some similarities and differences between IGA and classical FEM are illustrated in this thesis. Firstly, some basic differences are summarized in Table 4.2. Next, some similarities are also examined in Table 4.3.

Table 4.3: Similarities between IGA and FEM [1]

IGA and FEM
Isoparametric concept
Galerkin's method
Compactly supported basic
Partition of unity
Patch tests are satisfied

4.7 Concluding remarks

Some features of IGA are presented in this chapter. One of their most notable features is that they can achieve any desired degree of smoothness through the choice of the interpolation order. In IGA, the geometry is obtained from CAD model and there are two types of meshes, namely the control mesh and the physical mesh. And the physical

mesh represents the exact geometry. Hence, geometry models are directly used for FEA without mesh generators.

Chapter 5

Piezoelectric composite plates

5.1 Overview

In this chapter, we deal with the first objective of the thesis, which was shown in section 2.3 of chapter 2. The governing equations for piezoelectric composite plates are presented and the weak form is established. In the composite plates, the mechanical displacement field is approximated according to the third-order shear deformation theory (TSDT), which was presented in section 3.3.2.3, using isogeometric elements based on Non-Uniform Rational B-Spline (NURBS) basis functions. The electric potential is assumed to vary linearly through the thickness for each piezoelectric sub-layer. A displacement and velocity feedback control algorithm is used for the active control of the static deflection and dynamic response of the plates through a closed-loop control with bonded or embedded distributed piezoelectric sensors and actuators. The accuracy and reliability of the proposed method is verified by comparing its numerical predictions with those of other available numerical approaches.

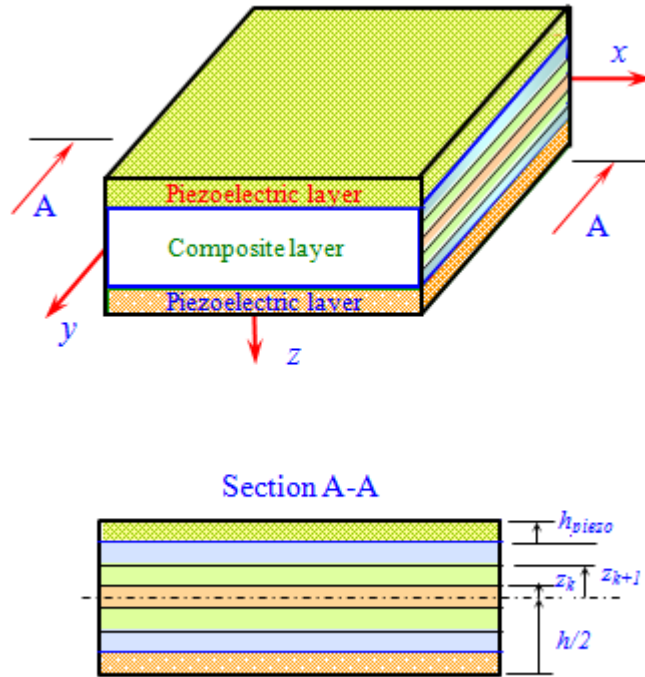


Figure 5.1. Model of a piezoelectric composite plate.

5.2 Governing equations for smart piezoelectric plates

Now we consider a composite plate integrated with piezoelectric layer as shown in Figure 5.1. The layers are assumed to be bonded perfectly, orthotropic [81] with small strains [82] and isothermal conditions. Moreover, the piezoelectric actuators and sensors are made of homogenous dielectric materials [83] and high electric fields are excluded [84,85]. According to these assumptions, next section introduces formulations for the piezoelectric composite plates.

5.2.1 Weak form for piezoelectric composite plates

Based on Hamilton's variational principle [90], the weak form equations for piezoelectric composite plates can be defined as follows:

$$\delta L = 0 \quad (5.1)$$

Where L is the energy functional written in the following form:

$$L = \int \left(\frac{1}{2} \rho \dot{\mathbf{u}}^T \dot{\mathbf{u}} - \frac{1}{2} \boldsymbol{\sigma}^T \boldsymbol{\varepsilon} + \frac{1}{2} \mathbf{D}^T \mathbf{E} + \mathbf{u} \mathbf{f}_s - \phi \mathbf{q}_s \right) d\Omega + \sum \mathbf{u}^T \mathbf{F}_p - \sum \phi \mathbf{Q}_p \quad (5.2)$$

where \mathbf{u} and $\dot{\mathbf{u}}$ are displacements and velocities of the mechanical field, respectively, \mathbf{f}_s and \mathbf{F}_p are the external forces including the surface forces and point forces, respectively, ϕ is the electric potential; \mathbf{Q}_p and \mathbf{q}_s are point charges and surface charges, respectively, and $\boldsymbol{\sigma}$, $\boldsymbol{\varepsilon}$, \mathbf{D} , \mathbf{E} are defined in Eq. (3.1), in which \mathbf{E} is gradient of the electric potential field ϕ [89] defined as follows:

$$\mathbf{E} = -\text{grad}\phi \quad (5.3)$$

In Eq. (5.2), there are two unknown variable fields, namely the electric potential field ϕ and the mechanical field \mathbf{u} . To solve numerically for these unknowns, it is necessary to choose a suitable approximation for the mechanical field and the electric potential field. In this research, isogeometric finite elements are used to approximate these two unknown variable fields.

5.2.1.1 Approximation of the mechanical displacement field

According to the TSDT proposed by Reddy [191], the displacements of an arbitrary point in the plate can be expressed by:

$$\begin{aligned}
u(x, y, z) &= u_0 + z\beta_x + cz^3(\beta_x + w_{,x}) \\
v(x, y, z) &= v_0 + z\beta_y + cz^3(\beta_y + w_{,y}), \quad (-h/2 \leq z \leq h/2) \\
w(x, y, z) &= w_0
\end{aligned} \tag{5.4}$$

Where $c = 4h^2/3$

The in-plane strains are expressed by the following equation:

$$\boldsymbol{\varepsilon} = [\varepsilon_{xx} \ \varepsilon_{yy} \ \gamma_{xy}]^T = \boldsymbol{\varepsilon}_0 + z\boldsymbol{\kappa}_1 + z^3\boldsymbol{\kappa}_2 \tag{5.5}$$

Where

$$\boldsymbol{\varepsilon}_0 = \begin{bmatrix} u_{0,x} \\ v_{0,y} \\ u_{0,y} + v_{0,x} \end{bmatrix}, \quad \boldsymbol{\kappa}_1 = \begin{bmatrix} \beta_{x,x} \\ \beta_{y,y} \\ \beta_{x,y} + \beta_{y,x} \end{bmatrix}, \quad \boldsymbol{\kappa}_2 = c \begin{bmatrix} \beta_{x,x} + w_{0,xx} \\ \beta_{y,y} + w_{0,yy} \\ \beta_{x,y} + \beta_{y,x} + 2w_{0,xy} \end{bmatrix} \tag{5.6}$$

and the transverse shear strains are given by:

$$\boldsymbol{\gamma} = [\gamma_{xz} \ \gamma_{yz}]^T = \boldsymbol{\varepsilon}_s + z^2\boldsymbol{\kappa}_s \tag{5.7}$$

with

$$\boldsymbol{\varepsilon}_s = \begin{bmatrix} \beta_x + w_{0,x} \\ \beta_y + w_{0,y} \end{bmatrix}, \quad \boldsymbol{\kappa}_s = 3c \begin{bmatrix} \beta_x + w_{0,x} \\ \beta_y + w_{0,y} \end{bmatrix} \tag{5.8}$$

From Hooke's law and Eqs. (5.5) and (5.7), the stress for the mechanical field is a function of z -coordinate and is defined as follows:

$$\boldsymbol{\sigma} = \begin{bmatrix} \boldsymbol{\sigma}_p \\ \boldsymbol{\tau} \end{bmatrix} = \underbrace{\begin{bmatrix} \bar{\mathbf{D}} & \mathbf{0} \\ \mathbf{0} & \bar{\mathbf{D}}_s \end{bmatrix}}_{\mathbf{c}} \underbrace{\begin{bmatrix} \boldsymbol{\varepsilon} \\ \boldsymbol{\gamma} \end{bmatrix}}_{\bar{\boldsymbol{\varepsilon}}} = \mathbf{c}\bar{\boldsymbol{\varepsilon}} \tag{5.9}$$

Where $\boldsymbol{\tau}$ and $\boldsymbol{\sigma}_p$ are the shear stress and the in-plane stress, respectively, and $\bar{\mathbf{D}}$ and $\bar{\mathbf{D}}_s$ are expressed as follows:

$$\bar{\mathbf{D}} = \begin{bmatrix} \mathbf{A} & \mathbf{B} & \mathbf{E} \\ \mathbf{B} & \mathbf{D} & \mathbf{F} \\ \mathbf{E} & \mathbf{F} & \mathbf{H} \end{bmatrix}, \quad \bar{\mathbf{D}}_s = \begin{bmatrix} \mathbf{A}_s & \mathbf{B}_s \\ \mathbf{B}_s & \mathbf{D}_s \end{bmatrix} \tag{5.10}$$

In which

$$\begin{aligned}
(\mathbf{A}, \mathbf{B}, \mathbf{D}, \mathbf{E}, \mathbf{F}, \mathbf{H}) &= \int_{-h/2}^{h/2} (1, z, z^2, z^3, z^4, z^6) \bar{Q}_{ij} dz \quad i, j = 1, 2, 6 \\
(\mathbf{A}_s, \mathbf{B}_s, \mathbf{D}_s) &= \int_{-h/2}^{h/2} (1, z^2, z^4) \bar{Q}_{ij} dz \quad i, j = 4, 5
\end{aligned} \tag{5.11}$$

Where \bar{Q}_{ij} is defined in Eq. (3.8).

Using the NURBS basis functions defined in Eq. (4.17), the displacement field \mathbf{u} of the plate is approximated as:

$$\mathbf{u}^h(\xi, \eta) = \sum_I^{m \times n} N_I(\xi, \eta) \mathbf{d}_I \quad (5.12)$$

Where $\mathbf{d}_I = [u_{0I} \ v_{0I} \ w_{0I} \ \beta_{xI} \ \beta_{yI}]^T$ is the vector of degrees of freedom associated with the control point I .

Substituting Eq. (5.12) into Eqs. (5.5) to (5.8), the in-plane and shear strains can be rewritten as:

$$\begin{bmatrix} \boldsymbol{\varepsilon}_0^T & \boldsymbol{\kappa}_1^T & \boldsymbol{\kappa}_2^T & \boldsymbol{\varepsilon}_s^T & \boldsymbol{\kappa}_s^T \end{bmatrix}^T = \sum_{A=1}^{m \times n} \begin{bmatrix} (\mathbf{B}_I^m)^T & (\mathbf{B}_I^{b1})^T & (\mathbf{B}_I^{b2})^T & (\mathbf{B}_I^{s0})^T & (\mathbf{B}_I^{s1})^T \end{bmatrix}^T \mathbf{d}_I \quad (5.13)$$

Where

$$\mathbf{B}_I^m = \begin{bmatrix} N_{I,x} & 0 & 0 & 0 & 0 \\ 0 & N_{I,y} & 0 & 0 & 0 \\ N_{I,y} & N_{I,x} & 0 & 0 & 0 \end{bmatrix}, \quad \mathbf{B}_I^{b1} = \begin{bmatrix} 0 & 0 & 0 & N_{I,x} & 0 \\ 0 & 0 & 0 & 0 & N_{I,y} \\ 0 & 0 & 0 & N_{I,y} & N_{I,x} \end{bmatrix}, \quad (5.14)$$

$$\mathbf{B}_I^{b2} = c \begin{bmatrix} 0 & 0 & N_{I,xx} & N_{I,x} & 0 \\ 0 & 0 & N_{I,yy} & 0 & N_{I,y} \\ 0 & 0 & 2N_{I,xy} & N_{I,y} & N_{I,x} \end{bmatrix},$$

$$\mathbf{B}_I^{s0} = \begin{bmatrix} 0 & 0 & N_{I,x} & N_I & 0 \\ 0 & 0 & N_{I,y} & 0 & N_I \end{bmatrix}, \quad \mathbf{B}_I^{s1} = 3c \begin{bmatrix} 0 & 0 & N_{I,x} & N_I & 0 \\ 0 & 0 & N_{I,y} & 0 & N_I \end{bmatrix} \quad (5.15)$$

5.2.1.2 Approximation of the electrical potential field

In the present study, the electric potential field is approximated as [82]:

$$\phi^i(z) = \mathbf{N}_\phi^i \boldsymbol{\phi}^i \quad (5.16)$$

Where \mathbf{N}_ϕ^i is the vector of the shape functions for the electric potential, defined through Eq. (4.2) with $p = 1$, and $\boldsymbol{\phi}^i = [\phi^{i-1} \ \phi^i]$ ($i = 1, 2, \dots, n_{sub}$), in which n_{sub} is the number of piezoelectric layer.

In each piezoelectric element, electric potentials are assumed to be equal at the same height along the thickness [86]. Hence, the electric field \mathbf{E} in Eq. (5.3) can be rewritten as:

$$\mathbf{E} = -\nabla \mathbf{N}_\phi^i \phi^i = -\mathbf{B}_\phi \phi^i \quad (5.17)$$

Note that approximated equations of electrical potential field in this section will also be used in chapters 6 and 8.

5.2.2 Governing equations

The final governing equations can be obtained by substituting Eqs. (5.9), (5.16) and (5.17) into Eq. (3.1); i.e.:

$$\begin{bmatrix} \mathbf{M}_{uu} & 0 \\ 0 & 0 \end{bmatrix} \begin{bmatrix} \ddot{\mathbf{d}} \\ \ddot{\phi} \end{bmatrix} + \begin{bmatrix} \mathbf{K}_{uu} & \mathbf{K}_{u\phi} \\ \mathbf{K}_{\phi u} & \mathbf{K}_{\phi\phi} \end{bmatrix} \begin{bmatrix} \mathbf{d} \\ \phi \end{bmatrix} = \begin{bmatrix} \mathbf{F} \\ \mathbf{Q} \end{bmatrix} \quad (5.18)$$

Where

$$\begin{aligned} \mathbf{K}_{uu} &= \int_{\Omega} \mathbf{B}_u^T \mathbf{c} \mathbf{B}_u d\Omega & ; & \quad \mathbf{K}_{u\phi} = \int_{\Omega} \mathbf{B}_u^T \mathbf{e}^T \mathbf{B}_\phi d\Omega \\ \mathbf{K}_{\phi\phi} &= -\int_{\Omega} \mathbf{B}_\phi^T \mathbf{p} \mathbf{B}_\phi d\Omega & ; & \quad \mathbf{M}_{uu} = \int_{\Omega} \tilde{\mathbf{N}}^T \mathbf{m} \tilde{\mathbf{N}} d\Omega \end{aligned} \quad (5.19)$$

in which $\mathbf{B}_u = [\mathbf{B}^m \ \mathbf{B}^{b1} \ \mathbf{B}^{b2} \ \mathbf{B}^{s0} \ \mathbf{B}^{s1}]^T$; \mathbf{m} is defined as:

$$\mathbf{m} = \begin{bmatrix} \mathbf{I}_0 & 0 & 0 \\ 0 & \mathbf{I}_0 & 0 \\ 0 & 0 & \mathbf{I}_0 \end{bmatrix} \text{ where } \mathbf{I}_0 = \begin{bmatrix} I_1 & I_2 & cI_4 \\ I_2 & I_3 & cI_5 \\ cI_4 & cI_5 & c^2 I_7 \end{bmatrix} \quad (5.20)$$

$$(I_1, I_2, I_3, I_4, I_5, I_7) = \int_{-h/2}^{h/2} \rho (1, z, z^2, z^3, z^4, z^7) dz$$

and

$$\begin{aligned} \tilde{\mathbf{N}} &= \begin{Bmatrix} \mathbf{N}_1 \\ \mathbf{N}_2 \\ \mathbf{N}_3 \end{Bmatrix}, \quad \mathbf{N}_1 = \begin{bmatrix} N_I & 0 & 0 & 0 & 0 \\ 0 & N_I & 0 & 0 & 0 \\ 0 & 0 & N_I & 0 & 0 \end{bmatrix}, \\ \mathbf{N}_2 &= \begin{bmatrix} 0 & 0 & 0 & N_I & 0 \\ 0 & 0 & 0 & 0 & N_I \\ 0 & 0 & 0 & 0 & 0 \end{bmatrix}, \quad \mathbf{N}_3 = \begin{bmatrix} 0 & 0 & N_{I,x} & N_I & 0 \\ 0 & 0 & N_{I,y} & 0 & N_I \\ 0 & 0 & 0 & 0 & 0 \end{bmatrix} \end{aligned} \quad (5.21)$$

Substituting the second line of Eq. (5.18) into the first line, we obtain the shortened form as:

$$\mathbf{M} \ddot{\mathbf{d}} + \left(\mathbf{K}_{uu} + \mathbf{K}_{u\phi} \mathbf{K}_{\phi\phi}^{-1} \mathbf{K}_{\phi u} \right) \mathbf{d} = \mathbf{F} + \mathbf{K}_{u\phi} \mathbf{K}_{\phi\phi}^{-1} \mathbf{Q} \quad (5.22)$$

5.3 Active control

We now consider a composite plate integrated piezoelectric with n ($n \geq 2$) layers, as depicted in Figure 5.2. The actuator layer, i.e. the top layer, is labeled with the subscript a , and the sensor layer, i.e. the bottom layer, is denoted with the subscript s . In this section, the displacement feedback control [86] and the velocity feedback control [87-92] are considered. The displacement feedback control is based on the actuator, which generates the charge, and the velocity feedback control gives the velocity component. In addition, the consistent method [91,70], which can predict the dynamic responses of smart piezoelectric composite plates is adopted. Relation between the output sensor voltage vector ϕ_s and the input actuator voltage vector ϕ_a can be expressed as [91]:

$$\phi_a = G_d \phi_s + G_v \dot{\phi}_s \quad (5.23)$$

Where G_d and G_v are the constant gains of the displacement feedback control and the velocity feedback control, respectively.

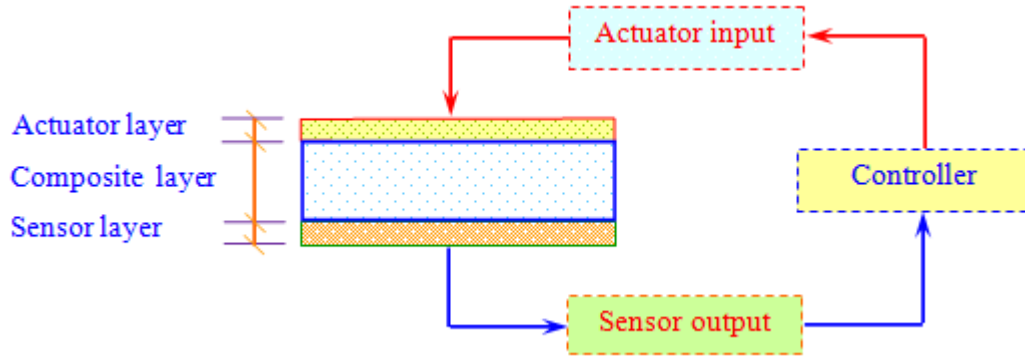


Figure 5.2. A schematic diagram of a laminated plate with integrated piezoelectric sensors and actuators.

Using the second row of Eq. (5.18), and considering zero charge \mathbf{Q} , the sensor output can be derived as:

$$\phi_s = \begin{bmatrix} \mathbf{K}_{\phi\phi}^{-1} \end{bmatrix}_s \begin{bmatrix} \mathbf{K}_{\phi u} \end{bmatrix}_s \mathbf{d}_s \quad (5.24)$$

Generally speaking, when a plate subjected to external forces is deformed, electric charges in the piezoelectric sensor layer are generated, and through the closed loop control the charges are amplified and converted into signal. Then, the distributed actuators receive this converted signal and an input voltage is generated in the

piezoelectric actuators. Finally, a resultant force arises through the converse piezoelectric effect and actively controls the smart piezoelectric composite plate.

The magnitude of the voltage is defined by substituting Eqs. (5.23) and (5.24) into the second line of Eq. (5.18):

$$\mathbf{Q}_a = [\mathbf{K}_{uu}]_a \mathbf{d}_a - G_d [\mathbf{K}_{\phi\phi}]_a [\mathbf{K}_{\phi\phi}^{-1}]_s [\mathbf{K}_{\phi u}]_s \mathbf{d}_s - G_v [\mathbf{K}_{\phi\phi}]_a [\mathbf{K}_{\phi\phi}^{-1}]_s [\mathbf{K}_{\phi u}]_s \dot{\mathbf{d}}_s \quad (5.25)$$

Substituting Eqs. (5.23) and (5.24) into Eq. (5.22), one writes:

$$\mathbf{M}\ddot{\mathbf{d}} + \mathbf{C}\dot{\mathbf{d}} + \mathbf{K}^* \mathbf{d} = \mathbf{F} \quad (5.26)$$

Where

$$\mathbf{K}^* = \mathbf{K}_{uu} + G_d [\mathbf{K}_{u\phi}]_s [\mathbf{K}_{\phi\phi}^{-1}]_s [\mathbf{K}_{\phi u}]_s \quad (5.27)$$

and \mathbf{C} is the active damping matrix computed by

$$\mathbf{C} = G_v [\mathbf{K}_{u\phi}]_a [\mathbf{K}_{\phi\phi}^{-1}]_s [\mathbf{K}_{\phi u}]_s \quad (5.28)$$

If the structural damping effect is considered in Eq. (5.26), it can be rewritten as:

$$\mathbf{M}\ddot{\mathbf{d}} + (\mathbf{C} + \mathbf{C}_R) \dot{\mathbf{d}} + \mathbf{K}^* \mathbf{d} = \mathbf{F} \quad (5.29)$$

Where \mathbf{C}_R is the Rayleigh damping matrix, which is assumed to be a linear combination of \mathbf{M} and \mathbf{K}_{uu} :

$$\mathbf{C}_R = \alpha \mathbf{M} + \beta \mathbf{K}_{uu} \quad (5.30)$$

In which α and β are the Rayleigh damping coefficients.

For static analyses, Eq. (5.26) reduces to:

$$\mathbf{K}^* \mathbf{d} = \mathbf{F} \quad (5.31)$$

5.4 Numerical results

5.4.1 Free vibration analysis

In this section, free vibration analysis of the smart composite plate is examined. A square five-ply piezoelectric composite plate [*pie*/0/90/0/*pie*], in which *pie* denotes a piezoelectric layer, is shown in Figure 5.3. The boundary condition of the plate is simply supported and in each composite ply, the thickness to length ratio is $h/a = 1/50$. The

laminate layer includes three layers and made of Graphite/Epoxy (Gp/Ep) with configuration $[0/90/0]$. Two PZT-4 piezoelectric layers are bonded to the top and bottom surfaces of the plate, and thickness of each piezoelectric layer is $0.1h$. In this research, we consider two types of electric boundary condition including: (1) an open-circuit condition, where the electric potential remains free and (2) a closed-circuit condition, in which the electric potential is kept zero (grounded). The analytical approach [202] of this problem was only available for the first natural frequency and several FE formulations [94,116] were then adopted to obtain other natural frequencies.

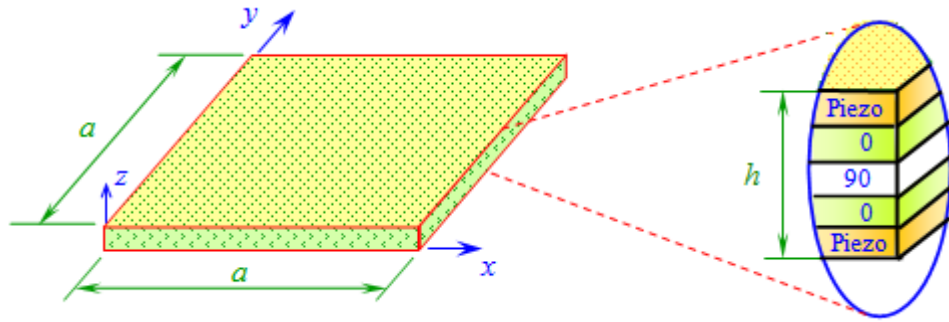


Figure 5.3. Model of a 5-ply piezoelectric composite plate.

Table 5.1. Dimensionless first natural frequency of the simply supported square piezoelectric composite plate $[pie/0/90/0/pie]$

Method	Meshing	Degrees of freedom (DOFs)	$\bar{f} = \omega_1 a^2 / (10000t\sqrt{\rho})$	
			Closed circuit	Open circuit
IGA ($p = 2$)	8×8	500	235.900	236.100
IGA ($p = 3$)	8×8	605	235.100	235.300
IGA ($p = 4$)	8×8	720	235.100	235.300
FE layerwise [116]	12×12	2208	234.533	256.765
Q9 – HSDT [94]	-	-	230.461	250.597
Q9 – FSDT [94]	-	-	206.304	245.349
Ref [202]			245.941	245.942

Table 5.2. Convergence of the first five natural frequencies of the square piezoelectric composite plate $[pie/0/90/0/pie]$ for the open circuit condition case

Meshing	Method	Mode sequence number				
		Mode 1	Mode 2	Mode 3	Mode 4	Mode 5
5×5	IGA ($p = 2$)	240.100	600.600	750.400	1027.500	1537.800
	IGA ($p = 3$)	235.700	535.200	685.500	940.700	1137.591
	FE layerwise [116]	276.185	-	-	-	-
9×9	IGA ($p = 2$)	235.800	537.300	686.900	942.700	1095.302
	IGA ($p = 3$)	235.300	529.000	680.400	933.300	1038.290
	FE layerwise [116]	261.703	-	-	-	-
13×13	IGA ($p = 2$)	235.300	530.500	681.500	934.900	1047.801
	IGA ($p = 3$)	235.200	528.600	680.100	932.800	1035.791
	FE layerwise [116]	259.655	-	-	-	-
	Q9 - HSDT [94]	250.497	583.185	695.697	980.361	1145.410
	Q9 - FSDT [94]	245.349	558.988	694.196	962.017	1093.010
	Ref [202]	245.942	-	-	-	-

Table 5.3. Convergence of the first five natural frequencies of the square piezoelectric composite plate $[pie/0/90/0/pie]$ for the close circuit condition case

Meshing	Method	Mode sequence number				
		Mode 1	Mode 2	Mode 3	Mode 4	Mode 5
5×5	IGA ($p = 2$)	239.500	599.000	749.200	1025.500	1535.101
	IGA ($p = 3$)	235.100	533.700	684.300	938.800	1134.900
	FE layerwise [116]	249.860	-	-	-	-
9×9	IGA ($p = 2$)	235.600	536.800	686.600	942.000	1094.402
	IGA ($p = 3$)	235.100	528.500	680.000	932.600	1037.300
	FE layerwise [116]	236.833	-	-	-	-
13×13	IGA ($p = 2$)	235.200	530.200	681.3	934.500	1047.302
	IGA ($p = 3$)	235.100	528.400	679.9	932.400	1035.301
	FE layerwise [116]	234.533				
	Q9 - HSDT [94]	230.461	520.384	662.915	908.459	1022.091
	Q9 - FSDT [94]	206.304	519.444	663.336	907.636	1020.101
	Ref [202]	245.941	-	-	-	-

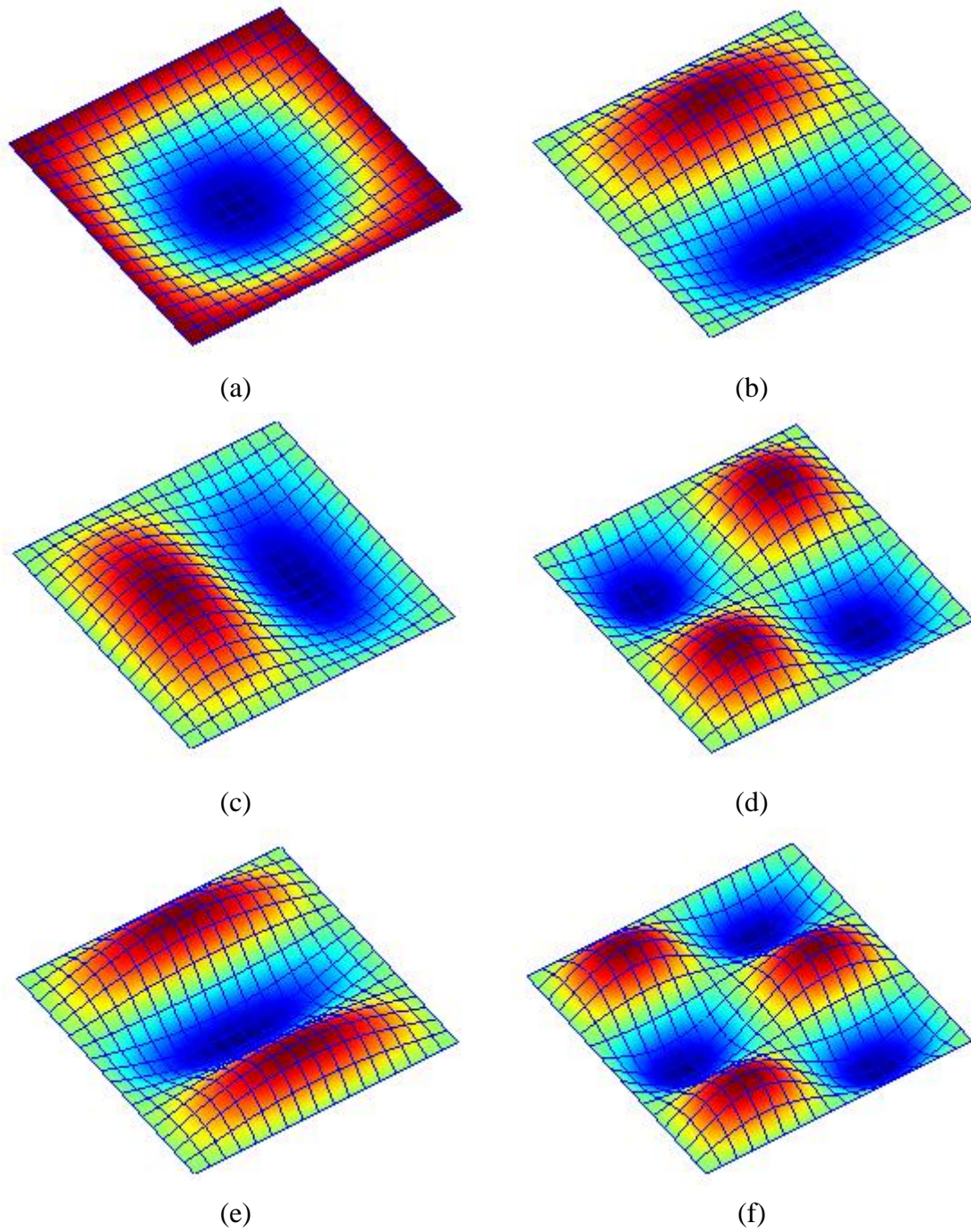


Figure 5.4. Shape of the first six eigenmodes of a simply supported piezoelectric composite plate: (a) mode 1, (b) mode 2, (c) mode 3, (d) mode 4, (e) mode 5 and (f) mode 6.

Table 5.1 shows the dimensionless first natural frequency of the piezoelectric composite plate with meshing of 8×8 quadratic ($p = 2$), cubic ($p = 3$) and quartic ($p = 4$) elements. The dimensionless first natural frequency is defined as $\bar{f} = \omega_1 a^2 / (10000t\sqrt{\rho})$, where ω_1 is the first natural frequency. In this study, the isogeometric elements use the HSDT with only 5 DOFs per control point, while Ref [116] used the layerwise theory and Ref [94] used HSDT with 11 DOFs per node. We can see that the proposed results are slightly lower than the analytical solution [202], however the errors are less than 5%. We observe that the isogeometric results are stable in both a closed-circuit condition and an open-circuit condition similar to the analytical solution [202], while those of Refs. [116,94] are very different for a closed-circuit condition and an open-circuit condition. This is because in FEM, the geometry and unknown variables need to be approximated using Lagrange basis functions. Therefore, there are two approximation errors. Especially, in piezoelectric composites and electro-mechanical coupling, one more unknown variable, i.e. the electric potential, is added and approximated. Hence, one more approximation error is added. The better performance of NURBS-based IGA over the conventional FE method in the solution of the eigenvalue problem is well known and has recently been further addressed in a comprehensive study [203]. Moreover, the results obtained using cubic and quartic elements coincide (for the chosen mesh), which suggests the use of cubic element. Furthermore, the convergence of the first five natural frequencies with meshing of 5×5 , 9×9 and 13×13 for a closed-circuit condition and an open-circuit condition is listed in Table 5.2 and Table 5.3, respectively. Again, it can be seen that the isogeometric results do not vary between closed- and open-circuit conditions, unlike those of the FE layerwise approach in Ref. [116].

Table 5.4. Deflections of the piezoelectric bimorph beam at various locations ($\times 10^{-6}$ m)

Method	Position				
	1	2	3	4	5
IGA ($p = 2$)	0.0138	0.0550	0.1236	0.2201	0.3443
IGA ($p = 3$)	0.0140	0.0552	0.1242	0.2207	0.3448
EFG [96]	0.0142	0.0555	0.1153	0.2180	0.3416
3D FE [89]	0.0136	0.0546	0.1232	0.2193	0.3410
RPIM [91]	0.0136	0.0547	0.1234	0.2196	0.3435
Analytical solution [93]	0.0140	0.0552	0.1224	0.2208	0.3451

Finally, Figure 5.4 plots the shape of the first six eigenmodes. It is seen that these shapes reflect correctly the physical modes of the piezoelectric composite plates as given by the analytical solution.

5.4.2 Static analysis

5.4.2.1 A smart piezoelectric bimorph beam

A piezoelectric bimorph beam with boundary condition, thickness and geometry is shown in Figure 5.5. The beam consists of two opposite polarities layers. The cantilever beam is modeled by five identical plate elements. Dimensions of the beam are $20 \times 5 \times 1$ mm. The beam is made of PVDF with material properties given in Table 3.1.

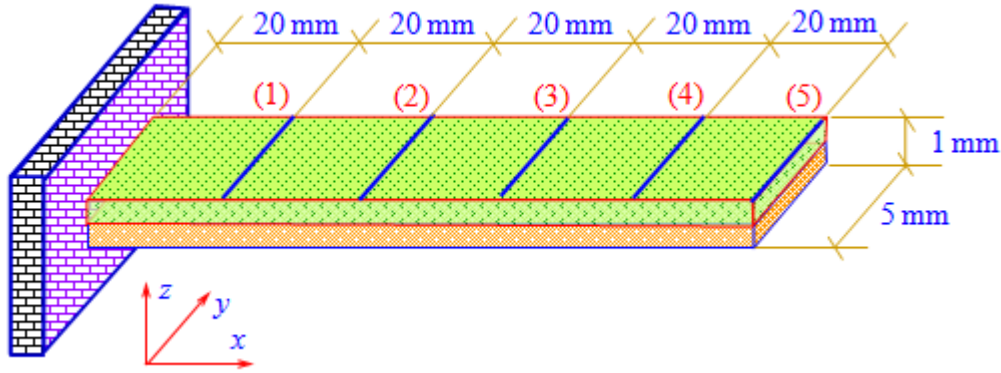


Figure 5.5. Model of the smart piezoelectric bimorph beam.

Table 5.4 lists the deflections of the beam with meshing of 101×6 subjected to a unit voltage (1V). It can be seen that the present results match well the analytical solution [93] and agree very well with results in Refs. [96,89,91], which are however less accurate. When the order of the basis functions is increased, the accuracy improves and results coincide (for the shown number of digits) with those of the analytical solution [93]. Table 5.5 reports tip deflections of the smart piezoelectric bimorph beam under several input voltages. Again, results obtained with the isogeometric formulation match well the analytical solution [93]. Finally, Figure 5.6 shows the deflection of the beam subjected to different input voltages. We observe that when the input voltage increases, the deflection of beam also increases, as expected.

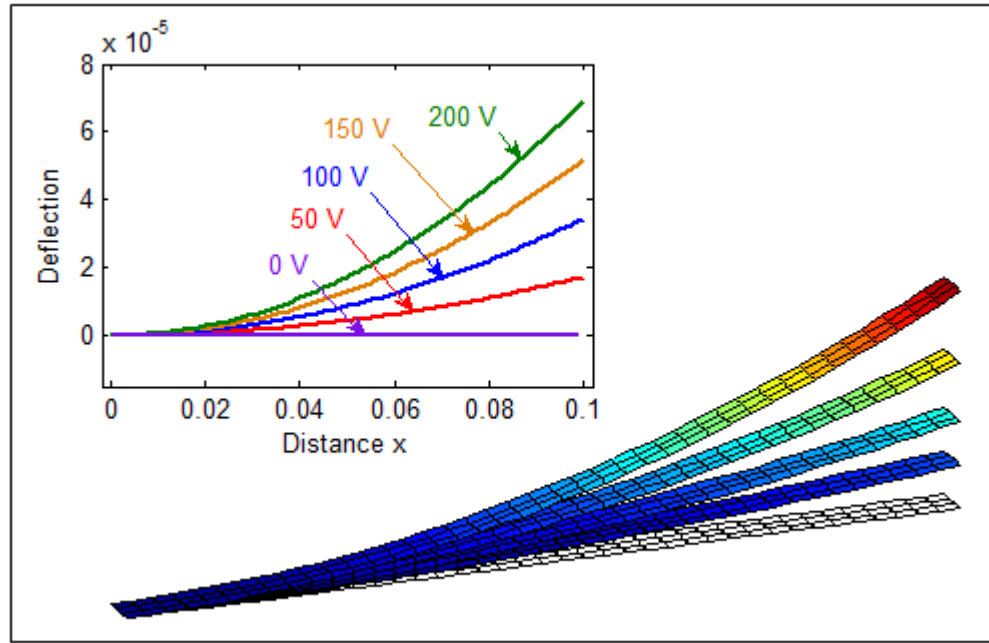


Figure 5.6. Deformed shape and centerline deflection of the smart piezoelectric bimorph beam subjected to different input voltages.

Table 5.5. Tip deflections of the beam ($\times 10^{-4}$ m)

Method	Input voltage			
	50 V	100 V	150 V	200 V
IGA ($p = 2$)	0.1721	0.3443	0.5164	0.6885
IGA ($p = 3$)	0.1724	0.3448	0.5173	0.6897
Analytical solution [93]	0.1725	0.3451	0.5175	0.6900

5.4.2.2 A smart piezoelectric composite plate

Now, we consider a plate ($200\text{ mm} \times 200\text{ mm}$) under a uniform load $q = 100\text{ N/m}^2$ as shown in Figure 5.7. The plate has six layers: two outer piezo layers represented by *pie* and four composite layers. The plate is simply supported. The configurations of the plate are $[pie/-\theta/\theta]_s$ and $[pie/-\theta/\theta]_{as}$, where subscripts “s” and “as” indicate symmetric and anti-symmetric laminates, respectively, and θ is the fiber orientation. Each layer thickness of the non-piezoelectric composite plate is 0.25 mm and the thickness of the piezoelectric layer is 0.1 mm. The composite layers are made of T300/976 graphite/epoxy and the piezoelectric layers are PZTG1195N. And the material properties are listed in Table 3.1.

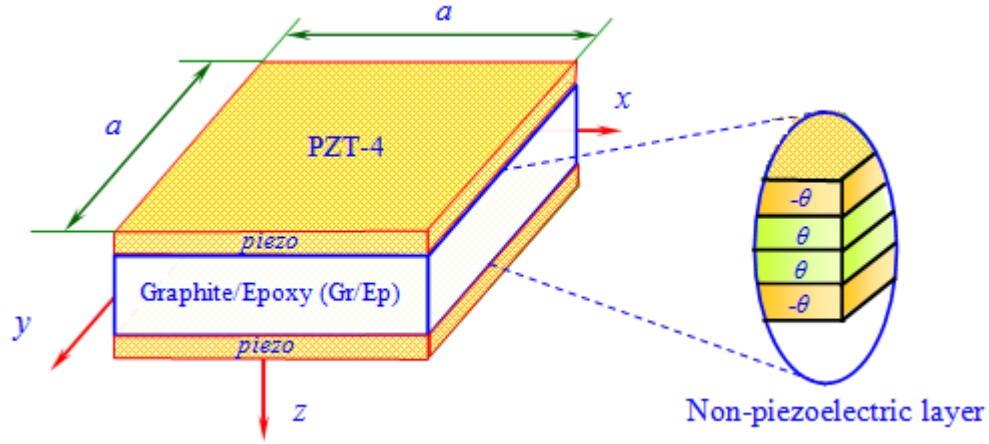


Figure 5.7. Square piezoelectric composite plate model.

Table 5.6. Central deflection of the smart piezoelectric composite plate under a uniform load and input voltages ($\times 10^{-4}$ m)

Input voltage	Scheme	Method			
		CS-DSG3 [98]	RPIM [91]	IGA ($p = 2$)	IGA ($p = 3$)
0V	$[pie \ /-45/45]_s$	-0.6326	-0.6038	-0.6343	-0.6375
	$[pie/-45/45]_{as}$	-0.6323	-0.6217	-0.6217	-0.6239
	$[pie \ /-30/30]_{as}$	-0.6688	-0.6542	-0.6593	-0.6617
	$[pie \ /-15/15]_{as}$	-0.7442	-0.7222	-0.7422	-0.7452
5V	$[pie \ /-45/45]_s$	-0.2863	-0.2717	-0.2799	-0.2842
	$[pie \ /-45/45]_{as}$	-0.2801	-0.2717	-0.2773	-0.2817
	$[pie \ /-30/30]_{as}$	-0.2957	-0.2862	-0.2923	-0.2968
	$[pie \ /-15/15]_{as}$	-0.3259	-0.3134	-0.3233	-0.3283
10V	$[pie \ /-45/45]_s$	0.0721	0.0757	0.0745	0.0691
	$[pie \ /-45/45]_{as}$	0.0601	0.0604	0.0672	0.0606
	$[pie \ /-30/30]_{as}$	0.0774	0.0819	0.0749	0.0682
	$[pie \ /-15/15]_{as}$	0.0924	0.0954	0.0957	0.0886

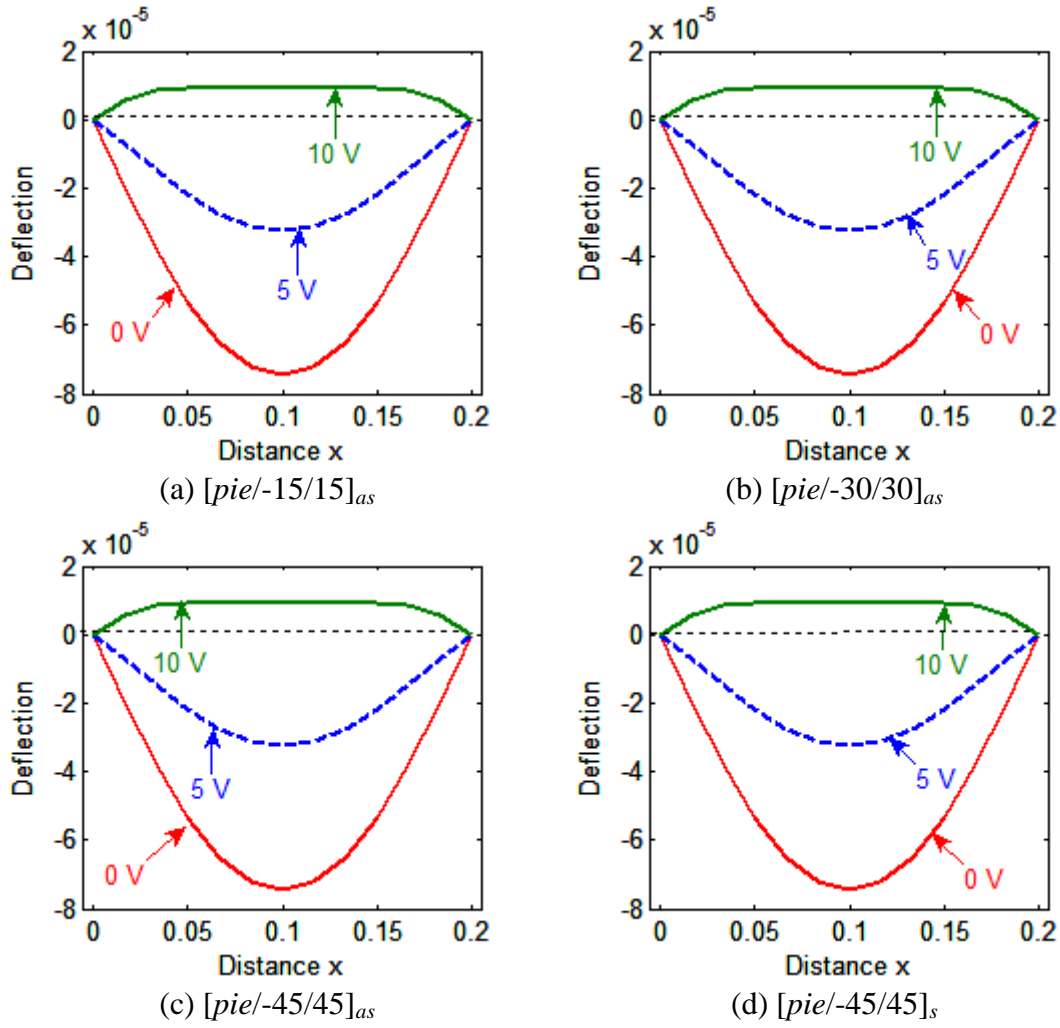


Figure 5.8. Centerline deflection of the plate under different input voltage and a uniform load.

Table 5.6 reports the central point deflection of the simply supported piezoelectric composite plate subjected to the uniform load and different input voltages. Again, the results by the IGA agree well with those of Refs. [91,98]. Besides, the centerline deflection of the piezoelectric composite plate is shown in Figure 5.8. Four configurations of the composite plate with different fiber orientation angles are investigated including $[pie/-15/15]_{as}$, $[pie/-30/30]_{as}$, $[pie/-45/45]_{as}$ and $[pie/-45/45]_s$. As expected, the deflection decreases for increasing input voltage. The reason is that the input voltage induces an upward deflection of the plate due to the piezoelectric effect. This upward contribution becomes prevalent for applying an input voltage of 10V to *pie* layers with opposite sign. Similar results were obtained in Refs. [91,98].

5.4.3 Dynamic control of the plate

We now consider the plate $[pie/-45/45]_s$ subjected to a uniform load $q = 100 \text{ N/m}^2$ with the geometry, boundary conditions and material properties as specified in section 5.4.2.2. The plate consists of two outer piezoelectric layers and four composite layers. The upper and lower surfaces of plate are bonded to a piezoelectric actuator layer and a piezoelectric sensor layer, respectively.

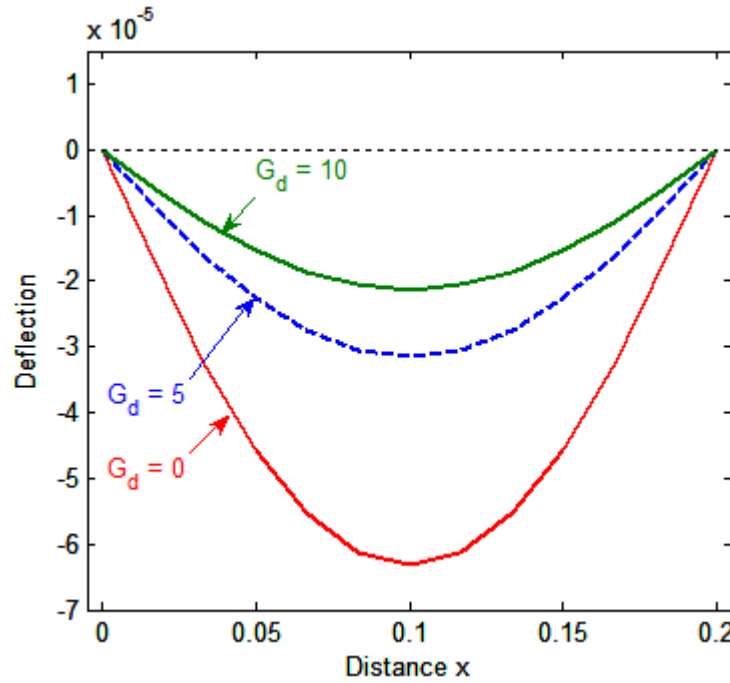


Figure 5.9. Effect of the displacement feedback control on the deflection of a plate under a uniform load.

Firstly, the static control of the plate is studied. The effect of the displacement feedback control on the deflection of the plate is plotted in Figure 5.9. It can be seen that when the control gain G_d becomes higher, the deflection of the plate becomes smaller, which is similar to what reported in [91]. The reason is that when the plate subjected to external forces is deformed, the electric charges in the piezoelectric sensor layer are generated, and through the closed loop control the charges are amplified and converted into signal. Then, the distributed actuators receive this converted signal and an input voltage is generated in the piezoelectric actuators. A resultant force arises from the converse piezoelectric effect and actively controls the smart piezoelectric composite plate.

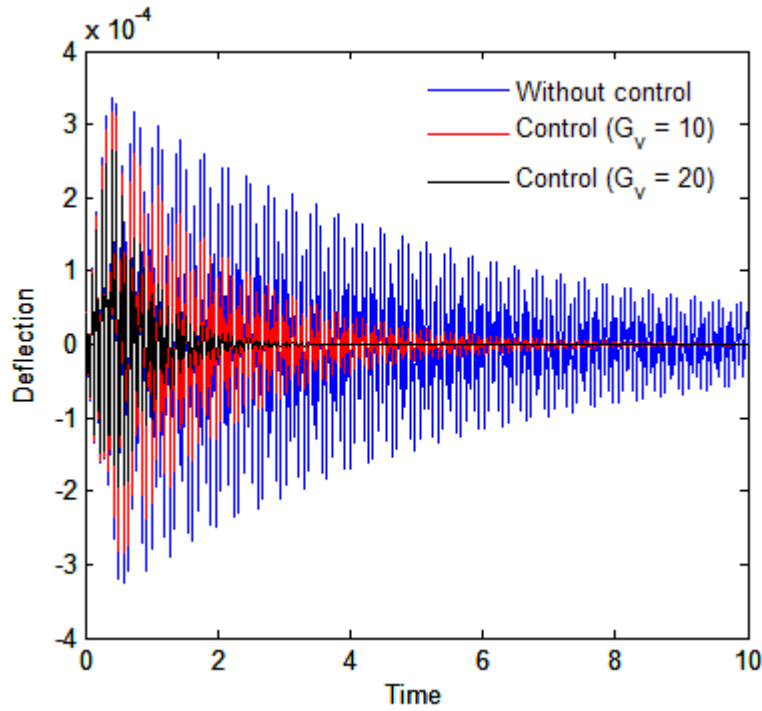


Figure 5.10. Effect of the velocity feedback control on the dynamic deflection response of the piezoelectric composite plate.

Next, the plate is subjected to a harmonic load $F = \sin(\bar{\omega}t)$ applied at its central point, where $\bar{\omega}$ is chose to be the first natural angular frequency (ω_1) of the plate. The eigenvalue problem is first solved with a mesh of 13×13 cubic B-spline elements and a value of $\omega_1 = 167.34$ Hz is determined. Figure 5.10 shows the transient responses of the central point of the piezoelectric composite plate with and without the velocity feedback gain. It can be seen that when the gain G_v is equal to zero (without control), the response decreases in time due to the structural damping. By increasing the velocity feedback gain, the transient response is further attenuated and the amplitude of the central point deflection decreases faster, as expected. This is due to an increase of the active damping as per Eq. (5.28).

5.5 Concluding remarks

This chapter presents a simple and effective approach based on the combination of IGA and HSDT for the static, free vibration analyses and dynamic control of composite plates

integrated with piezoelectric sensors and actuators. In the piezoelectric composite plates, the mechanical displacement field is approximated according to the HSDT using isogeometric elements based on NURBS and featuring at least C^1 -continuity, whereas the electric potential is assumed linearly through the thickness of each piezoelectric layer. For active control of the piezoelectric composite plates, a close-loop system is used. Several numerical examples are performed to analyze the static deflection, natural vibration mode and dynamic control of piezoelectric laminated plates with different stacking sequence schemes. Through the presented formulation and numerical results, the following main conclusions can be drawn:

- i) Due to the use of the HSDT, the proposed method does not require shear correction factors. The use of NURBS elements of at least second order naturally fulfils the C^1 -continuity requirement of the HSDT, thereby significantly reducing the number of degrees of freedom per control point over conventional finite element approaches featuring C^0 inter-element continuity.
- ii) In free vibration analyses, the predictions of the proposed approach agree well with analytical solutions, and are more stable (passing from closed- to open-circuit conditions) than those of several other approaches available in the literature.
- iii) In static analyses, the predictions of the proposed approach are more accurate than those of several other approaches with a lower number of degrees of freedoms.
- iv) In dynamic control analyses, the proposed approach produces predictions, which appear reasonable and consistent with the observed physical behavior.

Chapter 6

*Smart piezoelectric functionally graded
material plates*

6.1 Overview

We deal with the second objective of the thesis in this chapter. Isogeometric approach based on a generalized shear deformation theory for geometrically nonlinear transient of smart piezoelectric functionally graded material plates is introduced. The nonlinear transient formulation for plates is formed in the total Lagrange approach based on the von Kármán strains, which includes thermo-piezoelectric effects, and solved by Newmark time integration. The electric potential through the thickness of each piezoelectric layer is assumed linearly. The material properties varying through the thickness of FGM are determined by the rule of mixture and the Mori–Tanaka scheme as explained in section 3.2.2. Many numerical examples are investigated to show the effectiveness of the present method.

6.2 The piezoelectric FGM model

A sandwich plate, shown in Figure 6.1a, is made of one core that is graded from ceramic to metal and two outside skins that are piezoelectric layers. In the core layer, the volume fraction of ceramic and metal phase across thickness is described as follows [181]:

$$V_c(z) = \left(\frac{1}{2} + \frac{z_c}{h_c} \right)^n, \quad V_m(z) = 1 - V_c(z) \quad (6.1)$$

Where c and m refer to the ceramic and metal, respectively; $z_c \in [z_2, z_3]$ and $h_c = z_3 - z_2$ is thickness of core, which is illustrated in Figure 6.1b. The material constituents of piezoelectric FGM can be obtained as:

$$\begin{aligned} V_c(z) &= 1, \quad h_c \in [z_1, z_2] \text{ for bottom skin} \\ V_c(z) &= \left(\frac{1}{2} + \frac{z_c}{h_c} \right)^n, \quad h_c \in [z_2, z_3] \text{ for core} \\ V_c(z) &= 1, \quad h_c \in [z_3, z_4] \text{ for top skin} \\ V_m(z) &= 1 - V_c(z) \end{aligned} \quad (6.2)$$

The material properties including Poisson's ratio (ν), Young's modulus (E) and density (ρ) based on the rule of mixture are defined in section 3.2.1.2.

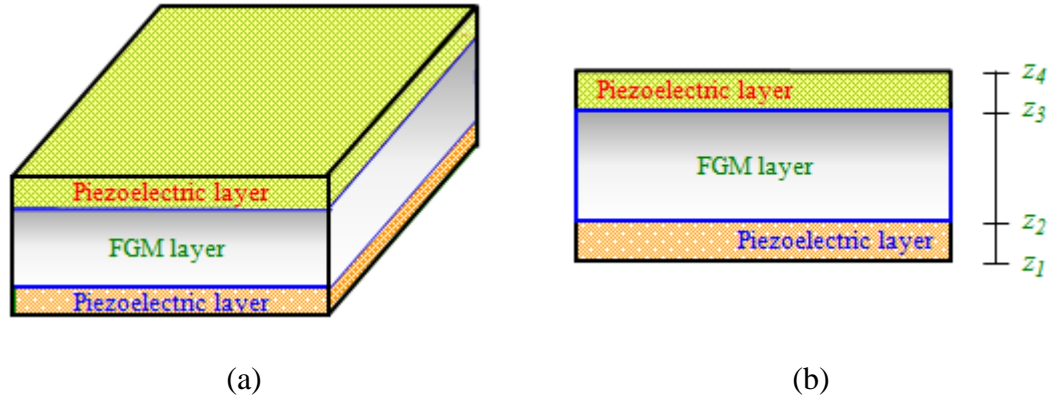


Figure 6.1. (a) Configuration of a piezoelectric FGM plate; (b) The sandwich plate with piezoelectric skins and FGM core.

Temperature distributions of the bottom surface and top surface of piezoelectric FGM model are assumed to be constant. The temperature variation along the thickness is obtained by solving the one-dimensional steady state heat equation that is given by:

$$-\frac{d}{dz} \left(k(z) \frac{dT}{dz} \right) = 0 \quad (6.3)$$

With boundary condition

$$\begin{aligned} T &= T_{\text{top}} & \text{at } z &= h/2 \\ T &= T_{\text{bot}} & \text{at } z &= -h/2 \end{aligned} \quad (6.4)$$

Where T_{top} and T_{bot} are the top and bottom surface temperatures, respectively; and $k(z)$ represents the thermal conductivity coefficient at z position and is also expressed similar to Eq. (6.1).

Material properties of some FGMs are given in Table 6.1.

Table 6.1. Material properties of some FGMs

	E (Pa)	ν	α (K^{-1})	k (K)	ρ (kg/m^3)
Al	70×10^9	0.3	23×10^{-6}	204	2707
Ti6Al4V	320.24×10^9	0.26	7.2×10^{-6}	10.4	3750
ZrO2-1	151×10^9	0.3	10×10^{-6}	2.09	3000
Al2O3	105.7×10^9	0.2981	6.9×10^{-6}	18.1	4429

Figure 6.2 illustrates the temperature distributions through the thickness of a FGP made from Aluminum-Zirconia (Al/ZrO₂-1) for the various value of n , where the top and bottom surfaces are held at 300°C and 20°C, respectively. It is evident that temperature in the FGPs constituted by both ceramic and metal components.

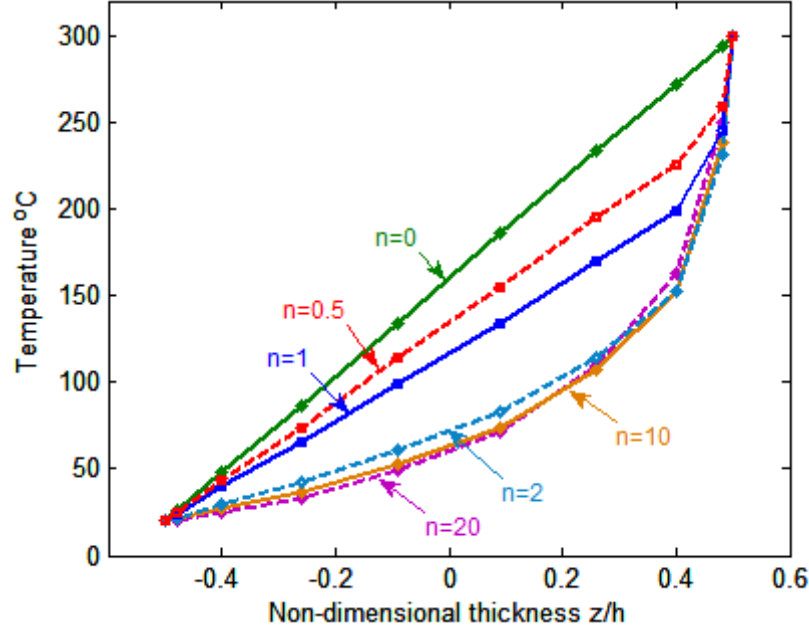


Figure 6.2. Temperature distributions through the thickness of Al/ZrO₂-1 FGM plate corresponding to different values of volume fraction exponents n .

6.3 The generalized higher order shear deformation theory

In the piezoelectric FGM plates, there are also two-field variables including a mechanical displacement field and an electrical field that needs to be approximated. In this chapter, the electrical field is assumed to be independent on each layer and the mechanical displacements are approximated by the generalized higher order shear deformation theory and expressed as follows [192-194]:

$$\begin{aligned}
 u(x, y, z) &= u_0(x, y) - z \frac{\partial w}{\partial x} + f(z) \beta_x(x, y) \\
 v(x, y, z) &= v_0(x, y) - z \frac{\partial w}{\partial y} + f(z) \beta_y(x, y) \\
 w(x, y, z) &= w(x, y)
 \end{aligned} \tag{6.5}$$

Where u_0 , v_0 , β_x , β_y and w are displacement variables. The function $f(z)$ is a continuous function through the plate thickness and chosen as $f(z) = \frac{7}{8} - 2\frac{z^3}{h^2} + 2\frac{z^5}{h^4}$, which was recently published in Ref. [195].

For a bending plate, the Green's strain vector can be represented by:

$$\boldsymbol{\varepsilon} = \begin{Bmatrix} \varepsilon_{xx} \\ \varepsilon_{yy} \\ \gamma_{xy} \\ \gamma_{xz} \\ \gamma_{yz} \end{Bmatrix} = \begin{Bmatrix} \frac{\partial u}{\partial x} + \frac{1}{2} \left(\frac{\partial u}{\partial x} \right)^2 + \frac{1}{2} \left(\frac{\partial v}{\partial x} \right)^2 + \frac{1}{2} \left(\frac{\partial w}{\partial x} \right)^2 \\ \frac{\partial v}{\partial y} + \frac{1}{2} \left(\frac{\partial u}{\partial y} \right)^2 + \frac{1}{2} \left(\frac{\partial v}{\partial y} \right)^2 + \frac{1}{2} \left(\frac{\partial w}{\partial y} \right)^2 \\ \frac{\partial u}{\partial y} + \frac{\partial v}{\partial x} + \frac{\partial u}{\partial x} \frac{\partial u}{\partial y} + \frac{\partial v}{\partial x} \frac{\partial v}{\partial y} + \frac{\partial w}{\partial x} \frac{\partial w}{\partial y} \\ \frac{\partial u}{\partial z} + \frac{\partial w}{\partial x} + \frac{\partial u}{\partial x} \frac{\partial u}{\partial z} + \frac{\partial v}{\partial x} \frac{\partial v}{\partial z} + \frac{\partial w}{\partial x} \frac{\partial w}{\partial z} \\ \frac{\partial v}{\partial z} + \frac{\partial w}{\partial y} + \frac{\partial u}{\partial y} \frac{\partial u}{\partial z} + \frac{\partial v}{\partial y} \frac{\partial v}{\partial z} + \frac{\partial w}{\partial y} \frac{\partial w}{\partial z} \end{Bmatrix} \quad (6.6)$$

Using the Von Kármán assumptions [204,205], which imply that derivatives of u and v are small and noting that w is independent of z , Eq. (6.6) can be rewritten as:

$$\begin{aligned} \boldsymbol{\varepsilon} &= \boldsymbol{\varepsilon}_m + z\boldsymbol{\kappa}_1 + f(z)\boldsymbol{\kappa}_2 \\ \boldsymbol{\gamma} &= f'(z)\boldsymbol{\kappa}_s \end{aligned} \quad (6.7)$$

Where $f'(z)$ is the derivative of the $f(z)$ function and the strain vectors are given by:

$$\begin{aligned} \boldsymbol{\varepsilon}_m &= \begin{bmatrix} u_{0,x} \\ v_{0,y} \\ u_{0,y} + v_{0,x} \end{bmatrix} + \frac{1}{2} \begin{bmatrix} w_{,x}^2 \\ w_{,y}^2 \\ 2w_{,xy} \end{bmatrix} = \boldsymbol{\varepsilon}_L + \boldsymbol{\varepsilon}_{NL} ; \\ \boldsymbol{\kappa}_1 &= - \begin{bmatrix} w_{,xx} \\ w_{,yy} \\ 2w_{,xy} \end{bmatrix} ; \boldsymbol{\kappa}_2 = \begin{bmatrix} \beta_{x,x} \\ \beta_{y,y} \\ \beta_{x,y} + \beta_{y,x} \end{bmatrix} ; \boldsymbol{\kappa}_s = \begin{bmatrix} \beta_x \\ \beta_y \end{bmatrix} \end{aligned} \quad (6.8)$$

In which the nonlinear component can be expressed as:

$$\boldsymbol{\varepsilon}_{NL} = \frac{1}{2} \begin{bmatrix} w_{,x} & 0 \\ 0 & w_{,y} \\ w_{,y} & w_{,x} \end{bmatrix} \begin{Bmatrix} w_{,x} \\ w_{,y} \end{Bmatrix} = \frac{1}{2} \mathbf{A}_\theta \boldsymbol{\theta} \quad (6.9)$$

From Hooke's law and the strains in Eq. (6.7), the stress for the mechanical field, which is similar to Eq. (5.9), is computed as:

$$\boldsymbol{\sigma} = \begin{bmatrix} \boldsymbol{\sigma}_p \\ \boldsymbol{\tau} \end{bmatrix} = \underset{\bar{\boldsymbol{\varepsilon}}}{\mathbf{c}} \begin{bmatrix} \boldsymbol{\varepsilon} \\ \boldsymbol{\gamma} \end{bmatrix} = \mathbf{c} \bar{\boldsymbol{\varepsilon}} \quad (6.10)$$

Where \mathbf{c} is the elasticity matrix and defined as:

$$\mathbf{c} = \begin{bmatrix} \mathbf{A} & \mathbf{B} & \mathbf{N} & \mathbf{0} \\ \mathbf{B} & \mathbf{C} & \mathbf{F} & \mathbf{0} \\ \mathbf{N} & \mathbf{F} & \mathbf{H} & \mathbf{0} \\ \mathbf{0} & \mathbf{0} & \mathbf{0} & \mathbf{D}^S \end{bmatrix} \quad (6.11)$$

In which

$$\begin{aligned} A_{ij}, B_{ij}, C_{ij}, N_{ij}, F_{ij}, H_{ij} &= \int_{-h/2}^{h/2} (1, z, z^2, f(z), zf(z), f^2(z)) Q_{ij} dz \quad ; \quad i, j = 1, 2, 6 \\ D_{ij}^S &= \int_{-h/2}^{h/2} [f'(z)]^2 G_{ij} dz \quad ; \quad i, j = 4, 5 \end{aligned} \quad (6.12)$$

and

$$\mathbf{Q} = \frac{E_e}{1-\nu_e^2} \begin{bmatrix} 1 & \nu_e & 0 \\ \nu_e & 1 & 0 \\ 0 & 0 & \frac{1}{2}(1-\nu_e) \end{bmatrix} \quad ; \quad \mathbf{G} = \frac{E_e}{2(1+\nu_e)} \begin{bmatrix} 1 & 0 \\ 0 & 1 \end{bmatrix} \quad (6.13)$$

6.4 Approximation of mechanical field

The displacement field \mathbf{u} of the plate using NURBS basic function is approximated as:

$$\mathbf{u}^h(\xi, \eta) = \sum_{I=1}^{m \times n} R_I(\xi, \eta) \mathbf{d}_I \quad (6.14)$$

Where $\mathbf{d}_I = [u_{0I} \ v_{0I} \ \beta_{xI} \ \beta_{yI} \ w_I]^T$ is the vector of degrees of freedom associated with the control point I , and R_I is the shape function as defined in Eq. (4.2).

Substituting Eq. (6.14) into Eqs. (6.7)-(6.9), the strains can be rewritten as:

$$\bar{\boldsymbol{\varepsilon}} = [\boldsymbol{\varepsilon} \ \boldsymbol{\gamma}]^T = \sum_{I=1}^{m \times n} \left(\mathbf{B}_I^L + \frac{1}{2} \mathbf{B}_I^{NL} \right) \mathbf{d}_I \quad (6.15)$$

Where $\mathbf{B}_I^L = \left[(\mathbf{B}_I^m)^T \ (\mathbf{B}_I^{b1})^T \ (\mathbf{B}_I^{b2})^T \ (\mathbf{B}_I^s)^T \right]^T$, in which

$$\begin{aligned}
\mathbf{B}_I^m &= \begin{bmatrix} R_{I,x} & 0 & 0 & 0 & 0 \\ 0 & R_{I,y} & 0 & 0 & 0 \\ R_{I,y} & R_{I,x} & 0 & 0 & 0 \end{bmatrix}, \quad \mathbf{B}_I^{b1} = - \begin{bmatrix} 0 & 0 & R_{I,xx} & 0 & 0 \\ 0 & 0 & R_{I,yy} & 0 & 0 \\ 0 & 0 & 2R_{I,xy} & 0 & 0 \end{bmatrix}, \\
\mathbf{B}_I^{b2} &= \begin{bmatrix} 0 & 0 & 0 & R_{I,x} & 0 \\ 0 & 0 & 0 & 0 & R_{I,y} \\ 0 & 0 & 0 & R_{I,y} & R_{I,x} \end{bmatrix}, \quad \mathbf{B}_I^s = \begin{bmatrix} 0 & 0 & 0 & R_I & 0 \\ 0 & 0 & 0 & 0 & R_I \end{bmatrix}
\end{aligned} \tag{6.16}$$

and \mathbf{B}_I^{NL} is calculated by:

$$\mathbf{B}_I^{NL}(\mathbf{d}) = \begin{bmatrix} w_{I,x} & 0 \\ 0 & w_{I,y} \\ w_{I,y} & w_{I,x} \end{bmatrix} \begin{bmatrix} 0 & 0 & R_{I,x} & 0 & 0 \\ 0 & 0 & R_{I,y} & 0 & 0 \end{bmatrix} = \mathbf{A}_\theta \mathbf{B}_I^s \tag{6.17}$$

6.5 The governing equations for piezoelectric FGM plates

The governing equations for piezoelectric FGM plates can be written as:

$$\underbrace{\begin{bmatrix} \mathbf{M}_{uu} & 0 \\ 0 & 0 \end{bmatrix}}_{\mathbf{M}} \underbrace{\begin{bmatrix} \ddot{\mathbf{d}} \\ \ddot{\boldsymbol{\phi}} \end{bmatrix}}_{\ddot{\mathbf{q}}} + \underbrace{\begin{bmatrix} \mathbf{K}_{uu} & \mathbf{K}_{u\phi} \\ \mathbf{K}_{\phi u} & \mathbf{K}_{\phi\phi} \end{bmatrix}}_{\mathbf{K}} \underbrace{\begin{bmatrix} \mathbf{d} \\ \boldsymbol{\phi} \end{bmatrix}}_{\mathbf{q}} = \underbrace{\begin{bmatrix} \mathbf{f} \\ \mathbf{q} \end{bmatrix}}_{\bar{\mathbf{f}}} \quad \Leftrightarrow \quad \bar{\mathbf{M}}\ddot{\mathbf{q}} + \bar{\mathbf{K}}\mathbf{q} = \bar{\mathbf{f}} \tag{6.18}$$

Where

$$\begin{aligned}
\mathbf{K}_{uu} &= \int_{\Omega} (\mathbf{B}^L + \mathbf{B}^{NL})^T \mathbf{c} (\mathbf{B}^L + \frac{1}{2} \mathbf{B}^{NL}) d\Omega \quad ; \quad \mathbf{K}_{u\phi} = \int_{\Omega} (\mathbf{B}^L)^T \mathbf{e}^T \mathbf{B}_\phi d\Omega \\
\mathbf{K}_{\phi\phi} &= \int_{\Omega} \mathbf{B}_\phi^T \mathbf{p} \mathbf{B}_\phi d\Omega \quad ; \quad \mathbf{M}_{uu} = \int_{\Omega} \tilde{\mathbf{N}}^T \mathbf{m} \tilde{\mathbf{N}} d\Omega \quad ; \quad \mathbf{f} = \int_{\Omega} \bar{q}_0 \bar{\mathbf{R}} d\Omega
\end{aligned} \tag{6.19}$$

in which \bar{q}_0 is a uniform load; $\bar{\mathbf{R}} = [0 \ 0 \ 0 \ 0 \ R_I]$; \mathbf{m} is defined by:

$$\mathbf{m} = \begin{bmatrix} I_1 & I_2 & I_4 \\ I_2 & I_3 & I_5 \\ I_4 & I_5 & I_7 \end{bmatrix}, \quad (I_1, I_2, I_3, I_4, I_5, I_7) = \int_{-h/2}^{h/2} \rho (1, z, z^2, f(z), zf(z), f^2(z)) dz \tag{6.20}$$

and

$$\begin{aligned}
\tilde{\mathbf{N}} &= \begin{Bmatrix} \tilde{\mathbf{N}}_1 \\ \tilde{\mathbf{N}}_2 \\ \tilde{\mathbf{N}}_3 \end{Bmatrix}, \quad \tilde{\mathbf{N}}_1 = \begin{bmatrix} R_I & 0 & 0 & 0 & 0 \\ 0 & R_I & 0 & 0 & 0 \\ 0 & 0 & R_I & 0 & 0 \end{bmatrix}; \\
\tilde{\mathbf{N}}_2 &= - \begin{bmatrix} 0 & 0 & R_{I,x} & 0 & 0 \\ 0 & 0 & R_{I,y} & 0 & 0 \\ 0 & 0 & 0 & 0 & 0 \end{bmatrix}; \quad \tilde{\mathbf{N}}_3 = \begin{bmatrix} 0 & 0 & 0 & R_I & 0 \\ 0 & 0 & 0 & 0 & R_I \\ 0 & 0 & 0 & 0 & 0 \end{bmatrix}
\end{aligned} \tag{6.21}$$

6.6 Nonlinear transient solution

6.6.1 Time integration

We now consider the discretized system of equations for nonlinear transient problem, which is similar to that of Eq. (6.18). For the dynamic analysis, the Newmark method [206] is used in this thesis. At initial time, $t = 0$, displacements, velocities and accelerations are set to zero, and we aim to find a new state, i.e. the first and second derivative of displacements with respect to time, at $(m+1)\Delta t$, using the following formulations:

$$\ddot{\mathbf{q}}_{m+1} = \frac{1}{\beta\Delta t^2}(\mathbf{q}_{m+1} - \mathbf{q}_m) - \frac{1}{\beta\Delta t}\dot{\mathbf{q}}_m - \left(\frac{1}{2\beta} - 1\right)\ddot{\mathbf{q}}_m \quad (6.22)$$

$$\dot{\mathbf{q}}_{m+1} = \dot{\mathbf{q}}_m + \Delta t(1-\gamma)\ddot{\mathbf{q}}_m + \gamma\Delta t\ddot{\mathbf{q}}_{m+1} \quad (6.23)$$

where $\beta = 0.25$ and $\gamma = 0.5$ as in Ref. [207].

Substituting Eq. (6.22) into Eq. (6.18), the following equation is obtained:

$$\tilde{\mathbf{K}}_{m+1}\mathbf{q}_{m+1} = \tilde{\mathbf{f}}_{m+1} \quad (6.24)$$

Where $\tilde{\mathbf{K}}_{m+1}$ and $\tilde{\mathbf{f}}_{m+1}$ are defined as:

$$\begin{aligned} \tilde{\mathbf{K}}_{m+1} &= \bar{\mathbf{K}}_{m+1} + \frac{1}{\beta\Delta t^2}\bar{\mathbf{M}} \\ \tilde{\mathbf{f}}_{m+1} &= \bar{\mathbf{f}}_{m+1} + \bar{\mathbf{M}}\left[\frac{1}{\beta\Delta t^2}\mathbf{q}_m + \frac{1}{\beta\Delta t}\dot{\mathbf{q}}_m + \left(\frac{1}{2\beta} - 1\right)\ddot{\mathbf{q}}_m\right] \end{aligned} \quad (6.25)$$

Note that, the effective stiffness $\hat{\mathbf{K}}_{m+1}$ in Eq. (6.24) is dependent on the displacements \mathbf{q}_{m+1} . Thus, the Newton-Raphson method [208] is used in this work and presented in the next section.

6.6.2 Iterative method

In nonlinear analysis, the residual force, $\boldsymbol{\phi}$, is introduced to represent errors of the approximation and tends to zeros during each iteration. From Eq. (6.24), the residual force at time step $(m+1)\Delta t$, $\boldsymbol{\phi}_{m+1}$, can be defined as follows:

$$\boldsymbol{\phi}_{m+1} = \tilde{\mathbf{K}}_{m+1}\mathbf{q}_{m+1} - \tilde{\mathbf{f}}_{m+1} \quad (6.26)$$

To make unbalance residual force if ${}^i\mathbf{q}_{m+1}$ is an approximate trial solution at the i^{th} iteration, an improved solution, ${}^{i+1}\mathbf{q}_{m+1}$, can be introduced and considered as:

$${}^{i+1}\mathbf{q}_{m+1} = {}^i\mathbf{q}_{m+1} + \Delta\mathbf{q} \quad (6.27)$$

Where $\Delta\mathbf{q}$ is the incremental displacement and calculated as [209]:

$$\Delta\mathbf{q} = -{}^i\boldsymbol{\phi}_{m+1} / \mathbf{K}_T \quad (6.28)$$

In which \mathbf{K}_T is called tangent stiffness matrix and computed using to the Newton-Raphson method [208]

$$\mathbf{K}_T = \partial\boldsymbol{\phi}({}^i\mathbf{q}) / \partial\mathbf{q} \quad (6.29)$$

At each time step, Eq. (6.28) is solved until the error in the displacements between two consecutive iterations is satisfied and becomes less than the tolerance error given by:

$$\frac{\|{}^{i+1}\mathbf{q}_{m+1} - {}^i\mathbf{q}_{m+1}\|}{\|{}^i\mathbf{q}_{m+1}\|} < tol \quad (6.30)$$

6.7 Numerical results

In this section, many numerical examples are investigated and compared to other available numerical methods to show the accuracy and effectiveness of the present method. Table 3.1 lists the properties of the piezoelectric FGM plates. The boundary conditions used, are: simply supported (S), clamped (C) or free (F) edges. For instance, the symbol, CFSF, represents clamped, free, simply supported and free edges.

6.7.1 Free vibration and static analyses of piezoelectric FGM plates

6.7.1.1 Free vibration analysis

A square Al₂O₃/Ti-6Al-4V plate (400 mm × 400 mm) is considered as shown in Figure 6.3. The thickness of the plate, h , is 5 mm and thickness of each piezoelectric layer, h_{pie} , is 0.1 mm. The reference solution using FEM with Hermite cubic shape functions was reported by He et al. [210].

Firstly, free vibration of a SSSS plate with various volume fraction exponents $n = 0, 0.5, 5, 100, 1000$ is investigated. Table 6.2 gives frequencies of the first seven modes of the

plate with meshing 11×11 and three types of elements: quadratic ($p = 2$), cubic ($p = 3$), quartic ($p = 4$). It can be seen that the results of IGA match well with those of the reference solution [210]. In addition, frequencies of the plate with $p = 3$ and those with $p = 4$ are similar. Thus, we choose $p = 3$ for simulating the results of next examples.

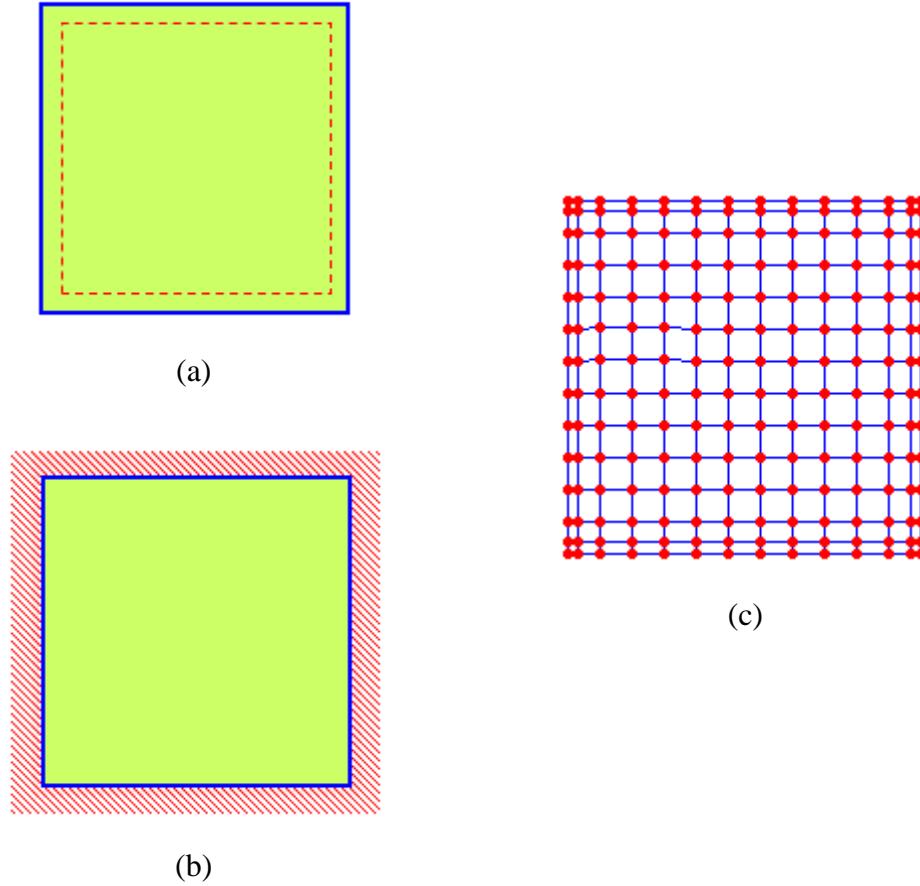


Figure 6.3. Square plate models and their discretization: (a) simply supported plate, (b) clamped plate and (c) meshing of 13×13 cubic elements.

Next, the effect of volume fraction exponents to frequencies of the CCCC plate is shown in Table 6.3. It is again confirmed that the results of the present method match well with those of Ref. [210].

Further, a comparison of frequencies for CCCC and SSSS plates with various volume fracture exponents is plotted in Figure 6.4. We can see that the frequencies of the CCCC plate are larger than those of the SSSS plate, as expected. Besides, Figure 6.5 shows the shape of the first eight eigen-modes of the CCCC plate.

Table 6.2. Natural frequencies of the first seven modes of the piezoelectric FGM (SSSS) plate

n	Method	Mode						
		1	2	3	4	5	6	7
1000	IGA ($p = 2$)	255.2	642.2	642.3	1025.0	1304.6	1304.6	1679.6
	IGA ($p = 3$)	254.7	636.3	636.5	1017.6	1271.9	1271.9	1651.5
	IGA ($p = 4$)	254.7	636.3	636.5	1017.6	1271.5	1271.5	1651.2
	FEM [210]	261.7	651.5	651.5	1024.3	1302.6	1302.6	1649.7
100	IGA ($p = 2$)	252.2	634.8	635.0	1013.3	1289.6	1289.6	1660.3
	IGA ($p = 3$)	251.8	629.0	629.2	1005.9	1257.3	1257.3	1632.5
	IGA ($p = 4$)	251.8	629	629.2	1005.9	1256.8	1256.9	1632.2
	FEM [210]	259.4	645.6	645.6	1014.9	1290.8	1290.8	1634.7
5	IGA ($p = 2$)	223.8	558.1	561.4	896.3	1138.5	1141.5	1461.5
	IGA ($p = 3$)	223.4	552.9	552.9	889.6	1106.5	1109.0	1436.3
	IGA ($p = 4$)	223.4	552.9	555.8	889.5	1106.1	1108.7	1436.0
	FEM [210]	230.5	573.8	573.8	902.0	1148.1	1148.1	1453.3
0.5	IGA ($p = 2$)	181.2	448.5	453.0	723.6	914.9	917.8	1175.0
	IGA ($p = 3$)	180.8	444.2	448.4	717.8	889.5	893.3	1154.0
	IGA ($p = 4$)	180.8	444.2	448.4	717.8	889.2	893.0	1153.8
	FEM [210]	185.5	462.5	462.5	731.1	925.5	925.5	1180.9
0	IGA ($p = 2$)	142.4	358.2	258.3	571.8	727.8	727.8	936.8
	IGA ($p = 3$)	142.1	354.9	355.0	567.4	709.0	709.0	920.4
	IGA ($p = 4$)	142.1	354.8	354.9	567.3	708.8	708.8	920.2
	FEM [210]	144.3	359	359.0	564.1	717.8	717.8	908.3

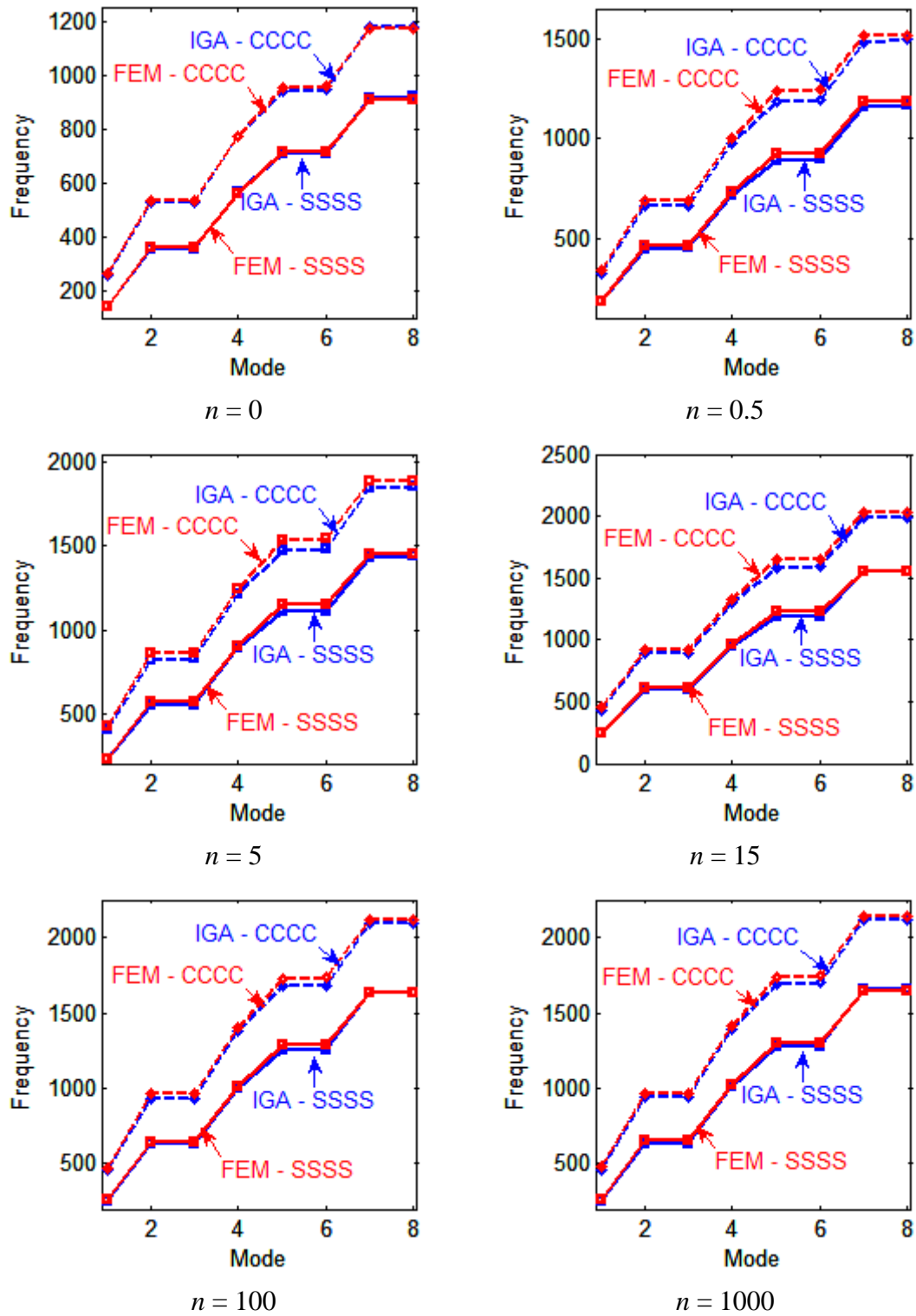
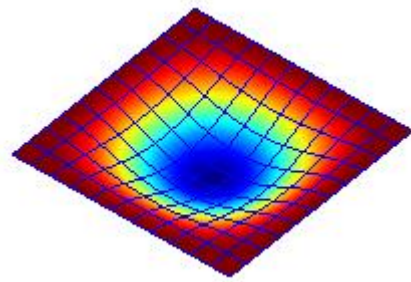


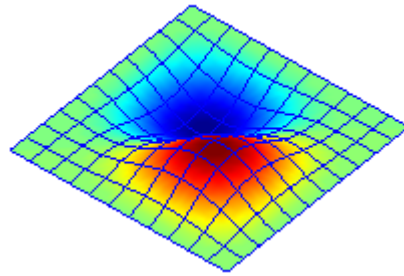
Figure 6.4. The first eight natural frequencies of the simply supported (SSSS) and clamped (CCCC) piezoelectric FGM plate with different volume fraction exponents.

Table 6.3. Natural frequencies of the first seven modes of the piezoelectric FGM (CCCC) plate

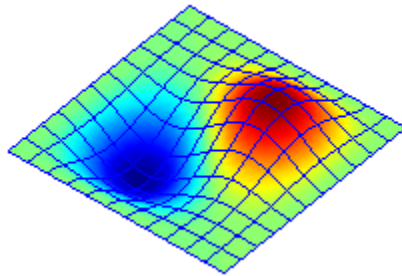
n	Method	Mode						
		1	2	3	4	5	6	7
1000	IGA	464.0	945.4	945.8	1393.1	1693.8	1701.9	2121.1
	FEM [210]	477.1	970.6	970.6	1411.9	1740.2	1750.1	2140.4
100	IGA	458.7	934.5	934.9	1377.1	1674.3	1682.3	2096.7
	FEM [210]	472.8	961.8	961.8	1399.0	1724.3	1734.2	2120.9
15	IGA	434.5	885	886.0	1304.8	1585.9	1593.5	1985.7
	FEM [210]	450.3	917.2	917.2	1334.1	1644.5	1653.9	2022.6
5	IGA	404.1	821.3	825.0	1214.1	1473.5	1480.6	1843.1
	FEM [210]	420.3	855.3	855.3	1244.0	1534.2	1543	1886.5
1	IGA	351.8	712.3	719.9	1057.6	1280.2	1286.8	1598.0
	FEM [210]	363.0	739.3	739.3	1075.3	1327.9	1335.5	1632.0
0.5	IGA	325.2	659.5	664.5	977.0	1183.9	1189.8	1479.0
	FEM [210]	337.5	687.2	687.2	999.4	1234	1241	1516.6
0.2	IGA	294.0	597.8	599.6	882.5	1071.4	1076.6	1340.3
	FEM [210]	306.4	623.5	623.5	904.4	1119.2	1125.8	1370.8
0	IGA	258.7	526.9	527.1	776.1	943.3	947.9	1180.9
	FEM [210]	262.5	533.8	533.8	774.2	957.3	963.0	1172.7



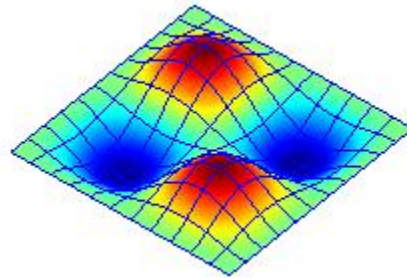
Mode 1



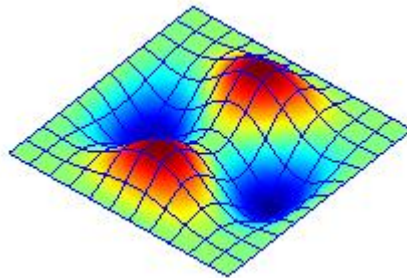
Mode 2



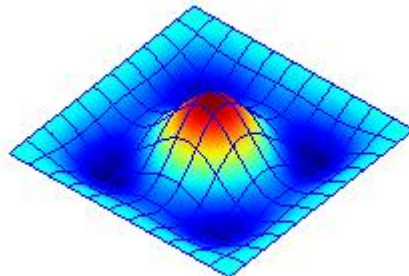
Mode 3



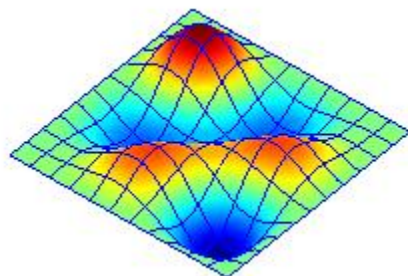
Mode 4



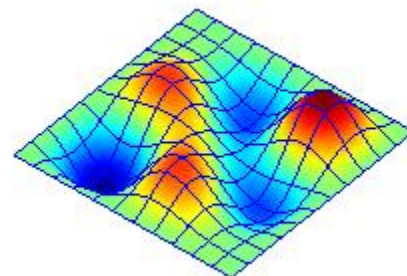
Mode 5



Mode 6



Mode 7



Mode 8

Figure 6.5. Shape of the first eight eigenmodes of the piezoelectric FGM plates with $n=1$.

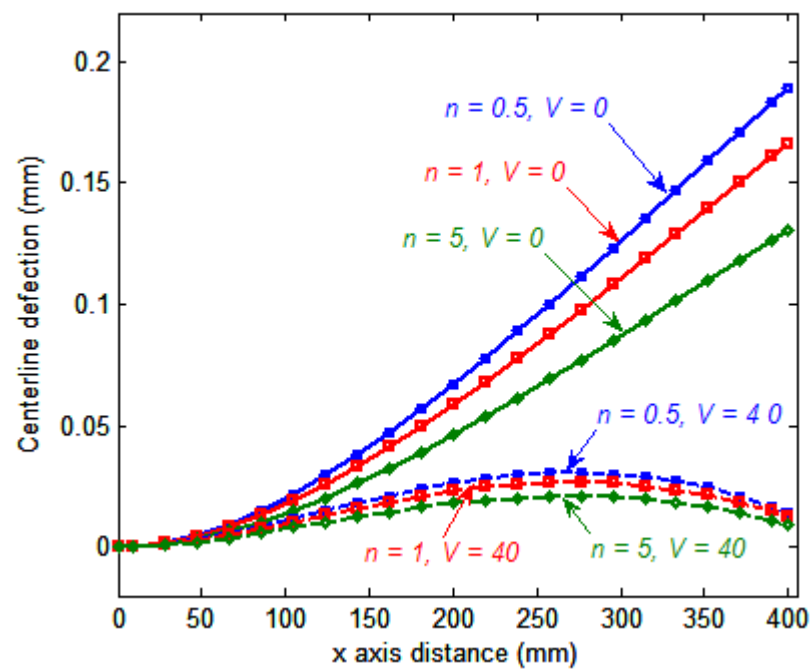


Figure 6.6. Centerline deflection of the CFFF plate under mechanical load and electro-mechanical load.

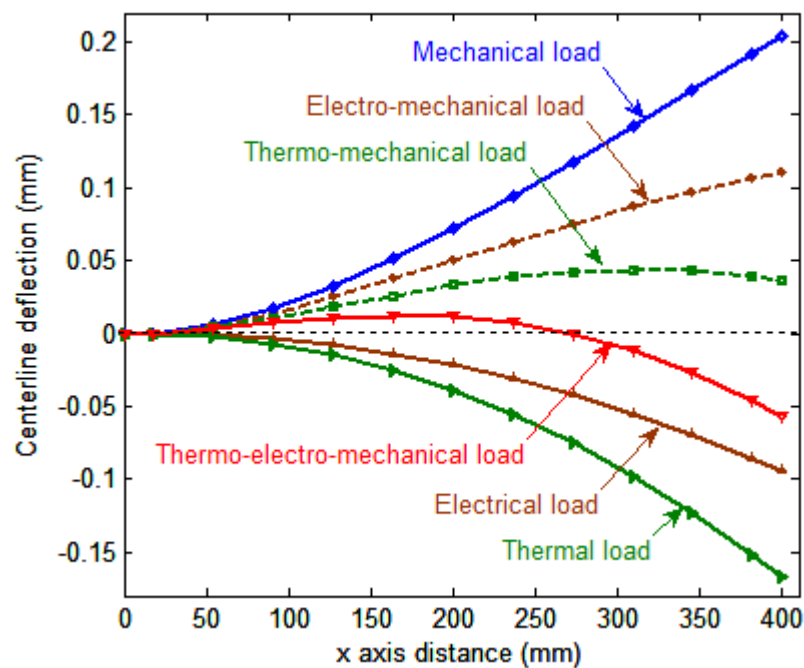


Figure 6.7. Centerline deflection of the CFFF plate under thermo-electro-mechanical load.

6.7.1.2 Static analysis

Now, we consider a CFFF piezoelectric FGM plate subjected to a uniform load $q = 100 \text{ N/m}^2$ with the material properties and geometry as specified in section 6.7.1.1. The upper and lower surfaces of plate are made of piezoelectric actuator layers. Firstly, centerline deflections of the CFFF plate with $p = 3$ and meshing 11×11 under uniform load and actuator voltages $V = 0$ and 40 are shown in Figure 6.6. It can be observed that with the increase of volume fraction exponent n , the deflection of the plate decreases. Besides, the deflection decreases for increasing input voltage. Similar results were obtained in Ref. [210]. Thus, we can see that in order to control the deflection of the piezoelectric FGM plate, we can apply equal-amplitude voltages at the bottom and top piezoelectric actuator layers. Next, Figure 6.7 shows the centerline deflection of the plate under thermal-electro-mechanical load. It can be seen that the deflection changes when the plate is subjected to mechanical, thermal, electrical, thermo-mechanical, electro-mechanical and thermo-electro-mechanical load. This is because of effect of piezoelectric converse, thermal converse or thermo-piezoelectric converse.

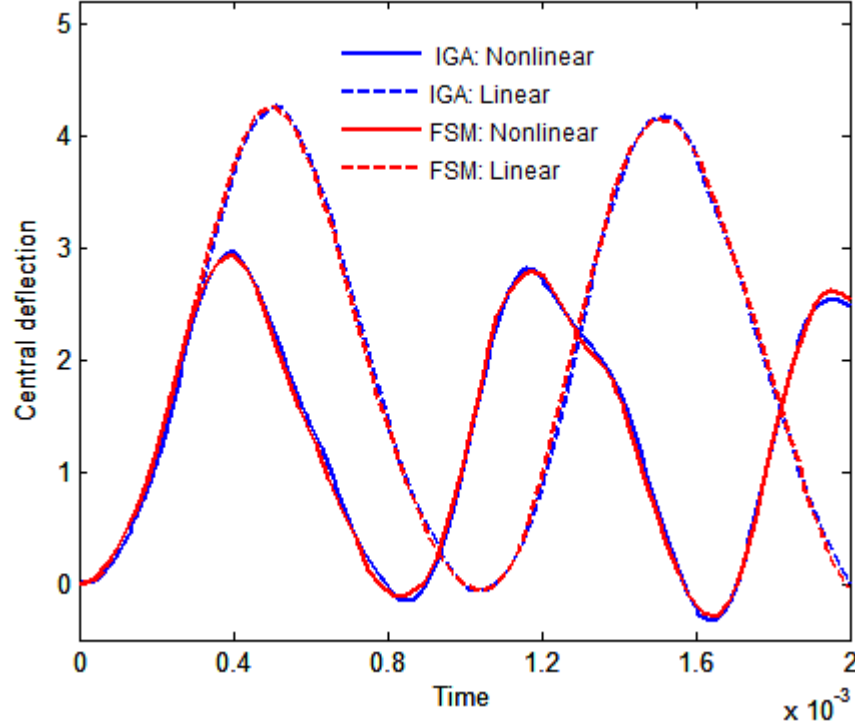


Figure 6.8. Displacement of the plate under step uniform load.

6.7.2 Nonlinear transient analysis of piezoelectric FGM plates

6.7.2.1 An orthotropic plate

This example aims to verify the accuracy of the present method for geometrically nonlinear transient analysis.

A SSSS square plate under a uniform loading of $q_0 = 1$ MPa is considered. Material properties and the geometry are given as: $E_1 = 525$ GPa, $E_2 = 21$ GPa, $G_{12} = G_{23} = G_{13} = 10.5$ GPa, $\nu = 0.25$, $\rho = 800$ kg/m³, length $L = 250$ mm, thickness $h = 5$ mm. The normalized central deflection, $\bar{w} = w/h$, of linear and nonlinear analyses is plotted in Figure 6.8. We can see that deflection responses of present method match well with those of finite strip method (FSM) [211]. In addition, magnitudes of nonlinear response are smaller than those of linear response and wavelength of the nonlinear response also changes compared to that of linear case.

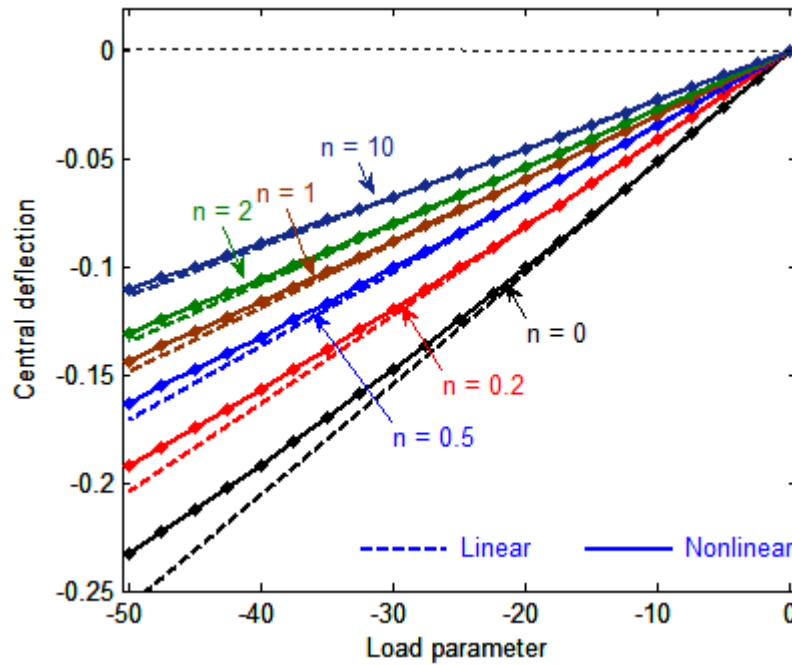


Figure 6.9. Effect of volume fraction exponent n on deflection of piezoelectric FGM (Al₂O₃/Ti₆Al₄V) plates under mechanical load.

6.7.2.2 Geometrically nonlinear static analysis

In this example, geometrically nonlinear analysis of the piezoelectric FGM plates under mechanical load, thermo-mechanical load and thermo-electro-mechanical load is

investigated. The square piezoelectric FGM plate has length $L = 1$, thickness of FGM layer $h_{\text{FGM}} = L/20$ and thickness of each piezoelectric layer $h_{\text{piezo}} = h_{\text{FGM}}/10$. The boundary condition of the plate is SSSS.

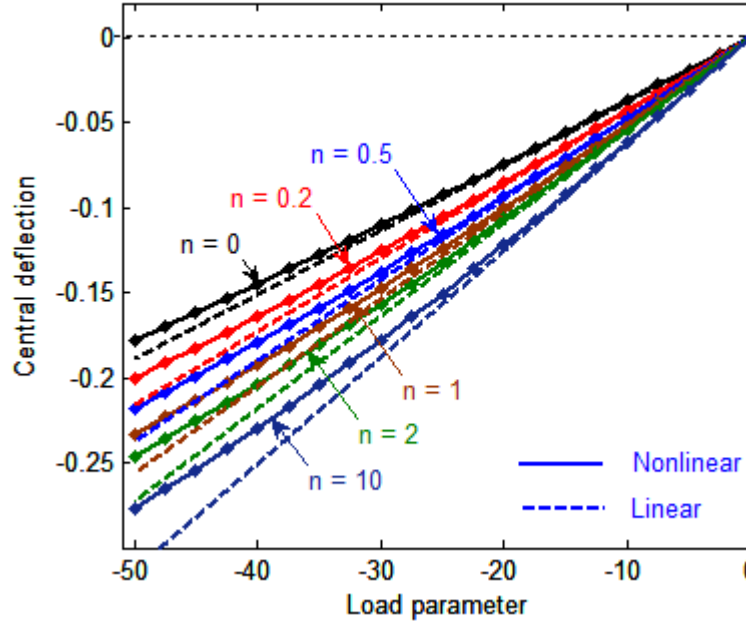


Figure 6.10. Effect of volume fraction exponent n on deflection of piezoelectric FGM (Al/ZrO₂-2) plates subjected to mechanical load.

For the plate subjected to mechanical load (parameter load $\bar{q} = q_o \times 10^5$), Figure 6.9 and Figure 6.10 show the effect of volume fraction exponent n on deflection of piezoelectric FGM (Al₂O₃/Ti₆Al₄V) and (Al/ZrO₂-2) plates under mechanical load, respectively. It is again confirmed that magnitude of deflection of nonlinear analysis is smaller than that of linear analysis. With the piezoelectric FGM (Al₂O₃/Ti₆Al₄V) plate, when volume fraction exponent increases, the deflection of the plate, shown in Figure 6.9, decreases. In contrast with the piezoelectric FGM (Al/ZrO₂-2) plate, the deflection of the plate plotted in Figure 6.10 increases when n increases.

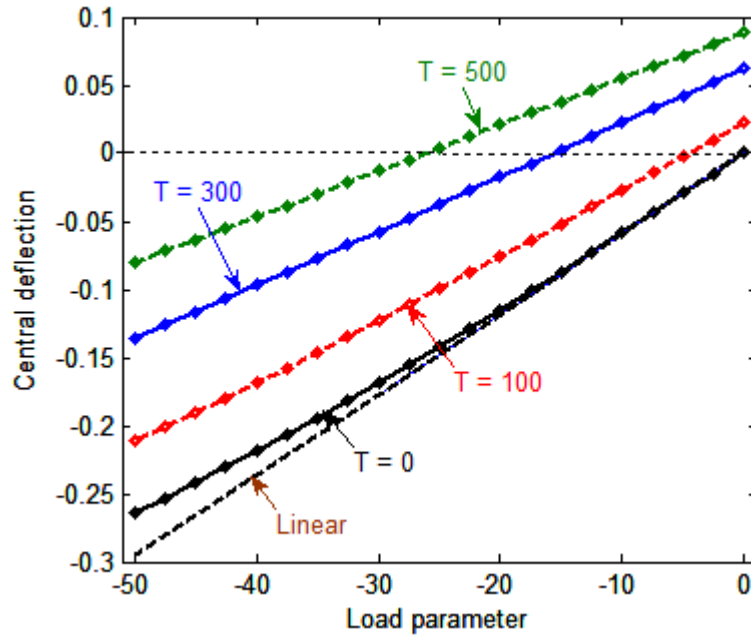


Figure 6.11. Effect of temperature on deflection of piezoelectric FGM (Al/ZrO₂-2) plates with $n = 5$ under thermo-mechanical load.

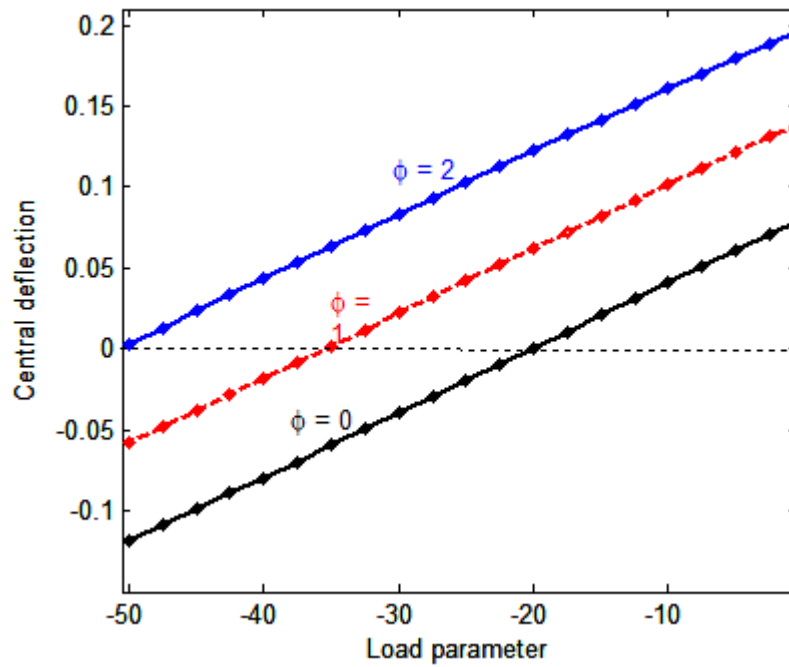


Figure 6.12. Effect of input voltage on deflection of piezoelectric FGM (Al/ZrO₂-2) plates with $n = 100$ under thermo-electro-mechanical load.

Next, the effect of temperature on nonlinear deflection of the plate under thermo-mechanical load with $n = 5$ is shown in Figure 6.11. It is observed that the behavior of deflection subjected to thermo-mechanical load is different from the pure mechanical loading. When the mechanical load is zero, the deflection of the plate is not zero. This is because of the thermal expansion phenomenon. Also, the deflection decreases correspondingly to the increase of the temperature.

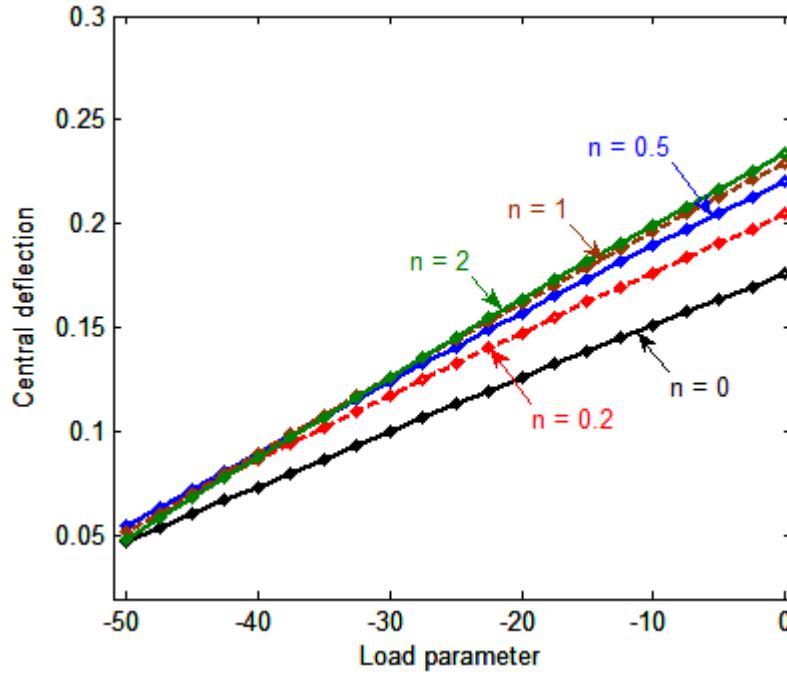


Figure 6.13. Effect of volume fraction exponent n on deflection of piezoelectric FGM (Al/ZrO2-2).

We further study the deflection of the plate under thermo-electro-mechanical load. The temperature at the ceramic surface is held at $T_c = 300^\circ\text{C}$ and temperature at the metal surface is set to $T_m = 20^\circ\text{C}$. Figure 6.12 plots the effect of parameter input voltage ($\phi = V \times 10^3 / p_{33}$) on deflection of the plate with $n = 100$. We can see that under the piezoelectric effect, the deflection of the plate is converse, when parameter input voltage becomes larger. Further, Figure 6.13 shows the effect of volume fraction exponent n on deflection of piezoelectric FGM (Al/ZrO2-2) plates under thermo-electro-mechanical load. Again, we can see that the deflection decreases when n increases.

6.7.2.3 Geometrically nonlinear transient analysis

Now, a piezoelectric FGM plate subjected to sinusoidally distribute transverse loads is investigated. The CCCC square plate has length $L = 0.2$, thickness of FGM layer $h_{\text{FGM}} = L/10$ and thickness of each piezoelectric layer $h_{\text{piezo}} = h_{\text{FGM}}/10$. The FGM layer is made of Al/ ZrO_2 -2.

The sinusoidally distributed transverse load is expressed as follows:

$$q = q_0 \sin\left(\frac{\pi x}{L}\right) \sin\left(\frac{\pi y}{L}\right) F(t) \quad (6.31)$$

Where

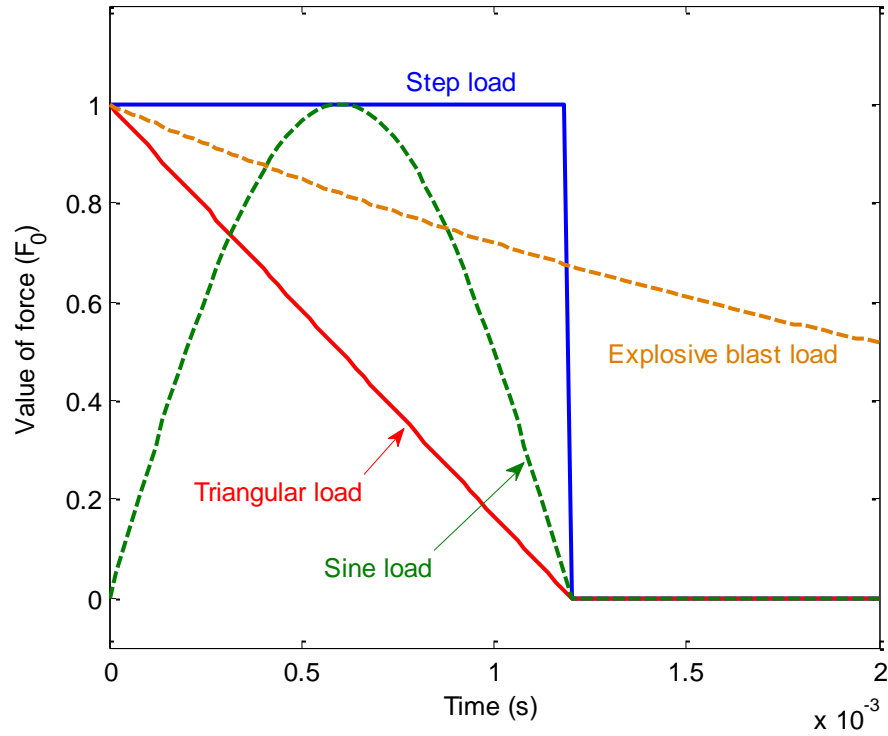


Figure 6.14. Types of load: step, triangular, sinusoidal and explosive blast.

$$F(t) = \begin{cases} \begin{cases} 1 & 0 \leq t \leq t_1 \\ 0 & t > t_1 \end{cases} & \text{Step load} \\ \begin{cases} 1-t/t_1 & 0 \leq t \leq t_1 \\ 0 & t > t_1 \end{cases} & \text{Triangular load} \\ \begin{cases} \sin(\pi t / t_1) & 0 \leq t \leq t_1 \\ 0 & t > t_1 \end{cases} & \text{Sinusoidal load} \\ e^{-\gamma t} & \text{Explosive blast load} \end{cases} \quad (6.32)$$

in which $q_0 = 4 \times 10^8$ Pa, $\gamma = 330 \text{ s}^{-1}$ and $F(t)$ is plotted in Figure 6.14.

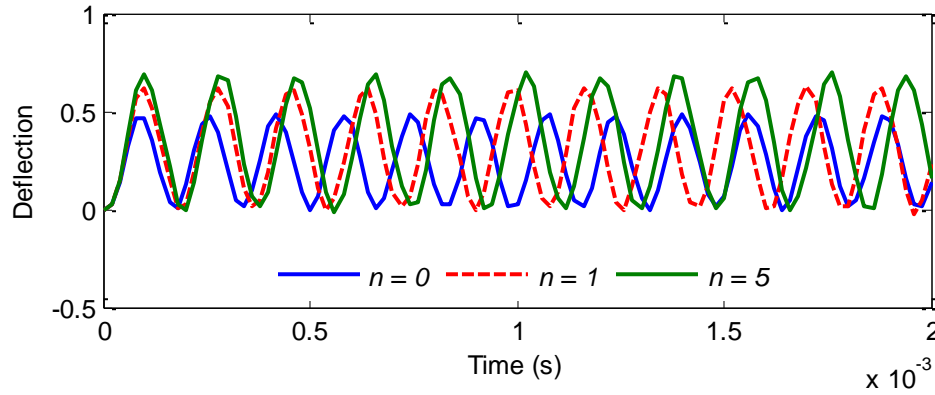


Figure 6.15. Effect of volume fraction exponent n on nonlinear transient responses of piezoelectric FGM plates subjected to step load.

Figure 6.15 to Figure 6.18 show the effect of volume fraction exponent on nonlinear transient response of the plate subjected to the step, triangular, sine and explosive blast load, respectively. It can be observed that when n increases, the deflection increases. Next, linear and nonlinear response of the plate under the step, triangular, sine and explosive blast load is studied and illustrated in Figure 6.19 to Figure 6.22, respectively. Again, it can be seen that nonlinear response has lower central deflection and higher frequency than that of the linear response. Lastly, Figure 6.23 to Figure 6.26 plot nonlinear response of the Al/ ZrO_2 -2 and $\text{Al}_2\text{O}_3/\text{Ti6Al4V}$ plate subjected to the step, triangular, sine and explosive blast load, respectively. We can see that the deflection of the Al/ ZrO_2 -2 plate is larger than that of the $\text{Al}_2\text{O}_3/\text{Ti6Al4V}$ plate.

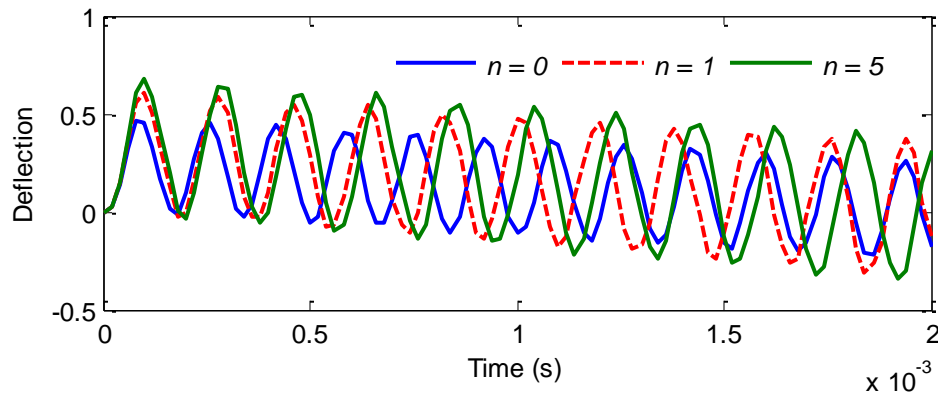


Figure 6.16. Effect of volume fraction exponent n on nonlinear transient responses of piezoelectric FGM plates subjected to triangular load.

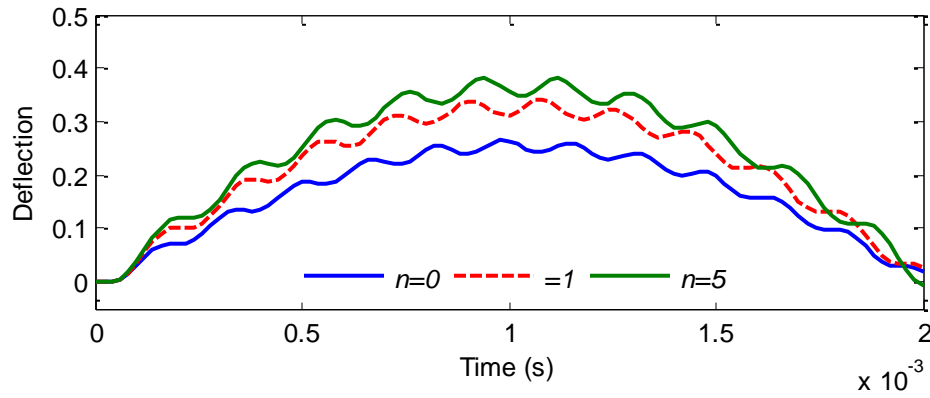


Figure 6.17. Effect of volume fraction exponent n on nonlinear transient responses of piezoelectric FGM plates subjected to sine load.

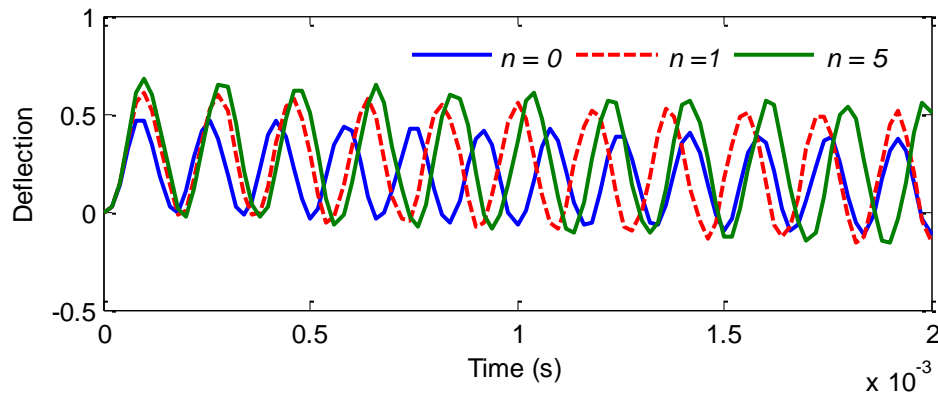


Figure 6.18. Effect of volume fraction exponent n on nonlinear transient responses of piezoelectric FGM plates subjected to explosive blast load.

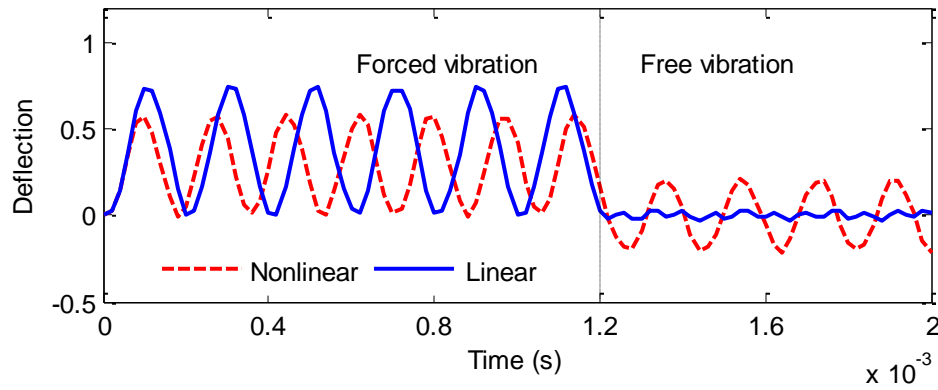


Figure 6.19. Linear and nonlinear transient responses of piezoelectric FGM plates subjected to step load with $n = 0.5$.

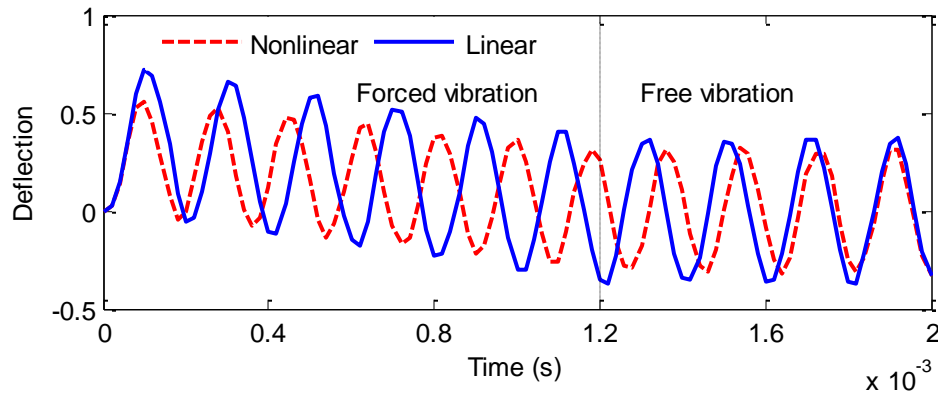


Figure 6.20. Linear and nonlinear transient responses of piezoelectric FGM plates subjected to triangular load with $n = 0.5$.

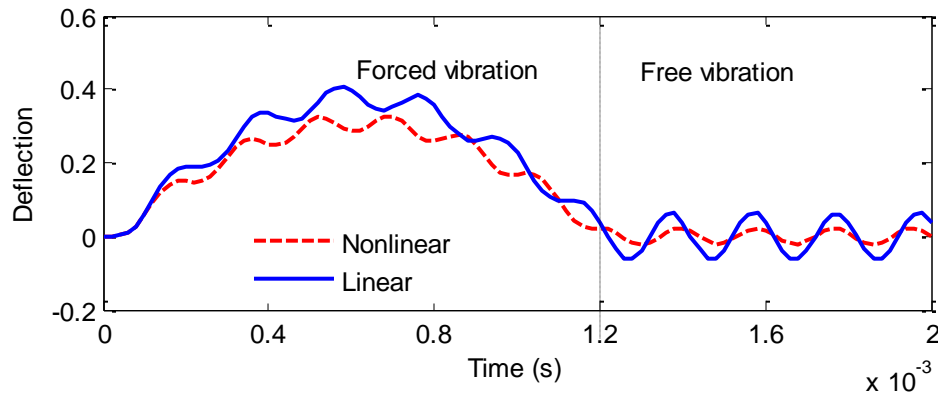


Figure 6.21. Linear and nonlinear transient responses of piezoelectric FGM plates subjected to sine load with $n = 0.5$.

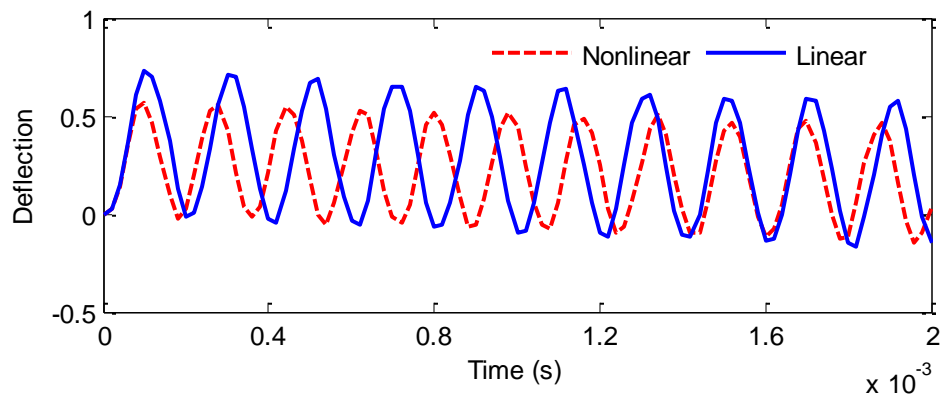


Figure 6.22. Linear and nonlinear transient responses of piezoelectric FGM plates subjected to explosive blast load with $n = 0.5$.

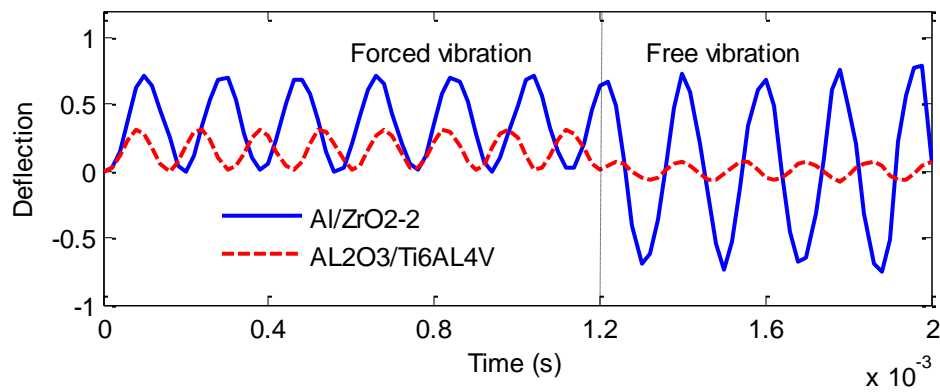


Figure 6.23. Nonlinear transient responses of piezoelectric FGM plates under step load with $n = 10$.

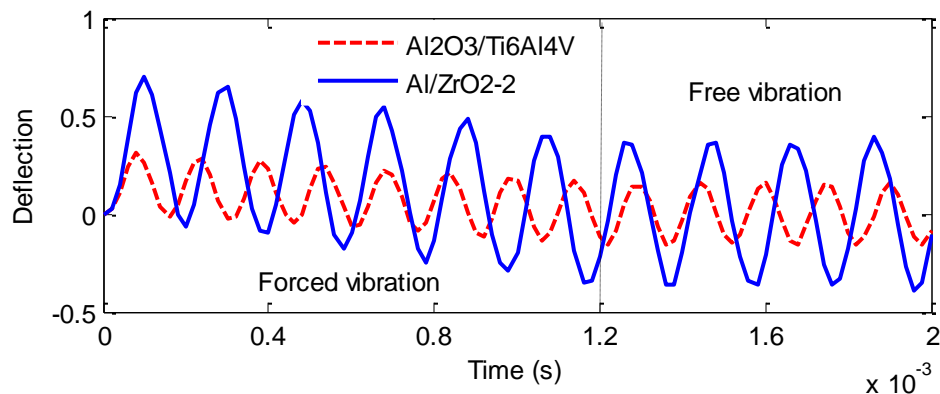


Figure 6.24. Nonlinear transient responses of piezoelectric FGM plates under triangular load with $n = 10$.

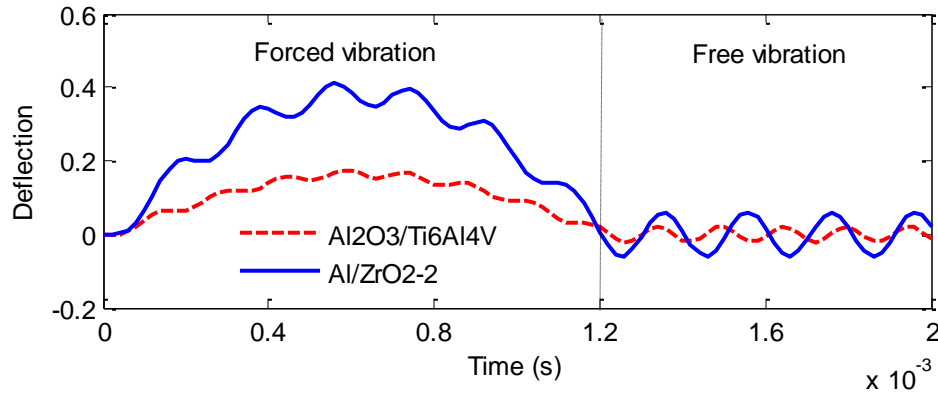


Figure 6.25. Nonlinear transient responses of piezoelectric FGM plates under sinusoidal load with $n = 10$.

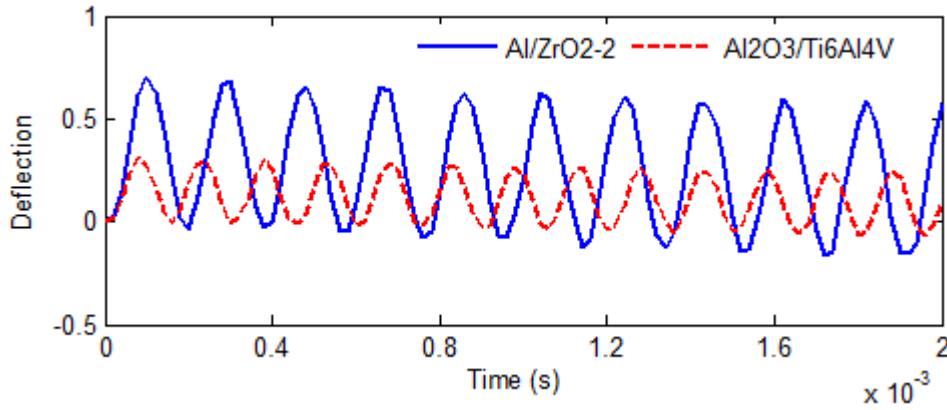


Figure 6.26. Nonlinear transient responses of piezoelectric FGM plates under explosive blast load with $n = 10$.

6.8 Concluding remarks

This chapter presents geometrically nonlinear transient of piezoelectric functionally graded plates (FGPs) using IGA based on the generalized shear deformation model. The electric potential of each piezoelectric layer is assumed linearly through the thickness of each piezoelectric layer. The material properties of FGM are assumed to vary through the thickness by the rule of mixture and the Mori–Tanaka scheme. The nonlinear formulation for plates is formed in the total Lagrange approach based on the von Kármán strains, which includes thermo-piezoelectric effects, and solved by Newmark time integration associated with the iteration methods.

Through the present formulation and numerical results, we can draw the following conclusions:

- In the analysis process, the thermal, electrical and mechanical loadings are considered and a two-step procedure is proposed including a step of calculating the temperature field through the thickness of the plate and a step of analyzing the geometrically nonlinear behavior of the plate under thermo-electro-mechanical loadings.
- Comparison between the nonlinear and linear behaviors reveals that nonlinear response has lower central deflection and higher frequency than that of the linear response. Wavelength of the nonlinear response also changes compared to that of linear case. Because of thermal expansion phenomenon, the deflection of the plates is upward and decreases when temperature increases.
- Effects of various parameters on the geometrically nonlinear responses of the piezoelectric FGP plate are also investigated. With the piezoelectric FGM (Al₂O₃/Ti₆Al₄V) plate, when volume fraction exponent, n , increases, the deflection of the plate decreases. However, in the piezoelectric FGM (Al/ZrO₂-2) plate, the deflection of the plate increases when n increases. Moreover, nonlinear response has lower central deflection and higher frequency than that of the linear response under nonlinear transient analysis.
- Numerous numerical examples have been carried out to show the accuracy and reliability of the present method for the geometrically nonlinear responses of the piezoelectric FGM plate by comparing its numerical solutions with those of other available numerical results.

Chapter 7

Functionally graded carbon nanotube-reinforced composite plates

7.1 Overview

In this chapter, we deal with the third objective of the thesis. A simple and effective formulation based on IGA and HSDT to investigate the static and dynamic vibration behaviors of functionally graded carbon nanotube-reinforced composite plates is presented. The material properties of functionally graded carbon nanotube-reinforced composites (FG-CNTRCs) are assumed to be graded through the thickness direction according to several linear distributions of the volume fraction of carbon nanotubes, which are introduced in section 3.2.2 of chapter 3. The governing equation is approximated according to the HSDT model using isogeometric elements based on Non-Uniform Rational B-Spline (NURBS) basis functions. This achieves naturally any desired degree of continuity through the choice of the interpolation order, so that the method easily fulfils the C^1 -continuity requirement of the HSDT model. The accuracy and reliability of the proposed method is verified by comparing its numerical predictions with those of other available numerical approaches.

7.2 Governing equations for functionally graded CNTRC plates

7.2.1 Displacement field

According to the third-order shear deformation theory as presented in Eq. (5.4), the displacements of the CNTRC plate can be rewritten as:

$$\begin{aligned} u(x, y, z) &= u_0 + z\beta_x + cz^3(\beta_x + w_{,x}) \\ v(x, y, z) &= v_0 + z\beta_y + cz^3(\beta_y + w_{,y}), \quad (-h/2 \leq z \leq h/2) \\ w(x, y, z) &= w_0 \end{aligned} \quad (7.1)$$

And the variables $\mathbf{u}_0 = [u_0 \ v_0]^T$, w_0 and $\boldsymbol{\beta} = [\beta_x \ \beta_y]^T$ are the membrane displacements, the deflection of the mid-plane and the rotations of the mid-plane around the y -axis and the x -axis, respectively.

The in-plane strains are expressed by the following equation:

$$\boldsymbol{\varepsilon} = [\varepsilon_{xx} \ \varepsilon_{yy} \ \gamma_{xy}]^T = \boldsymbol{\varepsilon}_0 + z\boldsymbol{\kappa}_1 + z^3\boldsymbol{\kappa}_2 \quad (7.2)$$

Where

$$\boldsymbol{\varepsilon}_0 = \begin{bmatrix} u_{0,x} \\ v_{0,y} \\ u_{0,y} + v_{0,x} \end{bmatrix}, \quad \boldsymbol{\kappa}_1 = \begin{bmatrix} \beta_{x,x} \\ \beta_{y,y} \\ \beta_{x,y} + \beta_{y,x} \end{bmatrix}, \quad \boldsymbol{\kappa}_2 = c \begin{bmatrix} \beta_{x,x} + w_{0,xx} \\ \beta_{y,y} + w_{0,yy} \\ \beta_{x,y} + \beta_{y,x} + 2w_{0,xy} \end{bmatrix} \quad (7.3)$$

and the transverse shear strains are given by:

$$\boldsymbol{\gamma} = \begin{bmatrix} \gamma_{xz} \\ \gamma_{yz} \end{bmatrix} = \begin{bmatrix} \beta_x + w_{0,x} \\ \beta_y + w_{0,y} \end{bmatrix} + 3c \begin{bmatrix} \beta_x + w_{0,x} \\ \beta_y + w_{0,y} \end{bmatrix} z^2 = \boldsymbol{\varepsilon}_s + z^2 \boldsymbol{\kappa}_s \quad (7.4)$$

The constitutive equations of the anisotropic plate are derived as:

$$\begin{Bmatrix} \sigma_{xx} \\ \sigma_{yy} \\ \tau_{xy} \\ \tau_{xz} \\ \tau_{yz} \end{Bmatrix} = \begin{bmatrix} Q_{11} & Q_{12} & Q_{16} & 0 & 0 \\ Q_{21} & Q_{22} & Q_{26} & 0 & 0 \\ Q_{61} & Q_{62} & Q_{66} & 0 & 0 \\ 0 & 0 & 0 & Q_{55} & Q_{54} \\ 0 & 0 & 0 & Q_{45} & Q_{44} \end{bmatrix} \begin{Bmatrix} \varepsilon_{xx} \\ \varepsilon_{yy} \\ \gamma_{xy} \\ \gamma_{xz} \\ \gamma_{yz} \end{Bmatrix} - \begin{Bmatrix} \alpha_{11} \\ \alpha_{22} \\ 0 \\ 0 \\ 0 \end{Bmatrix} \Delta T \quad (7.5)$$

Where the material constants are given by:

$$Q_{11} = \frac{E_{11}}{1 - \nu_{12}\nu_{21}}, Q_{12} = \frac{\nu_{12}E_{22}}{1 - \nu_{12}\nu_{21}}, Q_{22} = \frac{E_{22}}{1 - \nu_{12}\nu_{21}} \quad (7.6)$$

$$Q_{66} = G_{12}, Q_{55} = G_{13}, Q_{44} = G_{23}$$

And ΔT is the temperature change with respect to a reference state.

7.2.2 Weak form equations

A weak form of the static analysis for the plates subjected to uniform loading q_0 can be expressed as:

$$\int_{\Omega} \delta \boldsymbol{\varepsilon}^T \mathbf{D}_b \boldsymbol{\varepsilon} d\Omega + \int_{\Omega} \delta \boldsymbol{\gamma}^T \mathbf{D}_s \boldsymbol{\gamma} d\Omega = \int_{\Omega} \delta w q_0 d\Omega \quad (7.7)$$

Where material constant matrices, \mathbf{D}_b and \mathbf{D}_s , are given as:

$$\mathbf{D}_b = \begin{bmatrix} \mathbf{A} & \mathbf{B} & \mathbf{E} \\ \mathbf{B} & \mathbf{D} & \mathbf{F} \\ \mathbf{E} & \mathbf{F} & \mathbf{H} \end{bmatrix}, \quad \mathbf{D}_s = \begin{bmatrix} \mathbf{A}_s & \mathbf{B}_s \\ \mathbf{B}_s & \mathbf{D}_s \end{bmatrix} \quad (7.8)$$

In which

$$(\mathbf{A}, \mathbf{B}, \mathbf{D}, \mathbf{E}, \mathbf{F}, \mathbf{H}) = \int_{-h/2}^{h/2} (1, z, z^2, z^3, z^4, z^6) Q_{ij} dz \quad i, j = 1, 2, 6 \quad (7.9)$$

$$(\mathbf{A}_s, \mathbf{B}_s, \mathbf{D}_s) = \int_{-h/2}^{h/2} (1, z^2, z^4) Q_{ij} dz \quad i, j = 4, 5$$

For free vibration analysis of the plates, the weak form can be derived as:

$$\int_{\Omega} \delta \boldsymbol{\epsilon}^T \mathbf{D}_b \boldsymbol{\epsilon} d\Omega + \int_{\Omega} \delta \boldsymbol{\gamma}^T \mathbf{D}_s \boldsymbol{\gamma} d\Omega = \int_{\Omega} \delta \tilde{\mathbf{u}}^T \mathbf{m} \ddot{\mathbf{u}} d\Omega \quad (7.10)$$

Where \mathbf{m} is defined by:

$$\mathbf{m} = \begin{bmatrix} \mathbf{I}_0 & 0 & 0 \\ 0 & \mathbf{I}_0 & 0 \\ 0 & 0 & \mathbf{I}_0 \end{bmatrix} \text{ where } \mathbf{I}_0 = \begin{bmatrix} I_1 & I_2 & cI_4 \\ I_2 & I_3 & cI_5 \\ cI_4 & cI_5 & c^2 I_7 \end{bmatrix} \quad (7.11)$$

$$(I_1, I_2, I_3, I_4, I_5, I_7) = \int_{-h/2}^{h/2} \rho (1, z, z^2, z^3, z^4, z^7) dz$$

And

$$\tilde{\mathbf{u}} = \begin{Bmatrix} \mathbf{u}_1 \\ \mathbf{u}_2 \\ \mathbf{u}_3 \end{Bmatrix}, \quad \mathbf{u}_1 = \begin{Bmatrix} u_0 \\ v_0 \\ w_0 \end{Bmatrix}, \quad \mathbf{u}_2 = \begin{Bmatrix} \beta_x \\ \beta_y \\ 0 \end{Bmatrix}, \quad \mathbf{u}_3 = \begin{Bmatrix} \beta_x + w_{0,x} \\ \beta_y + w_{0,y} \\ 0 \end{Bmatrix} \quad (7.12)$$

7.2.3 NURBS-based novel CNTRC plate formulation

Using the NURBS basis functions presented in Eq. (4.17), the displacement field \mathbf{u} of the plate is approximated as:

$$\mathbf{u}^h(\xi, \eta) = \sum_I^{m \times n} R_I(\xi, \eta) \mathbf{d}_I \quad (7.13)$$

Where $\mathbf{d}_I = [u_{0I} \ v_{0I} \ w_{0I} \ \beta_{xI} \ \beta_{yI}]^T$ is the vector of degrees of freedom associated with the control point I .

Substituting Eq. (7.13) into Eqs. (7.2) and (7.4), the in-plane and shear strains can be rewritten as:

$$[\boldsymbol{\epsilon}_0^T \ \boldsymbol{\kappa}_1^T \ \boldsymbol{\kappa}_2^T \ \boldsymbol{\epsilon}_s^T \ \boldsymbol{\kappa}_s^T]^T = \sum_{I=1}^{m \times n} \left[(\mathbf{B}_I^m)^T \ (\mathbf{B}_I^{b1})^T \ (\mathbf{B}_I^{b2})^T \ (\mathbf{B}_I^{s0})^T \ (\mathbf{B}_I^{s1})^T \right]^T \mathbf{d}_I \quad (7.14)$$

Where

$$\mathbf{B}_I^m = \begin{bmatrix} N_{I,x} & 0 & 000 \\ 0 & N_{I,y} & 000 \\ N_{I,y} & N_{I,x} & 000 \end{bmatrix}, \quad \mathbf{B}_I^{b1} = \begin{bmatrix} 000 & N_{I,x} & 0 \\ 000 & 0 & N_{I,y} \\ 000 & N_{I,y} & N_{I,x} \end{bmatrix}, \quad (7.15)$$

$$\mathbf{B}_I^{b2} = c \begin{bmatrix} 00 & N_{I,xx} & N_{I,x} & 0 \\ 00 & N_{I,yy} & 0 & N_{I,y} \\ 00 & 2N_{I,xy} & N_{I,y} & N_{I,x} \end{bmatrix}$$

$$\mathbf{B}_I^{s0} = \begin{bmatrix} 00 & N_{I,x} & N_I & 0 \\ 00 & N_{I,y} & 0 & N_I \end{bmatrix}, \quad \mathbf{B}_I^{s1} = 3c \begin{bmatrix} 00 & N_{I,x} & N_I & 0 \\ 00 & N_{I,y} & 0 & N_I \end{bmatrix} \quad (7.16)$$

Substituting Eq. (7.14) into Eqs. (7.7) and (7.10), the discretized system of equations for CNTRC plates for static and free vibration analyses can be expressed as:

$$\mathbf{Kd} = \mathbf{F} \quad (7.17)$$

$$(\mathbf{K} - \omega^2 \mathbf{M})\mathbf{d} = \mathbf{0} \quad (7.18)$$

Where

$$\mathbf{K} = \int_{\Omega} \left(\begin{bmatrix} \mathbf{B}^m \\ \mathbf{B}^{b1} \\ \mathbf{B}^{b2} \end{bmatrix}^T \begin{bmatrix} \mathbf{A} & \mathbf{B} & \mathbf{E} \\ \mathbf{B} & \mathbf{D} & \mathbf{F} \\ \mathbf{E} & \mathbf{F} & \mathbf{H} \end{bmatrix} \begin{bmatrix} \mathbf{B}^m \\ \mathbf{B}^{b1} \\ \mathbf{B}^{b2} \end{bmatrix} + \begin{bmatrix} \mathbf{B}^{s0} \\ \mathbf{B}^{s1} \end{bmatrix}^T \begin{bmatrix} \mathbf{A}_s & \mathbf{B}_s \\ \mathbf{B}_s & \mathbf{D}_s \end{bmatrix} \begin{bmatrix} \mathbf{B}^{s0} \\ \mathbf{B}^{s1} \end{bmatrix} \right) d\Omega \quad (7.19)$$

and the load vector is computed as:

$$\mathbf{F} = \int_{\Omega} q_0 \mathbf{N} d\Omega \quad (7.20)$$

ω is the natural frequency and \mathbf{M} is the global mass matrix computed by:

$$\mathbf{M} = \int_{\Omega} \tilde{\mathbf{N}}^T \mathbf{m} \tilde{\mathbf{N}} d\Omega \quad (7.21)$$

Where

$$\tilde{\mathbf{N}} = \begin{Bmatrix} \mathbf{N}_1 \\ \mathbf{N}_2 \\ \mathbf{N}_3 \end{Bmatrix}, \quad \mathbf{N}_1 = \begin{bmatrix} N_I & 0 & 0 & 0 \\ 0 & N_I & 0 & 0 \\ 0 & 0 & N_I & 0 \end{bmatrix}, \quad \mathbf{N}_2 = \begin{bmatrix} 000 & N_I & 0 \\ 000 & 0 & N_I \\ 000 & 0 & 0 \end{bmatrix}, \quad (7.22)$$

$$\mathbf{N}_3 = \begin{bmatrix} 00 & N_{I,x} & N_I & 0 \\ 00 & N_{I,y} & 0 & N_I \\ 00 & 0 & 0 & 0 \end{bmatrix}$$

It is worthwhile emphasizing that the stiffness matrix formulation (7.19) contains the second derivative of the shape functions, as seen in \mathbf{B}_I^{b2} . As a result, the C^1 continuity requirement is taken into account the computations. Hence, the NURBS-based isogeometric approach may be a good choice in our study.

For transient analysis, the discretized system of equations for CNTRC plates can be written as:

$$\mathbf{M}\ddot{\mathbf{d}} + \mathbf{Kd} = \mathbf{F}(t) \quad (7.23)$$

To solve this time dependent problems, the Newmark method is used. When the current state at $t = t_0$ is known as $(\mathbf{x}_0, \dot{\mathbf{x}}_0, \ddot{\mathbf{x}}_0)$, we aim to find a new state $(\mathbf{x}_1, \dot{\mathbf{x}}_1, \ddot{\mathbf{x}}_1)$ at $t_1 = t_0 + \theta\Delta t$, using the following formulations:

$$\begin{aligned} \left[\left(\alpha + \frac{1}{\theta\Delta t} \right) \mathbf{M} + (\beta + \theta\Delta t) \tilde{\mathbf{K}} \right] \mathbf{x}_1 &= \theta\Delta t \mathbf{F}_1 + (1 - \theta) \Delta t \mathbf{F}_0 \\ &+ \left(\alpha + \frac{1}{\theta\Delta t} \right) \mathbf{M} \mathbf{x}_0 + \frac{1}{\theta} \mathbf{M} \dot{\mathbf{x}}_0 + [\beta - (1 - \theta) \Delta t] \tilde{\mathbf{K}} \mathbf{x}_0 \end{aligned} \quad (7.24)$$

$$\dot{\mathbf{x}}_1 = \frac{1}{\theta\Delta t} (\mathbf{x}_1 - \mathbf{x}_0) - \frac{1 - \theta}{\theta} \dot{\mathbf{x}}_0 \quad (7.25)$$

$$\ddot{\mathbf{x}}_1 = \frac{1}{\theta\Delta t} (\dot{\mathbf{x}}_1 - \dot{\mathbf{x}}_0) - \frac{1 - \theta}{\theta} \ddot{\mathbf{x}}_0 \quad (7.26)$$

7.3 Numerical results

Many numerical examples are performed in this section to demonstrate the stability and accuracy of the present method compared to reference solutions. Poly {(m-phenylenevinylene) -co- [(2,5-dioctoxy-p-phenylene) vinylene]} referred as PmPV [212] is considered as matrix. Material properties of PmPV are assumed to be: $E^m = 2.1$ GPa, $\nu^m = 0.34$, $\rho^m = 1.16$ g/cm³ at room temperature ($T = 300$ K). And the armchair (10, 10) SWCNTs are selected as the reinforcements. Based on the results of Ref. [213], material properties of SWCNTs are given by $E_{11}^{CNT} = 5.6466$ (TPa), $E_{22}^{CNT} = 7.08$ (TPa), $G_{12}^{CNT} = 1.9445$ (TPa), $\alpha_{11}^{CNT} = 3.4584(10^{-6}/K)$, $\alpha_{22}^{CNT} = 5.1682(10^{-6}/K)$. The CNT efficiency parameter (V_{CNT}^*) shown in Eqs. (3.19)-(3.21) is reported in Ref. [212] as: $\eta_1 = 0.149$, $\eta_2 = 0.934$ for the case $V_{CNT}^* = 0.11$; $\eta_1 = 0.15$, $\eta_2 = 0.941$ for the case $V_{CNT}^* = 0.14$, and $\eta_1 = 0.14$, $\eta_2 = 1.381$ for the case $V_{CNT}^* = 0.17$. Besides, we assume $\eta_3 = \eta_2$ and $G_{23} = G_{13} = G_{12}$.

7.3.1 Static and free vibration analyses of CNTRC plates

We now consider a square CNTRC plate with two boundary conditions: simply supported (SSSS) and clamped (CCCC) with thickness-to-length ratios $h/a = 0.05, 0.02, 0.1$ and subjected to a uniform load $q = 0.1$ MPa. A non-dimensional deflection $\bar{w} = w/h$ is used.

Table 7.1. Non-dimensional central deflection of the simply supported CNTRC plate under a uniform load

V_{CNT}^*	h/a	Types	Method			
			IGA			FEM [150]
			$p = 2$	$p = 3$	$p = 4$	
0.11	0.02	UD	1.1630	1.1615	1.1643	1.1550
		FG-V	1.6772	1.6748	1.6794	1.6530
		FG-O	2.2001	2.1967	2.2033	2.1570
		FG-X	0.7877	0.7868	0.7884	0.7900
	0.05	UD	3.546e-02	3.542e-02	3.551e-02	3.628e-02
		FG-V	4.847e-02	4.841e-02	4.854e-02	4.879e-02
		FG-O	6.170e-02	6.161e-02	6.179e-02	6.155e-02
		FG-X	2.591e-02	2.588e-02	2.594e-02	2.701e-02
0.14	0.02	UD	0.9168	0.9157	0.9178	0.9175
		FG-V	1.3350	1.3330	1.3370	1.3260
		FG-O	1.7591	1.7564	1.7614	1.7380
		FG-X	0.6195	0.6189	0.6200	0.6271
	0.05	UD	2.890e-02	2.893e-02	2.900e-02	3.001e-02
		FG-V	3.960e-02	3.960e-02	3.962e-02	4.025e-02
		FG-O	5.030e-02	5.030e-02	5.040e-02	5.070e-02
		FG-X	2.140e-02	2.140e-02	2.140e-02	2.256e-02
0.17	0.02	UD	0.7579	0.7569	0.7588	0.7515
		FG-V	1.0992	1.0976	1.1010	1.0820
		FG-O	1.4405	1.4383	1.4426	1.4160
		FG-X	0.5121	0.5115	0.5126	0.5132
	0.05	UD	2.299e-02	2.296e-02	2.301e-02	2.348e-02
		FG-V	3.162e-02	3.157e-02	3.166e-02	3.174e-02
		FG-O	4.025e-02	4.018e-02	4.031e-02	4.020e-02
		FG-X	1.673e-02	1.672e-02	1.675e-02	1.737e-02

Table 7.2. Non-dimensional central deflection of the clamped CNTRC plate under a uniform load

V_{CNT}^*	h/a	Types	Method			
			IGA			FEM [150]
			$p = 2$	$p = 3$	$p = 4$	
0.11	0.02	UD	0.2539	0.2543	0.2554	0.2618
		FG-V	0.3599	0.3592	0.3607	0.3649
		FG-O	0.4687	0.4686	0.4706	0.4719
		FG-X	0.1806	0.1813	0.1825	0.1894
	0.05	UD	1.187e-02	1.197e-02	1.205e-02	1.339e-02
		FG-V	1.452e-02	1.463e-02	1.472e-02	1.593e-02
		FG-O	1.726e-02	1.736e-02	1.747e-02	1.860e-02
		FG-X	9.971e-03	1.008e-02	1.016e-02	1.150e-02
0.14	0.02	UD	0.2045	0.2051	0.2062	0.2131
		FG-V	0.2881	0.2884	0.2896	0.2955
		FG-O	0.3750	0.3751	0.3767	0.3805
		FG-X	0.1471	0.1479	0.1489	0.1560
	0.05	UD	1.038e-02	1.048e-02	1.056e-02	1.188e-02
		FG-V	1.250e-02	1.260e-02	1.270e-02	1.390e-02
		FG-O	1.470e-02	1.480e-02	1.490e-02	1.604e-02
		FG-X	8.900e-03	9.000e-03	9.100e-03	1.036e-02
0.17	0.02	UD	0.1649	0.1652	0.1659	0.1698
		FG-V	0.2352	0.2353	0.2363	0.2384
		FG-O	0.3071	0.3071	0.3084	0.3085
		FG-X	0.1168	0.1173	0.1180	0.1223
	0.05	UD	8.608e-03	8.675e-03	8.729e-03	8.561e-03
		FG-V	9.379e-03	9.440e-03	9.510e-03	1.021e-02
		FG-O	1.118e-02	1.123e-02	1.131e-02	1.198e-02
		FG-X	7.366e-03	7.437e-03	7.485e-03	7.290e-03

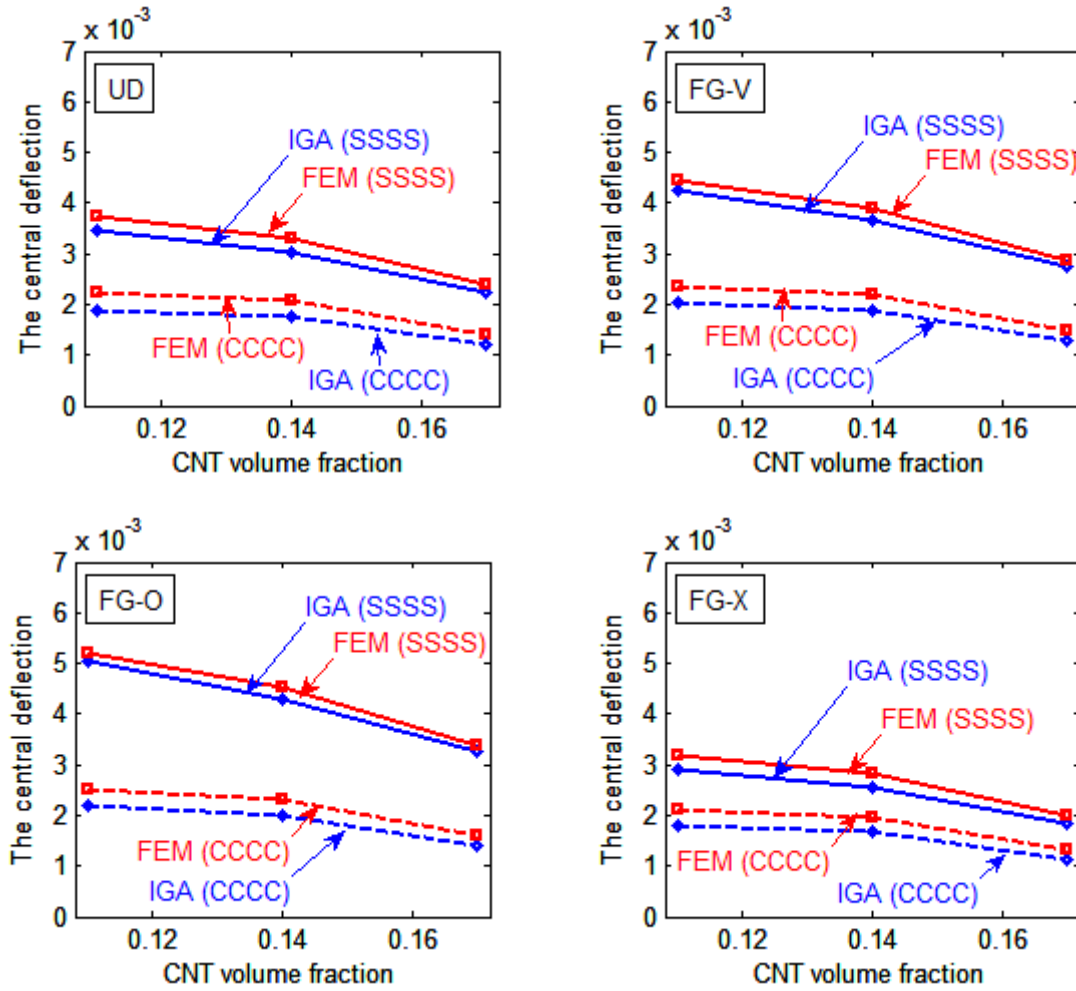


Figure 7.1. Non-dimensional central deflection of CNTRC plates with $h/a = 0.1$.

Firstly, we analyze the SSSS plate with four types of CNTRC: UD, FG-V, FG-O and FG-X. Table 7.1 shows the effect of the volume fraction of CNT, V_{CNT}^* , to the non-dimensional central deflection of the SSSS CNTRC plate with meshing of quadratic ($p = 2$), cubic ($p = 3$) and quartic ($p = 4$) elements. We can see that results of the present method for $h/a = 0.02$ and 0.05 match very well with those of FEM by Liew [150]. It is clear that V_{CNT}^* has a large influence on the central deflection of the plate. Furthermore, it can be observed that the central deflections of UD and FG-X plate are smaller than those of FG-O and FG-V plate. This shows that the stiffness of CNTRC plate depends on the distributions of CNTs along the thickness direction of the plate. Such distributions (types of UD CNTRC and FG-X CNTRC) have more CNTs at the top and the bottom surface and as a result the plate becomes stiffer in bending.

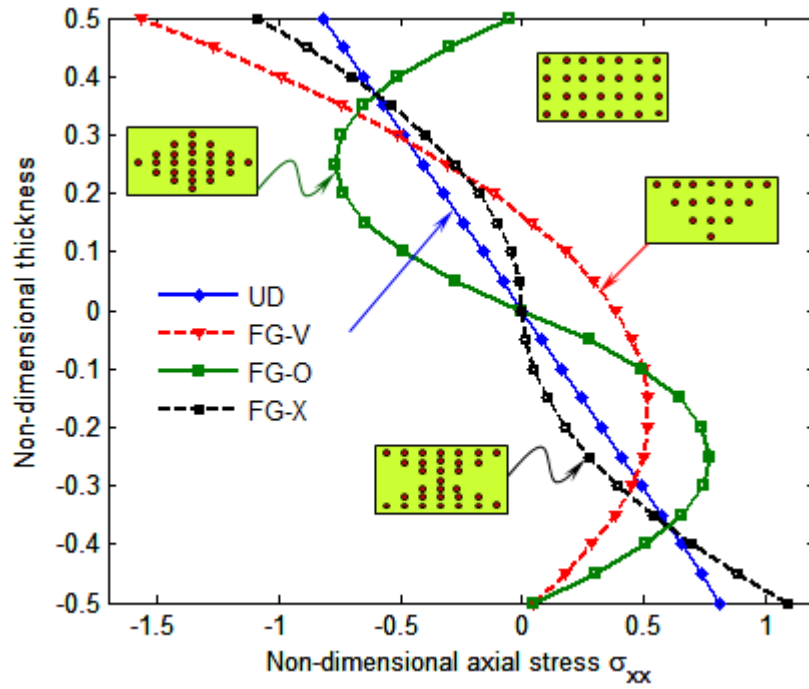


Figure 7.2. Non-dimensional axial stress of SSSS CNTRC plate with $h/a = 0.1$ and $V_{CNT}^* = 0.11$.

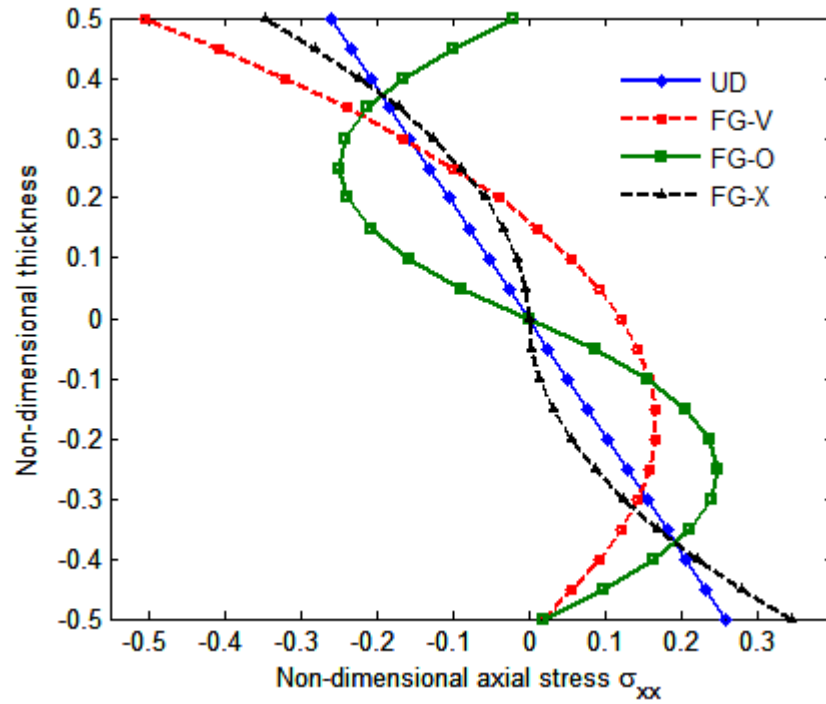


Figure 7.3. Non-dimensional axial stress of CCCC CNTRC plate with $h/a = 0.1$ and $V_{CNT}^* = 0.11$.

Next, we analyze CCCC square plates. Table 7.2 gives the non-dimensional central deflection of the plate with $h/a = 0.02$ and 0.05 . It is seen that the SSSS plates behave similarly to the CCCC plates.

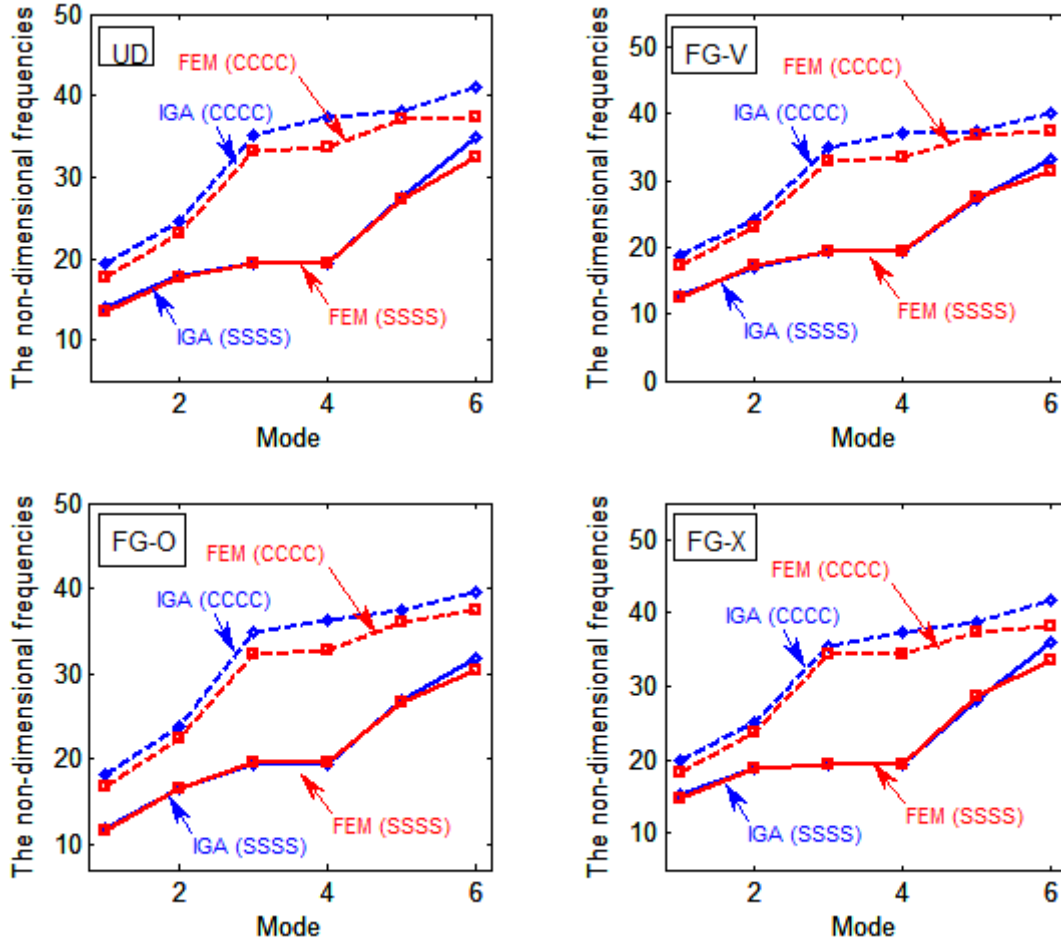


Figure 7.4. The six lowest non-dimensional natural frequencies of CNTRC plates with $h/a = 0.1$ and $V_{CNT}^* = 0.11$.

In addition, Figure 7.1 plots the effect of boundary conditions on the non-dimensional central deflection of the plate with $h/a = 0.1$. It is observed that the deflections of CCCC plate are smaller than those of SSSS plate, as expected. Figure 7.2 shows the effect of the distribution of CNTs along the thickness direction of the plate on the non-dimensional axial stress ($\bar{\sigma}_{xx} = \sigma_{xx} h^2 / qa^2$) of SSSS CNTRC plate with $h/a = 0.1$ and $V_{CNT}^* = 0.11$. We can see that distributions of the axial stress in UD, FG-O, and FG-X are symmetry and those in FG-V are anti-symmetric. This is because the reinforcements of

UD, FG-O and FG-X are symmetric with respect to the mid-surface. For the clamped CNTRC plate, the non-dimensional axial stress is also presented in Figure 7.3, which shows similar behavior to the SSSS plate studied above.

Table 7.3. The first six non-dimensional frequency parameters of the SSSS CNTRC plate with $V_{CNT}^* = 0.11$

h/a	Type	Method	Mode					
			1	2	3	4	5	6
0.1	UD	IGA	14.02	17.94	19.42	19.42	27.52	34.76
		FEM [150]	13.53	17.70	19.42	19.42	27.15	32.56
	FG-V	IGA	12.75	17.12	19.42	19.42	27.15	33.22
		FEM [150]	12.45	17.06	19.49	19.49	27.34	31.41
	FG-O	IGA	11.77	16.46	19.42	19.42	26.82	31.85
		FEM [150]	11.55	16.26	19.49	19.49	26.51	30/28
	FG-X	IGA	15.25	18.82	19.42	19.42	28.00	35.98
		FEM [150]	14.61	18.64	19.49	19.49	28.51	33.58
0.05	UD	IGA	17.50	21.34	31.73	38.85	38.85	48.71
		FEM [150]	17.35	21.51	32.39	32.39	38.89	50.19
	FG-V	IGA	15.12	19.60	30.79	38.85	38.85	48.29
		FEM [150]	15.11	19.90	31.56	38.99	38.99	47.73
	FG-O	IGA	13.50	18.37	30.03	38.85	38.85	44.75
		FEM [150]	13.52	18.48	30.16	38.99	38.99	43.94
	FG-X	IGA	20.24	23.57	33.19	38.85	38.85	49.58
		FEM [150]	19.93	23.77	34.38	38.99	38.99	52.26
0.02	UD	IGA	19.09	22.96	34.01	53.66	70.80	70.80
		FEM [150]	19.22	23.40	34.66	54.04	70.81	72.90
	FG-V	IGA	16.09	20.68	32.70	53.04	59.87	62.11
		FEM [150]	16.25	21.14	33.35	53.43	60.18	62.78
	FG-O	IGA	14.15	19.15	31.71	52.42	52.61	55.12
		FEM [150]	14.30	19.37	31.61	51.37	53.03	55.82
	FG-X	IGA	22.88	26.18	36.23	55.06	83.60	83.70
		FEM [150]	22.98	26.78	37.59	56.94	83.15	84.89

7.3.2 Free vibration of CNTRC plates

7.3.2.1 A square plate

Table 7.4. The first six non-dimensional frequency parameters of the SSSS CNTRC plate with $V_{CNT}^* = 0.14$

h/a	Type	Method	Mode					
			1	2	3	4	5	6
0.1	UD	IGA	14.92	18.73	19.77	19.77	28.28	33.06
		FEM [150]	14.30	18.36	19.79	19.79	28.23	33.64
	FG-V	IGA	13.65	17.88	19.77	19.77	27.87	34.66
		FEM [150]	13.25	17.73	19.87	19.87	28.02	32.67
	FG-O	IGA	12.66	17.20	19.77	19.77	27.53	33.41
		FEM [150]	12.33	16.84	19.87	19.87	27.00	31.63
	FG-X	IGA	16.10	19.59	19.77	19.77	28.75	37.12
		FEM [150]	15.36	19.38	19.87	19.87	29.39	34.63
0.05	UD	IGA	19.19	22.83	33.02	39.54	39.54	50.02
		FEM [150]	18.92	22.86	33.57	39.58	39.58	51.42
	FG-V	IGA	16.60	20.86	31.88	39.54	39.54	49.46
		FEM [150]	16.51	21.08	32.61	39.75	39.75	51.07
	FG-O	IGA	14.83	19.48	31.01	39.54	39.54	38.48
		FEM [150]	14.78	19.46	30.90	39.75	39.75	47.34
	FG-X	IGA	22.08	25.24	34.63	39.54	39.54	50.99
		FEM [150]	21.64	25.35	35.93	39.75	39.75	54.06
0.02	UD	IGA	21.29	24.93	35.67	55.28	78.46	80.08
		FEM [150]	21.35	25.29	36.26	55.60	78.11	80.01
	FG-V	IGA	17.87	22.22	34.01	54.41	66.43	68.50
		FEM [150]	17.99	22.64	34.66	54.83	66.55	68.94
	FG-O	IGA	15.70	20.45	32.84	53.66	58.49	60.80
		FEM [150]	15.80	20.56	32.50	52.18	58.74	61.27
	FG-X	IGA	25.52	28.61	38.31	56.98	85.79	92.22
		FEM [150]	25.55	29.19	39.83	59.33	87.81	91.29

Table 7.5. The first six non-dimensional frequency parameters of the SSSS CNTRC plate with $V_{CNT}^* = 0.17$

h/a	Type	Method	Mode					
			1	2	3	4	5	6
0.1	UD	IGA	17.40	22.35	24.30	24.30	34.39	43.35
		FEM [150]	16.81	22.06	24.33	24.33	34.44	40.63
	FG-V	IGA	15.78	21.32	24.30	24.30	33.94	41.34
		FEM [150]	15.46	21.30	24.51	24.51	34.27	39.26
	FG-O	IGA	14.56	20.51	24.30	24.30	33.56	39.59
		FEM [150]	14.28	20.09	24.51	24.51	32.76	37.76
	FG-X	IGA	18.96	23.45	24.30	24.30	34.95	44.90
		FEM [150]	18.27	23.54	24.51	24.51	36.24	42.15
0.05	UD	IGA	21.62	26.48	39.56	48.61	48.61	60.86
		FEM [150]	21.45	26.70	40.40	48.67	48.67	62.72
	FG-V	IGA	18.63	24.32	38.42	48.61	48.61	60.40
		FEM [150]	18.63	24.73	39.47	49.02	49.02	59.19
	FG-O	IGA	16.62	22.81	37.50	48.61	48.61	55.25
		FEM [150]	16.62	22.73	37.13	49.02	49.02	54.36
	FG-X	IGA	25.04	29.26	41.36	48.61	48.61	61.90
		FEM [150]	24.76	29.81	43.61	49.02	49.02	66.61
0.02	UD	IGA	23.52	28.44	42.36	67.01	87.32	89.56
		FEM [150]	23.69	28.98	43.16	67.47	87.38	90.03
	FG-V	IGA	19.77	25.62	40.78	66.31	73.56	76.44
		FEM [150]	19.98	26.20	41.64	66.94	74.03	77.34
	FG-O	IGA	17.39	23.75	39.57	64.62	65.57	57.83
		FEM [150]	17.54	23.78	38.85	63.17	65.15	68.57
	FG-X	IGA	28.22	32.41	45.09	68.72	103.3	104.6
		FEM [150]	28.41	33.43	47.54	72.57	102.9	105.3

Table 7.6. The first six non-dimensional frequency parameters of the CCCC CNTRC plate with $V_{CNT}^* = 0.11$

h/a	Type	Method	Mode					
			1	2	3	4	5	6
0.1	UD	IGA	19.47	24.65	35.23	37.29	38.03	41.07
		FEM [150]	17.62	23.04	33.59	33.72	37.01	37.31
	FG-V	IGA	18.81	24.22	35.02	37.04	37.33	40.26
		FEM [150]	17.21	22.81	33.07	33.55	36.52	37.43
	FG-O	IGA	18.19	23.81	34.82	36.17	37.33	39.55
		FEM [150]	16.70	22.25	32.37	32.85	35.80	37.44
	FG-X	IGA	19.99	25.02	35.42	37.33	38.83	41.73
		FEM [150]	18.08	23.06	34.33	34.46	37.44	37.78
0.05	UD	IGA	30.39	34.82	45.82	64.01	65.38	67.82
		FEM [150]	28.40	33.11	44.55	59.19	61.85	63.04
	FG-V	IGA	27.70	32.65	44.37	61.23	63.17	63.99
		FEM [150]	26.30	31.49	43.58	56.24	59.22	62.60
	FG-O	IGA	25.59	30.93	43.20	57.72	60.74	62.45
		FEM [150]	24.48	29.79	41.89	53.55	56.61	58.74
	FG-X	IGA	32.90	36.96	47.37	65.02	68.98	71.20
		FEM [150]	30.42	35.03	46.48	61.98	64.56	65.17
0.02	UD	IGA	40.33	44.43	55.89	78.24	101.5	103.7
		FEM [150]	39.73	43.87	54.76	74.48	98.29	100.5
	FG-V	IGA	34.41	39.27	52.07	75.79	87.87	90.64
		FEM [150]	34.16	39.04	51.20	72.20	86.29	89.05
	FG-O	IGA	30.45	35.84	49.53	74.08	78.41	81.42
		FEM [150]	30.30	35.44	47.87	58.84	77.46	80.46
	FG-X	IGA	47.23	50.74	60.96	81.88	116.1	117.4
		FEM [150]	45.16	49.93	60.93	60.22	108.6	110.9

Table 7.7. The first six non-dimensional frequency parameters of the CCCC CNTRC plate with $V_{CNT}^* = 0.14$

h/a	Type	Method	Mode					
			1	2	3	4	5	6
0.1	UD	IGA	20.11	25.31	25.99	37.95	39.15	42.18
		FEM [150]	18.12	23.57	34.25	34.65	37.92	37.92
	FG-V	IGA	19.51	24.91	35.79	37.98	38.24	41.43
		FEM [150]	17.79	23.41	34.10	34.27	37.53	38.15
	FG-O	IGA	18.96	24.54	35.62	37.45	37.99	40.79
		FEM [150]	17.31	22.78	33.41	33.41	36.78	38.16
	FG-X	IGA	20.56	25.62	36.14	37.99	39.87	42.76
		FEM [150]	18.59	24.24	35.22	35.41	38.16	38.78
0.05	UD	IGA	32.26	36.58	47.47	65.71	68.49	70.86
		FEM [150]	29.91	34.51	45.89	61.62	64.19	64.49
	FG-V	IGA	29.62	34.40	45.97	64.56	64.81	67.21
		FEM [150]	27.92	32.97	44.98	58.95	61.81	64.13
	FG-O	IGA	27.51	32.66	44.77	61.23	64.07	64.11
		FEM [150]	25.12	31.18	43.03	56.40	59.27	61.79
	FG-X	IGA	34.63	38.62	48.96	66.68	71.81	73.97
		FEM [150]	31.85	36.48	48.08	64.33	66.91	67.14
0.02	UD	IGA	44.51	48.37	59.38	81.41	110.8	112.8
		FEM [150]	43.58	47.47	57.96	77.39	106.3	106.4
	FG-V	IGA	38.01	42.58	54.96	78.45	96.50	98.98
		FEM [150]	37.56	42.17	53.96	74.78	94.02	96.57
	FG-O	IGA	33.67	38.76	52.05	76.46	86.36	89.15
		FEM [150]	33.36	38.14	50.05	70.64	84.79	87.51
	FG-X	IGA	51.89	55.19	65.00	85.52	121.0	125.8
		FEM [150]	50.40	54.02	64.11	83.39	112.8	119.1

Table 7.8. The first six non-dimensional frequency parameters of the CCCC CNTRC plate with $V_{CNT}^* = 0.17$

h/a	Type	Method	Mode					
			1	2	3	4	5	6
0.1	UD	IGA	24.29	30.80	44.05	46.66	47.48	51.30
		FEM [150]	22.01	28.90	42.01	42.13	46.25	46.69
	FG-V	IGA	23.43	30.24	43.79	46.20	46.71	50.25
		FEM [150]	21.54	28.61	41.43	42.11	45.79	47.05
	FG-O	IGA	22.65	29.73	43.57	45.10	46.72	49.37
		FEM [150]	20.83	27.65	40.05	40.78	44.69	47.07
	FG-X	IGA	24.97	31.26	44.26	46.72	48.51	52.13
		FEM [150]	22.74	29.87	43.29	43.58	47.07	47.60
0.05	UD	IGA	37.74	43.33	57.16	79.97	81.39	84.46
		FEM [150]	35.31	41.25	55.62	73.76	77.10	78.80
	FG-V	IGA	34.30	40.56	55.34	76.01	78.95	79.52
		FEM [150]	32.68	39.27	54.56	70.14	73.92	78.52
	FG-O	IGA	31.64	38.41	53.89	71.56	75.41	78.10
		FEM [150]	30.32	36.84	51.75	66.65	70.40	75.01
	FG-X	IGA	40.93	46.04	59.11	81.21	85.98	88.76
		FEM [150]	38.06	44.10	58.92	77.64	81.04	82.93
0.02	UD	IGA	49.77	54.98	69.44	97.56	125.5	128.3
		FEM [150]	49.07	54.32	68.06	92.86	121.6	124.5
	FG-V	IGA	42.32	48.51	64.72	94.57	108.3	111.7
		FEM [150]	42.07	48.30	63.75	90.29	106.5	110.0
	FG-O	IGA	37.44	44.30	61.62	92.49	96.47	100.3
		FEM [150]	37.24	43.57	58.89	84.71	95.46	99.14
	FG-X	IGA	58.40	62.84	75.74	102.0	143.9	146.2
		FEM [150]	57.24	62.23	75.74	100.8	137.9	138.4

In this example, the CNTRC model is similar to section 7.3.1. A non-dimensional frequency parameter $\bar{\omega} = (\omega a^2 / h) \sqrt{\rho^m / E^m}$ is used. Firstly, Figure 7.4 shows the first six non-dimensional natural frequencies of CNTRC plates with $h/a = 0.1$ and $V_{CNT}^* = 0.11$ for four types of CNTRC: UD, FG-V, FG-O and FG-X. It can be seen that the results of the present method match well with those of FEM [150] for the SSSS and CCCC plate. In addition, Table 7.3 to Table 7.5 present the six lowest non-dimensional frequencies of the SSSS and Table 7.6 to Table 7.8 present the those of CCCC plate with $h/a = 0.02, 0.05, 0.1$. Again, it can be seen that the results of IGA agree with those of FEM [150].

7.3.2.2 A circular plate

We consider a CNTRC circular plate (radius R , thickness h) as shown in Figure 7.5a. A non-dimensional frequency parameter $\bar{\omega} = (\omega R^2 / h) \sqrt{\rho^m / E^m}$ is used. The effect of ratios $2R/h$ on the first three non-dimensional frequencies of plate with a mesh of 18×18 quadratic (Figure 7.5b) is shown in Figure 7.6. It can be observed that when ratio $2R/h$ increases, the frequency increases. Figure 7.7 shows the shape of the first six eigenmodes of a simply supported CNTRC circle plate with $2R/h = 10$. Again, we can see that these shapes reflect correctly the expected physical modes of CNTRC plates.

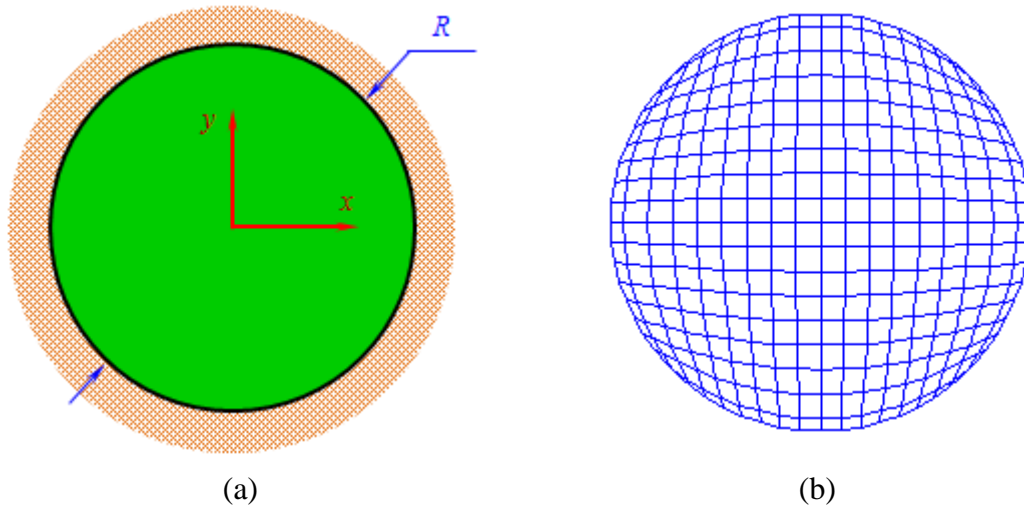
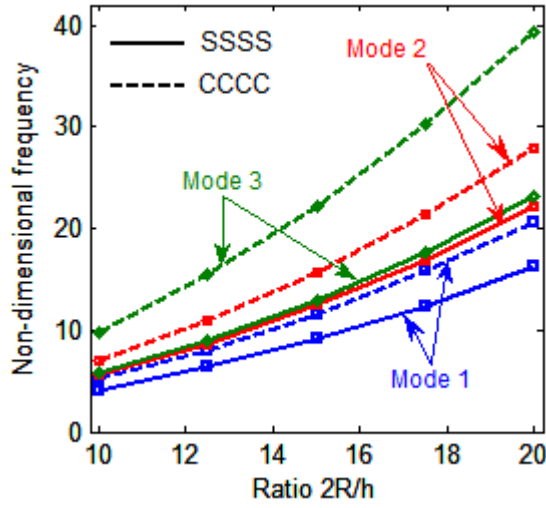
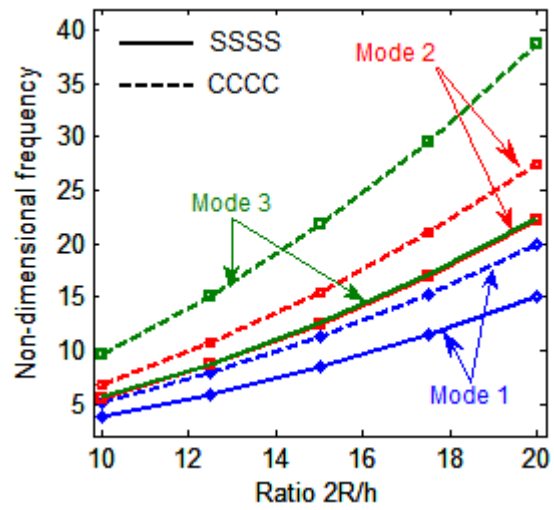


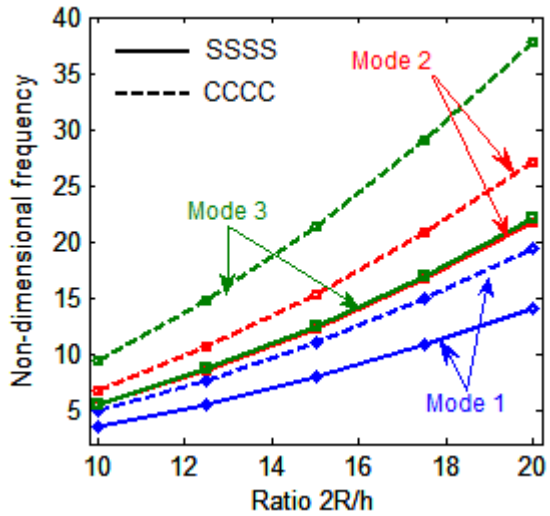
Figure 7.5. (a) Circular FG-CNTRC composite plate model; (b) meshing of 18×18 cubic elements.



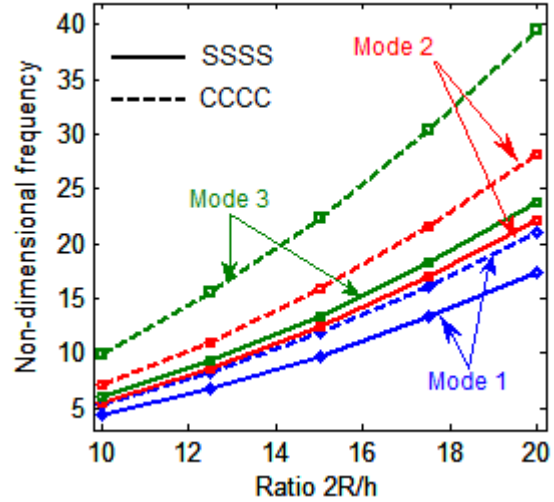
(a) UD CNTRC



(b) FG-V CNTRC



(b) FG-O CNTRC



(b) FG-X CNTRC

Figure 7.6. Effects of ratios $2R/h$ on non-dimensional frequency of CNTRC circle plate with $V_{CNT}^* = 0.11$.

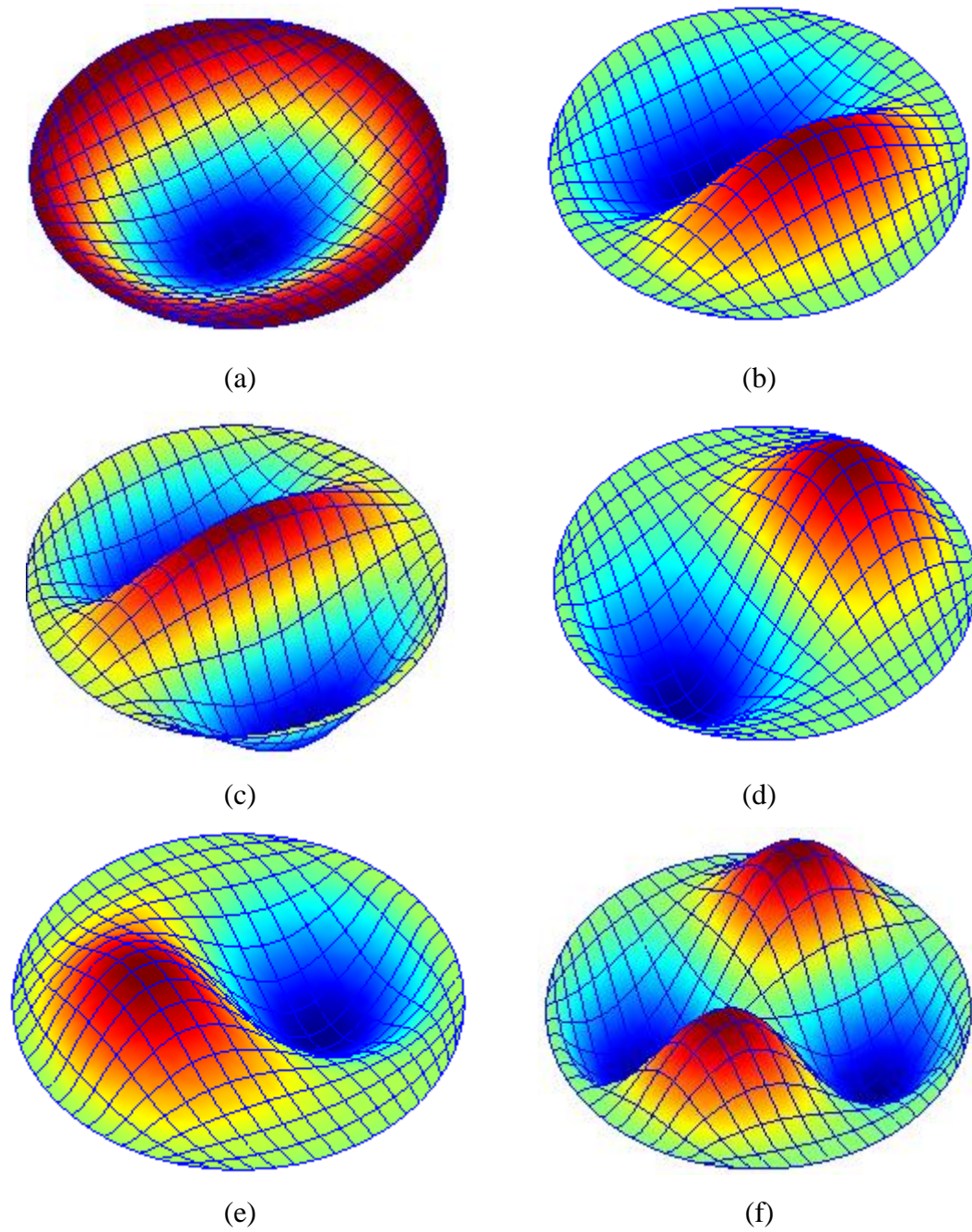


Figure 7.7. Shape of the first six eigenmodes of a simply supported CNTRC circle plate with $2R/h = 10$: (a) mode 1, (b) mode 2, (c) mode 3, (d) mode 4, (e) mode 5 and (f) mode 6.

7.3.3 Time-dependent dynamic analysis of CNTRC plates

We now examine the time-dependent dynamic responses of the simply supported CNTRC plate subjected to a transverse load, which is sinusoidally distributed in spatial domain and varies with time as:

$$q = q_0 \sin\left(\frac{\pi x}{a}\right) \sin\left(\frac{\pi y}{a}\right) F(t) \quad (7.27)$$

Where

$$F(t) = \begin{cases} \text{step loading} & \begin{cases} 1 & 0 \leq t \leq t_1 \\ 0 & t > t_1 \end{cases} \\ \text{triangular loading} & \begin{cases} 1 - \frac{t}{t_1} & 0 \leq t \leq t_1 \\ 0 & t > t_1 \end{cases} \\ \text{sine loading} & \begin{cases} \sin(\frac{\pi t}{t_1}) & 0 \leq t \leq t_1 \\ 0 & t > t_1 \end{cases} \\ \text{explosive blast loading} & \begin{cases} e^{\gamma t} \end{cases} \end{cases} \quad (7.28)$$

in which $t_1 = 0.006\text{s}$, $\gamma = 330\text{s}^{-1}$, $q_0 = 3.448\text{MPa}$. The CNTRC model is similar to that presented in section 5.1 with $h/a = 0.02$ and $V_{CNT}^* = 0.11$. Figure 7.9 to Figure 7.11 show the time histories of central deflection of UD, FG-V, FG-O and FG-X plate under step, triangular, sine, explosive blast loadings, respectively. It is again observed that the central deflections of UD and FG-X plate are smaller than those of FG-O and FG-V plate. Note that, in Figure 7.9 to Figure 7.10, we can see that the responses of plate are separated into two states. In the first state, the plate is subjected to the transverse load (forced vibration). In this state, the response of central deflection of plate belong to type of loadings, which is step, triangular, sine or explosive blast loading. And in the second state, the plate oscillates freely (free vibration) and the vibration amplitude of plate is harmonic.

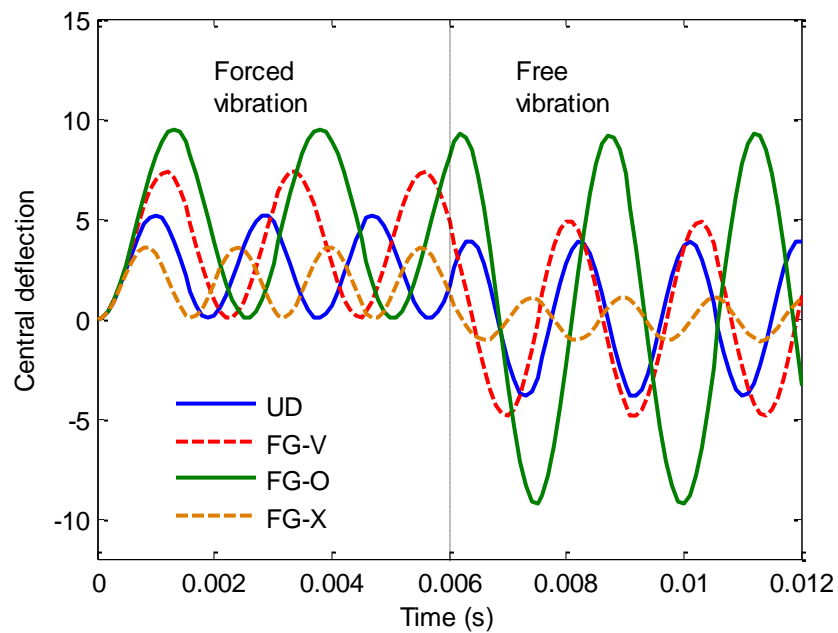


Figure 7.8. Central deflection of the square laminated plate subjected to step loading.

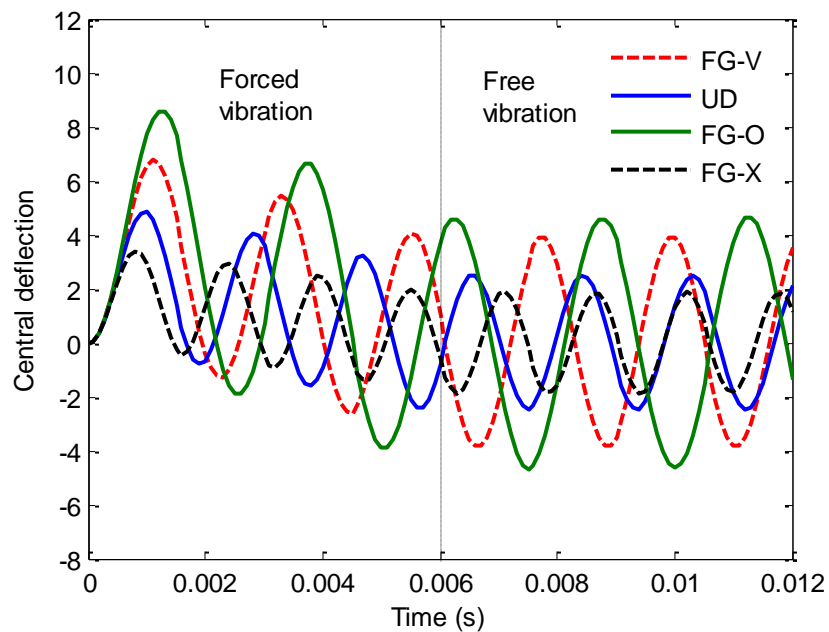


Figure 7.9. Central deflection of the square laminated plate subjected to triangular loading.

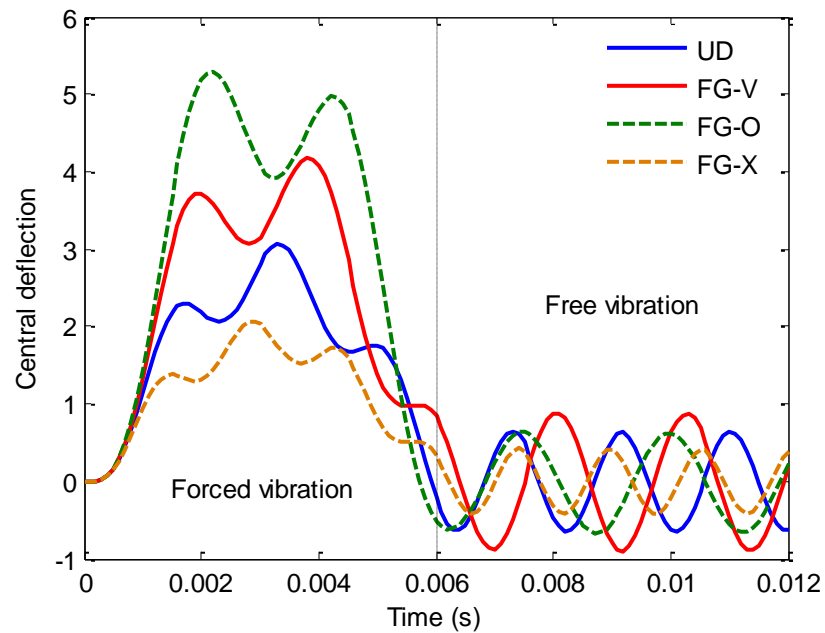


Figure 7.10. Central deflection of the square laminated plate subjected to sinusoidal loading.

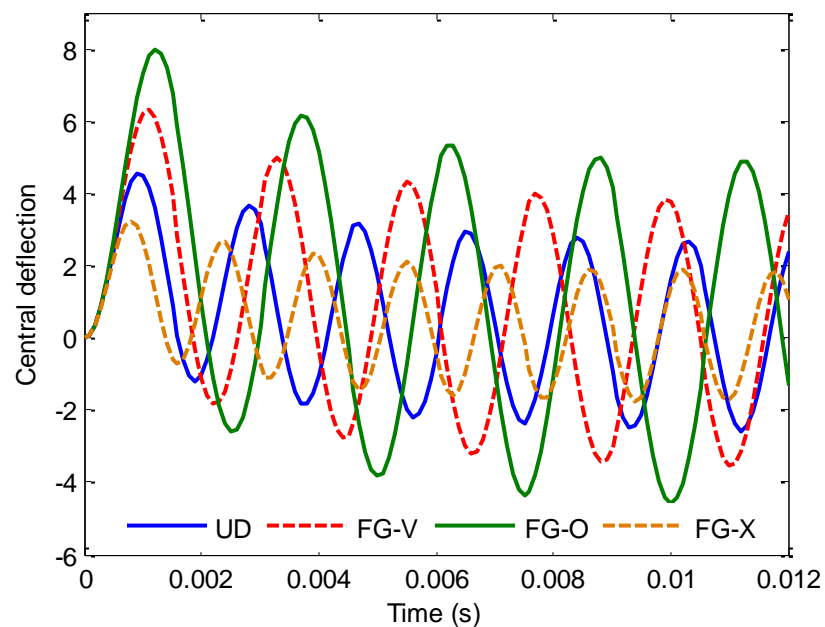


Figure 7.11. Central deflection of the square laminated plate subjected to explosive blast loading.

7.4 Concluding remarks

In this chapter, we presented a simple and effective approach based on the combination of IGA and HSDT for static, free vibration and dynamic behaviors of FG-CNTRCs. The material properties of FG-CNTRCs are assumed to be graded through the thickness direction according to several linear distributions of the volume fraction of carbon nanotubes. The governing equation is approximated according to the HSDT model using isogeometric elements based on Non-Uniform Rational B-Spline (NURBS) basis functions. These achieve naturally any desired degree of continuity through the choice of the order of basis functions, so that the method easily fulfils the C^1 -continuity requirement of the HSDT model. In this model, no shear correction factor is used, which leads to zero-shear stresses at the bottom and top surfaces of plates. The effects of carbon nanotube volume fraction, plate width-to-thickness ratio on natural frequencies and deflections of FG-CNTRC plates are considered. Especially, the distributions of CNTs along the thickness direction of the plate have a large influence on the central deflection of the plate. And thickness-to-length ratios are sensitive and also have a large effect on responses of the plates. When a plate becomes thinner, the deflection is larger. In dynamic transient, deflections of FG-X are the smallest and those of FG-O are the largest. In addition, after removing external forces, the plates are harmonically oscillated, as expected. Numerical results proved high accuracy and reliability of the proposed method in comparison with other available numerical approaches.

Chapter 8

*The generalized unconstrained
plate theory*

8.1 Overview

In this chapter, the last objective of this thesis is dealt with. An efficient computational approach based on a generalized unconstrained approach in conjunction with IGA are proposed for dynamic control of smart piezoelectric composite plates. In composite plates, the mechanical displacement field is approximated according to the proposed model using isogeometric elements and the nonlinear transient formulation for plates is formed in the total Lagrange approach based on the von Kármán strains and solved by Newmark time integration. Various numerical examples are investigated to show the high accuracy and reliability of the proposed method. Linear, geometrically nonlinear analysis, dynamic control and optimization are studied. For active control of the piezoelectric composite plates, a close-loop system, which is presented in section 5.3, is used. An optimization procedure using genetic algorithm (GA) is considered to search optimal design for actuator input voltages.

8.2 The unconstrained third-order shear deformation theory

In section 3.3, it can be seen that CPT and FSDT [187,188] are the simplest and commonly used. In FSDT [187,188], displacement field is assumed to have the first-order functions and the shear correction factor is required for attenuating the non-zero transverse shear strain on the bottom and top surfaces. In TDST [191], shear stresses are a parabolic distribution through the thickness and equal to zeros on the top and bottom surfaces. To consider shear traction parallel and without any correction factors, an Unconstrained Third-Order Shear Deformation Theory (UTSDT) was proposed by Leung [117,118]. The presence of a finite transverse shear strain on the top and bottom surfaces of the plate is allowed in this theory, releasing the additional constraint, which has to be imposed in the TSDT of Reddy. There are seven displacements, such as two in-plane displacements, one transverse displacement, two linear rotations and two cubic variations of in-plane displacements that are higher-order rotations. Comparisons between UTSDT and both TSDT and analytical analysis of Pagano [214,215] were also reported in Refs. [117,118]. In this chapter, IGA is extended to investigate the piezoelectric composite plates using UTSDT.

The UTSDT can be rewritten in a general form using an arbitrary function $f(z)$ as follows:

$$\begin{aligned} u(x, y, z, t) &= u_0(x, y, t) + zu_1(x, y, t) + f(z)u_2(x, y, t) \\ v(x, y, z, t) &= v_0(x, y, t) + zv_1(x, y, t) + f(z)v_2(x, y, t) \\ w(x, y, z, t) &= w(x, y, t) \end{aligned} \quad (8.1)$$

Where $u_0, u_1, u_2, v_0, v_1, v_2$ and w are displacement variables; x, y, z are components of the Cartesian coordinate system ($Oxyz$) and t is the time. For UTSDT in Ref. [117], the function $f(z) = z^3$ is used. Generally speaking, $f(z)$ can be defined as a continuous function so that its first derivative is nonlinear through the plate thickness. Moreover, there exists an optimal function $f_{op}(z)$ yielding best accurate solutions. However, the finding of $f_{op}(z)$ remains an open question. In what follows, we introduce a new function $f(z) = \arctan(z)$ that ensures that its first derivative is nonlinear through the plate thickness and solutions are more accurate than those for the case of $f(z) = z^3$.

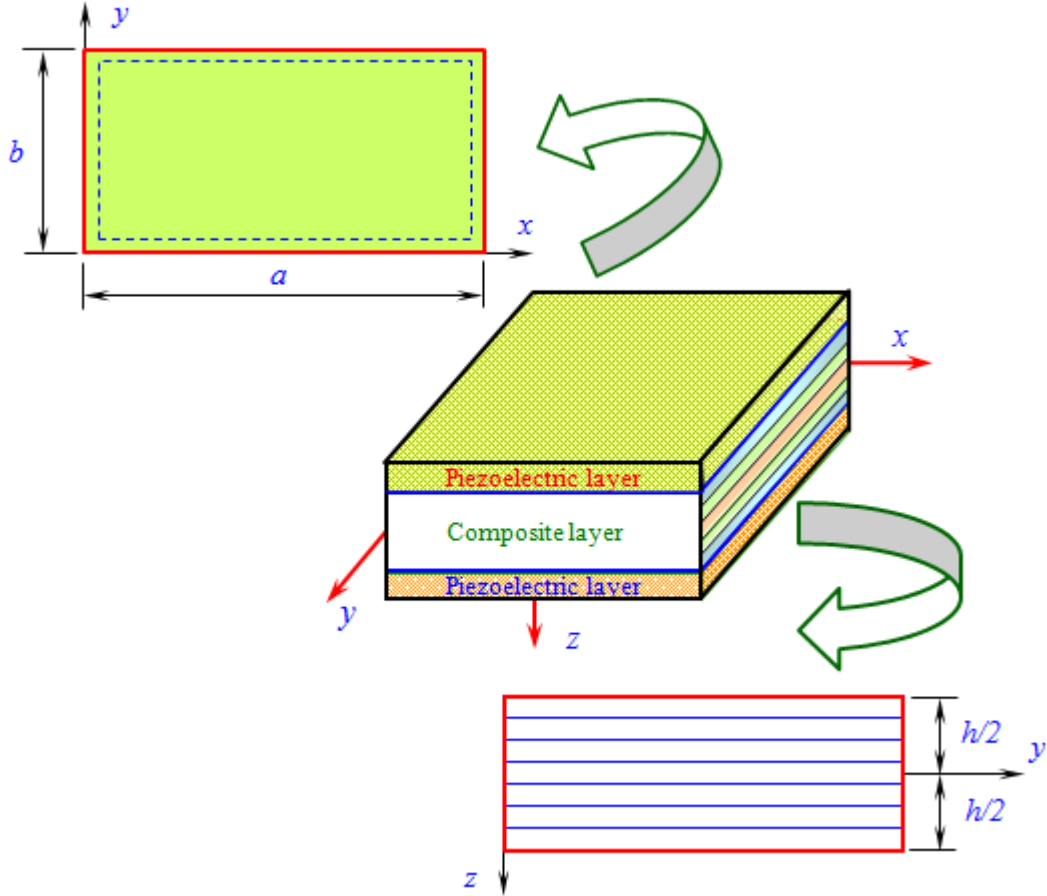


Figure 8.1. The configuration of piezoelectric composite plates.

For a plate bending, the strain vector is represented by:

$$\varepsilon_{ij} = \frac{1}{2} \left(\frac{\partial u_i}{\partial x_j} + \frac{\partial u_j}{\partial x_i} \right) + \frac{1}{2} \frac{\partial u_k}{\partial x_i} \frac{\partial u_k}{\partial x_j} \quad (8.2)$$

Following the Von Kármán theory, Eq. (8.2) can be rewritten as:

$$\begin{aligned} \boldsymbol{\varepsilon}_p &= \boldsymbol{\varepsilon}_m + z\boldsymbol{\varepsilon}_1 + f(z)\boldsymbol{\varepsilon}_2 \\ \boldsymbol{\varepsilon}^s &= \boldsymbol{\varepsilon}_0^s + f'(z)\boldsymbol{\varepsilon}_1^s \end{aligned} \quad (8.3)$$

Where

$$\begin{aligned} \boldsymbol{\varepsilon}_m &= \begin{bmatrix} u_{0,x} \\ v_{0,y} \\ u_{0,y} + v_{0,x} \end{bmatrix} + \frac{1}{2} \begin{bmatrix} w_{,x}^2 \\ w_{,y}^2 \\ 2w_{,xy} \end{bmatrix} = \boldsymbol{\varepsilon}_L + \boldsymbol{\varepsilon}_{NL}, \quad \boldsymbol{\varepsilon}_1 = \begin{bmatrix} u_{1,x} \\ v_{1,y} \\ u_{1,y} + v_{1,x} \end{bmatrix}, \quad \boldsymbol{\varepsilon}_2 = \begin{bmatrix} u_{2,x} \\ v_{2,y} \\ u_{2,y} + v_{2,x} \end{bmatrix}, \\ \boldsymbol{\varepsilon}_0^s &= \begin{bmatrix} u_1 + w_{,x} \\ v_1 + w_{,y} \end{bmatrix}, \quad \boldsymbol{\varepsilon}_1^s = \begin{bmatrix} u_2 \\ v_2 \end{bmatrix} \end{aligned} \quad (8.4)$$

in which the nonlinear component is computed as:

$$\boldsymbol{\varepsilon}_{NL} = \frac{1}{2} \begin{bmatrix} w_{,x} & 0 \\ 0 & w_{,y} \\ w_{,y} & w_{,x} \end{bmatrix} \begin{Bmatrix} w_{,x} \\ w_{,y} \end{Bmatrix} = \frac{1}{2} \mathbf{A}_\theta \boldsymbol{\theta} \quad (8.5)$$

The material behavior of the smart composite plates is given in Eq. (3.1), where \mathbf{c} is the elasticity matrix defined as follows:

$$\mathbf{c} = \begin{bmatrix} \mathbf{A} & \mathbf{B} & \mathbf{L} & \mathbf{0} & \mathbf{0} \\ \mathbf{B} & \mathbf{G} & \mathbf{F} & \mathbf{0} & \mathbf{0} \\ \mathbf{L} & \mathbf{F} & \mathbf{H} & \mathbf{0} & \mathbf{0} \\ \mathbf{0} & \mathbf{0} & \mathbf{0} & \mathbf{A}_s & \mathbf{B}_s \\ \mathbf{0} & \mathbf{0} & \mathbf{0} & \mathbf{B}_s & \mathbf{D}_s \end{bmatrix} \quad (8.6)$$

In which

$$\begin{aligned} (\mathbf{A}, \mathbf{B}, \mathbf{G}, \mathbf{L}, \mathbf{F}, \mathbf{H}) &= \int_{-h/2}^{h/2} (1, z, z^2, f(z), zf(z), f^2(z)) \bar{Q}_{ij} dz \quad i, j = 1, 2, 6 \\ (\mathbf{A}_s, \mathbf{B}_s, \mathbf{D}_s) &= \int_{-h/2}^{h/2} (1, f'(z), (f'(z))^2) \bar{Q}_{ij} dz \quad i, j = 4, 5 \end{aligned} \quad (8.7)$$

where \bar{Q}_{ij} is calculated as in Eqs. (3.8)-(3.9).

8.3 NURBS-based novel smart plate formulation

The displacement field \mathbf{u} of the plate using NURBS basic function is approximated as:

$$\mathbf{u}^h(\xi, \eta) = \sum_{I=1}^{m \times n} R_I(\xi, \eta) \mathbf{d}_I \quad (8.8)$$

Where $\mathbf{d}_I = [u_{0I} \quad v_{0I} \quad u_{1I} \quad v_{1I} \quad u_{2I} \quad v_{2I} \quad w_I]^T$, and N_I is the shape function.

Substituting Eq. (8.8) into Eqs. (8.3) to (8.5), the strains can be rewritten as:

$$\bar{\boldsymbol{\varepsilon}} = [\boldsymbol{\varepsilon}_p \quad \boldsymbol{\varepsilon}_s]^T = \sum_{I=1}^{m \times n} \left(\mathbf{B}_I^L + \frac{1}{2} \mathbf{B}_I^{NL} \right) \mathbf{d}_I \quad (8.9)$$

Where $\mathbf{B}_I^L = [\mathbf{B}_I^0 \quad \mathbf{B}_I^1 \quad \mathbf{B}_I^2 \quad \mathbf{B}_I^{s0} \quad \mathbf{B}_I^{s1}]^T$, in which

$$\begin{aligned} \mathbf{B}_I^0 &= \begin{bmatrix} N_{I,x} & 0 & 0 & 0 & 0 & 0 & 0 \\ 0 & N_{I,y} & 0 & 0 & 0 & 0 & 0 \\ N_{I,y} & N_{I,x} & 0 & 0 & 0 & 0 & 0 \end{bmatrix}, \quad \mathbf{B}_I^1 = \begin{bmatrix} 0 & 0 & N_{I,x} & 0 & 0 & 0 & 0 \\ 0 & 0 & 0 & N_{I,y} & 0 & 0 & 0 \\ 0 & 0 & N_{I,y} & N_{I,x} & 0 & 0 & 0 \end{bmatrix}, \\ \mathbf{B}_I^2 &= \begin{bmatrix} 0 & 0 & 0 & 0 & N_{I,x} & 0 & 0 \\ 0 & 0 & 0 & 0 & 0 & N_{I,y} & 0 \\ 0 & 0 & 0 & 0 & N_{I,y} & N_{I,x} & 0 \end{bmatrix}, \\ \mathbf{B}_I^{s0} &= \begin{bmatrix} 0 & 0 & N_I & 0 & 0 & 0 & N_{I,x} \\ 0 & 0 & 0 & N_I & 0 & 0 & N_{I,y} \end{bmatrix}, \quad \mathbf{B}_I^{s1} = \begin{bmatrix} 0 & 0 & 0 & 0 & N_I & 0 & 0 \\ 0 & 0 & 0 & 0 & 0 & N_I & 0 \end{bmatrix} \end{aligned} \quad (8.10)$$

and \mathbf{B}_I^{NL} is calculated by:

$$\mathbf{B}_I^{NL}(\mathbf{d}) = \begin{bmatrix} w_{I,x} & 0 \\ 0 & w_{I,y} \\ w_{I,y} & w_{I,x} \end{bmatrix} \begin{bmatrix} 0 & 0 & 0 & 0 & 0 & 0 & N_{I,x} \\ 0 & 0 & 0 & 0 & 0 & 0 & N_{I,x} \end{bmatrix} = \mathbf{A}_\theta \mathbf{B}_I^g \quad (8.11)$$

The equations for the smart plate are written as:

$$\begin{bmatrix} \mathbf{M}_{uu} & 0 \\ 0 & 0 \end{bmatrix} \begin{bmatrix} \ddot{\mathbf{d}} \\ \ddot{\boldsymbol{\phi}} \end{bmatrix} + \begin{bmatrix} \mathbf{K}_{uu} & \mathbf{K}_{u\phi} \\ \mathbf{K}_{\phi u} & \mathbf{K}_{\phi\phi} \end{bmatrix} \begin{bmatrix} \mathbf{d} \\ \boldsymbol{\phi} \end{bmatrix} = \begin{bmatrix} \mathbf{f} \\ \mathbf{Q} \end{bmatrix} \Leftrightarrow \bar{\mathbf{M}}\ddot{\mathbf{q}} + \bar{\mathbf{K}}\mathbf{q} = \bar{\mathbf{f}} \quad (8.12)$$

Where

$$\begin{aligned} \mathbf{K}_{uu} &= \int_{\Omega} (\mathbf{B}^L + \mathbf{B}^{NL})^T \mathbf{c} (\mathbf{B}^L + \frac{1}{2} \mathbf{B}^{NL}) d\Omega \quad ; \quad \mathbf{K}_{u\phi} = \int_{\Omega} (\mathbf{B}^L)^T \mathbf{e}^T \mathbf{B}_{\phi} d\Omega \\ \mathbf{K}_{\phi\phi} &= \int_{\Omega} \mathbf{B}_{\phi}^T \mathbf{p} \mathbf{B}_{\phi} d\Omega \quad ; \quad \mathbf{M}_{uu} = \int_{\Omega} \tilde{\mathbf{N}}^T \mathbf{m} \tilde{\mathbf{N}} d\Omega \quad ; \quad \mathbf{f} = \int_{\Omega} \bar{q}_0 \bar{\mathbf{N}} d\Omega \end{aligned} \quad (8.13)$$

in which q_0 is a uniform load; $\bar{\mathbf{N}} = [0 \quad 0 \quad 0 \quad 0 \quad 0 \quad 0 \quad N_I]$; \mathbf{m} is defined by:

$$\mathbf{m} = \begin{bmatrix} I_1 & I_2 & I_4 \\ I_2 & I_3 & I_5 \\ I_4 & I_5 & I_7 \end{bmatrix}, \quad (I_1, I_2, I_3, I_4, I_5, I_7) = \int_{-h/2}^{h/2} \rho (1, z, z^2, f(z), zf(z), f^2(z)) dz \quad (8.14)$$

and

$$\begin{aligned} \tilde{\mathbf{N}} &= \begin{Bmatrix} \mathbf{N}_1 \\ \mathbf{N}_2 \\ \mathbf{N}_3 \end{Bmatrix}, \quad \mathbf{N}_1 = \begin{bmatrix} N_I & 0 & 0 & 0 & 0 & 0 \\ 0 & N_I & 0 & 0 & 0 & 0 \\ 0 & 0 & 0 & 0 & 0 & N_I \end{bmatrix}, \\ \mathbf{N}_2 &= \begin{bmatrix} 0 & 0 & N_I & 0 & 0 & 0 \\ 0 & 0 & 0 & N_I & 0 & 0 \\ 0 & 0 & 0 & 0 & 0 & 0 \end{bmatrix}, \quad \mathbf{N}_3 = \begin{bmatrix} 0 & 0 & 0 & 0 & N_I & 0 \\ 0 & 0 & 0 & 0 & 0 & N_I \\ 0 & 0 & 0 & 0 & 0 & 0 \end{bmatrix} \end{aligned} \quad (8.15)$$

8.4 Numerical validations

This section shows the performance of the method through various numerical examples. Table 3.1 shows the properties of the piezoelectric composite plates, including Poisson's ratio (ν), mass density (ρ), elastic modulus (E), piezoelectric coefficient (d) and electric permittivity (p) and shear modulus (G). Note that the properties 1, 2 and 3 in Table 3.1 refer to the directions of axes x , y and z , respectively.

8.4.1 Static and free vibration analyses

8.4.1.1 Static analysis

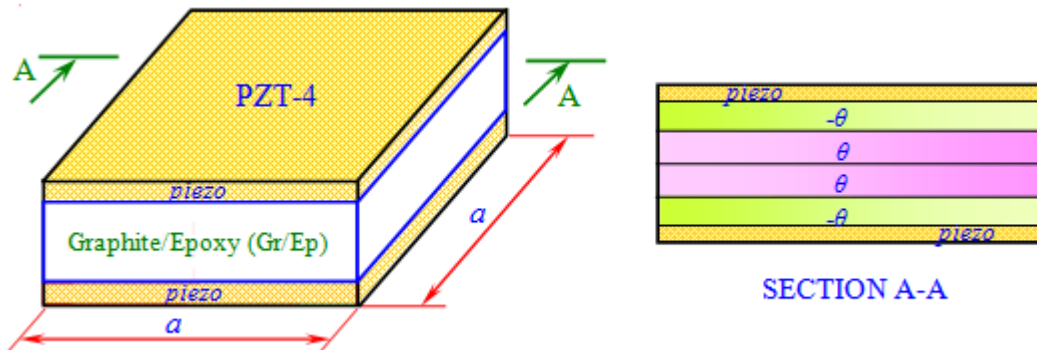


Figure 8.2. Square piezoelectric composite plate model.

Table 8.1. Central control point/node deflection of the simply supported piezoelectric composite plate subjected to a uniform load and different input voltages ($\times 10^{-4}$ m)

Input	Mesh	Method	Scheme			
			I	II	III	IV
0V	5×5	IGA-UTSDT ($p = 2$)	-0.5618	-0.5634	-0.5940	-0.6611
		IGA-UTSDT ($p = 3$)	-0.6390	-0.6260	-0.6635	-0.7467
	9×9	IGA-UTSDT ($p = 2$)	-0.6174	-0.6082	-0.6441	-0.7236
		IGA-UTSDT ($p = 3$)	-0.6373	-0.6240	-0.6618	-0.7453
	13×13	IGA-UTSDT ($p = 2$)	-0.6322	-0.6202	-0.6576	-0.7401
		IGA-UTSDT ($p = 3$)	-0.6370	-0.6239	-0.6617	-0.7452
		RPIM [91]	-0.6038	-0.6217	-0.6542	-0.7222
5V	5×5	IGA-UTSDT ($p = 2$)	-0.1619	-0.1627	-0.1712	-0.1898
		IGA-UTSDT ($p = 3$)	-0.2856	-0.2827	-0.2975	-0.3279
	9×9	IGA-UTSDT ($p = 2$)	-0.2512	-0.2494	-0.2625	-0.2899
		IGA-UTSDT ($p = 3$)	-0.2847	-0.2819	-2.9701	-0.3287
	13×13	IGA-UTSDT ($p = 2$)	-0.2766	-0.2741	-0.2888	-0.3194
		IGA-UTSDT ($p = 3$)	-0.2842	-0.2817	-0.2968	-0.3283
		RPIM [91]	-0.2717	-0.2717	-0.2862	-0.3134
10V	5×5	IGA-UTSDT ($p = 2$)	0.2379	0.2380	0.2514	0.2815
		IGA-UTSDT ($p = 3$)	0.0678	0.0600	0.0685	0.0909
	9×9	IGA-UTSDT ($p = 2$)	0.1150	0.1093	0.1191	0.1437
		IGA-UTSDT ($p = 3$)	0.0680	0.0601	0.0677	0.0880
	13×13	IGA-UTSDT ($p = 2$)	0.0791	0.0721	0.0801	0.1013
		IGA-UTSDT ($p = 3$)	0.0690	0.0605	0.0682	0.0880
		RPIM [91]	0.0757	0.0604	0.0819	0.0954

A square smart plate with length 200 mm under a uniform load $q = 100 \text{ N/m}^2$ plotted in Figure 8.2 is considered. The plate has six layers: two outer piezo layers represented by pie and four composite layers. The configurations of the plate are $[pie/-\theta/\theta]_s$ and $[pie/-\theta/\theta]_{as}$ where “ as ” and “ s ” indicate anti-symmetric and symmetric, respectively, and θ is the fiber orientation. Each layer thickness of the non-piezoelectric composite plate is

0.25 mm and the thickness of the piezo layer is 0.1 mm. The composite layers are made of T300/976 graphite/epoxy and the piezo-ceramic layers are PZTG1195N.

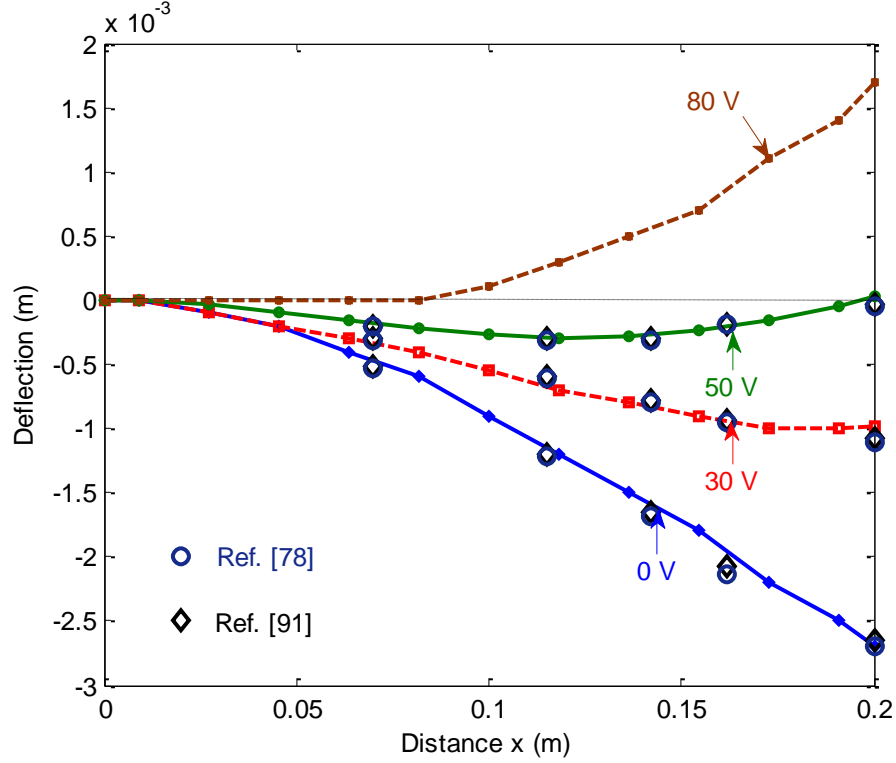


Figure 8.3. Effect of actuator input voltages on deflection of the piezoelectric composite plate $[pie/-45/45]_{as}$ subjected to a uniform loading.

Firstly, the effect of input voltages on deflection of the CFFF plate $[pie/-45/45]_{as}$ is shown in Figure 8.3. It can be seen that the present results agree well with those of Refs [91,78].

For the SSSS plate, different fiber orientation angles such as I: $[pie/-45/45]_s$, II: $[pie/-45/45]_{as}$, III: $[pie/-30/30]_{as}$ and IV: $[pie/-15/15]_{as}$ are investigated. Table 8.1 lists the central control point/node deflection of the plate. It can be seen that the results of IGA-UHSDT match well with those of Ref. [91]. In addition, the deflection of plate under different input voltages 0V, 5V, 8V, 10V is shown in Figure 8.4. The deflection decreases for increasing input voltage as expected. The reason is that the input voltage induces an upward deflection of the plate due to the piezoelectric effect. This upward contribution becomes prevalent for an input voltage of 10V. Similar results were obtained in Ref. [91]. Next, the centerline deflection of a plate with configurations [-

$45/pie/45]_{as}$ and $[-15/pie/15]_{as}$ is plotted in Figure 8.5. Again, we can see that the results in Figure 8.5a match well with those of RPIM in Ref. [91]. Also, as the fiber orientation angle decreases, the deflection of the plate increases.

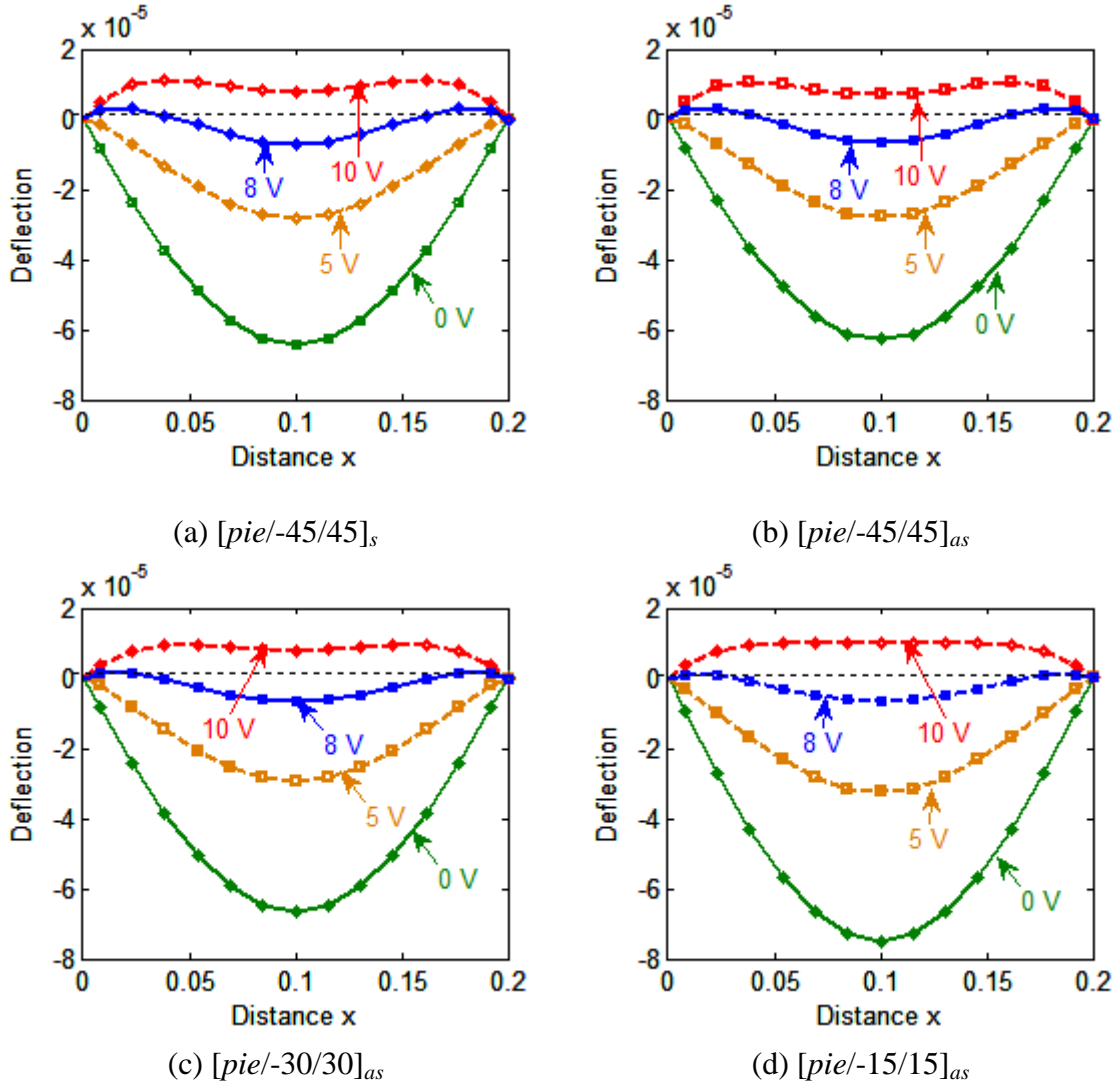


Figure 8.4. Centerline deflection of the plate subjected to different input voltages and a uniform load.

Furthermore, the deflection of the plate using only mesh of 9×9 elements with different boundary conditions (CFFF, SSFF, SSSS) is shown in Figure 8.6. Again, it can be seen that the present method agrees very well with those of RPIM [91].

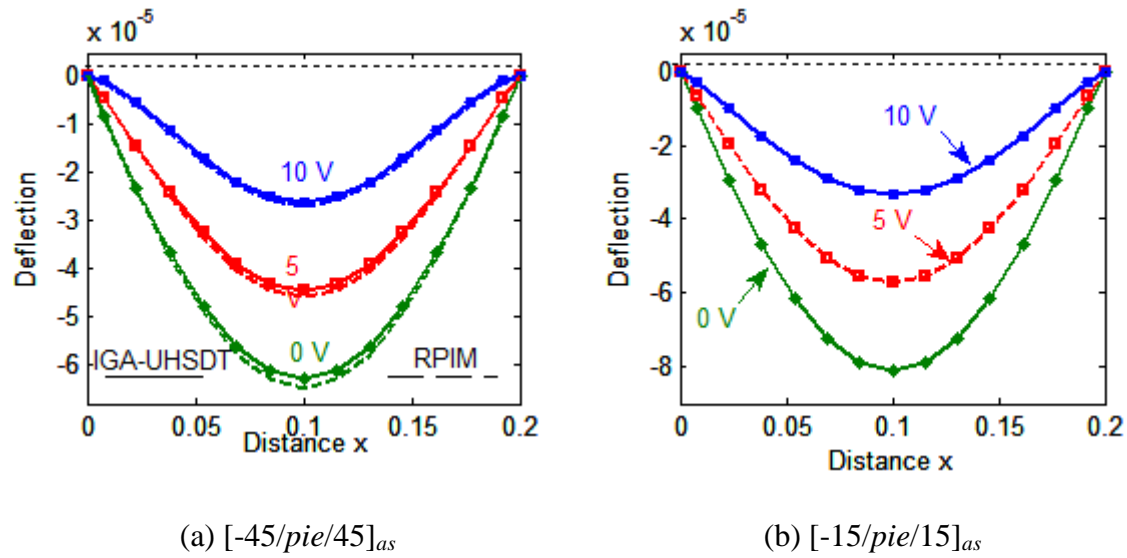


Figure 8.5. Effect of the stacking sequence scheme and the fiber orientations on deflection of piezoelectric composite plate under uniform load and different input voltages.

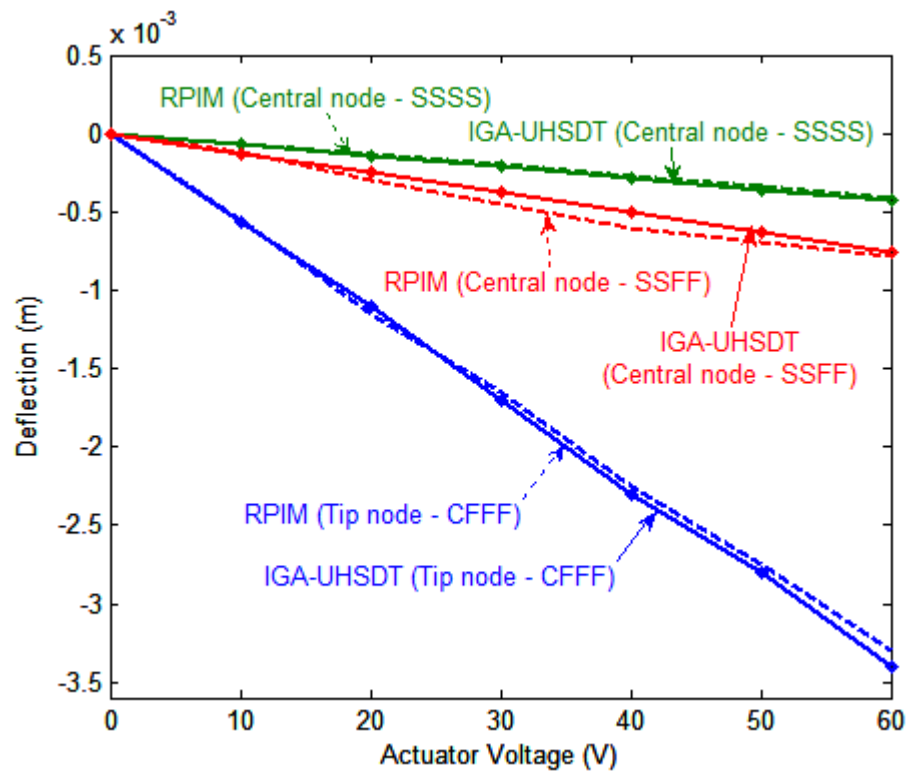


Figure 8.6. The deflection of the piezoelectric composite plates with various boundary conditions.

8.4.1.2 Free vibration

In this section, the accuracy of isogeometric finite elements is investigated in case of free vibration of plates. A SSSS plate $[pie/0/90/0/pie]$ (length a , thickness h and $h/a = 1/50$) is considered and shown in Figure 8.7. The composite layers are made of Gp/Ep and the thickness of two PZT-4 piezoelectric layers is $0.1h$. Two electric boundary conditions are investigated: (1) an open-circuit condition, where the electric potential remains free; and (2) a closed-circuit condition, in which the electric potential is kept zero (grounded). The analytical solution for the first natural frequency was studied by Heyliger and Saravanos [202]. Using finite element formulations, Victor et al. [94] and Saravanos et al. [116] have also reported to obtain different natural frequencies.

Table 8.2. Dimensionless first natural frequency of the simply supported square piezoelectric composite plate $[pie/0/90/0/pie]$

Method	Meshing	Degrees of freedom (DOFs)	$\bar{f} = \omega_1 a^2 / (1000t\sqrt{\rho})$	
			Closed circuit	Open circuit
IGA-UHSDT ($p=2$)	6 x 6	448	233.900	233.900
IGA-UHSDT ($p=3$)	6 x 6	567	231.400	231.400
IGA-UHSDT ($p=4$)	6 x 6	700	231.400	231.400
FEM layerwise [116]	12 x 12	2208	234.533	256.765
Q9 - HSDT [94]	-	-	230.461	250.597
Q9 - FSDT [94]	-	-	206.304	245.349
Reference solution [202]			245.941	245.942

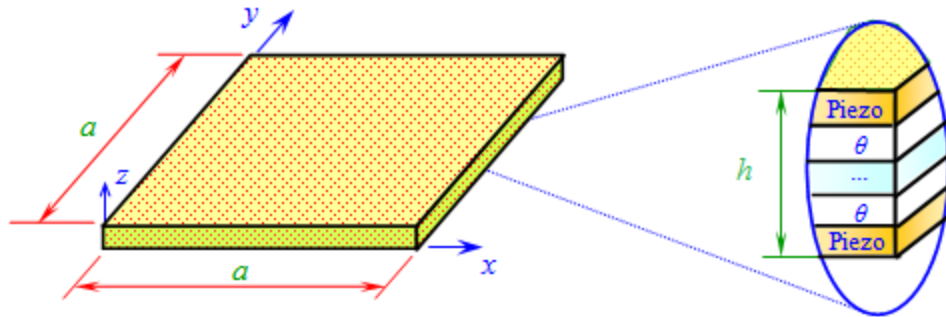


Figure 8.7. Model of an n -ply piezoelectric composite plate.

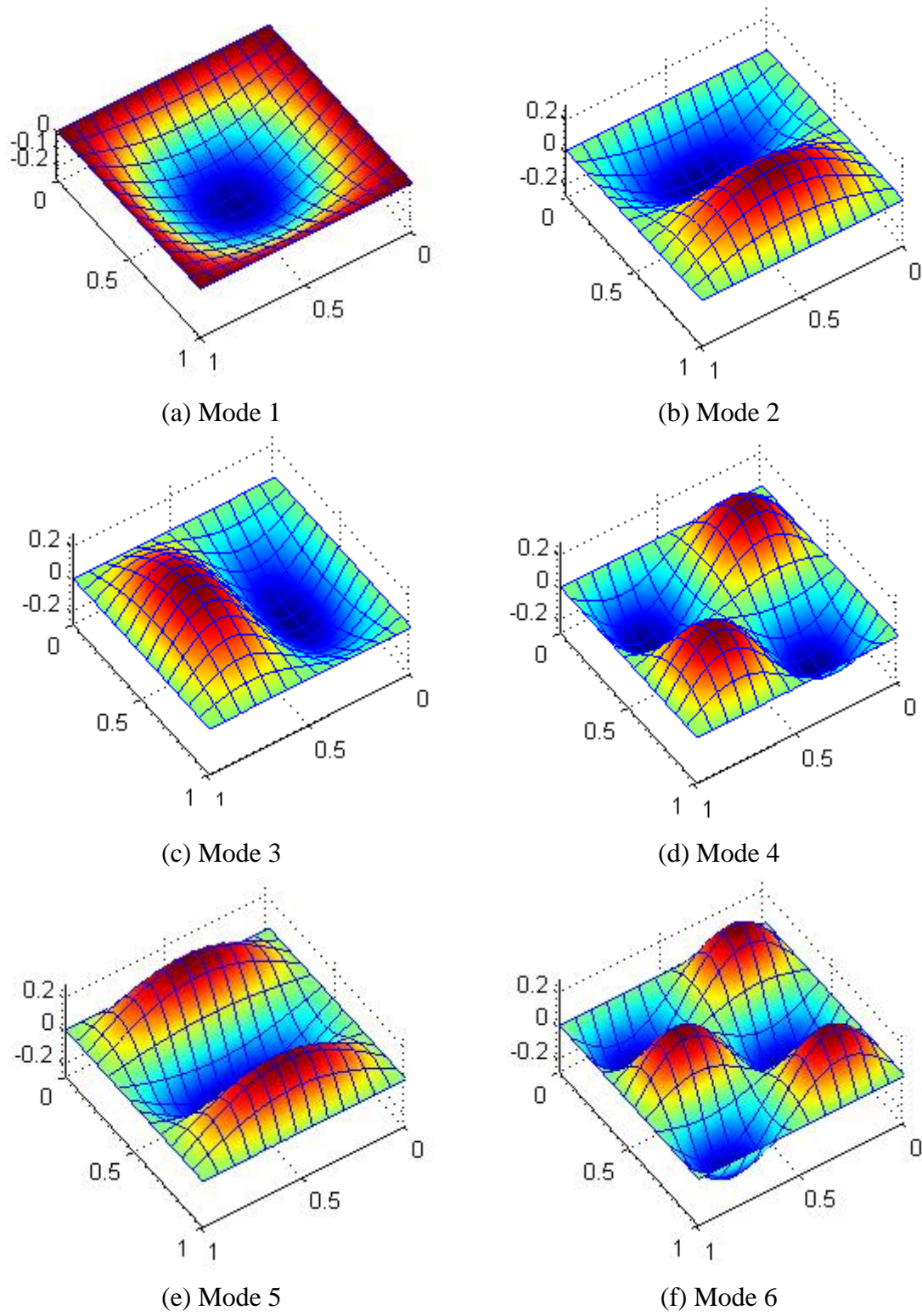


Figure 8.8. Shape of the first six eigenmodes of a simply supported piezoelectric composite plate.

Table 8.3. Convergence of the first five natural frequencies of the square piezoelectric composite plate [$pie/0/90/0/pie$]

Mesh	Method	Mode sequence number				
		Mode 1	Mode 2	Mode 3	Mode 4	Mode 5
Open circuit						
5×5	IGA-UHSDT ($p = 2$)	236.00	594.50	741.3	1014.3	1531.8
	IGA-UHSDT ($p = 3$)	231.50	528.50	673.60	925.00	1128.7
	FE layerwise [116]	276.19	-	-	-	-
9×9	IGA-UHSDT ($p = 2$)	231.90	531.60	676.00	928.4	1087.8
	IGA-UHSDT ($p = 3$)	231.40	523.20	669.00	918.5	1030.0
	FE layerwise [116]	261.70	-	-	-	-
13×13	IGA-UHSDT ($p = 2$)	231.50	525.00	670.40	920.60	1040.1
	IGA-UHSDT ($p = 3$)	231.40	523.10	668.90	918.4	1027.9
	FE layerwise [116]	259.66	-	-	-	-
	Q9 - HSDT [94]	250.50	583.19	695.70	980	1145.4
	Q9 - FSDT [94]	245.35	559.00	694.20	962	1093.0
	Ref [202]	245.94	-	-	-	-
Closed circuit						
5×5	IGA-UHSDT ($p = 2$)	236.00	594.50	741.30	1014.3	1531.8
	IGA-UHSDT ($p = 3$)	231.50	528.50	673.60	925.00	1128.7
	FE layerwise [116]	249.86	-	-	-	-
9×9	IGA-UHSDT ($p = 2$)	231.90	531.60	676.00	928.40	1087.8
	IGA-UHSDT ($p = 3$)	231.40	523.20	669.00	918.50	1030.0
	FE layerwise [116]	236.83	-	-	-	-
13×13	IGA-UHSDT ($p = 2$)	231.50	525.00	670.40	920.60	1040.1
	IGA-UHSDT ($p = 3$)	231.40	523.10	668.90	918.40	1027.9
	FE layerwise [116]	234.53				
	Q9 - HSDT [94]	230.46	520.38	662.92	908	1022.09
	Q9 - FSDT [94]	206.30	519.44	663.34	908	1020.10
	Ref [202]	245.94	-	-	-	-

The dimensionless first natural frequency, $\bar{f} = \omega_1 a^2 / (1000t\sqrt{\rho})$, is considered where ω_1 is the first natural frequency. Table 8.2 shows the dimensionless first natural frequency of the plate with three types of elements: quadratic ($p = 2$), cubic ($p = 3$) and quartic ($p = 4$). The results given by the IGA-UHSDT formulation are slightly lower than the analytical solution [202]. Besides, we can see that the results of the present method are stable in both closed-circuit condition and open-circuit condition similarly to the analytical solution in [202], while those of Refs. [94,116] are slightly deviated. This was also addressed in [203] to show the better performance of IGA over the conventional FEM in the solution of eigenvalue problems. In addition, Table 8.3 shows the convergence of the first five natural frequencies. Again, it can be seen that the IGA-UHSDT results match well with those of Refs. [94,116,202] and are stable for both closed- and open-circuit conditions. Figure 8.8 shows the shapes of the first six eigenmodes. We can see that these shapes reflect correctly physical modes of the piezoelectric composite plates as given by the analytical solution.

Next, a square six-ply plate $[pie/-45/45]_{as}$ is considered. The length of plate is 20 cm, thickness of the non-piezoelectric composite plate is 1 mm and each layer has the same thickness. The thickness of the piezo-layer is 0.1 mm. The plate is made of T300/976 graphite/epoxy layers and the piezo-ceramic is PZTG1195N. Table 8.4 shows the first ten natural frequencies of the plate using a mesh of 13×13 B-spline elements with boundary conditions CFFF and SSSS. It is again confirmed that the results of the present method match well with those of Refs. [91,78].

8.4.2 Nonlinear analysis of smart plates

Now, we consider a smart plate with material properties and geometrical dimensions similar to those in section 8.4.1.1. For the plate under mechanical load (parameter load $\bar{q} = q_o \times 10^2$), Figure 8.9 shows the nonlinear deflection of the plate subjected to input voltages. We can see that when voltage inputs increase, geometrically nonlinear deflection is upward. Moreover, the central deflection of the plate under input voltage 8V with different fiber orientation angles is shown in Figure 8.10.

8.4.3 Dynamic control and optimization

It is well known that structural controls have advantages and benefits in real life, such as reduced energy consumption, improved product, increased safety, etc. The sentence, “control will be the physics of the 21st century”, as spoken by Doyle JC (2001) at Conference on Decision and Control. It is well known, feedback and control are important in most technological aspects. In this work, we investigate behaviors of the plate under dynamic control.

Table 8.4. The first ten natural frequencies of the square piezoelectric composite plate $[pie/-45/45]_{as}$

Mode	CFFF				SSSS			
	IGA-UHSDT		FEM	RPIM	IGA-UHSDT		FEM	RPIM
	$p = 2$	$p = 3$	[78]	[91]	$p = 2$	$p = 3$	[78]	[91]
1	21.61	21.44	21.46	22.13	144.00	143.30	141.64	143.12
2	63.78	63.16	63.34	68.08	345.90	337.90	348.37	353.48
3	133.95	129.39	130.81	149.41	575.80	565.70	605.09	597.03
4	186.13	182.55	182.40	199.40	702.00	652.10	711.67	605.09
5	222.91	217.15	218.25	-	705.50	654.80	-	-
6	398.21	375.52	381.90	-	941.40	900.80	-	-
7	421.25	398.57	395.66	-	1273.70	1092.60	-	-
8	430.06	408.24	410.80	-	1322.90	1268.10	-	-
9	507.56	472.58	476.32	-	1507.10	1353.40	-	-
10	679.99	653.93	642.72	-	1887.60	1677.50	-	-

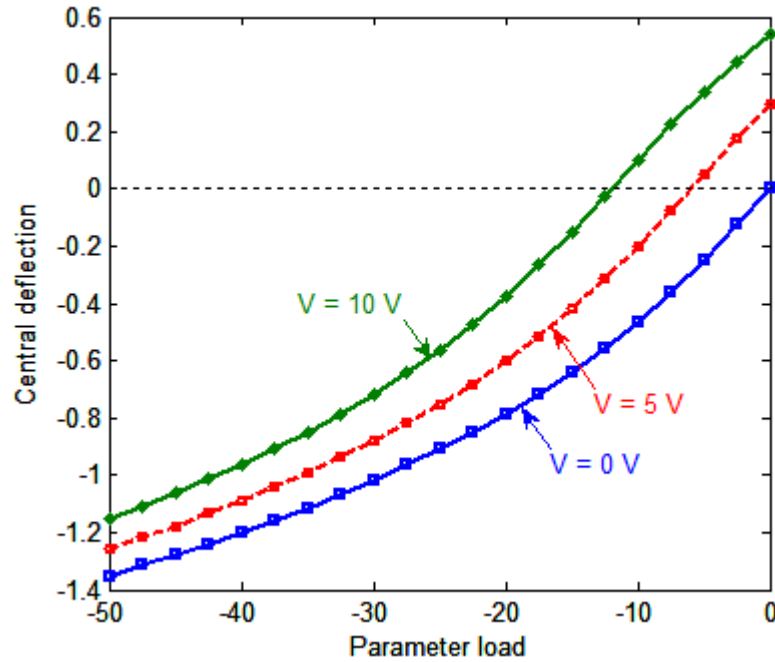


Figure 8.9. Effect of input voltages on nonlinear deflection of the piezoelectric composite plates $[-45/pie/45]_{as}$.

8.4.3.1 Nonlinear transient vibration

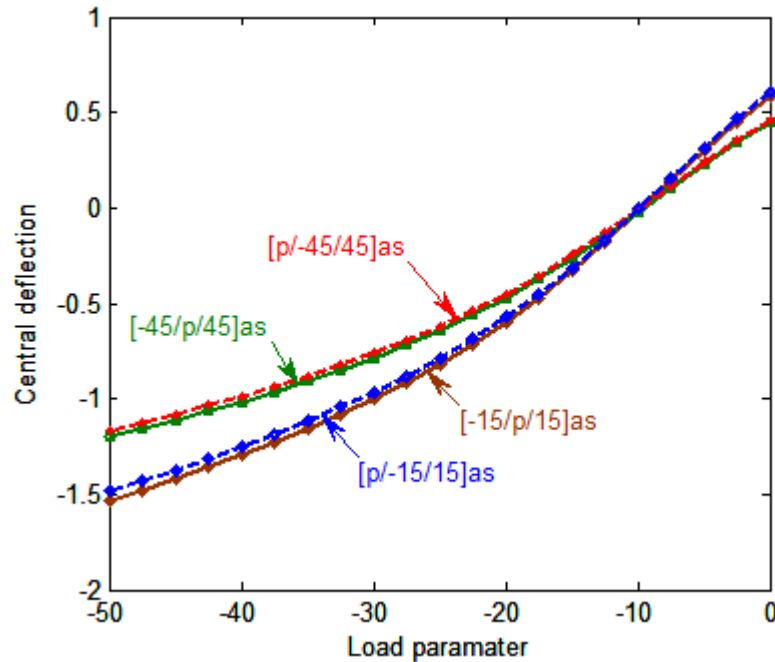


Figure 8.10. Effect of different fiber orientation angles on deflection of the plate subjected to input voltage 8V.

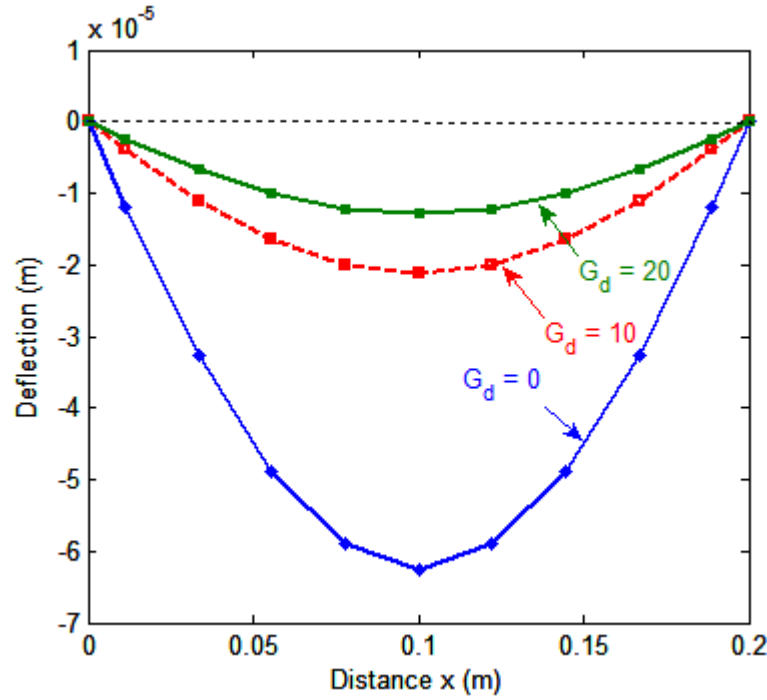


Figure 8.11. Effect of the gain G_d of the displacement feedback control on static deflection of the piezoelectric composite plate.

We now consider a plate $[pie/-45/45]_s$ under a uniform load $q = 100 \text{ N/m}^2$ that is similar to that presented in section 8.4.1.1. The upper and lower surfaces of the plate are bonded to a piezoelectric actuator layer and a piezoelectric sensor layer, respectively. We first study the response of static control with meshing 9×9 and $p = 2$. The effect of the displacement feedback control gain G_d on the static deflection of the plate is shown in Figure 8.11. It is seen that when G_d increases, the deflections decrease, similarly to what reported in [91]. It is observed that as the plate is subjected to loadings, electric charges are generated and amplified through the control. Then, the signal is sent to the actuator and a voltage is generated. Through the converse effect of piezoelectric, a force is generated and actively controls the behavior of the plate.

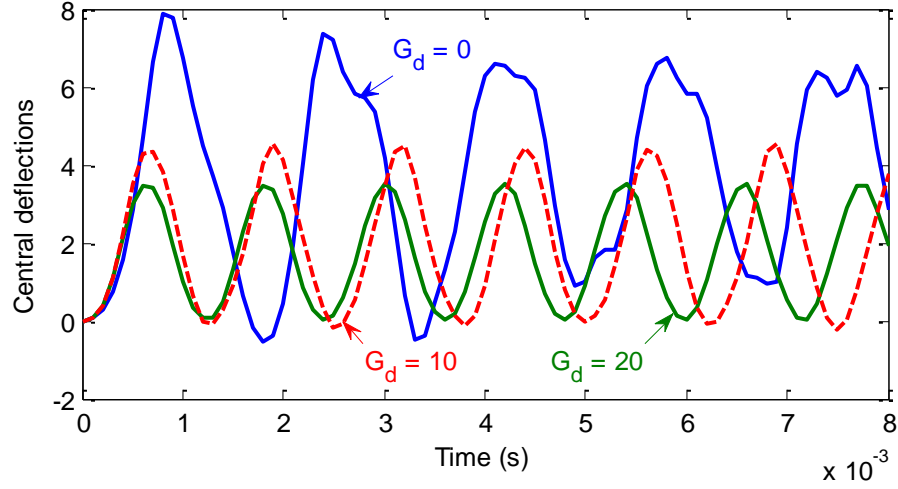


Figure 8.12. Effect of the control gain on the geometrically nonlinear response of the piezoelectric composite plate under step load.

Next, a smart composite plate subjected to sinusoidally distributed transverse load is investigated. The sinusoidally distributed transverse load is expressed as follows:

$$q = q_0 \sin\left(\frac{\pi x}{L}\right) \sin\left(\frac{\pi y}{L}\right) F(t) \quad (8.16)$$

Where

$$F(t) = \begin{cases} \begin{cases} 1 & 0 \leq t \leq t_1 \\ 0 & t > t_1 \end{cases} & \text{Step load} \\ \begin{cases} 1 - t/t_1 & 0 \leq t \leq t_1 \\ 0 & t > t_1 \end{cases} & \text{Triangular load} \\ -e^{-\gamma t} & \text{Explosive blast load} \end{cases} \quad (8.17)$$

in which $q_0 = 4 \times 10^8$ Pa and $\gamma = 330 \text{ s}^{-1}$. Figure 8.12 to Figure 8.14 show nonlinear transient vibrations of the central point of the plate under a closed-loop control. We observe that the response with control is smaller than those without control, as expected.

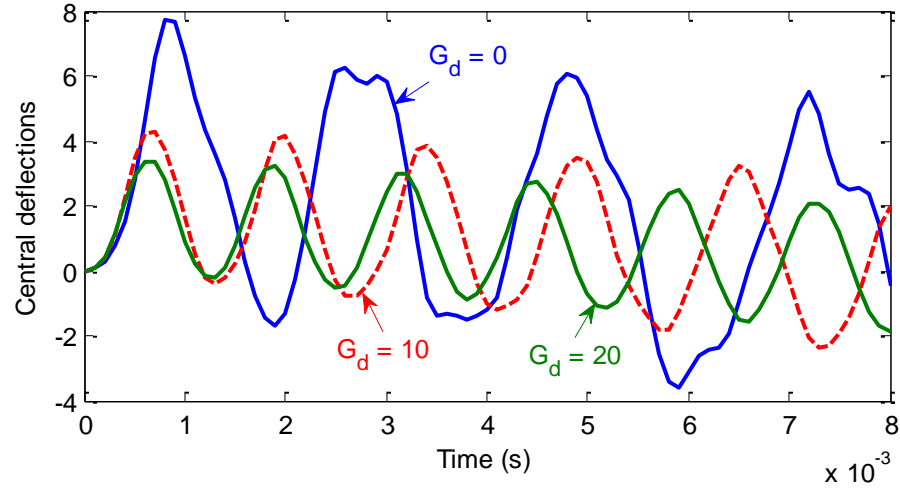


Figure 8.13. Effect of the control gain on the geometrically nonlinear response of the piezoelectric composite plate under triangular load.

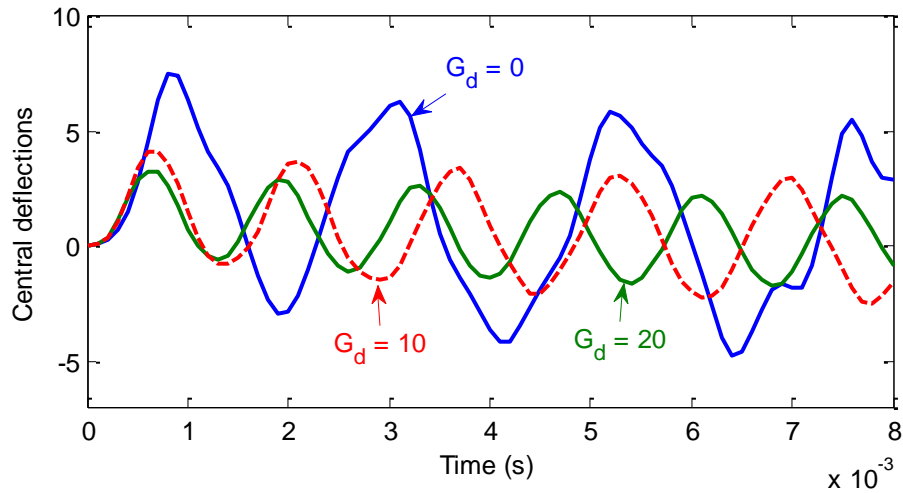


Figure 8.14. Effect of the control gain on the geometrically nonlinear response of the piezoelectric composite plate under explosive blast load.

8.4.3.2 Optimization

Finally, we investigate the optimization problem for actuator input voltages. Material properties and dimensions of piezoelectric plate are the same as in section 8.4.1.1. From Figure 8.3 and Figure 8.4, it can be seen that when the actuator input voltage increases, the deflection shape of plate increases. Here, we can search an optimal voltage for piezoelectric plate with minimum elastic energy. Figure 8.15 depicts the convergence of objective function using GA with 20 generations for the $[pie/-45/45]_{as}$ plate (SSSS) using a mesh of 9×9 cubic elements. Table 8.5 gives the energy of plate with different

actuator input voltages, as shown in Figure 8.3 and Figure 8.4, and the optimal input voltage. We can see that the energy of plate for case optimal voltage $V = 20.7$ and 5.4 for CFFF and SSSS plates, respectively, is minimum.

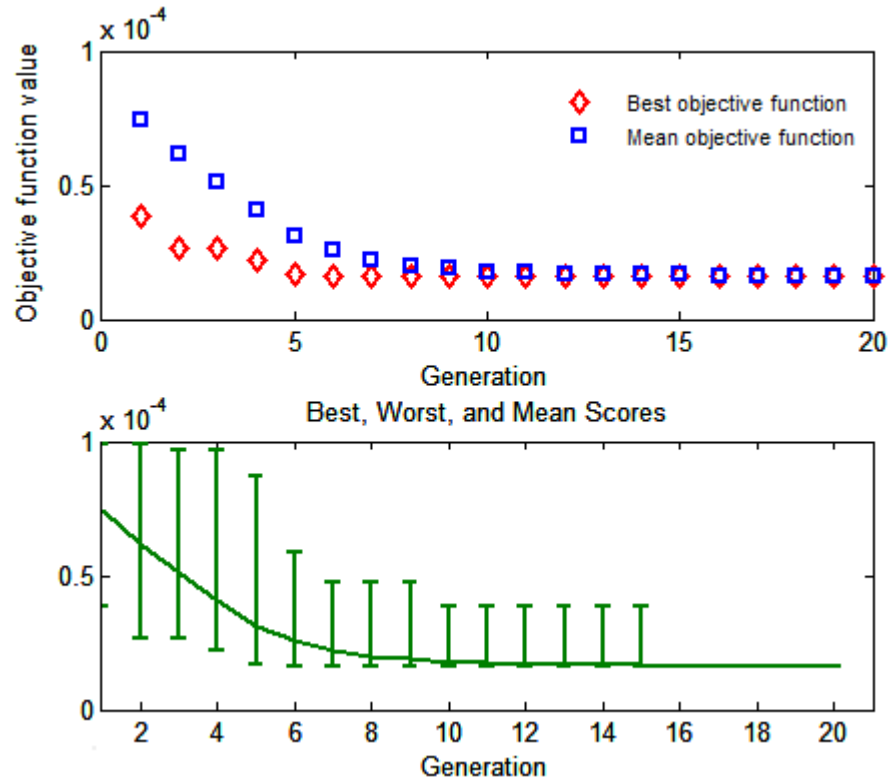


Figure 8.15. Convergence of objective function using GA with 20 generations.

Table 8.5. Energy of plate with different input voltage and optimal input voltage.

Boundary condition		CFFF			
Actuator input voltages	0 V	30 V	50 V	80 V	20.7 (optimal)
Energy (J) ($\times 10^{-3}$)	4.2476	3.0362	6.0570	16.3300	2.67
Boundary condition		SSSS			
Actuator input voltages	0 V	5 V	8 V	10 V	5.4 (optimal)
Energy (J) ($\times 10^{-5}$)	10.370	3.0670	4.7090	8.3139	3.0249

8.5 Concluding remarks

This chapter presents a simple and effective approach based on the combination of IGA and a generalized unconstrained approach for dynamic control and optimization of smart piezoelectric composite plates. Through the presented formulation and numerical results, some main conclusions can be drawn as follows:

- i) Based on the integration of IGA and UHSDT, no shear correction factor is used, which leads to zero-shear stresses at the bottom and top surfaces of plates.
- ii) The linear electric potential is approximated through the thickness of each piezoelectric layer. And the NURBS basis functions are used for electric potential, mechanical displacement field and exact geometry.
- iii) The closed-loop control algorithm based on displacements and velocities feedback is used to reduce vibration attitudes of the piezoelectric composite plates. When gain factors of the displacement and velocity increase, the deflections decrease.
- iv) In static and free vibration analyses, the results of the present method are more accurate than those of many other methods with a lower number of degrees of freedom. The proposed approach for free vibration analysis is more stable than these of other approaches.
- v) The nonlinear transient formulation for smart plates is formed in the total Lagrange approach based on the von Kármán strains and solved by Newmark time integration. Nonlinear response has lower central deflection and higher frequency than that of the linear response. Wavelength of the nonlinear response also changes compared to that of linear case.
- vi) In optimization analysis, a procedure using genetic algorithm (GA) is investigated to search optimal design for actuator input voltages, which makes the plate be at the equilibrium state, i.e. minimization of energy, under external forces.

Finally, the present approach would provide a reliable source of reference when calculating laminated composite plates with other methods.

Chapter 9

Conclusions and recommendations

9.1 Conclusions

In this thesis, the concept of isogeometric analysis has been developed to analyze smart plate structures. Geometry domains generated from CAD can be used directly for FEA. Hence, the exact geometry is expressed in both design and mechanical analysis. The present method allows exact representation of various geometries, i.e., spheres, circles, ellipsoids, cylinders, etc., using very coarse meshes. For smart plates, three models have been considered including piezoelectric composite plates, piezoelectric functionally graded material plates, functionally graded carbon nanotube-reinforced composite plates. In piezoelectric plates, the electric potential is assumed to vary linearly through the thickness for each piezoelectric sublayer. A displacement and velocity feedback control algorithm is used for the active control of the static deflection and dynamic response of the plates through a closed-loop control with bonded or embedded distributed piezoelectric sensors and actuators. Several numerical examples are performed to show that the present method is very well suited to simulate and analyze smart plate structures. Through the presented formulation and numerical results, the following main conclusions can be made:

- A simple and effective approach based on the combination of IGA and HSDT for the static, free vibration analyses and dynamic control of composite plates integrated with piezoelectric sensors and actuators has been developed. Due to the use of the HSDT, the proposed method does not require shear correction factors. The use of NURBS elements of at least second order naturally fulfils the C^1 -continuity requirement of the HSDT, thereby significantly reducing the number of degrees of freedom per control point compared to conventional finite element approaches featuring C^0 inter-element continuity. In free vibration analyses, the predictions of the proposed approach agree well with analytical solutions, and are more stable (passing from closed- to open-circuit conditions) than those of several other approaches available in the literature. In static analyses, the predictions of the proposed approach are more accurate than those of several other approaches with a lower number of degrees of freedom. In dynamic control analyses, the proposed approach produces predictions, which appear reasonable and consistent with the observed physical behavior.

- Geometrically nonlinear transient of piezoelectric functionally graded plates (FGPs) using IGA based on the generalized shear deformation model have been proposed for the first time. The material properties of FGM are assumed to vary through the thickness by the rule of mixture and the Mori–Tanaka scheme. In the analysis process, the thermal, electrical and mechanical loadings are considered and a two-step procedure is proposed including a step of calculating the temperature field along the thickness of the plate and a step of analyzing the geometrically nonlinear behavior of the plate under thermo-electro-mechanical loadings. The nonlinear formulation for plates is formed in the total Lagrange approach based on the von Kármán strains, which includes thermo-piezoelectric effects, and solved by Newmark time integration associated with the iteration methods. Comparison between the nonlinear and linear behaviors showed that nonlinear response had lower central deflection and higher frequency than that of the linear response. Effects of various parameters on the geometrically nonlinear responses of the piezoelectric FGM plate have been carried out to show the accuracy and reliability of the present method for the geometrically nonlinear responses of the piezoelectric FGM plate by comparing its numerical solutions with those of other available numerical results.
- The combination of IGA and a generalized unconstrained approach for dynamic control and optimization of smart piezoelectric composite plates has been proposed. The new function through the plate thickness for the UHSDT is introduced, which can achieve any desired degree of smoothness through the choice of the interpolation order and easily fulfills the C^1 -continuity requirements for plate elements stemming from the HSDT. In static and free vibration analyses, the results of the present method are more accurate than those of many other methods with a lower number of degrees of freedom. The proposed approach for free vibration analysis is more stable than those of other approaches. Moreover, the present approach would provide a reliable source of reference for calculating the responses of laminated composite plates.
- An approach based on the combination of IGA and HSDT for dynamic behaviors of FG-CNTRCs has been developed. The material properties of FG-

CNTRCs are assumed to be graded through the thickness direction according to several linear distributions of the volume fraction of carbon nanotubes. The effects of carbon nanotube volume fraction, plate width-to-thickness ratio on natural frequencies and deflections of FG-CNTRC plates are considered. Especially, the distributions of CNTs along the thickness direction of the plate have a large influence on the central deflection of the plate. Numerical results proved high accuracy and reliability of the proposed method in comparison with other available numerical approaches

Finally, based on the results of the numerical examples, the present approach would provide a reliable source of reference for calculating the behaviors of smart plate structures. However, there are still some limitations of the present work, which can be explained as follows:

- In this thesis, almost all numerical examples are either square or circle/ellipse, which are the simplest geometries. It can be modeled straightforwardly with only a single patch. Multi-patch geometries and piezoelectric patches are not considered.
- Homogeneous Dirichlet boundary conditions are only chosen to examine the plate behaviors.
- The practical problems or complex geometries are also not considered in this thesis.

9.2 Recommendations for future work

It is obvious that the developing field of the smart plate structures using IGA cannot be covered in one single PhD thesis. Many aspects have therefore not been studied here. Relevant unresolved issues are discussed in the following points:

- The present work can be extended to micro smart structures using the nonlocal elasticity theory or the modified couple stress theory. It is important

to consider the size effect of microstructures in theoretical and experimental investigations of the microscale or nanoscale.

- The present method can be employed in micro-electro-mechanical systems (MEMs) to Nano-electro-mechanical systems (NEMS) to reach the high sensitivity and desired performance [216-218].
- In the design of the smart plate structures or the plate/shell structures, a feature, which should be considered, is their resistance to buckling under loading conditions or temperature environments. For this purpose, buckling and post-buckling behaviors of the smart plates need to be investigated.
- For large structures, in order to save piezo materials, the piezoelectric patches are often used. Therefore, the present work can be extended to study effect of the piezoelectric patches on the behaviors of the structures.
- Adaptive local refinement strategies need to be developed as future extension of the present work.
- For industrial perspectives, the present method should be developed to analyze engineering problems, such as automotive, aerospace, marine or offshore components.

List of publications

A1 - Peer reviewed journal publications included in Science Citation Index

Related to the thesis

1. **Phung-Van P**, De Lorenzis L, Thai H Chien, Abdel-Wahab M, Nguyen-Xuan H. Analysis of laminated composite plates integrated with piezoelectric sensors and actuators using higher-order shear deformation theory and isogeometric finite elements. Computational Materials Science 2015; 95:495-505 (IF: 2.131)
<http://www.sciencedirect.com/science/article/pii/S0927025614003243>
2. **Phung-Van P**, Abdel-Wahab M, Liew KM, Bordas SPA, Nguyen-Xuan H. Isogeometric analysis of functionally graded carbon nanotube-reinforced composite plates using higher-order shear deformation theory. Composite Structures 2015; 123:137-149 (IF = 3.318)
<http://www.sciencedirect.com/science/article/pii/S0263822314006771>
3. **Phung-Van P**, Nguyen B Lieu, Tran V Loc, Dinh TD, Thai H Chien, Bordas SPA, Abdel-Wahab M, Nguyen-Xuan H. An efficient computational approach for control of nonlinear transient responses of smart piezoelectric composite plates. International Journal of Non-Linear Mechanics 2015; 76:190-202 (IF: 1.977)
<http://www.sciencedirect.com/science/article/pii/S0020746215001134>

4. **Phung-Van P**, Nguyen-Thoi T, Le-Dinh T, Nguyen-Xuan H. Static, free vibration analyses and dynamic control of composite plates integrated with piezoelectric sensors and actuators by the cell-based smoothed discrete shear gap method (CS-FEM-DSG3). *Smart Materials and Structures* 2013; 22: 095026 (IF: 2.502)
<http://iopscience.iop.org/0964-1726/22/9/095026>
5. **Phung-Van P**, Nguyen-Thoi T, Bui-Xuan T, Lieu-Xuan Q. A cell-based smoothed three-node Mindlin plate element (CS-FEM-MIN3) based on the C0-type higher-order shear deformation for geometrically nonlinear analysis of laminated composite plates. *Computational Materials Science* 2015; 96:549-558 (IF: 2.131)
<http://www.sciencedirect.com/science/article/pii/S0927025614002857>
6. **Phung-Van P**, Tran V Loc, Ferreira AJM, Abdel-Wahab M, Nguyen-Xuan H. Nonlinear transient isogeometric analysis of smart piezoelectric functionally graded material plates based on generalized shear deformation theory under thermo-electro-mechanical loads. *Nonlinear Dynamics* 2015; under review (IF: 2.849)

Other publications

7. Tran V Loc, **Phung-Van P**, Lee Jaehong, Abdel Wahab M, Nguyen-Xuan H. Isogeometric analysis for nonlinear thermomechanical stability of functionally graded plates. *Composite Structures* 2015; DOI: 10.1016/j.compstruct.2016.01.001 (IF = 3.318)
<http://www.sciencedirect.com/science/article/pii/S0263822316000131>
8. Nguyen-Hoang S, **Phung-Van P**, Natarajan S, Hyun-Gyu K. A combined scheme of edge-based and node-based smoothed finite element methods for Reissner-Mindlin flat shells. *Engineering with Computers* 2015; DOI:10.1007/s00366-015-0416-z (IF = 1.451)
<http://link.springer.com/article/10.1007%2Fs00366-015-0416-z>
9. Nguyen-Thoi T, **Phung-Van P**, Nguyen-Thoi MH, Dang-Trung H. An upper-bound limit analysis of Mindlin plates using CS-DSG3 method and second-order cone programming. *Journal of Computational and Applied Mathematics* 2015; 281:32-48

(IF = 1.266)

<http://www.sciencedirect.com/science/article/pii/S0377042714005470>

10. Nguyen-Thoi T, **Phung-Van P**, Ho-Huu V, Le-Anh L. An edge-based smoothed finite element method (ES-FEM) for dynamic analysis of 2D Fluid-Solid interaction problems. *KSCE Journal of Civil Engineering* 2015; 19:641-650 (IF: 0.484)
<http://link.springer.com/article/10.1007/s12205-015-0293-4>
11. **Phung-Van P**, Nguyen-Thoi T, Luong-Van H, Thai-Hoang C, Nguyen-Xuan H. A cell-based smoothed discrete shear gap method (CS-FEM-DSG3) using layerwise deformation theory for dynamic response of composite plates resting on viscoelastic foundation. *Computer Methods in Applied Mechanics and Engineering* 2014; 272: 138-159 (IF: 2.959)
<http://www.sciencedirect.com/science/article/pii/S0045782514000140>
12. **Phung-Van P**, Nguyen-Thoi T, Luong-Van H, Lieu-Xuan Q. Geometrically nonlinear analysis of functionally graded plates using a cell-based smoothed three-node plate element (CS-MIN3) based on the C0-HSDT. *Computer Methods in Applied Mechanics and Engineering* 2014; 270: 15–36 (IF: 2.959)
<http://www.sciencedirect.com/science/article/pii/S0045782513003277>
13. **Phung-Van P**, Thai H Chien, Nguyen-Thoi T, Nguyen-Xuan H. Static and free vibration analyses of composite and sandwich plates by an edge-based smoothed discrete shear gap method (ES-DSG3) using triangular elements based on layerwise theory. *Composites part B - Engineering* 2014; 60: 227-238 (IF: 2.983)
<http://www.sciencedirect.com/science/article/pii/S1359836813007749>
14. **Phung-Van P**, Nguyen-Thoi T, Dang-Trung H, Nguyen-Minh N. A cell-based smoothed discrete shear gap method (CS-FEM-DSG3) using layerwise theory based on the C0-type higher-order shear deformation for static and free vibration analyses of sandwich and composite plates. *Composite Structures* 2014; 111: 553-565 (IF: 3.318)
<http://www.sciencedirect.com/science/article/pii/S0263822314000518>
15. **Phung-Van P**, Luong-Van H, Nguyen-Thoi T, Nguyen-Xuan H. A cell-based

- smoothed discrete shear gap method (CS-FEM-DSG3) based on the C0-type higher-order shear deformation theory for dynamic responses of Mindlin plates on viscoelastic foundations subjected to a moving sprung vehicle. *International Journal for Numerical Methods in Engineering* 2014; 98: 988-1014 (IF: 2.055)
<http://onlinelibrary.wiley.com/doi/10.1002/nme.4662/abstract>
16. Luong-van H, Nguyen-Thoi T, Liu GR, **Phung-Van P**. A cell-based smoothed finite element method using Mindlin plate element (CS-FEM-MIN3) for dynamic response of composite plates on viscoelastic foundation. *Engineering Analysis with Boundary Elements* 2014; 42: 8-19 (IF: 1.392)
<http://www.sciencedirect.com/science/article/pii/S0955799713002439>
17. Nguyen-Thoi T, **Phung-Van P**, Nguyen-Hoang S, Lieu-Xuan Q. A smoothed coupled NS/*n*ES-FEM for dynamic analysis of 2D fluid-solid interaction problems. *Applied Mathematics and Computation* 2014; 232: 324-346 (IF: 1.551)
<http://www.sciencedirect.com/science/article/pii/S0096300314000897>
18. Nguyen-Thoi T, Rabczuk T, Lam-Phat T, Ho-Huu V, **Phung-Van P**. Free vibration analysis of cracked Mindlin plate using an extended cell-based smoothed discrete shear gap method (XCS-DSG3). *Theoretical and Applied Fracture Mechanics* 2014; 72:150-163 (IF: 1.262)
<http://www.sciencedirect.com/science/article/pii/S016784421400041X>
19. Nguyen-Thoi T, **Phung-Van P**, Nguyen-Hoang S, Lieu-Xuan Q. A coupled alpha-FEM for dynamic analyses of 2D fluid-solid interaction problems. *Journal of Computational and Applied Mathematics* 2014; 271: 130-149 (IF: 1.266)
<http://www.sciencedirect.com/science/article/pii/S037704271400185X>
20. Nguyen-Thoi T, Bui-Xuan T, **Phung-Van P**, Nguyen-Hoang S, Nguyen-Xuan H. An edge-based smoothed three-node Mindlin plate element (ES-MIN3) for static and free vibration analyses of plates. *KSCE Journal of Civil Engineering* 2014, 18(4): 1072-1082 (IF: 0.484)
<http://link.springer.com/article/10.1007%2Fs12205-014-0002-8>

- 21 **Phung-Van P**, Nguyen-Thoi T, Tran V Loc, Nguyen-Xuan H. A cell-based smoothed discrete shear gap method (CS-DSG3) based on the C^0 -type higher-order shear deformation theory for static and free vibration analyses of functionally graded plates. Computational Materials Science 2013, 79:857-872 (IF: 2.131)
<http://www.sciencedirect.com/science/article/pii/S0927025613003248>
22. Nguyen-Thoi T, **Phung-Van P**, Luong-Van H, Nguyen-Van H, Nguyen-Xuan H. A cell-based smoothed three-node Mindlin plate element (CS-MIN3) for static and free vibration analyses of plates. Computational Mechanics 2013; 51 (1): 65-81 (IF: 2.525)
<http://link.springer.com/article/10.1007%2Fs00466-012-0705-y>
23. Nguyen-Thoi T, **Phung-Van P**, Thai-Hoang C, Nguyen-Xuan H. A cell-based smoothed discrete shear gap method (CS-DSG3) using triangular elements for static and free vibration analyses of shell structures. International Journal of Mechanical Sciences 2013; 74: 32-45 (IF: 2.034)
<http://www.sciencedirect.com/science/article/pii/S002074031300129X>
24. Nguyen-Thoi T, Bui-Xuan T, **Phung-Van P**, Nguyen-Xuan H, Ngo-Thanh P. Static, free vibration and buckling analyses of stiffened plates by CS-FEM-DSG3 using triangular elements. Computers and Structures 2013; 125: 100-113 (IF: 2.134)
<http://www.sciencedirect.com/science/article/pii/S0045794913001582>
25. Nguyen-Thoi T, **Phung-Van P**, Rabczuk T, Nguyen-Xuan H, Le-Van C. Free and forced vibration analysis using the n -sided polygonal cell-based smoothed finite element method (n CS-FEM). International Journal of Computational Methods 2013; 10(1): 1340008 (IF: 0.571)
<http://www.worldscientific.com/doi/abs/10.1142/S0219876213400082>
26. Nguyen-Thoi T, **Phung-Van P**, Rabczuk T, Nguyen-Xuan H, Le-Van C. An application of the ES-FEM in solid domain for dynamic analysis of 2D fluid-solid interaction problems. International Journal of Computational Methods 2013; 10(1): 1340003 (IF: 0.571)
<http://www.worldscientific.com/doi/abs/10.1142/S0219876213400033>

27. Nguyen-Thoi T, **Phung-Van P**, Nguyen-Xuan H, Thai H Chien. A cell-based smoothed discrete shear gap method using triangular elements for static and free vibration analyses of Reissner-Mindlin plates. *International Journal for Numerical Methods in Engineering* 2012; 91(7): 705-741 (IF: 2.055)
<http://onlinelibrary.wiley.com/doi/10.1002/nme.4289/abstract>

References

- [1] Cottrell J, Hughes T, Bazilevs Y. Isogeometric analysis toward integration of CAD and FEA. Wiley, 2009.
- [2] Hughes T, Cottrell J, Bazilevs Y. Isogeometric analysis: CAD, finite elements, NURBS, exact geometry and mesh refinement. *Computer Methods in Applied Mechanics and Engineering* 2005; 194(39-41):4135–4195.
- [3] Robert C. Beach. An introduction to curves and surfaces of computeraided design. Van Nostrand Reinhold, 1991.
- [4] Rogers D. An introduction to NURBS with historical perspective. Academic Press, 2001.
- [5] Schoenberg IJ. Contributions to the problem of approximation of equidistant data by analytic functions. *Quarterly of Applied Mathematics* 1946; 4:112–141.
- [6] Ahlberg JH, Nilson EN, Walsh JL. The theory of splines and their applications. Academic Press, New York, 1967.
- [7] De Boor C. Bicubic spline interpolation. *Journal of Mathematical Physics* 1962; 41:212–218.
- [8] Riesenfeld RF. Application of B-spline Approximation to Geometric problems of Computer Aided Design. PhD thesis, Syracuse University, 1972.
- [9] Versprille KJ. Computer-aided Design Applications of the Rational B-spline Approximation Form. PhD thesis, SyracuseUniversity, 1975.
- [10] Cox MG. The numerical evaluation of B-splines. Technical report, National Physics Laboratory DNAC 4, 1971.
- [11] De Boor C. On calculation with B-splines. *Journal of Approximation Theory* 1972; 6:50–62.
- [12] De Boor C. A Practical Guide to Splines. Springer-Verlag, 1978.

- [13] Cohen E, Lyche T, Riesenfeld R. Discrete B-spline and subdivision techniques in computer aided geometric design and computer graphics. *Computer Graphics and Image Processing* 1980; 14:87–111.
- [14] Ramshaw L. Blossoming: a connect-the-dots approach to splines. Technical report, Digital Systems Research Center, Palo Alto, CA, 1987.
- [15] Ramshaw L. Blossoms are polar forms. *Computer Aided Geometric Design* 1989; 6:323–358.
- [16] Gomez H, Hughes T, Nogueira X, Calo VM. Isogeometric analysis of the isothermal Navier-Stokes-Korteweg equations. *Computer Methods in Applied Mechanics and Engineering* 2010; 199:1828–1840.
- [17] Nielsen P, Gersborg A, Gravesen J, Pedersen NL. Discretizations in isogeometric analysis of Navier-Stokes flow. *Computer Methods in Applied Mechanics and Engineering* 2011; 200:3242–3253.
- [18] Bazilevs Y, Hughes TJR. NURBS-based isogeometric analysis for the computation of flows about rotating components. *Computational Mechanics* 2008; 43:143-150.
- [19] Nguyen Ngoc Minh, Bui Quoc Tinh, Yud Tiantang, Hirose Sohichi. Isogeometric analysis for unsaturated flow problems. *Computers and Geotechnics* 2014; 62:257-267.
- [20] Akkermana I, Bazilevs Y, Keesb CE, Farthing MW. Isogeometric analysis of free-surface flow. *Journal of Computational Physics* 2011; 230:4137-4152.
- [21] Bazilevs Y, Calo V, Hughes T, Zhang Y. Isogeometric fluidstructure interaction: theory, algorithms and computations. *Computational Mechanics* 2008; 43(1):3–37.
- [22] Bazilevs Y, Calo VM, Zhang Y, Hughes TJR. Isogeometric fluid–structure interaction analysis with applications to arterial blood flow. *Computational Mechanics* 2006; 38:310-322.
- [23] Bazilevs Y, Gohean J, Hughes T, Moser R, Zhang Y. Patient-specific isogeometric fluid–structure interaction analysis of thoracic aortic blood flow due to implantation of the Jarvik 2000 left ventricular assist device. *Computer Methods in Applied Mechanics and Engineering* 2009; 198:3534–3550.
- [24] Bazilevs Y, Hsua MC, Scott MA. Isogeometric fluid–structure interaction analysis with emphasis on non-matching discretizations, and with application to wind turbines. *Computer Methods in Applied Mechanics and Engineering* 2012; 249-252:28-41.

- [25] Temizer I, Wriggers P, Hughes T. Contact treatment in isogeometric analysis with NURBS. *Computer Methods in Applied Mechanics and Engineering* 2011; 200:1100–1112.
- [26] Temizer I, Wriggers P, Hughes TJR. Three-dimensional mortar-based frictional contact treatment in isogeometric analysis with NURBS. *Computer Methods in Applied Mechanics and Engineering* 2012; 209-212:115-128.
- [27] Lorenzis De L, Wriggers P, Zavarise G. A mortar formulation for 3D large deformation contact using NURBS-based isogeometric analysis and the augmented Lagrangian method. *Computational Mechanics* 2012; 49:1-20.
- [28] Lorenzis De L, Temizer I, Wriggers P, Zavarise G. A large deformation frictional contact formulation using NURBS-based isogeometric analysis. *International Journal for Numerical Methods in Engineering* 2011; 87:1278–1300.
- [29] Fischer P, Klassen M, Mergheim J, Steinmann P, Muller R. Isogeometric analysis of 2D gradient elasticity. *Computational Mechanics* 2010; 47:325–334.
- [30] Verhoosel C, Scott M, Hughes T, Borst R. An isogeometric analysis approach to gradient damage models. *Computer Methods in Applied Mechanics and Engineering* 2011; 86:115–134.
- [31] Luycker E, Benson D, Belytschko T, Bazilevs Y, Hsu MC. XFEM in isogeometric analysis for linear fracture mechanics. *International Journal for Numerical Methods in Engineering* 2011; 87:541–565.
- [32] Benson DJ, Bazilevs Y, Luycker De E, Hsu MC, Scott M, Hughes TJR and Belytschko T. A generalized finite element formulation for arbitrary basis functions: From isogeometric analysis to XFEM. *International Journal for Numerical Methods in Engineering* 2010; 83:765-785.
- [33] Myung-Jin C, Seonho C. Isogeometric analysis of stress intensity factors for curved crack problems. *Theoretical and Applied Fracture Mechanics* 2015; 75:89-103.
- [34] Bhardwaj G, Singh IV. Fatigue crack growth analysis of a homogeneous plate in the presence of multiple defects using extended isogeometric analysis. *Journal of the Brazilian Society of Mechanical Sciences and Engineering* 2014; DOI: 10.1007/s40430-014-0232-1.
- [35] Ghorashia SSh, Valizadehb N, Mohammadic S, Rabczuk T. T-spline based XIGA for fracture analysis of orthotropic media. *Computers & Structures* 2015; 147: 138-146.

- [36] Singh IV, Bhardwaj G, Mishra BK. A new criterion for modeling multiple discontinuities passing through an element using XIGA. *Journal of Mechanical Science and Technology* 2015; 29:1131-1143.
- [37] Bhardwaj G, Singha IV, Mishraa BK, Bui TQ. Numerical simulation of functionally graded cracked plates using NURBS based XIGA under different loads and boundary conditions. *Composite Structures* 2015; 126:347-359.
- [38] Cottrell J, Reali A, Bazilevs Y, Hughes T. Isogeometric analysis of structural vibrations. *Computer Methods in Applied Mechanics and Engineering* 2006; 195(41-43):5257–5296.
- [39] Antonio Cazzani, Marcello Malagù. Isogeometric analysis of plane-curved beams. *Mathematics and Mechanics of Solids* 2014; DOI: 10.1177/1081286514531265.
- [40] Lezgy-Nazargaha M, Vidalb P, Polit O. NURBS-based isogeometric analysis of laminated composite beams using refined sinus model. *European Journal of Mechanics - A/Solids* 2015; 53: 34-47.
- [41] Thai H Chien, Nguyen-Xuan H, Nguyen-Thanh N, Le TH, Nguyen-Thoi T, Rabczuk T. Static, free vibration, and buckling analysis of laminated composite Reissner-Mindlin plates using NURBS-based isogeometric approach. *International Journal for Numerical Methods in Engineering* 2012; 91:571–603
- [42] Valizadeh N, Natarajan S, Gonzalez-Estrada O, Rabczuk T, Bui QT, Bordas S. NURBS-based finite element analysis of functionally graded plates: Static bending, vibration, buckling and flutter. *Composite Structures* 2013; 99:309–326.
- [43] Nguyen-Xuan H, Tran V Loc, Thai H Chien, Kulasegaram S, Bordas S. Isogeometric finite element analysis of functionally graded plates using a refined plate theory. *Composite Part B* 2014; 64:222-234.
- [44] Thai H Chien, Kulasegaram S, Tran V Loc, Nguyen-Xuan H. Generalized shear deformation theory for functionally graded isotropic and sandwich plates based on isogeometric approach. *Computers and Structures* 2014; 141:94-112.
- [45] Thai H Chien, Nguyen-Xuan H, Bordas S, Nguyen-Thanh N, Rabczuk T. Isogeometric analysis of laminated composite plates using the higherorder shear deformation theory. *Mechanics of Advanced Materials and Structures* 2015; 22:451-469.

- [46] Tran V Loc, Thai H Chien, Nguyen-Xuan H. An isogeometric finite element formulation for thermal buckling analysis of functionally graded plates. *Finite Elements in Analysis and Design* 2013; 73:65–76.
- [47] Guo Y, Nagy A, Grdal Z. A layerwise theory for laminated composites in the framework of isogeometric analysis. *Composite Structures* 2014; 107:447–457.
- [48] Thai H Chien, Ferreira A, Carrera E, Nguyen-Xuan H. Isogeometric analysis of laminated composite and sandwich plates using a layerwise deformation theory. *Composite Structures* 2013b; 104:196–214.
- [49] Kiendl J, Bazilevs Y, Hsu M, Wüchner R, Bletzinger K. The bending strip method for isogeometric analysis of Kirchhoff-Love shell structures comprised of multiple patches. *Computer Methods in Applied Mechanics and Engineering* 2010; 199(37-40):2403–2416.
- [50] Kiendl J, Bletzinger K, Linhard J, Wüchner R. Isogeometric shell analysis with Kirchhoff-Love elements. *Computer Methods in Applied Mechanics and Engineering* 2009; 198(49-52):3902–3914.
- [51] Benson D, Bazilevs Y, Hsu M, Hughes T. Isogeometric shell analysis: The Reissner–Mindlin shell. *Computer Methods in Applied Mechanics and Engineering* 2010; 199(5-8):276–289.
- [52] Benson DJ, Bazilevs Y, Hsu M, Hughes T. A large deformation, rotation-free, isogeometric shell. *Computer Methods in Applied Mechanics and Engineering* 2011; 200(13-16):1367–1378.
- [53] Kapoor H, Kapania R. Geometrically nonlinear NURBS isogeometric finite element analysis of laminated composite plates. *Composite Structures* 2012; 94:3434–3447.
- [54] Le-Manh T, Lee J. Postbuckling of laminated composite plates using NURBS-based isogeometric analysis. *Composite Structures* 2014; 109:286–293.
- [55] Tran V Loc, Lee J, Nguyen-Van H, Nguyen-Xuan H, Wahab MA. Geometrically nonlinear isogeometric analysis of laminated composite plates based on higher-order shear deformation theory. *International Journal of Non-Linear Mechanics* 2015; 72:42–52/
- [56] Hosseini S, Joris JC Remmersa, Clemens V Verhoosela, René de Borst. An isogeometric solid-like shell element for non-linear analysis. *International Journal for Numerical Method in Engineering* 2013; 95:238–256.

- [57] Hosseini S, Joris JC Remmers, Clemens V Verhoosel, René de Borst. An isogeometric continuum shell element for non-linear analysis. *Computer Methods in Applied Mechanics and Engineering* 2014; 271:1-22.
- [58] Oliver Weeger, Utz Wever, Bernd Simeon. Isogeometric analysis of nonlinear Euler–Bernoulli beam vibrations. *Nonlinear Dynamic* 2013; 72:813-835.
- [59] Scott MA, Simpson RN, Evans JA, Lipton S, Bordas SPA, Hughes TJR, Sederb TW. Isogeometric boundary element analysis using unstructured T-splines. *Computer Methods in Applied Mechanics and Engineering* 2013; 254:197-1921.
- [60] Simpson RN, Bordas SPA, Trevelyan J, Rabczuk T. A two-dimensional Isogeometric boundary element method for elastostatic analysis. *Computer Methods in Applied Mechanics and Engineering* 2012; 209-212:87-100.
- [61] Gu J, Zhang J, Li G. Isogeometric analysis in BIE for 3D potential problem. *Engineering Analysis with Boundary Elements* 2012; 36(5):858-865.
- [62] Wang Y, Benson DJ, Nagy AP. A multi-patch nonsingular isogeometric boundary element method using trimmed elements. *Computational Mechanics* 2015; 56(1):173-191.
- [63] Washington GN. Introduction to smart materials and intelligent systems ME774 class notes. The Ohio State University.
- [64] Phung-Van P, Abdel-Wahab M, Liew KM, Bordas SPA, Nguyen-Xuan H. Isogeometric analysis of functionally graded carbon nanotube-reinforced composite plates using higher-order shear deformation theory. *Composite Structures* 2015; 123:137-149.
- [65] Phung-Van P, De Lorenzis L, Thai H. Chien, Abdel-Wahab M, Nguyen-Xuan H. Analysis of laminated composite plates integrated with piezoelectric sensors and actuators using higher-order shear deformation theory and isogeometric finite elements. *Computational Materials Science* 2015; 96:495-505.
- [66] Iijima S. Helical microtubules of graphitic carbon. *Nature* 1991; 354:56–58.
- [67] Wang Z, Chen S, Han W. The static shape control for intelligent structures. *Finite Elements in Analysis and Design* 1997; 26:303-314.
- [68] Thostenson ET, Li C, Chou TW. Nanocomposites in context. *Composites Science and Technology* 2005; 65:491–516.
- [69] Lau AKT, Hui D. The revolutionary creation of new advanced materials-carbon nanotube composites. *Composite Part B: Engineering* 2002; 33:263–277.

- [70] Hong CH, Chopra I. Modeling and validation of induced strain actuation of composite coupled plates. *AIAA Journal* 1999; 37:372–377.
- [71] Yang SM, Lee YJ. Interaction of structure vibration and piezoelectric actuation. *Smart Materials and Structures* 1994; 3:494–500.
- [72] Kim J, Varadan VV, Varadan VK, Bao XQ. Finite element modeling of a smart cantilever plate and comparison with experiments. *Smart Materials and Structures* 1996; 5:165–170.
- [73] Pletner B, Abramovich H. Consistent methodology for the modelling of piezolaminated shells. *AIAA Journal* 1997; 35:1316–1326.
- [74] Willberg C, Gabbert U. Development of a three-dimensional piezoelectric isogeometric finite element for smart structure applications. *Acta Mechanica* 2012; 223(8):1837-1850.
- [75] Wang SY, Quek ST, Ang KK. Dynamic stability analysis of finite element modeling of piezoelectric composite plates. *International Journal of Solids and Structures* 2004; 41:745-764.
- [76] Lyapunov AM. The general problem of the stability of motion. Taylor and Francis, 1992.
- [77] Ray MC, Mallik N. Finite element analysis of smart structures containing piezoelectric fiber-reinforced composite actuator. *AIAA journal* 2004; 42(7):1398-1405.
- [78] Lam KY, Peng XQ, Liu GR, Reddy JN. A finite-element model for piezoelectric composite laminates. *Smart Materials and Structures* 1997; 6:583-591.
- [79] Benjeddou A. Advances in piezoelectric finite element modeling of adaptive structural elements: a survey. *Computers and Structures* 2000; 76:347-363.
- [80] Allik H, Hughes TJR. Finite element method for piezo-electric vibration. *International Journal for Numerical Methods in Engineering* 1970; 2:151-157.
- [81] Kekana K. Finite element modeling of laminated piezo-elastic structures: Lypunov stability analysis. *Journal of Sound and Vibration* 2002; 256:463–473.
- [82] Wang SY. A finite element model for the static and dynamic analysis of a piezoelectric bimorph. *International Journal of Solids and Structures* 2004; 41:4075-4096.
- [83] Cheng DK. *Field and Wave Electromagnetics*, 2nd Edition. Addison-Wesley Publishing, 1989.

- [84] Ehlers SM, Weisshaar TA. Static aeroelastic behavior of an adaptive laminated piezoelectric composite wing. *AIAA Journal* 1990; 28:1611–1623.
- [85] Wang SY, Quek ST. A model for the analysis of beams with embedded piezoelectric layers. *Journal of Intelligent Material Systems and Structures* 2002; 13:61–70.
- [86] Wang SY, Quek ST, Ang KK. Vibration control of smart piezoelectric composite plates. *Smart Materials and Structures* 2001; 10:637–644.
- [87] Bailey T, Hubbard JE. Distributed piezoelectric-polymer active control of a cantilever beam. *Journal of Guidance Control and Dynamic* 1985; 8:605–611.
- [88] Shen IY. Bending and torsional vibration control of composite beams through intelligent constrained-layer damping treatments. *Smart Materials and Structures* 1995; 4:340–355.
- [89] Tzou HS, Tseng CI. Distributed piezoelectric sensor/actuation design for dynamic measurement/control of distributed systems: a piezoelectric finite element approach. *Journal of Sound and Vibration* 1990; 138:17–34.
- [90] Hwang WC, Park HC. Finite element modeling of piezoelectric sensors and actuators. *AIAA Journal* 1993; 31:930–937.
- [91] Liu GR, Dai KY, Lim KM. Static and vibration control of composite laminates integrated with piezoelectric sensors and actuators using the radial point interpolation method. *Smart Materials and Structures* 2004; 13:1438–1447.
- [92] Liu GR, Peng XQ, Lam KY, Tani J. Vibration control simulation of laminated composite plates with integrated piezoelectrics. *Journal of Sound and Vibration* 1999; 220:827–846.
- [93] Suleman A, Venkayya VB. A simple finite element formulation for a laminated composite plate with piezoelectric layers. *Journal of Intelligent Material Systems and Structures* 1995; 6:776–682.
- [94] Victor MFC, Maria AAG, Afzal S, Cristóvão MMS, Carlos AMS, Franco CVM. Modelling and design of adaptive composite structures. *Computer Methods in Applied Mechanics and Engineering* 2000; 185:325–346.
- [95] Liew KM, Yang J, Kittipornchai S. Postbuckling of piezoelectric FGM plates subjected to thermo-electro-mechanical loading. *International Journal of Solids and Structures* 2004; 40:3869–3892.
- [96] Liew KM, Lim HK, Tan MJ, He XQ. Analysis of laminated composite beams and plates with piezoelectric patches using the element free Galerkin method. *Computational Mechanics* 2002; 29:486–497.

- [97] Milazzo A, Orlando C. An equivalent single-layer approach for free vibration analysis of smart laminated thick composite plates. *Smart Material and Structures* 2012; 21:075031.
- [98] Phung-Van P, Nguyen-Thoi T, Le-Dinh T, Nguyen-Xuan H. Static and free vibration analyses and dynamic control of composite plates integrated with piezoelectric sensors and actuators by the cell-based smoothed discrete shear gap method (CS-FEM-DSG3). *Smart Materials and Structures* 2013; 22:095026.
- [99] Khdeir AA, Aldraihem OJ. Analysis of smart cross ply laminated shells with shear piezoelectric actuators. *Smart Materials and Structures* 2011; 20:105030.
- [100] Nguyen-Thoi T, Phung-Van P, Nguyen-Thoi MH, Dang-Trung H. An upper-bound limit analysis of Mindlin plates using CS-DSG3 method and second-order cone programming. *Journal of Computational and Applied Mathematics* 2015; 281:32-48.
- [101] Nguyen-Thoi T, Phung-Van P, Ho-Huu V, Le-Anh L. An edge-based smoothed finite element method (ES-FEM) for dynamic analysis of 2D Fluid-Solid interaction problems. *KSCE Journal of Civil Engineering* 2015; 19:641-650.
- [102] Phung-Van P, Nguyen-Thoi T, Luong-Van H, Thai-Hoang C, Nguyen-Xuan H. A cell-based smoothed discrete shear gap method (CS-FEM-DSG3) using layerwise deformation theory for dynamic response of composite plates resting on viscoelastic foundation. *Computer Methods in Applied Mechanics and Engineering* 2014; 272: 138-159.
- [103] Nguyen-Thoi T, Rabczuk T, Lam-Phat T, Ho-Huu V, Phung-Van P. Free vibration analysis of cracked Mindlin plate using an extended cell-based smoothed discrete shear gap method (XCS-DSG3). *Theoretical and Applied Fracture Mechanics* 2014; 72:150-163.
- [104] Nguyen-Thoi T, Bui-Xuan T, Phung-Van P, Nguyen-Xuan H, Ngo-Thanh P. Static, free vibration and buckling analyses of stiffened plates by CS-FEM-DSG3 using triangular elements. *Computers and Structures* 2013; 125: 100-113.
- [105] Nguyen-Thoi T, Phung-Van P, Rabczuk T, Nguyen-Xuan H, Le-Van C. Free and forced vibration analysis using the n -sided polygonal cell-based smoothed finite element method (n CS-FEM). *International Journal of Computational Methods* 2013; 10(1): 1340008.

- [106] Kumar RS, Ray MC. Active constrained layer damping of smart laminated composite sandwich plates using 1-3 piezoelectric composites. *International Journal of Mechanics and Materials in Design* 2012; 8:197–218.
- [107] Phung-Van P, Thai H Chien, Nguyen-Thoi T, Nguyen-Xuan H. Static and free vibration analyses of composite and sandwich plates by an edge-based smoothed discrete shear gap method (ES-DSG3) using triangular elements based on layerwise theory. *Composites part B - Engineering* 2014; 60: 227-238.
- [108] Phung-Van P, Nguyen-Thoi T, Dang-Trung H, Nguyen-Minh N. A cell-based smoothed discrete shear gap method (CS-FEM-DSG3) using layerwise theory based on the C0-type higher-order shear deformation for static and free vibration analyses of sandwich and composite plates. *Composite Structures* 2014; 111: 553-565.
- [109] Phung-Van P, Luong-Van H, Nguyen-Thoi T, Nguyen-Xuan H. A cell-based smoothed discrete shear gap method (CS-FEM-DSG3) based on the C0-type higher-order shear deformation theory for dynamic responses of Mindlin plates on viscoelastic foundations subjected to a moving sprung vehicle. *International Journal for Numerical Methods in Engineering* 2014; 98: 988-1014.
- [110] Luong-van H, Nguyen-Thoi T, Liu GR, Phung-Van P. A cell-based smoothed finite element method using Mindlin plate element (CS-FEM-MIN3) for dynamic response of composite plates on viscoelastic foundation. *Engineering Analysis with Boundary Elements* 2014; 42: 8-19.
- [111] Nguyen-Thoi T, Phung-Van P, Nguyen-Xuan H, Thai H Chien. A cell-based smoothed discrete shear gap method using triangular elements for static and free vibration analyses of Reissner-Mindlin plates. *International Journal for Numerical Methods in Engineering* 2012; 91(7): 705-741
- [112] Rezaiee-Pajand M, Sadeghi Y. A bending element for isotropic, multilayered and piezoelectric plates. *Latin American Journal of Solids and Structures* 2013; 10:323–348.
- [113] Mitchell JA, Reddy JN. A refined hybrid plate theory for composite laminates with piezoelectric laminae. *International Journal of Solids and Structures* 1995; 32:2345–2367.
- [114] Reddy JN. On laminated composite plates with integrated sensors and actuators. *Engineering Structures* 1999; 21:568–593.
- [115] Torres DAF, Mendonca PdTR, Barcellos CSD. Evaluation and verification of an HSDT-layerwise generalized finite element formulation for adaptive

- piezoelectric laminated plates. *Computer Methods in Applied Mechanics and Engineering* 2011; 200:675-691.
- [116] Saravanos DA, Heyliger PR, Hopkins DA. Layerwise mechanics and finite element for the dynamic analysis of piezoelectric composite plates. *International Journal of Solids and Structures* 1997; 34:359-378.
- [117] Leung AYT. An unconstrained third-order plate theory. *Computers and Structures* 1991; 40(4):871-875.
- [118] Leung AYT, Niu Junchuan, Lim CW, Song Kongjie. A new unconstrained third-order plate theory for Navier solutions of symmetrically laminated plates. *Computers and Structures* 2003; 81:2539-2548.
- [119] Dinis LMJS, Natal Jorge RM, Belinha J. Static and dynamic analysis of laminated plates based on an unconstrained third order theory and using a radial point interpolator meshless method. *Computers and Structures* 2011; 89:1771-1784.
- [120] Kumar RK, Narayanan S. Active vibration control of beams with optimal placement of piezoelectric sensor/actuator pairs. *Smart Materials and Structures* 2008; 17:055008.
- [121] Rao SS, Shii Pan T. Optimal placement of actuators in actively controlled structures using genetic algorithms. *AIAA Journal* 1991; 29:942-943.
- [122] Chang-Qing C, Ya-Peng S. Optimal control of active structures with piezoelectric modal sensors and actuators. *Smart Materials and Structures* 1997; 6:403-409.
- [123] Bruant I, Gallimard L, Nikoukar S. Optimal piezoelectric actuator and sensor location for active vibration control, using genetic algorithm. *Journal of Sound and Vibration* 2010; 329:1615-1635.
- [124] Ray MC. Optimal Control of Laminated Plate with Piezoelectric Sensor and Actuator Layers. *AIAA Journal* 1998; 36(12):2204-2208.
- [125] Koizumi M. The concept of FGM. *Ceramic Transactions. Functionally Graded Materials* 1993; 34:3-10.
- [126] Takagi K, Li JF, Yokoyama S, Watanabe R. Fabrication and evaluation of PZT/Pt piezoelectric composites and functionally graded actuators. *Journal of the European Ceramic Society* 2003; 23:1577-1583.
- [127] Praveen GN, Reddy JN. Nonlinear transient thermo elastic analysis of functionally graded ceramic-metal plates. *International Journal of Solids and Structures* 1998; 35:4457-4476.

- [128] Zhao X, Liew KM. Geometrically nonlinear analysis of functionally graded plates using the element-free *kp*-Ritz method. *Computer Methods in Applied Mechanics and Engineering* 2009; 198:2796–2811.
- [129] Phung-Van P, Nguyen-Thoi T, Luong-Van H, Lieu-Xuan Q. Geometrically nonlinear analysis of functionally graded plates using a cell-based smoothed three-node plate element (CS-MIN3) based on the C0-HSDT. *Computer Methods in Applied Mechanics and Engineering* 2014; 270: 15-36.
- [130] Aliaga JW, Reddy JN. Nonlinear thermoelastic analysis of functionally graded plates using the third-order shear deformation theory. *International Journal of Computational Engineering Science* 2004; 5:753-779.
- [131] Phung-Van P, Nguyen-Thoi T, Bui-Xuan T, Lieu-Xuan Q. A cell-based smoothed three-node Mindlin plate element (CS-FEM-MIN3) based on the C0-type higher-order shear deformation for geometrically nonlinear analysis of laminated composite plates. *Computational Materials Science* 2015; 96:549-558.
- [132] Reddy JN, Kim J. A nonlinear modified couple stress-based third-order theory of functionally graded plates. *Composite Structures* 2012; 94:1128-1143.
- [133] Shankara CA, Iyengar NGR. A C^0 element for the free vibration analysis of laminated composite plates. *Journal of Sound and Vibration* 1996; 191:721–738.
- [134] Liew KM, He XQ, Ng TY, Kitipornchai S. Finite element piezothermoelasticity analysis and active control of FGM plates with integrated piezoelectric sensors and actuators. *Computational Mechanics* 2003; 31:350–358.
- [135] Reddy JN, Cheng ZQ. Three-dimensional solutions of smart functionally graded plates. *Journal of Applied Mechanics, ASME* 2001; 68:234 –241.
- [136] Huang XL, Shen HS. Vibration and dynamic response of functionally graded plates with piezoelectric actuators in thermal environments. *Journal of Sound Vibration* 2006; 289:25–53.
- [137] Yang J, Kitipornchai S and Liew KM. Non-linear analysis of thermo-electromechanical behavior of shear deformable FGM plates with piezoelectric actuators. *International Journal for Numerical Methods in Engineering* 2004; 59:1605–1632.
- [138] Butz A, Klinkel S, Wagner W. A geometrically and materially non-linear piezoelectric three-dimensional-beam finite element formulation including

- warping effects. *International Journal for Numerical Methods in Engineering* 2008;76:601–635.
- [139] Panda S, Ray MC. Nonlinear analysis of smart functionally graded plates integrated with a layer of piezoelectric fiber reinforced composite. *Smart Materials and Structures* 2006; 15:1595–1604.
- [140] Behjat B, Khoshravan MR. Geometrically nonlinear static and free vibration analysis of functionally graded piezoelectric plates. *Composites Structures* 2012; 94:874–882.
- [141] Yiqi M, Yiming F. Nonlinear dynamic response and active vibration control for piezoelectric functionally graded plate. *Journal of Sound and Vibration* 2010; 329(11):2015–2028.
- [142] Vahid Fakhari, Abdolreza Ohadi, Peyman Yousefian. Nonlinear free and forced vibration behavior of functionally graded plate with piezoelectric layers in thermal environment. *Composite Structures* 2011; 93:2310–2321.
- [143] Harris PJF. Carbon nanotubes and related structures: new materials for the twenty-first century. Cambridge University Press; 2001.
- [144] Fiedler B, Gojny FH, Wichmann MHG, Nolte MCM, Schulte K. Fundamental aspects of nano-reinforced composites. *Composites Science and Technology* 2006; 66:3115–3125.
- [145] Gou J, Minaie B, Wang B, Liang Z, Zhang C. Computational and experimental study of interfacial bonding of single-walled nanotube reinforced composites stiffness. *Computational Materials Science* 2004; 31:225–236.
- [146] Vodenitcharova T, Zhang LC. Bending and local buckling of a nanocomposite beam reinforced by a single-walled carbon nanotube. *International Journal of Solids and Structures* 2006; 43:3006–3024.
- [147] Wuite J, Adali S. Deflection and stress behaviour of nanocomposite reinforced beams using a multiscale analysis. *Composite Structures* 2005; 71 :388–396.
- [148] Shen HS. Postbuckling of nanotube-reinforced composite cylindrical shells in thermal environments, Part II: pressure-loaded shells. *Composite Structures* 2011; 93:2496–2503.
- [149] Arani A, Maghamikia S, Mohammadimehr M, Arefmanesh S. Buckling analysis of laminated composite rectangular plates reinforced by SWCNTs using analytical and finite element methods. *Journal of Mechanical Science and Technology* 2011; 25:809–820.

- [150] Zhu P, Lei ZX, Liew KM. Static and free vibration analyses of carbon nanotube reinforced composite plates using finite element method with first order shear deformation plate theory. *Composite Structures* 2012; 94:1450-1460.
- [151] Ke LL, Yang J, Kitipornchai S. Nonlinear free vibration of functionally graded carbon nanotube-reinforced composite beams. *Composite Structures* 2010; 92:676–683.
- [152] Shen HS. Nonlinear bending of functionally graded carbon nanotube-reinforced composite plates in thermal environments. *Composite Structures* 2009; 91:9–19.
- [153] Wang ZX, Shen HS. Nonlinear vibration and bending of sandwich plates with nanotube-reinforced composite face sheets. *Composites Part B: Engineering* 2012; 43:411–421.
- [154] Liew KM, Lei ZX, Yu JL, Zhang LW. Postbuckling of carbon nanotube-reinforced functionally graded cylindrical panels under axial compression using a meshless approach. *Computer Methods in Applied Mechanics and Engineering* 2014; 268:1–17.
- [155] Lei ZX, Liew KM, Yu JT. Free vibration analysis of functionally graded carbon nanotube-reinforced composite plates using the element-free *kp*-Ritz method in thermal environment. *Computer Methods in Applied Mechanics and Engineering* 2013; 256:189–199.
- [156] Lei ZX, Liew KM, Yu JT. Large deflection analysis of functionally graded carbon nanotube-reinforced composite plates by the element-free *kp*-Ritz method. *Composite Structures* 2013; 106:128–138.
- [157] Alibeigloo A. Static analysis of functionally graded carbon nanotube-reinforced composite plate embedded in piezoelectric layers by using theory of elasticity. *Composite Structures* 2013; 95:612–622.
- [158] Alibeigloo A. Elasticity solution of functionally graded carbon-nanotube-reinforced composite cylindrical panel with piezoelectric sensor and actuator layers. *Smart Material and Structures* 2013; 22:075013.
- [159] Alibeigloo A, Liew KM. Thermoelastic analysis of functionally graded carbon nanotube-reinforced composite plate using theory of elasticity. *Composite Structures* 2013; 106:873-881.
- [160] Wattanasakulpong N, Ungbhakorn V. Analytical solutions for bending, buckling and vibration responses of carbon nanotube-reinforced composite

- beams resting on elastic foundation. *Computational Material Science* 2013; 71:201-208.
- [161] Sobhani Aragh B, Nasrollah Barati AH, Hedayati H. Eshelby–Mori–Tanaka approach for vibrational behavior of continuously graded carbon nanotube-reinforced cylindrical panels. *Composites Part B: Engineering* 2012; 43:1943–1954.
- [162] Yas MH, Pourasghar A, Kamarian S, Heshmati M. Three-dimensional free vibration analysis of functionally graded nanocomposite cylindrical panels reinforced by carbon nanotube. *Materials & Design* 2013; 49:583–590.
- [163] Ke LL, Yang J, Kitipornchai. Nonlinear free vibration of functionally graded carbon nanotube-reinforced composite beams. *Composites Structures* 2010; 92:676-683.
- [164] Heshmati M, Yas MH. Dynamic analysis of functionally graded multi-walled carbon nanotube-polystyrene nanocomposite beams subjected to multi-moving loads. *Materials & Design* 2013; 49:894–904.
- [165] Yas MH, Samadi N. Free vibrations and buckling analysis of carbon nanotube reinforced composite Timoshenko beams on elastic foundation. *International Journal of Pressure Vessels and Piping* 2012; 98:119–128.
- [166] Rafiee M, Yang J, Kitipornchai S. Thermal bifurcation buckling of piezoelectric carbon nanotube reinforced composite beams. *Computers & Mathematics with Applications* 2013; 66:1147–1160.
- [167] Wu CP, Chang SK. Stability of carbon nanotube-reinforced composite plates with surface-bonded piezoelectric layers and under bi-axial compression. *Composites Structures* 2014; 111:587–601.
- [168] Shen HS, Zhang CL. Thermal buckling and postbuckling behavior of functionally graded carbon nanotube-reinforced composite plates. *Materials & Design* 2010; 31:3403–3411.
- [169] Shen HS, Zhu ZH. Postbuckling of sandwich plates with nanotube-reinforced composite face sheets resting on elastic foundations. *European Journal of Mechanics - A/Solids* 2012; 35:10–21.
- [170] Shen HS, Xiang Y. Postbuckling of nanotube-reinforced composite cylindrical shells under combined axial and radial mechanical loads in thermal environment. *Composite Part B: Engineering* 2013; 52:311–322.

- [171] Shen HS. Postbuckling of nanotube-reinforced composite cylindrical shells in thermal environments, part I: axially-loaded shells. *Composites Structures* 2011; 93:2096–2108.
- [172] Shen HS. Postbuckling of nanotube-reinforced composite cylindrical shells in thermal environments, part II: pressure-loaded shells. *Composites Structures* 2011; 93:2496–2503.
- [173] Liew KM, Lei ZX, Yu JL, Zhang LW. Postbuckling of carbon nanotube-reinforced functionally graded cylindrical panels under axial compression using a meshless approach. *Computer Methods in Applied Mechanics and Engineering* 2014; 268:1–17.
- [174] Shen HS. Torsional postbuckling of nanotube-reinforced composite cylindrical shells in thermal environments. *Composites Structures* 2014; 116:477–488.
- [175] Tiersten HF. *Linear piezoelectric plate vibrations*. Plenum press, New York; 1969.
- [176] Reddy JN. *Laminated composite plates and shells: theory and analysis*. CRC Press, 2003.
- [177] Shen HS. *Functionally graded materials: Nonlinear analysis of plates and shells*. CRC Press, 2009.
- [178] Praveen GN, Reddy JN. Nonlinear transient thermoelastic analysis of functionally graded ceramic-metal plates. *International Journal of Solids and Structures* 1998; 35:4457-4476.
- [179] Reddy JN, Chin CD. Thermomechanical analysis of functionally graded cylinders and plates. *Journal of Thermal Stresses* 1998; 21:593-626.
- [180] Reddy JN, Cheng ZQ. Three-dimensional thermomechanical deformations of functionally graded rectangular plates. *European Journal of Mechanics – A/Solids* 2011; 20:841-855.
- [181] Reddy JN. Analysis of functionally graded plates. *International Journal for Numerical Method in Engineering* 2000; 47:663–684.
- [182] Shen HS, Zhang CL. Thermal buckling and postbuckling behavior of functionally graded carbon nanotube-reinforced composite plates. *Materials and Design* 2010; 31:3403–3411.
- [183] Mori T, Tanaka K. Average stress in matrix and average elastic energy of materials with misfitting inclusions. *Acta Metallurgica* 1973; 21:571–574.

- [184] Wang J, Pyrz R. Prediction of the overall moduli of layered silicate-reinforced nanocomposites – Part I: Basic theory and formulas. *Composites Science and Technology* 2004; 64:925–934.
- [185] Librescu L, Oh SY, Song O. Thin-walled beams made of functionally graded materials and operating in a high temperature environment: vibration and
- [186] Reddy JN. *Theory and analysis of elastic plates and shells*. CRC Press, 2007.
- [187] Reissner E. The effect of transverse shear deformation on the bending. *Journal of Applied Mechanics: ASME DC* 1945; 12:69–77.
- [188] Mindlin RD. Influence of rotatory inertia and shear on flexural motion of isotropic, elastic plates. *Journal of Applied Mechanics: ASME DC* 1951; 18:31–38.
- [189] Whitney JM. Shear correction factors for orthotropic laminates under static load. *Journal of Applied Mechanics* 1973; 302-304.
- [190] Bert CW. Simplified analysis of static shear correction factors for beam of non-homogeneous cross section. *Journal of Composite Materials* 1973; 7:525-529.
- [191] Reddy JN. A simple higher-order theory for laminated composite plates. *Journal of Applied Mechanics* 1984; 51:745–752.
- [192] Aydogdu M. A new shear deformation theory for laminated composite plates. *Composites Structures* 2009; 89:94–101.
- [193] Soldatos KP. A transverse shear deformation theory for homogenous monoclinic plates. *Acta Mechanica* 1992; 94:195–220.
- [194] Touratier M. An efficient standard plate theory. *International Journal of Engineering Science* 1991; 29:745–752.
- [195] Nguyen-Xuan H, Chien H. Thai, Nguyen-Thoi T. Isogeometric finite element analysis of composite sandwich plates using a higher order shear deformation theory. *Composite part B: Engineering* 2013; 55:558-574.
- [196] Arya H, Shimpi RP, Naik NK. A zigzag model for laminated composite beams. *Composite Structures* 2002; 56: 21-24.
- [197] Thai H Chien, Bordas SPA, Ferreira AJM, Rabczuk T, Nguyen-Xuan H. Isogeometric analysis of laminated composite and sandwich plates using a new inverse trigonometric shear deformation theory. *European Journal of Mechanics - A/Solids* 2014; 43:89-108.
- [198] Les Piegl, Wayne Tiller. *The NURBS book*. Springer 2nd edition. Germany, 1997.

- [199] Nguyen VP, Kerfriden P, Bordas SPA. Two- and three-dimensional isogeometric cohesive elements for composite delamination analysis. *Composites part B: Engineering* 2014; 60:193-212.
- [200] Nguyen VP, Nguyen-Xuan H. High-order B-splines based finite elements for delamination analysis of laminated composites. *Composite Structure* 2013; 102:261-275.
- [201] Nguyen VP, Kerfriden P, Bordas SPA, Rabczuk T. Isogeometric analysis suitable trivariate NURBS representation of composite panels with a new offset algorithm. *Computer Aided Design* 2014; 55:49-63.
- [202] Heyliger P, Saravanan DA. Exact free-vibration analysis of laminated plates with embedded piezoelectric layers. *Journal of the Acoustical Society of America* 1995; 98:1547-1557.
- [203] Hughes TJR, Evans JA, Reali A. Finite Element and NURBS Approximations of Eigenvalue, Boundary-value, and Initial-value Problems. *Computer Methods in Applied Mechanics and Engineering* 2014; 272:290–320.
- [204] Fung YC. *Foundation of Solid Mechanics*. Prentice Hall; 1965.
- [205] Reddy JN. *An introduction to nonlinear finite element analysis*. Oxford University Press; 2004.
- [206] Newmark NM. A method of computation for structural dynamics. *Journal of the Engineering Mechanics Division ASCE* 1959; 85:67-94.
- [207] Reddy JN. Geometrically nonlinear transient analysis of laminated composite plates. *AIAA Journal* 1983; 21:621-629.
- [208] Bathe KJ. *Finite element procedures*. NJ: Prentice-Hall; 1996.
- [209] Pica A, Wood RD, Hinton E. Finite element analysis of geometrically nonlinear plate behaviour using a mindlin formulation. *Computers & Structures* 1980; 11:203-215.
- [210] He XQ, Ng TY, Sivashanker S, Liew KM. Active control of FGM plates with integrated piezoelectric sensors and actuators. *International Journal of Solids and Structures* 2001; 38: 1641-1655.
- [211] Chen J, Dawe DJ, Wang S. Nonlinear transient analysis of rectangular composite laminated plates. *Composite Structures* 2000; 49:129-139.
- [212] Han Y, Elliott J. Molecular dynamics simulations of the elastic properties of polymer/carbon nanotube composites. *Computational Materials Science* 2007; 39:315–323.

- [213] Zhang CL, Shen HS. Temperature-dependent elastic properties of single-walled carbon nanotubes: prediction from molecular dynamics simulation. *Applied Physics Letters* 2006; 89:081904.
- [214] Pagano NJ. Exact solutions for rectangular bidirectional composites and sandwich plates. *Journal of Composite Materials* 1970; 4:20–34.
- [215] Pagano NJ, Hatfield SJ. Elastic behavior of multilayered composite bidirectional composites. *Mechanics of Composite Materials* 1994; 34:124–127.
- [216] Mahmud AS, Liu Y, Nam TH. Gradient anneal of functionally graded NiTi. *Smart Materials and Structures* 2008; 17:015031.
- [217] Hasanyan DJ, Batra RC, Harutyunyan RC. Pull-in instabilities in functionally graded micro-thermo-electromechanical systems. *Journal of Thermal Stresses* 2008; 31:1006–1021.
- [218] Witvrouw A, Mehta A. The use of functionally graded poly-SiGe layers for MEMS applications. *Materials Science Forum* 2005; 492–493:255–260.

